

République Algérienne Démocratique et Populaire  
Ministère de l'Enseignement Supérieur et de la Recherche Scientifique  
Université Frères Mentouri Constantine 1  
Faculté des Sciences Exactes  
Département de Physique

No d'ordre : 0 3 / D 3 C / 2 0 2 0  
No de série :01/phy/2020

# Thèse

Pour obtenir le diplôme de  
**Doctorat Troisième Cycle LMD en Physique**

Spécialité  
**Particules élémentaires et Cosmologie**

Thème

**New redshift and its implications**

Présentée par  
**MOHAMED LAMINE ABDELALI**

Le22 / 0 1 / 2020

Devant le jury

Président	Mr. Mimouni Jamel	Prof. à l'univ. Frères Mentouri - Constantine 1
Rapporteur	Mr. Mebarki Noureddine	Prof. à l'univ. Frères Mentouri - Constantine 1
Examineur	Mr. Aissaoui Habib	Prof. à l'univ. Frères Mentouri - Constantine 1
	Mr. Attallah Reda	Prof. à l'univ. Badji Mokhtar - Annaba
	Mr. Zaim Slimane	Prof. à l'univ. Hadj Lakhdar - Batna 1
	Mr. Boussahel Mounir	Prof. à l'univ. Mohamed Boudiaf - M'Sila

# Remerciement

Je remercie en premier lieu **Allah** le tout puissant pour toute la volonté et le courage qu'il m'a donné pour mener ce travail au terme. Tous les mots de remerciement ne suffirent pas à la femme qui ma tous donner pour ma réussite, **ma chère mère**.

La réalisation de cette recherche était possible par le soutien incondtionnel de mon encadreur et rapporteur de thèse **Prof. Mebarki Nourreddine**. Je lui remercie infiniment de croire en moi et pour ses commentaires qui ont aidé à l'élaboration de cette thèse. Je remercie sincèrement tous les honorables membres de jury en commençant par le président de jury **Prof. Mimouni Jamel** ainsi que les examinateurs **Prof. Aissaoui Habib**, **Prof. Attallah Reda**, **Prof. Zaim Slimane** et **Prof. Boussahel Mounir**.

Les simulations décrites dans cette thèse ont été réalisées à l'aide des codes publics comme **Enzo**, **YT** et **CRPROPA**. Je tiens donc à saluer l'engagement et les efforts de collaboration de nombreux de la communauté scientifique. Ce travail a été autorisé à accéder aux ressources HPC de l'UCI-UFMC "Unite de Calcul Intensif" de l'Université des Frères Mentouri Constantine 1. Je remercie cordialement le directeur de l'unité **Mr. Siaf Riad** et les deux ingénieurs **Mr. Oulbani Abdeldjalil** et **Mr. Mélizi Nouredine** pour l'accueil et l'aide dans la ralisation de nos simulations.

Un remerciement particulier pour **Prof. Aitmoussa Karim** et **Prof. Benslama Achour** pour leurs avis et remarques qui ont aidé le raffiner ce document. Je voudrais aussi remercier tout les enseignants du laboratoire de physique mathématique et subatomique (LPMS) qui m'ont enseignés durant ma formation. Je souhaite remercier mes collègues doctorants chacun avec son nom pour les échanges scientifiques ainsi que personnels qu'on a eu pendant ces années de thèse au sein du LPMS. Un grands merci à tous ceux qui ont contribué de manière directe ou indirecte à l'accomplissement de ce travaille de thèse.

To my Dear, to my Mother

# Contents

<b>List of Figures</b>	<b>8</b>
<b>List of Tables</b>	<b>9</b>
<b>Notation</b>	<b>10</b>
<b>Abbreviation</b>	<b>12</b>
<b>Introduction</b>	<b>15</b>
<b>1 Basic notions in astrophysics and cosmology</b>	<b>16</b>
1.1 Observational cosmology . . . . .	16
1.1.1 Distance ladder . . . . .	16
1.1.2 Redshifts, Hubble law and accelerated expansion of the Universe . .	19
1.1.3 Evidence for dark matter . . . . .	20
1.1.4 Cosmic microwave background . . . . .	21
1.2 Relativistic cosmology . . . . .	22
1.2.1 Friedmann Lemaitre Robertson Walker spacetime . . . . .	22
1.2.2 Cosmological parameters . . . . .	24
1.2.3 Cosmological fluid components . . . . .	25
1.2.4 Special particles . . . . .	26
1.2.5 Cosmological redshift . . . . .	27
1.2.6 Cosmic distances . . . . .	28
1.2.7 Thermal history . . . . .	30
1.3 Open problems in cosmology . . . . .	31
1.3.1 Uncertainties in distance measurements . . . . .	31
1.3.2 Estimating cosmological parameters . . . . .	32
1.3.3 Cosmological constant and dark energy . . . . .	35
1.3.4 Dark matter and small-scale anomalies . . . . .	35
1.3.5 Other problems . . . . .	36
1.3.6 Ingoing observational researches . . . . .	36
1.4 Cosmic magnetic fields . . . . .	37
1.4.1 Observations . . . . .	37
1.4.2 Origins . . . . .	39
1.4.3 Magnetogenesis . . . . .	40
1.4.4 Primordial magnetic fields constrains . . . . .	41
1.5 Cosmic rays . . . . .	43
1.5.1 Observations . . . . .	43
1.5.2 UHECR Cut-off . . . . .	44
1.6 Numerical simulations in cosmology and astrophysics . . . . .	47
1.7 Chapter conclusions . . . . .	48

<b>2</b>	<b>SCOPE: Constraining cosmological parameters using Boltzmann equations</b>	<b>49</b>
2.1	Recombination era and densities evolution . . . . .	49
2.2	Code algorithm . . . . .	51
2.3	First results and discussions . . . . .	54
2.4	Application on Neutrinos : massive vs. relativistic . . . . .	54
2.5	Chapter conclusions . . . . .	66
<b>3</b>	<b>Curvature conservation of primordial magnetic fields</b>	<b>68</b>
3.1	P.M.F. evolution through recombination . . . . .	68
3.2	New evolution equations . . . . .	69
3.3	Analytical solutions . . . . .	70
3.4	Discussions and impacts on CMB anisotropies . . . . .	73
3.5	Chapter conclusions . . . . .	74
<b>4</b>	<b>Magnetically induced redshift effect</b>	<b>75</b>
4.1	Conventional redshifts . . . . .	75
4.2	Exotic redshift effects . . . . .	77
4.3	New magnetically induced redshift : mathematical formalism . . . . .	78
4.4	Discussion of the new effect and possible implications . . . . .	82
4.5	Chapter conclusions . . . . .	84
<b>5</b>	<b>RPC - Interpolation from observed Redshift</b>	<b>86</b>
5.1	Magnetic fields models in cosmic environment . . . . .	86
5.2	Code algorithm . . . . .	87
5.3	Results and discussions . . . . .	89
5.4	Chapter conclusions . . . . .	94
<b>6</b>	<b>Possible explanation of trans-GZK events of UHECR</b>	<b>97</b>
6.1	Proposed explanation to GZK violation . . . . .	97
6.2	New explanation using our MIR effect . . . . .	100
6.3	Extended CRPROPA code and simulations done . . . . .	101
6.4	First results and discussions . . . . .	102
6.5	Chapter conclusions . . . . .	111
<b>7</b>	<b>Cosmological simulations and synthetic observations</b>	<b>112</b>
7.1	Need for cosmological simulations . . . . .	112
7.2	Customized cosmological simulations: code, common settings and variations	113
7.3	Synthetic observation: code and algorithm . . . . .	115
7.4	Chapter conclusions . . . . .	117
<b>8</b>	<b>Simulations results</b>	<b>118</b>
8.1	Possible misinterpretation of redshift deviations origins . . . . .	118
8.2	Impact on Hubble constant estimation . . . . .	125
8.3	Compact galaxy groups and galaxy-quasar associations : Synthetic equivalent examples . . . . .	126
8.4	Impacts on Stephan's quintet models . . . . .	130
8.5	Chapter conclusions . . . . .	132

# CONTENTS

<b>9</b>	<b>Discussions</b>	<b>133</b>
9.1	Results confirmed by other simulations . . . . .	133
9.2	Magnetic field evolution with feedback models . . . . .	142
9.3	Other magnetic field configurations tested . . . . .	151
9.4	Possible explanation of extra bias found in data . . . . .	155
9.5	Extreme cases and supernovae data . . . . .	156
9.6	Implication on CMB studies . . . . .	156
9.7	Extreme Universe scenarios . . . . .	160
9.8	Chapter conclusions . . . . .	160
	<b>Conclusion</b>	<b>164</b>
<b>A</b>	<b>Exact solutions to linearised Einstein equations</b>	<b>165</b>
<b>B</b>	<b>Extended ENZO</b>	<b>167</b>
<b>C</b>	<b>Scientific contributions</b>	<b>170</b>
C.1	Papers and proceedings . . . . .	170
C.2	Conferences . . . . .	170

# List of Figures

2.1	Free electron fraction evolution . . . . .	51
2.2	Accepted combinations SCOPE Sim.002 . . . . .	55
2.3	Accepted combinations SCOPE Sim.020 . . . . .	56
2.4	Accepted combinations SCOPE Sim.021 . . . . .	57
2.5	Accepted combinations SCOPE Sim.040 . . . . .	58
2.6	Accepted combinations SCOPE Sim.043 . . . . .	59
2.7	Accepted vs refused combinations SCOPE Sim.013 . . . . .	60
2.8	Accepted vs refused combinations SCOPE Sim.035 . . . . .	61
2.9	Accepted vs refused combinations SCOPE Sim.043 . . . . .	62
2.10	Accepted combinations SCOPE Sim.019, Sim.047 and Sim.001 . . . . .	63
2.11	Accepted combinations SCOPE Sim.002 and Sim.004 . . . . .	64
2.12	Accepted combinations SCOPE Sim.046 and Sim.013 . . . . .	65
5.1	Probability distribution dependence to magnetic fields means $b_0$ . . . . .	90
5.2	Probability distribution dependence to patches lengths mean $l_0$ . . . . .	91
5.3	Probability distribution dependence to patches randomness parameter $l_{ran}$ . . . . .	91
5.4	Probability distribution dependence to deceleration parameter $q_0$ 1 . . . . .	91
5.5	Probability distribution dependence to deceleration parameter $q_0$ 2 . . . . .	92
5.6	Probability distribution dependence to number of paths simulated done $N_{sim}$ . . . . .	92
5.7	Probability distribution dependence to observed redshift $Z_{Obs}$ 1 . . . . .	92
5.8	Probability distribution dependence to observed redshift $Z_{Obs}$ 2 . . . . .	93
5.9	Probability distribution dependence to observed redshift $Z_{Obs}$ 3 . . . . .	93
5.10	Probability distribution dependence to observed redshift $Z_{Obs}$ 4 . . . . .	93
5.11	Probability distribution dependence to observed redshift $Z_{Obs}$ 5 . . . . .	94
5.12	Probability densities for several observed redshift values $Z_{Obs}$ 1 . . . . .	94
5.13	Probability densities for several observed redshift values $Z_{Obs}$ 2 . . . . .	95
5.14	Probability densities for several cosmological redshift values $Z_{Cos}$ 1 . . . . .	95
5.15	Probability densities for several cosmological redshift values $Z_{Cos}$ 2 . . . . .	95
6.1	Apparent vs cosmological distance for all simulations of Extended CRPROPA . . . . .	103
6.2	Final Energy vs Travelled distances for all simulations of Extended CR- PROPA . . . . .	103
6.3	Final energy vs Initial energy for all simulations of Extended CRPROPA . . . . .	104
6.4	Final Energy vs Travelled distances for Extended CRPROPA simulation Sim.016 . . . . .	104
6.5	Final Energy vs Travelled distances for Extended CRPROPA simulation Sim.002 . . . . .	105
6.6	Final Energy vs Travelled distances for Extended CRPROPA simulation Sim.030 . . . . .	105
6.7	Apparent vs cosmological distance for observed particles of Extended CR- PROPA simulation Sim.003 . . . . .	106

## LIST OF FIGURES

6.8	Apparent vs cosmological distance for observed particles of Extended CR-PROPA simulation Sim.004 . . . . .	107
6.9	Apparent vs cosmological distance for observed particles of Extended CR-PROPA simulation Sim.016 . . . . .	107
6.10	Deviation angles vs Distances of Extended CRPROPA simulation Sim.001	108
6.11	Deviation angles vs Distances of Extended CRPROPA simulation Sim.004	108
6.12	Deviation angles histogram of Extended CRPROPA simulations . . . . .	109
6.13	Deviation angles vs Initial energies of all Extended CRPROPA simulations	109
8.1	Observed haloes' distances plotted vs. observed redshift 1 of ENZO-YT Sim.9 . . . . .	119
8.2	Observed haloes' distances plotted vs. observed redshift 2 of ENZO-YT Sim.9 . . . . .	120
8.3	Observed haloes' distances plotted vs. observed redshift 3 of ENZO-YT Sim.9 . . . . .	120
8.4	Redshifts vs. Distances of Virgo cluster . . . . .	121
8.5	All-sky map of ENZO-YT Sim.9 halos filtered by gravitational redshifts contributions . . . . .	122
8.6	All-sky map of ENZO-YT Sim.9 halos filtered by our MIR contributions .	122
8.7	All-sky map of ENZO-YT Sim.9 haloes filtered by MIR and gravitational redshifts contributions . . . . .	123
8.8	Gravitational potential vs. cosmic time for ENZO-YT Sim.9 . . . . .	124
8.9	Histograms for each redshift effect contribution for ENZO-YT Sim.9 . . . .	124
8.10	Hubble constant estimations of ENZO-YT Sim.9 . . . . .	126
8.11	All-sky map for special cases found in ENZO-YT Sim.9 . . . . .	127
8.12	Density projection annotated with the special cases of ENZO-YT Sim.9 . .	128
8.13	Magnetic fields projection annotated with the special cases of ENZO-YT Sim.9 . . . . .	128
8.14	Our redshift effect elementary contributions for galaxy 71 of ENZO-YT Sim.9	129
8.15	Our redshift effect elementary contributions for galaxy 169 of ENZO-YT Sim.9 . . . . .	129
9.1	All-sky map for all observed halos of of ENZO-YT Sim.9 . . . . .	134
9.2	All-sky map for all observed halos of of ENZO-YT Sim.10 . . . . .	134
9.3	All-sky map for all observed halos of of ENZO-YT Sim.17 . . . . .	135
9.4	All-sky map for all observed halos of of ENZO-YT Sim.8.1 . . . . .	135
9.5	Both observed redshifts vs. distances of observed halos of ENZO-YT Sim.13	138
9.6	Both observed redshifts vs. distances of observed halos of ENZO-YT Sim.12	138
9.7	Both observed redshifts vs. distances of observed halos of ENZO-YT Sim.18	139
9.8	Both observed redshifts vs. distances of observed halos of ENZO-YT Sim.10	139
9.9	Both observed redshifts vs. distances of observed halos of ENZO-YT Sim.17	140
9.10	Histograms of different effects contributions of ENZO-YT Sim.18 observed halos . . . . .	140
9.11	Histograms of different effects contributions of ENZO-YT Sim.13 observed halos . . . . .	141
9.12	Histograms of different effects contributions of ENZO-YT Sim.17 observed halos . . . . .	141
9.13	Histograms of different effects contributions of ENZO-YT Sim.10 observed halos . . . . .	142
9.14	All-sky map of ENZO-YT Sim.13 haloes filtered by MIR and gravitational redshifts contributions . . . . .	143

## LIST OF FIGURES

9.15 All-sky map of ENZO-YT Sim.17 haloes filtered by MIR and gravitational redshifts contributions . . . . .	143
9.16 All-sky map of ENZO-YT Sim.10 haloes filtered by MIR and gravitational redshifts contributions . . . . .	144
9.17 Hubble constant estimations of all deviations cases of ENZO-YT Sim.12 . .	144
9.18 Hubble constant estimations of all deviations cases of ENZO-YT Sim.18 . .	145
9.19 Hubble constant estimations of all deviations cases of ENZO-YT Sim.10 . .	145
9.20 Hubble constant estimations of all deviations cases of ENZO-YT Sim.13 . .	146
9.21 Hubble constant estimations of all deviations cases of ENZO-YT Sim.17 . .	146
9.22 Maximum magnetic fields plotted vs. cosmic time for initial values seeded .	148
9.23 Mean magnetic fields plotted vs. cosmic time for initial values seeded . . .	149
9.24 Minimum magnetic fields plotted vs. cosmic time for initial values seeded .	149
9.25 Maximum magnetic fields plotted vs. cosmic time for simulation resolution	150
9.26 Mean magnetic fields plotted vs. cosmic time for simulation resolution . . .	150
9.27 Minimum magnetic fields plotted vs. cosmic time for simulation resolution	151
9.28 Minimum magnetic fields plotted vs. cosmic time for feedbacks processes .	152
9.29 Maximum magnetic fields plotted vs. cosmic time for feedback models . . .	152
9.30 Mean magnetic fields plotted vs. cosmic time for feedback models . . . . .	153
9.31 Minimum gas densities plotted vs. cosmic time for feedbacks processes . .	153
9.32 Maximum gas densities plotted vs. cosmic time for feedback models . . . .	154
9.33 Mean gas densities plotted vs. cosmic time for feedback models . . . . .	154
9.34 All-sky map of CMB anisotropies from our effect of ENZO-YT Sim.9 . . .	158
9.35 All-sky map of CMB anisotropies from our effect of ENZO-YT Sim.13 . . .	158
9.36 All-sky map of CMB anisotropies from our effect of ENZO-YT Sim.10 . . .	159
9.37 All-sky map of CMB anisotropies from our effect of ENZO-YT Sim.16 . . .	159

# List of Tables

2.1	Input parameters for simulations done using SCOPE code . . . . .	53
2.2	Input parameters for special simulations done using SCOPE code . . . . .	53
4.1	Estimations of our magnetically induced redshift effect . . . . .	84
6.1	Common input parameters for simulations done using Extended CRPROPA code . . . . .	101
6.2	Input parameters for simulations done using Extended CRPROPA code . . . . .	102
6.3	All events observed in simulations done by Extended CRPROPA code . . . . .	110
8.1	Synthetic observational data for important abnormal cases in Sim.9 . . . . .	126
9.1	Mainly changed parameters in <code>inits.exe</code> parameter files . . . . .	136
9.2	Mainly changed parameters in ENZO parameter files . . . . .	136
9.3	Magnetic fields outcomes of the ENZO-YT simulations done . . . . .	137
9.4	Maximum and minimum cell side sizes of ENZO-YT simulations done . . . . .	147

# Notation

Latin indices (e.g.  $i, j, k$ ) run over the three spatial coordinates and assume values 1, 2, 3. In a Cartesian coordinate system, we shall use  $x^1 = x$ ,  $x^2 = y$  and  $x^3 = z$ . Greek indices (e.g.  $\mu, \nu, \rho$ ) run over the four spacetime coordinates and assume values 0, 1, 2, 3, with  $x^0$  being the time coordinate. Repeated high and low indices are summed unless otherwise stated, i.e.  $x^\mu y_\mu = \sum_{\mu=0}^3 x^\mu y_\mu$  or  $x^i y_i = \sum_{i=0}^3 x^i y_i$ . The signature employed for the metric is  $(-, +, +, +)$ . A dot over any quantity denotes the derivation with respect to the cosmic time, denoted with  $t$ , of this quantity.  $\partial_\mu$  is used as a shorthand for the partial derivative with respect the coordinate  $x_\mu$ . Except on vector and tensor, a 0 subscript means that a time-dependent quantity is evaluated today, i.e. at  $t = t_0$  where  $t_0$  represent the age of the Universe in the cosmic time. The subscripts  $k, b, dm, m, \Lambda, r, \gamma$  and  $\nu$  put on matter quantities such as density and pressure refer to curvature, baryons, cold dark matter, matter, cosmological constant, radiation, photons and neutrinos, respectively. Mostly, we use natural unit to describe temperature, mass, time and length in function of energy. In cosmological context, we use CMB temperatures (given in  $eV$ ) as time indicators of the Universe evolution or equivalently scale factor or redshift.

# Abbreviation

**AGN** Active galactic nuclei  
**AMR** Adaptive Mech Refinement  
**APOGEE** Apache Point Observatory Galaxy Evolution Experiment  
**BAO** Baryon Acoustic Oscillations  
**BBN** Big Bang Nucleosynthesis  
**BOOMERanG** Balloon Observations Of Millimetric Extragalactic Radiation ANd Geophysics  
**BOSS** Baryon Oscillation Spectroscopic Survey collaboration  
**CDM** Cold Dark Matter  
**CFL** Courant-Friedrichs-Lewy  
**CMB** Cosmic Microwave Background  
**CMF** Cosmic magnetic fields  
**CoBE** Cosmic Background Explorer  
**COre** Cosmic Origins Explorer  
**CP** Charge-Parity symmetry  
**CR** Cosmic Rays  
**DE** Dark Energy  
**DES** Dark Energy Survey  
**DM** Dark Matter  
**EGCR** Extragalactic cosmic rays  
**EGMF** Extra-Galactic Magnetic Fields  
**ESA** European Space Agency  
**EW** ElectroWeak  
**FIBR** Far Infrared Background radiations  
**FLRW** Friedmann-Lemaitre-Robertson-Walker metric  
**GAIA** Global Astrometric Interferometer for Astrophysics  
**GCR** Galactic cosmic rays  
**GR** General Relativity  
**GUT** Grand Unified Theory  
**GW** Gravitational waves  
**GZK** Greisen Zatsepin Kuzmin cut off  
**HDM** Hot Dark Matter  
**HFGW** High frequency gravitational waves background  
**HiRes** High Resolution Fly's Eye  
**HLL** Harten-Lax-van Leer  
**HR** Hertzsprung-Russell diagram  
**HST** Hubble Space Telescope  
**JLA** Joint light-curve analysis  
**J-PAS** Javalambre Physics of the accelerating Universe Astronomical Survey  
**LHC** Large Hadron Collider  
**LSST** Large Synoptic Survey Telescope

## ABBREVIATION

**MaNGA** Mapping Nearby Galaxies at Apache Point Observatory  
**MHD** Magneto-hydrodynamics  
**MIR** Magnetically Induced Redshift  
**NASA** National Aeronautics and Space Administration  
**PAO** Pierre Auger Observatory  
**PL** Period-Luminosity relation  
**PLM** Piecewise Linear Method  
**PMF** Primordial Magnetic Fields  
**QCD** Quantum Chromo-Dynamics  
**QED** Quantum Electro-Dynamics  
**QFT** Quantum Field Theory  
**QSO** Quasi Stellar Objects  
**RAX10** Renaud, Appleton and Xu (2010) [350]  
**RK** Runge-Kutta scheme  
**RPC** Redshift Project Code  
**SCOPE** Simulation for COsmological Parameters Estimation  
**SDSS** Sloan Digital Sky Survey  
**SN** Supernovae  
**SNIa** Type Ia supernovae  
**SPH** Smoothed Particle Hydrodynamics  
**SQ** Stephan's Quintet  
**SZ** Sunyaev-Zel'dovich Effect  
**TRGB** Tip of the Red Giant Branch Method  
**UHECR** Ultra high energy cosmic rays  
**WDM** Warm Dark Matter  
**WDW15** Wojtak, Davis and Wiis (2015) [271]  
**WFIRST** Wide Field Infrared Survey Telescope  
**WIMP** Weakly Interacting Massive Particles  
**WMAP** Wilkinson Microwave Anisotropy Probe

# Introduction

From ancient ages, heavens had captured the imagination and curiosity of human kind. Along with our evolution, our perception and understanding of the cosmos had evolved. The big bang is the theoretical model currently accepted by the scientific community to describe the origin and evolution of the cosmos. This model is based on the Einstein's general relativity theory. This theory is describing gravitational interactions which are the main interaction between the Universe components and are driven its evolution. In the precision era of cosmology, we still have open questions such as : accelerated expansion of the Universe, cosmological parameters estimations, velocity curves of galaxies, structure formation, cosmic magnetic fields and Ultra high energy cosmic rays. Two components of the Universe are theorized to account for these observations and complete our models : dark matter and dark energy. We still don't understand their elementary composition or origin. In big bang model, cosmological parameters are key indicators of the state and the fate of the Universe. But, there is still tension on the values of cosmological parameters from different research teams. For example, the Hubble constant is estimated to be  $H_0 = 73.03 \pm 1.79 \text{ km/s/Mpc}$  determined from the distance ladder (megamasers, Cepheids, and Type Ia supernovae) (see Ref. [1]) and to be  $H_0 = 67.51 \pm 0.64 \text{ km/s/Mpc}$  determined from Planck 2015 results (see Ref. [2]). We notice this discrepancy between estimations given by different observational and analysis techniques. These differences are not negligible and create the need for more accurate data and affined analysis methods.

In our research, we are trying to get more understanding and light on unsolved questions of modern cosmology and astrophysics. To solve those questions, lot of efforts are done to improve performance of instruments to eliminate data distortion by hardware (satellites and telescopes) and online-software imperfections. Starting from data collection, software and hardware failures and observational limitations such as pixilation or wavelength resolution are interfering with the quality of our data. Although all efforts on data collection, the processed data contain several signals that must be separated. Effects like foreground emitters, gravitational lensing, or galaxies' peculiar motion represent a noise on the main cosmological signal needed to estimate the cosmological parameters. This is part of experimental cosmology and astrophysics and is out of the scope of this work. Another approach used is testing new theories of gravity by extending Einstein's general relativity, or beyond standard model theories for particle physics. Those theories present new effects that could impacted our data for large scales or at extreme energies. Then, researches attempt to find ideal candidates to account for dark energy and dark matter compositions which are also out of the scope of this work. Our approach in this work is re-examining our perception of observations to account for all possible effects contributing to our data. Those effects could be conventional that were believed to be negligible or new ones predicted within standard theories such as Einstein's general relativity which were not considered in previous analysis methods.

Our data describing cosmic history are coming from a single messenger : photons of ancient and distant sources. Light from its far emitters in the Universe to observer had encountered several processes like dispersion, scattering and absorption in the cosmic

# INTRODUCTION

environment. The processes differ from a source to another and from a direction to another affected by the local inhomogeneities. Along with intensity and polarization, redshift is a major indicator of processes creating these photons and their trajectories. Redshift (and blueshift) is a shift the photon's frequency due to several effects. The most considered in astrophysical studies, conventional, are: cosmological, Doppler Effect and gravitational redshifts. The observed redshift represents a combination of all those effects and any other kind of redshift effects (of non cosmological nature) that could affect the travelling photons. Cosmological redshift is carrying the information about the Universe's expansion which is then needed to infer cosmological parameters. The two other effects represent a noise to this main signal by causing noticeable differences between observed redshift and the cosmological redshift of an extragalactic object. Doppler Effect impacts are estimated by considering the peculiar motion of galaxies. The gravitational redshift contribution was considered to be negligible. A number of recent articles had investigated the cosmological parameters bias caused by gravitational redshifts (e.g. Refs. [3] and [4]). But, we still have this discrepancy in cosmological parameters estimations of Calcino and Davis (2017) (see Ref. [5]). As an interesting possibility, this additional bias may represent the contribution of another redshift effect of non cosmological origin. This contribution must not be blamed on measurement errors.

Some other paradoxical observations are found also in local scales in astrophysics. For instance, several abnormal cases exist in redshift observations of galaxy-galaxy or galaxy-quasar associations like the case of Seyfert galaxy NGC 7603 (e.g. Ref. [6]). Several other cases were illustrated in Lopez-Corredoira and Gutierrez (2006) (e.g. Ref. [7]) and in the full Arp list of anomalous redshifts and connections between astrophysical objects with discordant redshifts (see Ref. [8]). The apparent physical connection between those objects is contradicting the high redshift differences between them. In all those cases, the discrepancy is in the observed redshifts of those objects which gives a contradicting indication on distance. From one side, big redshift differences must indicate big distance between them. And from the other side, we observe a physical connection or gravitational interaction that should be resulting from close positions of those objects. The only explanation of this paradox is to reconsider the observed redshift origin. Only cosmological contribution could be used to indicate distances. The contribution of other effects could be responsible for those discordant redshift observations. Both Doppler and gravitational redshift contributions fail to explain those cases. Those observations give further arguments in favor of another redshift effect that must be considered to get a correct understanding of the real configuration of those galaxies. Another famous case is Stephen's Quintet (e.g. Ref. [9]) in which 5 galaxies are interacting gravitationally with each other, but one of them has an abnormal high redshift and thought that is far behind the other galaxies. In that case, the galaxy NCG 7320 (with  $z = 0.0027$  and others are at 0.022 and 0.019) is not confirmed to be part the cluster or in gravitational interaction with the other galaxies. Arp (1973) (see Ref. [10]) believed that the light from NCG 7320 is affected by non-Doppler effects making it appear to be a foreground galaxy. Numerical simulations were done to test models recreating the evolution history of this cluster. The radial velocities are estimated from redshift measurements and are very influential on the model evolution. The existence of another redshift effect may contribute to the explanation of this case which was not considered before.

We present in this work new perspectives to several problems such as cosmological parameters estimations. Origins and evolution of cosmic magnetic fields and ultra high energy cosmic rays represent also enigmatic and unsolved problems in modern cosmology and are also studied with new approaches. But, the main subject of this work is a new redshift effect and the estimation of its potential to answer those unsolved questions

## INTRODUCTION

both on global and local scales. The cosmic magnetic fields existence is more and more confirmed by several studies and in all cosmic scales. These fields are creating an impact on cosmological and astrophysical data due this new redshift effect. Such an effect have its contribution in observed redshifts of different sources. This effect is likely affecting the cosmological parameters estimations similarly to gravitational redshifts. Cosmological simulations and synthetic observations are argued to be the best way to estimate the contribution of this new redshift and to compare it to other bias effects. We use a theoretical study to those problems with analytical and especially numerical methods. We progress in our work from simple theoretical predictions to synthetic observations creation which approaches eventually real conditions of the Universe evolution and current state.

# Chapter 1

## Basic notions in astrophysics and cosmology

In this Chapter, we present an overview of cosmology, addressing its most important aspects. We start from some observational experiments and its tremendous evolution during the last hundred years. Then, a short and concise presentation is given for theoretical foundations of Big bang and  $\Lambda$ CDM model. Next is the important topics of cosmological parameters estimations, cosmic magnetic fields and cosmic rays. Finally, the chapter ends with an overview of open problems in modern cosmology and new method used in their studies which is cosmological simulations.

### 1.1 Observational cosmology

We focus in this section on important ongoing cosmological observations or ended recently. This section introduces wide range of topics from the evidence for the expanding Universe to Cosmic Microwave Background anisotropies.

#### 1.1.1 Distance ladder

To understand distant objects physics, it is necessary to measure their physical extension and their total emitted energy. We observe only apparent magnitude and angular extension of an object. The distance to this object is then needed to convert the apparent quantities to the absolute magnitudes (and thereby luminosity/energy) and physical sizes. In cosmology, distances are also used to make 3 dimensional maps of the structure in the Universe in order to understand its evolution.

There are several methods available to measure distances of objects in the Universe. No single technique can measure distances at all ranges and all of them has the principal problem of calibration. They suffer from large uncertainties particularly when measuring largest distances. These methods used are based on assumptions which have not been properly verified. Fortunately, these assumptions are different and independent. Exact distance measurements could be then obtained using cross-checks between different methods. There are few main classes of methods to measure distances: Triognometric parallax, Distance indicators like Cepheid stars, supernovae and the Tully-Fisher relation and Hubble law. We present each of these in turn.

**Parallax** - The apparent angular shift of an object between two observations located at different positions with respect to this object is called the parallax effect. The parallax angle is defined as half this angular shift. This angle is proportional to the distance between the two observations positions and proportional inversely to the object's distance.

We can thus use the parallax angle to measure distance. From a simple trigonometric relation, we can show that distance  $d$  of an object is given by

$$d = \frac{B}{\tan p}, \quad (1.1)$$

where  $p$  represent the parallax angle (for small angles,  $\tan p \approx p$ ) and  $B$  is defined as half the distance between two observations or baseline. For distant objects, we can use the Sun-Earth distance as the baseline by making two observations half a year apart (with  $B = 1 AU$ )

$$d \approx \frac{1}{p} AU \approx \frac{206265}{p''} AU, \quad (1.2)$$

where  $p''$  is the angle  $p$  measured in arcseconds instead of radians. For a parallax of one arcsecond (par-sec), the distance is thus  $206265 AU$  which equals  $3.26 \text{ light year}$  which is the definition of one parsec ( $pc$ ). The Hipparcos satellite measured the parallax of 120 000 stars with a precision of  $0.001''$  (see Ref. [11])<sup>1</sup>. With such a precision, distances of stars out to about  $1000 pc$  ( $= 1 kpc$ ) could be measured. The diameter of the Milky Way is about  $30 kpc$  (e.g. Ref. [12]) so only distances to stars in our vicinity can be measured using parallax.

**Standard candles** - The luminosity  $L$  and the absolute magnitude  $M$  of stars are two different measures of the same property; total energy emitted per time interval. If you observe the apparent flux  $f$  of an object of known luminosity, you can infer its distance from the relation  $f = \frac{L}{4\pi d^2}$ . Equivalently, the absolute magnitude  $M$  could be calculated using the apparent magnitude  $m$  and distance  $d$

$$M = m - 5 \log_{10} \left( \frac{d}{10 pc} \right). \quad (1.3)$$

The apparent magnitude of a distant object could be measured. Then to obtain the distance, we need to know the absolute magnitude for an object. There are few classes of objects which reveal their absolute magnitude in different ways. These objects are called **standard candles** such as : Cepheid stars or supernova explosions.

**Standard rulers** - Another class of distance indicators are some objects for which the physical length is known. The basis for the distance determination from these objects is the small-angle formula

$$s = \theta d, \quad (1.4)$$

where  $s$  is the physical length of an object,  $d$  is the distance to the object and  $\theta$  is the apparent angular extension (length) of the object. Angular extension of an observed object could be measured. Only the physical length  $s$  is then needed to find distance. For instance, a special kind of galaxy has been shown to always have the same dimensions and are used as a standard ruler. The first use of standard rulers in a cosmological context appears to be due to C. Wirz in 1924 (without absolute calibration) and K. Lundmark in 1924-25 (with absolute calibration), who demonstrated a correlation between the angular diameter and distance of galaxies. The standard ruler assumption that galaxies of the same type have the same size has been used by numerous other astronomers to determine galaxy distances.

**Cepheid stars** - Several stars show periodic changes in their apparent magnitudes. These variations, between few tenths of magnitude and  $\sim 2$  magnitudes, are caused by pulsations where the star is periodically changing its radius and surface temperature. The pulsation period of these stars were found to be in the range between 1 and 50 days. In

---

<sup>1</sup><http://sci.esa.int/hipparcos>

1908, H. Leavitt at Harvard University discovered about 2400 of these pulsating stars in the Small Magellanic Cloud (one of the two small satellite galaxies orbiting Milky Way) (e.g. see Ref. [13]). These stars were called Cepheids named after one of the first pulsating stars to be discovered,  $\delta$  Cephei. She found that Cepheid variable stars exhibit a tight correlation between the stars' apparent magnitude (thus absolute magnitude also) and pulsation period. The shorter/longer the pulsation period, the fainter/brighter the star's absolute magnitude. She had found a period-luminosity (PL) relation allowing to infer the luminosity by measuring the period. To calibrate this relation and use it to estimate distances for distant galaxies, one had to find Cepheids in our vicinity for which the distance was determined by another method. One of the most recent measurements of the constants in the PL relation came from the parallax measurements of several nearby Cepheids in the Milky Way by the Hipparcos satellite. Those stars are about  $10^3$  to  $10^4$  times higher luminosity than the Sun. They can be observed over intergalactic distances in distant galaxies. Then, Cepheids are the first rung in the extragalactic distance ladder. In order to determine the distance of a whole galaxy, it suffices to find Cepheid stars in that galaxy and determine their distance by comparing its observed magnitude with the absolute magnitude determined from the calibrated PL relation. In this manner, the distance to several galaxies out to about  $30 Mpc$  has been measured.

**Supernovae explosions** - One of the most energetic events in the Universe are the supernovae (SN) explosions. In such an explosion, one star might emit more energy than the total energy emitted by all the stars in a galaxy. For this reason, supernovae explosions can be seen at very large distances. Supernovae were named and classified by the astrophysicist F. Zwicky in the 1930s. The last confirmed supernova in the Milky way was seen in 1604 and was studied by Kepler. The nearest supernova in modern times (since the invention of the telescope), called SN1987A, was observed in 1987 in the Large Magellanic Cloud (see Ref. [14]). Supernovae can be classified to 2 types according to absence (Type I: Ia, Ib and Ic) or presence (Type II) of hydrogen lines in explosion spectra. Supernovae of type Ib, Ic and II are core collapse supernovae leaving behind a neutron star or a black hole. According to the most popular hypothesis, the origin of type Ia supernova explosion occurs in a white dwarf star which has a binary companion (see Ref. [15]). Type Ia supernovae (SNIa) are usually brighter. At a certain point, the increased pressure and temperature from the accreted material from the other star may reignite fusion processes in the core of the white dwarf. It can be shown that this explosion occurs when the mass of the white dwarf is close to the so-called Chandrasekhar limit which is about  $1.4 M_{\odot}$ . After reaching maximum magnitude, the supernova fades off during days, weeks or months. In the early 1990s, it was recognized that supernovae rising and falling slower are more luminous, and vice versa. By measuring the shape of the light curve (the time required to rise and fall), one can determine the absolute magnitude of the supernova at its brightest and 'standardize' the type Ia 'candle' in order to determine its distance. Since the mass of the exploding star is always very similar, the luminosity of the explosion is also very similar. It is one of the most accurate means of measuring cosmological distances. Supernovae can be used to determine distances to galaxies beyond  $1000 Mpc$  (e.g. Ref. [16]).

**Tully-Fisher relation** - The maximum rotation velocities of stars around galaxy center are proportional to the total mass of the galaxy. We also know that the rotation curve for galaxies towards the edge of the galaxy was flat. Spiral galaxies have large quantities of neutral hydrogen and therefore emit 21 cm radiation from the whole disc. The 21 cm line is wide because of Doppler shifts : Hydrogen gas at different distances from the center of the galaxy orbits the center at different speeds giving rise to different Doppler shifts. So, gas clouds orbiting the galactic center at large distances all have the

same orbital velocity  $v_{max}$  and thus the same Doppler shift. There are therefore many more gas clouds with velocity  $v_{max}$  than with any other velocity. In 1977, A relation was found by B. Tully and R. Fisher between the maximal speed measured from the width of the 21 cm line and the absolute magnitude of the galaxy (see Ref. [17]). In a general sense, this relation can be understood in terms of the virial relation applied to rotationally supported disk galaxies, under the assumption of a constant mass-to-light ratio (If we assume that a higher total mass also means a higher content of luminous matter and therefore a higher luminosity). It is at present one of the most widely applied methods for distance measurements, providing distances to thousands of galaxies both in the general field and in groups and clusters. The Tully-Fisher relation can be used as a distance indicator out to distances beyond 100  $Mpc$  (e.g. Ref. [18]).

**Other distance indicators** - The typical main sequence stars of Hertzsprung-Russell (HR) diagram are used to measure distances. In this diagram of star populations, we plot surface temperature (or color) vs. absolute magnitude. The distance measurement is achieved by a comparison of a HR-diagram for clusters of distant stars with unknown distance with another diagram made from stars with known distances measured with parallax. The constant shift in the magnitude  $m - M$  of all stars is proportional to the distance of the cluster. This method is known as main sequence fitting and is used out to distances of about 7  $kpc$ , still not reaching out of our galaxy (see Ref. [19]). The distance to the Large Magellanic Cloud is measured using the light echoes of SN 1987A (see Ref. [20]). Approximately 240 days after the supernova explosion, a ring of circumstellar material, ejected during an earlier phase in the evolution of the supernova progenitor, became visible as the flash of UV radiation accompanying the SN explosion reached it and ionised it. We used the fact that the ring's physical radius is known (as it is  $R = c\Delta t$  with  $\Delta t = 240 \text{ days}$ ) and its known angular radius on the sky ( $\theta = 0.85 \text{ arcsec}$ ) to find the distance to the SN :

$$D_{LMC} = \frac{c\Delta t}{\theta} = 1.51 \times 10^{23} \text{ cm} = 48.9 \text{ kpc}. \quad (1.5)$$

Tip of the Red Giant Branch method (TRGB) method has a comparable precision to Cepheids (e.g. Ref. [21]). It uses the theoretically well-understood and observationally well-defined discontinuity in the luminosity function of stars evolving up the red giant branch in old, metal-poor stellar populations. This feature has been calibrated using Galactic globular clusters. TRGB method is observationally efficiency and is used for galaxies with distances  $d \lesssim 20Mpc$ . Consequently, there are 5 times more galaxies with distances determined by the TRGB method than via the PL relation of Cepheids. Other distance indicators use the luminosity of planetary nebula, globular clusters of stars or even brightest galaxies in clusters.

### 1.1.2 Redshifts, Hubble law and accelerated expansion of the Universe

Redshift is an important observable of cosmology and defined as follows

$$z = \frac{\lambda_{obs}}{\lambda_{em}} - 1. \quad (1.6)$$

Redshift is measured using two ways : spectroscopically or photometrically. For the former, a comparison between wavelengths of known emission or absorption lines from a source and their corresponding wavelengths measured in a laboratory on Earth, using Eq. 1.6. In photometric method, filters are used to measure relative brightness in certain

wavebands. Redshift is obtained by assuming certain spectral features for the source. Photometry is used instead of spectroscopy because it is less time-consuming. For far sources, photometry allows to obtain redshift which it is difficult to determine using spectroscopy. The downside of photometric method is the low precision of calculated redshifts. GN-z11 is the farthest known galaxy with  $z = 11.09$  (see Ref. [22]).

The beginning of modern cosmology is the evidence for the expansion of Universe. The astronomer Hubble (1929) (see Ref. [23]), working with data obtained at the Mount Wilson Observatory in California, published the first plot showing that galaxies are receding from us. This has later been found to be due to the expansion of the Universe : The galaxies are not moving away from us, the space between us and distant galaxies is expanding inducing a Doppler shift similar to that induced by a moving galaxy. Waves emitted by an object moving away from us have larger wavelengths than in the rest frame of the emitter. Thus, light from distant galaxies are redshifted. Hubble's discovery stands as a landmark discovery in cosmology for the twenty century. By measuring the redshift of distant galaxies, we can measure their velocities, or in reality the speed with which the distance is increasing due to the expansion of space. The expansion of the Universe is another way to solve Olbers's paradox. The redshift for Andromeda, the the closest galaxy, is negative. The observed wavelengths are bluer than emitted one. The peculiar motion caused by local gravitational effects overcome Hubble flow. From the radial component of the source's relative velocity, we can find their distance using the **Hubble's law**

$$v = H_0 d, \quad (1.7)$$

where  $d$  is the distance to the galaxy,  $H_0 \approx 70 \text{ km/s/Mpc}$  is the Hubble constant and  $v$  is the recessional velocity measured by the redshift

$$v = c \frac{\Delta\lambda}{\lambda}. \quad (1.8)$$

The Hubble law is only valid for large distances. Then, we find the Hubble law at the top of the distance ladder.

The discovery of type Ia supernova 1997ff (see Ref. [24]) represent the start of a new era in modern cosmology and astrophysics. The data of this type of supernovae led to the conclusion that our Universe is accelerating in its expansion (e.g. see Refs. [25] and [26]). The expected behaviour to the Universe dominated by gravity is a decelerated expansion if not a collapse. A probable cause for this acceleration in the expansion is that there exists a new form of matter, or rather energy, which acts as anti-gravity. This is widely known today as Dark Energy (DE) and its nature is still a mystery to us. The most simple and successful candidate for DE is the cosmological constant  $\Lambda$ .

### 1.1.3 Evidence for dark matter

The existence of another dark component, called Dark Matter (DM), of our Universe is indicated by several observations of different nature, sources and at different distance scales. Because the DM is essentially invisible to us, we must rely on visible objects that can act as tracers for it. It turns out that stars are collisionless and serve as the best DM tracers as their distribution is determined primarily by its gravitational interactions. It is a common understanding that DM is made of particles. All evidence in favor of particle DM thus far comes from observations of its gravitational effects on visible baryonic matter.

**Rotation curves of spiral galaxies.** - Rotation curve measurements provided the first strong indication that a significant fraction of matter in the Universe is non-baryonic (e.g. see Refs. [27] and [28]). Evidence for flat rotation curves began to build in the 1970s

(e.g. Refs. [29] and [30]), leading to several ground-breaking papers in the early 1980s (see Refs. [31] and [32]). The 21 Sc rotation curves measured by Rubin et al. (1980) (see Ref. [31]) illustrate the approximate flattening of the circular velocity at large radial distances (Sc is a galactic classification corresponding to galaxy shape e.g. see Ref. [33]). Since then, further evidence has continued to strengthen these conclusions (e.g. see Ref. [34]). The absence of visible matter to justify these curves is the surprising fact about them. Using Newtonian gravity and Gauss' theorem, one would expect a Keplerian fall of velocities such as  $V \sim \frac{1}{\sqrt{R}}$ , where  $R$  is the distance from the galactic centre. Instead, observations find that the circular velocity curve flattens out at these distances, implying that the galaxy mass is  $M(r) \propto r$ . This suggests that there is an additional 'dark' component of matter beyond the visible matter in the disk. The velocity curves of outer stars in spiral galaxies is sufficient to infer the density and velocity distribution of DM in the galaxy, and to posit the allowed mass range for the new matter particles. The assumption made is that the DM is distributed in a spherically symmetric halo about the center of the Galaxy, in contrast to the baryons which are concentrated in the disk. The estimate indicates that the DM halo extends out roughly an order of magnitude beyond the baryonic disk!

**Dynamics of galaxies in clusters.** - The pioneering Zwicky application of the virial theorem on Coma cluster (see Ref. [35]) resulted in a virial mass 500 times the estimated one by the light emission. This was the first indication of missing matter that is not inferred by light emissions. **The brightness in X-rays of galaxy clusters.** - It is related to the gravitational potential created by the cluster's total mass. Inference from observations indicate more mass than the visible matter only, giving then another argument for dark composition (e.g. see Ref. [36]). **The structure formation in the Universe.** - The observed highly non-linear baryonic matter density contrast is indicating a component catalysing this formation. The predictions from relativistic cosmology does not match observations of Cosmic Microwave Background (see Ref. [37]). **The structure of the Cosmic Microwave Background peaks.** - The existence of dark matter characterises the CMB spectrum by the observed **acoustic peaks** (see Ref. [38]). **Weak Lensing.** - An indirect indication of DM mass is its contribution to the light bending by foreground lenses (e.g. see Ref. [39] for a recent textbook reference on gravitational lensing). The famous **Bullet Cluster** is a direct empirical proof on the existence of DM (see Ref. [40]). In this case, the combination of X-ray and weak lensing observational techniques indicates a massive halo and a gravitational potential well different from the respective centre of mass.

#### 1.1.4 Cosmic microwave background

The most ancient light in the universe is a relic, thermal radiation from early hot dense phase of cosmic evolution. The cosmic microwave background (CMB) radiation gives indications onto the early composition and structure of the Universe. CMB existence had been predicted in the 1940s by Alpher and Gamow (see Ref. [41]). Its discovery was by Penzias and Wilson at Bell Labs in New Jersey, announced in 1965 (see Ref. [42]). This background is a convincing evidence for the Hot Big Bang more than 10 billion years ago. Several experiments have been performed to observe the CMB radiation at different frequencies, directions and polarisations, mostly with ground- and balloon-based detectors. These experiments confirmed the uniformity of the CMB radiation, at a temperature of 2.7 Kelvin in all directions.

The satellite missions have transformed the CMB study in the last thirty years. The

first of these was the Cosmic Background Explorer <sup>2</sup>, launched by NASA in 1990. In 1992, CoBE reported the detection of statistically significant temperature anisotropies in the CMB, at the level of  $\pm 30\mu K$  on 10 degree scales (e.g. Ref. [43]) and it confirmed the black body spectrum with an astonishing precision, with deviations less than 50 parts per million (e.g. Ref. [43]). This small deviation is due to the Doppler effect from our peculiar motion (at 1 million kilometres per hour) with respect to this background. Wilkinson Microwave Anisotropy Probe <sup>3</sup> satellite was launched by NASA in 2001. This mission produced full sky maps in five frequencies (from 23 to 94 GHz) mapping the temperature anisotropies to sub-degree scales and determining the CMB polarisation on large angular scales for the first time. The Planck satellite <sup>4</sup> was launched by European Space Agency (ESA) in 2009. It represent the current state of the art with nine separate frequency channels, measuring temperature fluctuations to a millionth of a degree at an angular resolution down to 5 arc-minutes. Planck's mission ended in 2013 and the full-mission data were released in Adam et al. (2016) (see Ref. [44]) and in many companion papers. A fourth generation of full-sky, microwave-band satellite recently proposed to ESA within Cosmic Vision 2015-2025 is the Cosmic Origins Explorer <sup>5</sup> (see Ref. [45]). Currently, great efforts are being devoted to the detection of the B-mode of CMB polarization to study primordial gravitational waves background. Located near the South Pole, BICEP3 <sup>6</sup> and the Keck Array are telescopes used to this purpose. Among the non-satellite CMB experiments, we find the Balloon Observations Of Millimetric Extragalactic Radiation ANd Geophysics (BOOMERanG) which was a balloon-based mission which flew in 1998 and in 2003 and measured CMB anisotropies with great precision (higher than CoBE). From these data the Boomerang collaboration first determined that the Universe is spatially flat (see Ref. [46]).

## 1.2 Relativistic cosmology

This section presents a short and concise overview of relativistic cosmology and specially the geometric basis of cosmology (see Ref. [47] for extensive introductory course of cosmology). The main topics are the expansion of the Universe, Friedmann equations, thermal history, Big Bang Nucleosynthesis and recombination. In order to do cosmology, we need a theory of gravity as a long-range interaction for the Universe compositions. With no evidence of a charged Universe, electromagnetism could not then be used even if it is a long-range interaction. Using GR to describe gravitational interactions, Einstein equations relate geometry and matter-energy

$$G_{\mu\nu} + \Lambda g_{\mu\nu} = \frac{8\pi G}{c^4} T_{\mu\nu}, \quad (1.9)$$

where  $\Lambda$  is the cosmological constant,  $G_{\mu\nu}$  is the Einstein tensor, computed from the metric using ( $G_{\mu\nu} = R_{\mu\nu} - \frac{1}{2}g_{\mu\nu}R$ ), and  $T_{\mu\nu}$  is the energy-momentum or stress-energy tensor describing the energy-matter content.

### 1.2.1 Friedmann Lemaitre Robertson Walker spacetime

The metric used to describe the Universe on large scales is the Friedmann-Lemaitre-Robertson-Walker (FLRW) metric. It is based on the **cosmological principle** assuming

---

<sup>2</sup>CoBE, <https://lambda.gsfc.nasa.gov/product/cobe/>

<sup>3</sup>WMAP, <https://map.gsfc.nasa.gov/>

<sup>4</sup>Planck, <http://sci.esa.int/planck/>

<sup>5</sup>CORe, <http://www.core-mission.org/>

<sup>6</sup>BICEP, <https://www.cfa.harvard.edu/CMB/bicep3/>

a very high symmetry and isotropy of the Universe with no preferred direction or preferred position. Observational data appear to confirm the cosmological principle to a large extent in large scales of the order of  $100 h^{-1} Mpc$  to  $300 h^{-1} Mpc$ . These observations include distribution of both mass and luminous sources, density fluctuations (see Ref. [48]) and quasar distribution (see Ref. [49]). Moreover, numerical relativity appear to show that the average evolution of a generic metric on large scales is compatible with FLRW metric evolution (see Ref. [50]). To account for the cosmological principle, the spacetime needed to describe the universe is a maximally symmetric space characterised by one number only which must be the scalar curvature  $R$ . Starting from Riemann tensor to construct Einstein tensor for such space, we find the Ricci tensor to be given by

$$R_{\nu\rho} = \frac{R}{D} g_{\nu\rho}, \quad (1.10)$$

where  $D$  represent the dimension of such space.

This space also have 3 possible configurations corresponding to positive, null or negative scalar curvature. After simplification, we introduce  $k$  a constant representing the three possible spaces where:  $k = 0$  for the Euclidean case,  $k = 1$  for the spherical case and  $k = -1$  for the hyperbolic case. When considering a 4-dimensional dynamical spacetime, we obtain FLRW metric

$$ds^2 = -c^2 dt^2 + a^2(t) \left( \frac{dr^2}{1 - kr^2} + r^2 d\sigma^2 \right), \quad (1.11)$$

where  $d\sigma^2 = d\theta^2 + \sin^2\theta d\phi^2$ .  $t$  in this line element is labelled **cosmic time** whereas the spatial coordinates are called **comoving coordinates**.  $a(t)$  is the **scale factor** characterizing the distance between two points scaled with time. The FLRW metric was first introduced by Friedmann (see Refs. [51] and [52]) and then derived on the basis of isotropy and homogeneity by Robertson and Walker (see Refs. [53]; [54] and [55]). Lemaitre's work (see Ref. [56]) had been also essential to develop it.

Given FLRW metric, Friedmann equations can be straightforwardly computed from the Einstein equations (see Eq. 1.9) to find

$$H^2 + \frac{kc^2}{a^2} = \frac{8\pi G}{3c^2} T_{00} + \frac{\Lambda c^2}{3}, \quad (1.12)$$

$$g_{ij} \left( H^2 + 2\frac{\ddot{a}}{a} + \frac{kc^2}{a^2} - \Lambda c^2 \right) = \frac{8\pi G}{c^2} T_{ij}. \quad (1.13)$$

These equations are called **Friedmann equations** or also called **Friedmann equation** and **acceleration equation** or even **Friedmann equation** and **Raychaudhuri equation**. We should define the stress-energy tensor  $T_{\mu\nu}$  to use in Eqs. 1.12 and 1.13. After we choose the FLRW metric, the energy momentum tensor have strong constraints

1. First of all:  $G_{0i} = 0$  imposing  $T_{0i} = 0$  forbidden the existence of any flux of energy which would violate isotropy;
2. Second, since  $G_{ij} \propto g_{ij}$  resulting in  $T_{ij} \propto g_{ij}$ ;
3. Finally, since  $G_{\mu\nu}$  is only time dependent, then it must be the case for  $T_{\mu\nu}$ .

Then, we can write a general form of the stress-energy tensor as follows

$$T_{\mu\nu} = \left( \rho + \frac{P}{c^2} \right) u_\mu u_\nu + P g_{\mu\nu}, \quad (1.14)$$

where  $u_\mu$  is the four-velocity of the fluid element,  $\rho(t)$  is the rest mass density and  $P(t)$  is the pressure. This stress-energy tensor does not contain any term for viscosity nor energy transport. Matter described by Eq. 1.14 is known as **perfect fluid** (see Ref. [57]). Rewriting Friedmann equation using Eqs. 1.12, 1.13 and ?? gives

$$H^2 = \frac{8\pi G}{3}\rho + \frac{\Lambda c^2}{3} - \frac{kc^2}{a^2}. \quad (1.15)$$

For the acceleration equation, it becomes

$$\frac{\ddot{a}}{a} = -\frac{4\pi G}{3}\left(\rho + \frac{3P}{c^2}\right) + \frac{\Lambda c^2}{3}. \quad (1.16)$$

$\rho$  and  $P$  represent the total density and pressure then the sums of all individual components contributions. The cosmological constant contribution can be considered as geometrically or as a matter component with the corresponding density and pressure

$$\rho_\Lambda = \frac{\Lambda c^2}{8\pi G}, P_\Lambda = -\rho_\Lambda c^2. \quad (1.17)$$

The scale factor  $a$  is, by definition, positive, but its derivative can be negative characterizing either an expanding or a contracting Universe. The Friedmann equations can be solved exactly for many cases of interest (See Appendix A).

## 1.2.2 Cosmological parameters

**Hubble constant** - The Hubble parameter  $H$  is defined by Friedmann equation as

$$H = \frac{\dot{a}}{a} \quad (1.18)$$

at the present time  $t_0$ , it is called the Hubble constant  $H_0$ . Conveniently,  $H_0$  is given by

$$H_0 = 100 h km s^{-1} Mpc^{-1}. \quad (1.19)$$

Hubble constant gives an estimation of the Universe age

$$\frac{1}{H_0} = 3.09 h^{-1} \times 10^{17} s = 9.78 h^{-1} Gyr, \quad (1.20)$$

and also gives an estimation of the size of visible Universe, so-called the Hubble radius at the present time

$$\frac{c}{H_0} = 9.27 h^{-1} \times 10^{25} m = 3.00 h^{-1} Gpc. \quad (1.21)$$

**The deceleration parameter** - The parameter named **deceleration parameter** measures the acceleration state of the Universe and is defined as follows

$$q = -\frac{\ddot{a}a}{\dot{a}^2}. \quad (1.22)$$

In papers of Perlmutter et al. (1999) (see Ref. [25]) and Riess et al. (1998) (see Ref. [26]), the analysis based on SNIa observations have indicated that  $q_0 < 0$ , showing that the Universe is accelerating in its expansion.

**Critical density and density parameters** - When rewriting Eq. 1.15 incorporating  $\Lambda$  in the total density  $\rho$ , we find

$$H^2 = \frac{8\pi G}{3}\rho - \frac{kc^2}{a^2}. \quad (1.23)$$

The value of the total  $\rho$  making  $k = 0$  is called **critical energy density** and is given by

$$\rho_{cr} = \frac{3H^2}{8\pi G}. \quad (1.24)$$

Its present value is given by

$$\rho_{cr,0} = 1.878 h^2 \times 10^{-29} g cm^{-3}. \quad (1.25)$$

It is a conventional practice the literature to use the normalisation of energy density to the critical density, also called the density parameter  $\Omega$ , which is given by

$$\Omega = \frac{\rho}{\rho_{cr}} = \frac{8\pi G \rho}{3H^2}. \quad (1.26)$$

because it shows more evidently the dependence of each component of the cosmic fluid to the scale factor. We shall use the definition  $\Omega_x = \rho_x/\rho_{cr,0}$  through-out this section. Friedmann equation (see Eq. 1.15) is given in term of  $\Omega$  to be

$$\frac{H^2}{H_0^2} = \sum_x \Omega_{x0} f_x(a) + \frac{\Omega_{k0}}{a^2}, \quad (1.27)$$

where  $f_x(a)$  is a function giving the dependence of the component  $x$  and  $f_x(a_0 = 1) = 1$ . We define

$$\Omega_k = -\frac{kc^2}{H^2 a^2}, \quad (1.28)$$

which associates an energy density

$$\rho_k = -\frac{3kc^2}{8\pi G a^2}, \quad (1.29)$$

to the spatial curvature. Consistently and at present time, we put

$$\sum_x \Omega_{x0} + \Omega_{k0} = 1, \quad (1.30)$$

also known as **closure relation**. It turns out that  $\rho_0$  is very close to  $\rho_{cr,0}$ . Then, we observed that  $\Omega_0 \simeq 1$  which imply  $\Omega_{k0} \simeq 0$ , corresponding to a spatially flat Universe (see Ref. [58]). Such an extreme fine-tuning of  $k$  is called the **flatness problem**. A possible solution to this problem is provided by inflationary theory.

### 1.2.3 Cosmological fluid components

**Energy conservation equation** - This equation is given by

$$\nabla_\nu T^{\mu\nu} = 0, \quad (1.31)$$

is part of GR as a result of the Bianchi identities. Then, it is related to the Friedmann equations (see Eqs. 1.15 and 1.16). It has a particularly simple form for a perfect fluid in FLRW spacetime

$$\dot{\rho} + 3H\left(\rho + \frac{P}{c^2}\right) = 0. \quad (1.32)$$

This is the  $\mu = 0$  component of  $\nabla_\nu T^{\mu\nu} = 0$  and it is also known from fluid dynamics as **continuity equation**. Analytical solutions to continuity equation can be found when assuming an equation of state such that  $P = w\rho c^2$ . This solution has the following general form

$$\rho = \rho_0 a^{-3(1+w)}, \quad (1.33)$$

where  $w$  is constant and  $\rho_0 = \rho(a_0 = 1)$ . We consider three values of  $w$  particularly important in cosmology

1. **Cold matter** : characterized by  $w = 0$  describing all non-relativistic particles with kinetic energy smaller than mass energy. Cold matter is also called **dust** which are overall baryons and possibly unknown non-relativistic particles labelled **cold dark matter** (CDM);
2. **Hot matter** : characterized by  $w = 1/3$  describing all relativistic particles also known as **radiation**: known as photons are massless neutrinos and may be unknown ones (i.e. **hot dark matter** (HDM));
3. **Vacuum energy** : characterized by  $w = -1$  describing dark energy in general and the cosmological constant in particular. For other forms of dark energy different from the cosmological constant, one needs to make this substitution  $\Omega_{\Lambda 0} \longrightarrow \Omega_{de0} \frac{\rho_{de}(z)}{\rho_{de0}} = \Omega_{de0}(1+z)^{3(1+w)}$ , where the last equality holds for constant  $w$ .

**thermally produced** DM particles would have sufficiently large mass. For lower masses, we find other DM candidates. Typically, **Warm Dark Matter** (WDM) is a thermally produced DM with mass around  $keV$ . HDM are also thermally produced but with smaller masses around  $eV$ , or even massless.  **$\Lambda$ CDM model** - The observational results are in favour of the existence DM and for being **cold**. In this thesis, we adopt a CDM paradigm for DM. The combined observational successes of  $\Lambda$  and CDM form the so-called  $\Lambda$ CDM model, which is the standard model of cosmology. This successful cosmological model is made up, along with  $\Lambda$  and CDM, of baryons and radiation (photons and massless neutrinos). See Bertone and Hooper (2016) (Ref. [59]) for a general overview of DM and Profumo (2017) (Ref. [60]) as a textbook on dark matter particles. In  $\Lambda$ CDM model, Friedmann equation is given by

$$\frac{H^2}{H_0^2} = \Omega_{\Lambda 0} + \frac{\Omega_{m0}}{a^3} + \frac{\Omega_{r0}}{a^4} + \frac{\Omega_{k0}}{a^2}. \quad (1.34)$$

Where  $\Omega_{m0}$  is density parameter of matter (baryonic and dark matter),  $\Omega_{r0}$  is the density parameter of radiation,  $\Omega_{\Lambda 0}$  is the density parameter of dark energy and  $\Omega_{k0}$  represents the curvature. We can rewrite the Friedmann equation in a most useful version for practical calculations

$$\frac{H^2(t)}{H_0^2} = \frac{\Omega_{r0}}{a^4} + \frac{\Omega_{m0}}{a^3} + \Omega_{\Lambda 0} + \frac{1 - \Omega_0}{a^2(t)}. \quad (1.35)$$

### 1.2.4 Special particles

**Photons** - In this part of section, we use "photons" as synonym of CMB even if photons from non cosmological origin produced in all stars or emitted by hot interstellar gas. These non-cosmological photons have a lower contribute (one order of magnitude or more) than CMB photons (see Ref. [61]) so our choice is partially justified. Starting from Bose-Einstein distribution for photons, we find that the photon energy density follows the Stefan-Boltzmann law, of the black-body radiation. From the continuity equation, we know that  $\epsilon_\gamma = \epsilon_{\gamma 0}/a^4$ , then we can infer temperature to be

$$T = \frac{T_0}{a}, \quad T_0 = 2.725K, \quad (1.36)$$

i.e. the photons temperature is inversely proportional to scale factor. Using the present day CMB temperature  $T_0$ , the photon density parameter is estimated to be

$$\Omega_{\gamma 0} h^2 = 2.47 \times 10^{-5}. \quad (1.37)$$

The present day photon number density is estimated to be  $n_{\gamma 0} = 411 \text{ cm}^{-3}$ .

**Neutrinos** - Similarly to photons, "neutrinos" in this section refers to cosmological, or primordial, and not those neutrinos produced in different astrophysical processes and sources. The energy density of massless neutrino is inversely proportional to  $a^4$ . Since neutrinos are fermions, we use Fermi-Dirac distribution to show that their energy-density is given by

$$\epsilon_{\nu} = \frac{7}{8} N_{\nu} g_{\nu} \frac{\pi^2}{30 \hbar^3 c^3} (k_B T_{\nu})^4, \quad (1.38)$$

where  $N_{\nu}$  is the number of neutrino families and  $g_{\nu}$  the value of the neutrino degeneracy. Of course, an equivalent expression holds true for antineutrinos. The total radiation energy content can thus be written as

$$\epsilon_r = \epsilon_{\gamma} + \epsilon_{\nu} + \epsilon_{\bar{\nu}} = \epsilon_{\gamma} \left(1 + \frac{7}{8} N_{\nu} g_{\nu} \left(\frac{4}{11}\right)^{4/3}\right). \quad (1.39)$$

The Planck collaboration (see Ref. [58]) has constrained the neutrino families to be

$$N_{eff} = N_{\nu} g_{\nu} = 3.04 \pm 0.33, \quad (1.40)$$

at a confidence level of 95% with one spin state for each neutrino ( $g_{\nu} = 1$ ). Neutrinos can be considered as a HDM candidate. But, since neutrino appear to have a mass around  $0.1 \text{ eV}$ , it is should be considered as cold. **Massive neutrinos** - The discovery of neutrino oscillations by T. Kajita and A. B. McDonald was awarded by a Nobel Prize in Physics in 2015. This property allows neutrinos to have mass. The total neutrino mass estimated from cosmology is  $\sum m_{\nu} < 0.194 \text{ eV}$  at 95% confidence level from the Planck collaboration (see Ref. [58]). The low neutrino mass does not change in the Universe evolution but with some impacts at late era of structure formation (see Ref. [62]).

**Matter-Radiation equality** - The instant for the equality between the energy density of matter and radiation is particularly important for the Universe evolution and its observable implications. The scale factor  $a_{eq}$  of the equivalence is then determined to be

$$a_{eq} = \frac{4.15 \times 10^{-5}}{\Omega_{m0} h^2}, \quad (1.41)$$

The equivalence scale factor  $a_{eq}$  is affected with the existence of massive neutrinos.

### 1.2.5 Cosmological redshift

Cosmological redshift ( $z_C$ , or shortly  $z$  in this section) is related to the Universe evolution. In FLRW space-time (see Eq. 1.11), the Universe evolution is characterised by the scale factor function  $a(t)$ . We suppose a situation where a photon is emitted at cosmic time  $t_E$  by a co-moving source with fixed spatial coordinates and then this photon is observed at time  $t_O$  by an observer at fixed co-moving coordinates. If we consider  $k = 0$  and  $d\sigma = 0$ , for simplicity. Then, the radial coordinate is the same as the distance. We use the geodesic equation

$$\frac{dP^{\mu}}{d\lambda} + \Gamma_{\nu\rho}^{\mu} P^{\nu} P^{\rho} = 0, \quad (1.42)$$

where  $P^{\mu} = dx^{\mu}/d\lambda$  is the four-momentum and  $\lambda$  is an affine parameter. A massless photon would have  $m = 0$  and  $E = pc$ . Considering the time-component of geodesic equation given by

$$\frac{dP^0}{d\lambda} + \frac{a\dot{a}}{c} \delta_{ij} P^i P^j = 0. \quad (1.43)$$

Introducing the proper momentum, one gets

$$\frac{dp}{d\lambda} + Hp^2 = 0. \quad (1.44)$$

By solving Eq. 1.44, we deduce that the photon's energy is inversely proportional to scale factor. Then, we obtain

$$\frac{E_{obs}}{E_{em}} = \frac{a_{em}}{a_{obs}}. \quad (1.45)$$

Knowing also that the photon energy is  $E = h\nu$ , with  $\nu$  its frequency. Therefore, we find

$$\frac{a_{em}}{a_{obs}} = \frac{E_{obs}}{E_{em}} = \frac{\nu_{obs}}{\nu_{em}} = \frac{\lambda_{em}}{\lambda_{obs}} = \frac{1}{1+z}. \quad (1.46)$$

This last expression represent the relation between redshift and scale factor and a direct connection between observation and theory. The redshift from this relation is time dependent. A phenomenon known as redshift drift that was first noticed by Sandage and McVittie (see Refs. [63] and [64]). Applications of the redshift drift phenomenon to gravitational lensing are proposed by Piattella and Giani (2017) (see Ref. [65]). This wavelength shift (defined in Eq. 1.46) is a redshift if the ratio is greater than 1 which is the case when the Universe is larger in observation time than in emission time which is the case in an expanding Universe. The shift is a blueshift when the Universe has become smaller and then it is collapsing.

Note that throughout this thesis, I have adopted a standard convention that the expansion parameter at the present day is  $a_{obs} = a_0 = a(t_0) = 1$ . The above Eq. 1.46 is simply written as  $1+z = 1/a$ . This convention represents a pure normalisation which is possible by the fact that the dynamics is the same even if we multiply the scale factor by a constant. For the classical kinetics, a particle's energy is averaged to  $k_B T$ . Therefore  $T \propto a^{-1}$ , for relativistic particles,  $T \propto a^{-2}$ , for non-relativistic particles. Then, we use also CMB temperatures as time indicators of the Universe evolution or equivalently scale factor or redshift.

### 1.2.6 Cosmic distances

This part of the section introduces the different notions of distance used in cosmology (e.g. see Ref. [66]).

**Comoving distance and proper distance** - Comoving coordinates of FLRW metric are presented previously (see Eq. 1.11) along with the proper radius. The comoving square infinitesimal distance  $d\chi^2$  from FLRW metric has a radial part and a transversal part. The radial coordinate is equal to the distance only when  $d\sigma = 0$ . The comoving distance does not include the expansion of the Universe and does not depend on time. So, if  $\chi$  is the comoving distance between two points, the proper distance at a certain time  $t$  is  $d(\chi, t) = a(t)\chi$ . The proper distance is the distance considered between two simultaneous events. Then, it does not consider the Universe expansion cumulatively. Then if we suppose  $d\sigma = 0$ , the comoving distance to an object with radial coordinate  $r$  is the following

$$\chi = \int_0^r \frac{dr'}{1 - kr'^2} \begin{cases} \arcsin r' & , fork = 1, \\ r' & , fork = 0, \\ \operatorname{arcsinh} r' & , fork = -1. \end{cases} \quad (1.47)$$

when we derive  $d$  to cosmic time, we get

$$\dot{d} = \dot{a}\chi = \frac{\dot{a}}{a}d = Hd, \quad (1.48)$$

which is Hubble's law for present time  $t = t_0$ . The right hand side of Eq. 1.48 is equivalent to  $v$  and using Eq. 1.8, it is written  $\dot{d} = v = cz$ . **Distances and horizons** - When determining the comoving distance to the big Bang, one finds the **comoving horizon**  $\chi_p$  (also known as **particle horizon** or **cosmological horizon**). It represents the maximum comoving distance possibly travelled by a photon. The maximum distance travelled by a photon from any time  $t$  is referred to be the **event horizon**.

**The lookback time** - The distance travelled by light from its emission at  $t_{em}$  to its observation at  $t_0$  on Earth is basically given by  $c(t_0 - t_{em})$ . The time difference  $t_0 - t_{em}$  is called lookback time. This is a reminder that we are always observing the past of our Universe. When we put  $ds^2 = 0$  in FLRW metric, we can deduce the lookback time as follows

$$cdt = a(t)d\chi. \quad (1.49)$$

The lookback time includes the Universe expansion and could be expressed in term of the redshift and vis-versa. Using Taylor expansion, a model-independent relation between lookback time and redshift is

$$z \sim H_0(t_0 - t) + \frac{1}{2}(q_0 + 2)H_0^2(t_0 - t)^2. \quad (1.50)$$

**The luminosity distance** - In FLRW space-time, we could define the luminosity distance of a distant light source that his light was travelling along a co-moving coordinate to reach us today. This notion of distance is crucial in observational cosmology. It is basically a comparison between the source's known intrinsic luminosity and the measured flux. Both are inversely proportional to the square luminosity distance (see previous subsection : distance ladder). In a cosmological context of an expanding Universe, several contributions affect the simple relation of luminosity-flux-distance : The redshift  $z$  of a source, the area of the sphere around this source with the proper distance as radius, photons affected by cosmological redshift, and finally the diffence between emission and observed time at source and observer. Considering all these contributions, luminosity distance is then defined by the following general formula

$$d_L(z) = a_0(1 + z)S(\chi(z)) \quad (1.51)$$

where  $a_0$  is the present time scale factor and  $z$  is the redshift of the light emitter. We define the rest of the terms by

$$a_0S(\chi(z)) = \frac{c}{H_0} \begin{cases} |\Omega_{k0}|^{-1/2} S(\sqrt{|\Omega_{k0}|}E(z)) & \text{for } \Omega_{k0} \neq 0, \\ E(z) & \text{for } \Omega_{k0} = 0, \end{cases} \quad (1.52)$$

and

$$E(z) = \int_{(1+z)^{-1}}^1 (\Omega_{m0}x + \Omega_{r0} + \Omega_{\Lambda 0}x^4 + \Omega_{k0}x^2)^{-1/2} dx \quad (1.53)$$

In the case were  $\Omega_{k0}$  is not null, the function  $S()$  in Eq. 1.52 is replaced by  $\sin()$  for  $k = +1$  and replaced by  $\sinh()$  for  $k = -1$ . The model-independent form of the last relation is given by

$$d_L = \frac{c}{H_0} (z - \frac{1}{2}(1 - q_0)z^2 + \dots). \quad (1.54)$$

We notice that the lowest order of the luminosity distance is  $cz/H_0$  which also represent Hubble law.

**Angular diameter distance** - This distance is deduced from known proper sizes of objects called **standard rulers** (see previous subsection : distance ladder). The angular diameter distance could be defined as

$$d_A = a(t)\chi. \quad (1.55)$$

In the case of small  $z$ , we find  $d_A \sim cz/H_0$ . All the distances defined are similar at the lowest order expansion in  $z$ . But, we notice the relation:

$$d_L = (1 + z)^2 d_A, \quad (1.56)$$

so-called **Etherington's distance duality** (see Ref. [67]) needed in gravitational lensing applications.

### 1.2.7 Thermal history

**Thermal equilibrium** - We have encountered previously the continuity equation (see Eq. 1.32) which could be obtained using laws of thermodynamics by assuming that the Universe evolution adiabatic reversible transformation. It could be also deduced from Boltzmann equation assuming no interactions or a very high rate of interactions resulting in a thermal equilibrium. Then, the frequent interaction of particles make them less sensitive to cosmological expansion and any energy density fluctuation is rapidly smoothed out. This recovers thermal equilibrium (see Ref. [68]). The above condition is broken at different times at early Universe for different species. This is the essence of the **thermal history of the Universe** (see Ref. [69]). Just after the Big Bang, all the particles were in thermal equilibrium in the so-called the **primordial plasma**. Each specie breaks the condition at different time and it **decouples** from the primordial plasma. It is said to **freeze out** and has a fixed abundance if it is stable or it disappears. We use Boltzmann equation when studying the formation of light elements during Big Bang Nucleosynthesis and recombination.

We present a brief presentation of the main events occurring in the thermal history of the Universe (see Ref. [69]).

1. **Planck scale, inflation and Grand Unified Theory.** - Planck scale is believed to be at  $10^{19} GeV$  characterising the limit where we must use Grand Unified Theory (GUT) instead of our classical theories. Inflation represent an important part of our description of primordial Universe and believed to happen at an energy scale of the order  $10^{16} GeV$
2. **Baryogenesis and Leptogenesis.** - Baryogenesis is the creation asymmetries (quark-antiquark) between the baryon compositions of the Universe. In order to maintain the neutrality of the Universe, a mechanism creates excess in electron and called Leptogenesis.
3. **Electroweak (EW) phase transition.** - At a thermal energy of about  $100 GeV$ , the electromagnetic and weak forces start to decouple. This happens after  $W^\pm$  and  $Z^0$  bosons gain their masses from Higgs mechanism.
4. **Quantum Chromo-Dynamics (QCD) phase transition.** - Below  $150 MeV$ , quarks leave their asymptotic freedom to be bounded in form of couples of two (mesons) or three (baryons).
5. **DM freeze-out.** - If DM is made up of particles then it has to decouple also. For the neutralino case, the freeze-out happens around  $25 MeV$ .
6. **Neutrino decoupling.** - Neutrinos maintain thermal equilibrium with the primordial plasma through several interactions down to a thermal energy of  $1 MeV$ .

7. **Electron-positron annihilation.** - This interaction is balanced for energies higher than electron mass. This is making the annihilation process relevant only for energies lower than  $511\text{ keV}$ . Positrons then disappear and only electrons are left as a consequence of leptogenesis.
8. **Big Bang Nucleosynthesis (BBN).** - It occurs at about  $0.1\text{ MeV}$  and it is related to the formation of the primordial light elements mainly deuterium and Helium. At temperatures larger than  $1\text{ MeV}$ , the primordial plasma was formed by photons, electrons, positrons, neutrinos, antineutrinos, protons and neutrons. The BBN is essentially a competition in capturing neutrons before they decay.
9. **Recombination and photon decoupling.** - **Recombination** is the process of forming neutral hydrogen from protons and electrons at about  $0.25\text{ eV}$ . **Decoupling** represent the epoch when photons travel freely without interact with free electrons. CMB photos are originated from this epoch coming from the **last scattering surface** at a redshift around 1100.
10. **reionisation.** - After decoupling, ultraviolet light emitted from primordial stars is able to ionise again hydrogen atoms. Reionization takes place at redshift around 10.

### 1.3 Open problems in cosmology

The fundamental issue in cosmology is to understand what are DM and DE. The effort of answering this question makes cosmology, particle physics and quantum field theory (QFT) to merge. The ways adopted in order to tackle these problems are essentially the search for particles beyond the standard model and the investigation of new theories of gravity, which in most of the cases are extensions of GR. Those problems facing modern cosmology and astrophysics are presented in this section.

#### 1.3.1 Uncertainties in distance measurements

From the definitions of all used methods, we understand the meaning of *cosmic distance ladder*. The calibration of one class of sources at nearby distances is used to calibrate the intrinsic luminosity of another type of distance indicators, which is being intrinsically more luminous (but also rarer) and can then be followed to larger distances, and so on. There are several uncertainties connected with distance measurements. Clearly, systematic errors can build very quickly. One of the main problems is caused by interstellar extinction where light from distant galaxies loose flux by scattering while passing through the dust clouds of our galaxy. Interstellar extinction increases the apparent magnitude (decreases the flux) of an object which appears dimmer. Clearly, if we use the apparent magnitude of a distance indicator and do not take into account interstellar extinction, we obtain the wrong distance. It is often difficult to know the exact amount of scattering on dust grains. This is an important source of error in distance measurements.

In the case of Cepheids, they are relatively rare and they are encountered a long way from the Sun. Consequently, there are just ten Cepheids with accurately measured trigonometric parallaxes. The resulting error in the Cepheid zero point is  $-0.06\text{ mag}$  ( $\pm 3\%$ ). This error will be reduced considerably when data from the on-going Global Astrometric Interferometer for Astrophysics (GAIA) mission are gathered and analysed (see Ref. [71]). Using Cepheids, E. Hubble first estimated the distance to our neighbour galaxy Andromeda. There are three different types of pulsating stars with different PL

relations: classical Cepheids, W Virginis stars and RR Lyrae stars. Hubble obtained a distance of about one million light years whereas the real distance is about twice as large. The reason for this error was that he observed W Virginis stars in Andromeda and applied the period-luminosity relation for classical Cepheids, thinking that they were the same. For Tully-Fisher relation, it doesn't consider the role of dark matter in producing spiral galaxies rotation curves. This remains a challenging task to improve the precision of this method. The challenge in using SNIa remains that few galaxies in which SNIa events have been observed are also close enough for Cepheid distances to be measured. At present, the number of galaxies for which there are high-quality Cepheid and SNIa measurements is limited to six objects. Each of the six galaxies has between 13 and 26 Cepheids observed with Hubble Space Telescope (HST) in the near-IR H-band. Hence, the calibration of the SNIa distance scale is still subject to small-number statistical uncertainties. Also, their peak luminosities has a scatter of about 40% from one supernova to another, leaving residual scatter of 10-15% in peak luminosity (0.1–0.15 magnitudes). This point affecting distance estimation was highlighted and deeply investigated (e.g. Refs. [72] and [73]). Several methods are developed to minimize the effect of those deviations on cosmological parameters estimation.

Another source of error in the measurement of large distances in the Universe is the fact that objects observed at a large distance are also observed at an earlier phase in the history of the Universe. The light from an object at a distance of 1000  $Mpc$  or 3260 million light years has travelled for 3260 million years or roughly one fourth of the lifetime of the Universe. Because of the Universe's evolution, we do not know if galaxies and stars at this early epoch had the same properties as they have today. This could imply that, for example, the relation between light curve and absolute magnitudes of supernovae were different at early epochs than today, leading to errors in measurements of the distance.

### 1.3.2 Estimating cosmological parameters

An accurate estimation of Hubble constant has a central importance in cosmology which has controversial results during modern cosmology history. The value determined by Hubble himself was  $H_0 = 500 \text{ km s}^{-1} \text{ Mpc}^{-1}$  with large error caused by the scatter of his data points (e.g. Ref. [23]). A more accurate estimate was made by Sandage  $H_0 = 75 \text{ km s}^{-1} \text{ Mpc}^{-1}$  (see Ref. [74]). For decades, there were two 'camps', one claiming  $H_0 = 50 \text{ km s}^{-1} \text{ Mpc}^{-1}$  and the other double that value (see Refs. [75] and [76]). Both groups estimated their error to be about 10% and were generally unwilling to concede that systematic uncertainties could significantly inflate their error estimates. The accurate measure was one of the original scientific motivations for building the HST. An important observing time was devoted to this 'Key Project' in the mid-1990s to solve this issue. The value generally accepted today of Hubble constant is  $H_0 \simeq 70 \text{ km s}^{-1} \text{ Mpc}^{-1}$  with an uncertainty of about 10%.

The main method to measure cosmological parameters is via expansion. It is relatively straightforward to measure the recession velocities of galaxies from the redshifts of emission and/or absorption lines in their spectra. The determination of distances to astronomical objects is fraught with difficulties and plagued by systematic uncertainties as discussed in our presentation of 'cosmic distance ladder'. In general terms and to measure  $H_0$ , distance measurements must be obtained far enough away to probe the smooth Hubble expansion and nearby enough to calibrate the absolute, not simply the relative, distance scale. This is done at sufficiently large distances where the random velocities induced by gravitational interactions with neighbouring galaxies are small relative to the Hubble velocity. The objects under study also need to be sufficiently abundant that their

statistical uncertainties do not dominate the error budget. Ideally the method should have a solid physical underpinning and high internal accuracy, amenable to empirical tests for systematic errors. Type Ia supernovae represent the ideal candidate especially supernovae in galaxies that are far enough away ( $50 - 200 Mpc$ ) (see Ref. [77]). Since redshift-distance relation is influenced by cosmological parameters, this is making the comparison and analysis of this relation to cosmological redshift of several cosmic objects a great mean to determine cosmological parameters. One can fit the data and determine  $q_0$ , deducing if the Universe expansion is decelerated or accelerated. For higher redshift, the exact relation must be used with density parameters of matter (baryonic and dark matter) and dark energy. Improvements in digital detector technology in the 1990s made it feasible to start searching large areas of sky for high-redshift supernovae. Two groups set out to do this, with the goal of measuring the deceleration of the Universe and determining  $\Omega_{m0}$  (see Refs. [26] and [78]). Instead they found an accelerating Universe and showed that  $\Omega_{\Lambda 0} > 0$ . Today, we are trying to do this at higher precision to test whether 'dark energy' really is a cosmological constant, with  $w = -1$ , or a new kind of field with a different value of  $w$ .

Among other methods that have been used to determine  $H_0$ , we briefly mention the following :

1. **Gravitational Lens Time Delay.** The pathlengths to two images of the same source produced by a foreground gravitational mass are different. If the source is variable, such as a quasar or a supernova, the delay in the arrival time of light from one image compared to the other is proportional to  $H_0^{-1}$ , and less dependent on other cosmological parameters, such as  $\Omega_{m0}$  and  $\Omega_{\Lambda 0}$ . Initially, the practical implementation of this method suffered from a number of difficulties, the most important being incomplete knowledge of the mass distribution of the lens. However, more recent careful studies of, for example, the quadruple lens system B1608+656, have resulted in improved precision, giving  $H_0 = 71 \pm 3 km s^{-1} Mpc^{-1}$  (see Ref. [79]).
2. **The Sunyaev-Zel'dovich (SZ) Effect in X-ray Galaxy Clusters.** - SZ decrement is produced by the redistribution of CMB photons from the Raleigh-Jeans to the Wien side of the blackbody spectrum through inverse Compton scattering of hot electrons in the intracluster medium. This phenomenon is shown to be distance independent. Since the measured X-ray flux from a cluster is distance dependent, the combination of CMB and X-ray observations can be used to deduce  $H_0$ . Again, the accuracy of this method has improved enormously in recent years, with high signal-to-noise, high angular resolution, S-Z images obtained with ground-based interferometric arrays and high-resolution X-ray spectra (see Ref. [80]).
3. **Luminosity of Giant H ii Regions.** - It has been shown that the luminosity of a star-forming galaxy in the  $H\beta$  emission line,  $L(H\beta)$ , is well correlated with the velocity dispersion,  $\sigma$ , measured from the same spectral feature. While this technique is not yet competitive with the others mentioned in this section, it could (with better observations) be used to probe cosmic expansion to the highest redshifts, since the  $H\beta$  emission line is one of the strongest spectral features of star-forming galaxies (see Ref. [81]).
4. **Cosmic Microwave Background and Baryonic Acoustic Oscillations.** - Statistical measures of the CMB temperature and polarization fluctuations, and of the large-scale distribution of galaxies encode a number of cosmological parameters.

$H_0$  is involved in combination with  $\Omega_{m0}$  and  $\Omega_{b0}$ , so that an accurate independent determination of  $H_0$  can help break degeneracies (see Ref. [82]).

The long-standing debate about Hubble constant value has largely, but not completely, been resolved in the 21st century. In their comprehensive 2010 review, Freedman & Madore (see Ref. [83]) concluded that

$$H_0 = 73 \pm 2 (\text{random}) \pm 4 (\text{systematic}) \text{ km s}^{-1} \text{ Mpc}^{-1}. \quad (1.57)$$

But, Planck measurements give its value to be

$$H_0 = 67.74 \pm 0.46 \text{ km s}^{-1} \text{ Mpc}^{-1}, \quad (1.58)$$

at the 68% confidence level (see Ref. [58]). In a recent measurement, the Baryon Oscillation Spectroscopic Survey (BOSS) collaboration (see Ref. [84]) gives

$$H_0 = 67.6_{-0.6}^{+0.7} \text{ km s}^{-1} \text{ Mpc}^{-1}. \quad (1.59)$$

So, the issue is not totally settled, although the two determinations agree to within  $\pm 1\sigma$  (if the systematic errors have been estimated correctly). Recently, the geometric maser distance to NGC 4258 has been revised to  $7.60 \pm 0.17 \pm 0.15 \text{ Mpc}$  which lowers  $H_0$  by  $3 \text{ km s}^{-1} \text{ Mpc}^{-1}$ , but also produces some tension with the zero-point of the Galactic Cepheids PL relation (see Ref. [85]). Most works now adopt  $h = H_0/100 \text{ km s}^{-1} \text{ Mpc}^{-1} = 0.7$  with an accuracy of 5-10%. **Hubble radius** denotes the distance where receding velocities are near the light velocity and observer can't see any farther. The Hubble constant can be measured also with fair precision by using the time-delay of variable signals of lensed distant sources (see Ref. [86]) and using gravitational waves (see Ref. [87]).

In the Planck data paper of Ade et al. (2016) (see Ref. [58]), they estimated cosmological parameters, at 68% confidence level, presented as follows

$$\Omega_{\Lambda 0} = 0.6911 \pm 0.0062, \Omega_{m0} = 0.3089 \pm 0.0062, \quad (1.60)$$

where  $\Omega_{m0}$  represent both CDM and baryons. For separate contributions, one observes

$$\Omega_{b0}h^2 = 0.02230 \pm 0.00014, \Omega_{dm0}h^2 = 0.1188 \pm 0.0010. \quad (1.61)$$

For the spatial curvature density parameter, Planck data give

$$\Omega_{k0} = 0.0008_{-0.0039}^{+0.0040}, \quad (1.62)$$

at the 95% confidence level. The photons and neutrinos contributions are calculated from the present day CMB temperature giving

$$\Omega_{\gamma 0}h^2 \approx 2.47 \times 10^{-5}, \Omega_{\nu 0}h^2 \approx 1.68 \times 10^{-5}. \quad (1.63)$$

For  $h = 0.68$ , and using the closure relation of Eq. 1.30, we can deduce that a present time 69% of DE, 26% of CDM and 5% of baryons. We can neglect both radiation and spatial curvature contributions. This is making the situation is pretty obscure in all senses as 95% of the Universe is made of unknown components. The age of the Universe in the  $\Lambda$ CDM model as reported by Ade et al. (2016) (see Ref. [58]) is  $13.799 \pm 0.021$  at 68% confidence level.

Looking ahead, there are still strong motivations for improving further the precision of the determination of Hubble constant : not only does  $H_0$  set the scale for all cosmological

distances and times, but its accurate determination is also needed to take full advantage of the increasingly precise measurements of other cosmological quantities. The on-going GAIA mission, and the imminent launch of the James Webb Space Telescope (e.g. see Ref. [88])<sup>7</sup> in particular, are expected to reduce the systematic uncertainty of the zero point of the Cepheid PL relation which underpins many subsequent astronomical distance measures. All of the other methods have undergone major improvements in recent years and will undoubtedly continue to improve in the years ahead.

### 1.3.3 Cosmological constant and dark energy

In GR, vacuum energy has the same dynamical behaviour as Pure geometrical energy. Estimating this energy using QFT gives an estimation of  $10^{76} GeV^4$ . But, the observed value is about  $10^{-47} GeV^4$  (see Ref. [58]). This discrepancy is the so-called **fine-tuning problem** of the cosmological constant. See Martin (2012) (Ref. [89]) for a comprehensive account of  $\Lambda$  and the issues related to it. Another problem is related to energy density of matter and of cosmological constant. The first decreases with the Universe expansion but the second remains constant. But, these two densities are very close at the present time. This observation give raise to the so-called **cosmic coincidence** (see Ref. [90]). Then, cosmological constant represent the simplest and a successful candidate for DE. However, it has those mentioned issues. Several research croups address those questions. Answers vary from : new theories of gravity, extensions or modifications of GR or even Multiverse. Those issues are out of the scoop of this thesis and then a textbook is more relevant for an interested reader (see e.g. Ref. [91], Ref. [?]).

### 1.3.4 Dark matter and small-scale anomalies

On sub-galactic scales, of about 1 kpc, the CDM paradigm displays some difficulties (see Ref. [92]). Those observations are labeled **CDM small-scales anomalies** (e.g. see Ref. [93] for complete overview). The main three of these anomalies merge from the analysis of numerical simulations for structure formation :

1. The Core/Cusp problem (see Ref. [94]) for halo centres profile;
2. The Missing satellites problem (e.g. Ref. [95]) for too few structures around simulated galaxies;
3. The Too big to fail problem (e.g. Ref. [96]) for structures predicted by simulation and not observed.

Some solutions to these small-scale anomalies are proposed as follows :

- **Baryon feedback.** - The cross section for DM particles and the standard model particles interaction must be very small. But in environments of high concentration, such interactions could become important providing an explanation for the anomalies (see Ref. [97]).
- **Warm dark matter.** - WDM having a mass around the  $keV$  decouple from the primordial plasma and are subject to free streaming. This property could possibly solve the anomalies of CDM.

---

<sup>7</sup><https://www.jwst.nasa.gov/>

- **Interacting Dark Matter.** - CDM anomalies may be a consequence of self-interactions between dark matter particles (see Ref. [98] or Ref. [99]). Maccio et al. (2015) (see Ref. [100]) argue that such interaction and mixing between CDM and WDM particles is very successful in resolution of the DM anomalies.

### 1.3.5 Other problems

Studying the nature of DE and DM has central importance in modern cosmology. There are other open problems and here is a short list of them :

1. The problem related to quantum formulation of gravity around the initial singularity : Big Bang.
2. Tensions in constraints on cosmological parameters, such as  $H_0$  and  $\sigma_8$ , between different confidence levels (i.e. CMB) (e.g. see Ref. [101], [102], Ref. [103] and Ref. [104]).
3. Tests for the cosmological principle and also the copernican principle (e.g. see Ref. [105]).
4. The CMB anomalies specially for low multipole (e.g. Ref. [106]).
5. The Lithium abundance problem between predicted and observed (e.g. Ref. [107]).

### 1.3.6 Ingoing observational researches

**Gravitational waves observatories.** - A new era in modern observational cosmology is opened by the recent direct detection of gravitational waves (GW) by the LIGO-Virgo collaboration <sup>8</sup> (see Refs. [108] and [109]). These detected events are originated from merging of black holes or neutron stars. GW has special importance as they could be the only relic from inflation transporting informations on very early Universe. Three ground-based GW observatories are now functional : 2 LIGO (in USA) and Virgo (in Italy). KAGRA <sup>9</sup> (in Japan) is under construction and another INDIGO <sup>10</sup> is planned (in India). The first space-based LISA GW observer is still under study (LISA pathfinder)<sup>11</sup>.

**Neutrino observation.** - Predictions argue that neutrinos should have a cosmic background similar to CMB. Neutrinos has, in general, a very low interaction with matter specially when having a low energy, such as cosmic ones, which represent the great problem for their detection. One of most important neutrino observatory is IceCube <sup>12</sup> located in the South Pole. It detects neutrinos indirectly using their emission of Cherenkov light. Other observatories under construction that may detect this cosmic background of neutrinos.

**Dark matter searches** - Identifying the nature of DM remains crucial open question in modern cosmology. Fortunately, we are in the era of a data-driven era in astroparticle physics that holds great promise towards addressing this question. A wide variety of experiments are currently reaching unprecedented sensitivity in their search for DM interactions in the lab and sky, and the field continues to evolve as new data forces re-evaluation of theoretical models. The Standard Model of particle physics alone cannot

---

<sup>8</sup>LIGO, <https://www.ligo.org/>

<sup>9</sup>KAGRA, <https://gwcenter.icrr.u-tokyo.ac.jp/en/>

<sup>10</sup>INDIGO, <http://www.gw-indigo.org>

<sup>11</sup>LISA, <https://lisa.nasa.gov/>

<sup>12</sup>IceCube, <http://icecube.wisc.edu/>

explain the nature of this DM, suggesting that the model must be extended (see Ref. [110]). Among these candidates, the most famous are the Sterile Neutrino (e.g. Ref. [111]), the Axion (e.g. Ref. [112]), and Weakly Interacting Massive Particles (WIMP) such as Neutralino. The search for DM particles counts on many observatories and the Large Hadron Collider (LHC). See Gaskins (2016) (Ref. [113]) and Liu et al. (2017) (Ref. [114]) for the state of the art review of DM searches.

**Redshift surveys** - These surveys determine mainly angular positions, redshifts and spectra of galaxies (sometimes along their extension and not only at the centre) in certain patches of sky. The Sloan Digital Sky Survey <sup>13</sup> is ground-based and uses a telescope located in New Mexico (USA) operating since the year 2000 and has 14 data releases. The stage IV of SDSS is formed by three sub-experiment:

1. The Extended Baryon Oscillation Spectroscopic Survey (eBOSS), dedicated to redshifts  $0.6 < z < 2.5$  and on the Baryon Acoustic Oscillations (BAO) phenomenon;
2. The Apache Point Observatory Galaxy Evolution Experiment (APOGEE-2) studying our Milky Way;
3. The Mapping Nearby Galaxies at Apache Point Observatory (MaNGA) focus on nearby galaxies.

The V generation of the SDSS starts in 2020 and includes three surveys : the Milky Way Mapper, the Black Hole Mapper and the Local Volume Mapper (see Ref. [115]). The Dark Energy Survey <sup>14</sup> measures redshifts photometrically. Planned surveys also include satellite Euclid <sup>15</sup>, satellite Wide Field Infrared Survey Telescope <sup>16</sup> and the Javalambre Physics of the accelerating Universe Astronomical Survey <sup>17</sup>. The main cosmological goals is to detect weak lensing, BAO and type Ia supernovae with high precision.

## 1.4 Cosmic magnetic fields

This section represent an overview of current state of the art in the field of cosmic magnetic fields. We start from observations, magnetogenesis processes and especially primordial fields generated in pre-recombination era.

### 1.4.1 Observations

Cosmic magnetic fields (CMF) are challenging subject in modern cosmology and astrophysics. The magnetic fields are important for various astrophysical processes from the collapse of proto-stellar clouds creating stars to large scale structure formation. Their existence has more and more observational evidence (e.g. Refs. [116]; [117]; [118] and [119]). Measurements indicate dynamically significant magnetic fields in several observations of galaxies, clusters and recently even in inter-clusters voids. Several observations of strong magnetic fields in high redshift galaxies and in inter-cluster voids put a lower limit on the amplitude of extragalactic magnetic fields of  $10^{-18} - 10^{-15}G$ . The cosmological data, from the gamma-ray observations of Blazars, give smaller limits of  $10^{-9}G$  on magnetic fields with correlation length larger than  $1 Mpc$ . The origin of these magnetic fields ranging from  $10^{-9}G$  to  $10^{-6}G$  has different proposed magnetogenesis processes.

<sup>13</sup>SDSS, <http://www.sdss.org/>

<sup>14</sup>DES, <https://www.darkenergysurvey.org/>

<sup>15</sup>Euclid, <http://sci.esa.int/euclid/>

<sup>16</sup>WFIRST, <https://www.nasa.gov/wfirst>

<sup>17</sup>J-PAS, <http://j-pas.org/>

As most astrophysical and cosmological observations, indirect techniques are used to get information from light collected to estimate magnetic fields in galaxies and intergalactic mediums. Those techniques include among others : Zeeman Effect, equi-partition, Goldreich-Kylafis effect, Chandrasekhar-Fermi method or Synchrotron emission. The main method used is Faraday rotation measurements. The Faraday effect is an interaction between light and a magnetic field in a medium causing a rotation of the plane of polarization. The Faraday rotation angle ( $\theta$ ) is linearly proportional to the longitudinal component of magnetic field projected to the direction of propagation. The rotation angle is also proportional to the wavelength ( $\lambda$ ) of the photons and can be given by the following equation

$$\theta = RM\lambda^2. \quad (1.64)$$

When the source is more distant, the rotation measure ( $RM$ ) will be affected by the expansion of the Universe and the cosmological redshift  $z$  must be included in the expression that will be in cgs units of the form

$$RM = \frac{e^3}{2\pi m^2 c^4} \int_d^0 \frac{1}{1+z(s)} n_e(s) B_{\parallel}(s) ds, \quad (1.65)$$

where  $n_e(s)$  is the density of electrons at each point  $s$  along the path,  $B_{\parallel}(s)$  is the component of the interstellar magnetic field in the direction of propagation at each point  $s$  along the path,  $e$  is the charge of an electron,  $c$  is the speed of light in a vacuum and  $m$  is the mass of an electron. Several teams are working in recent years to improve capabilities of observations in all scales (e.g. Ref. [120] and [121]). Signatures of magnetic fields in CMB observations are powerful tools to investigate them. Primordial magnetic fields can create B-modes from E-modes through the Faraday rotation of CMB photons. The variable correlations and mode coupling in CMB measurements would be a very useful tool to distinguish magnetic field caused B-modes from other causing sources (e.g. Refs. [122] and [123]). Other studies like ultra high energy cosmic rays (UHECR) could give insights to cosmic magnetic fields. As those charged particles are deflected by those fields, studying the deflections of arrival directions is a possible mean to constrain those magnetic fields (e.g. Ref. [124]).

Those techniques have number of unknowns causing imprecisions in magnetic fields estimates. Moreover, those techniques have very difficult task to create a detailed all scales all sky map of cosmic magnetic fields. The impossibility comes from the number of parameters to estimate and the 2 dimensional picture that we have of the Universe. For example and in the case of UHECR, we already don't know the exact sources and start energy of those particles or even the particle type that started the propagation to be iron ( $Fe$ ) or protons ( $p$ ). For Faraday rotation measurements, free electrons density in the medium where photons travels must be estimated which is not an easy task (e.g. Ref. [125]). This method suffers from a major problem that is Faraday ghosts. At predictable polarization angles, one could find possible unphysical Faraday ghosts causing rotation measurements ambiguity (see Ref. [126]). This is adding stress on the wavelength range to use (see Ref. [127]) and creating uncertainty in our estimations. Moreover, lot of statistical efforts and assumptions are made to separate galactic from extragalactic contributions or even primordial in case of CMB observations. Large scale surveys of extragalactic radio sources have great but not clear potential to investigate intergalactic magnetic fields. Techniques to discriminate Faraday rotations contributions are very ambiguous about the estimations degeneracy and danger of over-estimations of each part (see Refs. [128] and [129]).

## 1.4.2 Origins

Several magnetogenesis processes were proposed to explain the origin of cosmic magnetic fields (see Ref. [130]). In astrophysical scenario (bottom-up), seed fields are generated on smaller scales (see Ref. [131]). The astrophysical seed fields have sources including Biermann battery mechanisms for galactic magnetic fields (see Ref. [132]), Weibel instabilities during the structure formation (see Ref. [133]), and also plasma processes or efficient transport mechanism (see Ref. [134]) of magnetic flux from compact systems from the rapid rotation of stars or Active galactic nuclei (AGN). The intergalactic medium fields can be generated by outflows from proto-galaxies at late stages of the evolution of the Universe (see Ref. [135]). In cosmological scenario (top-down), seed fields can be of primordial origin in early Universe prior to galaxy formation (see Ref. [136]). The cosmological weak seed fields (e.g. Ref. [137]) have correlation length larger than the current Hubble radius when generated by quantum fluctuations during inflation (see Ref. [138]). Both of these scenarios require the presence of magneto-hydrodynamics (MHD) turbulence in cosmic plasma and have distinctive observational signatures. The infinite conductivity in the MHD limit provides an explanation of observation of the magnetic fields and not the electric fields in the Universe (see Ref. [139]). The strength of magnetic fields predicted by these different processes is many orders of magnitude lower than the present-day fields (e.g. Ref. [140]). They must have been amplified during cosmic history (e.g. Refs. [141] and [142]). The total energy density presented in magnetic field and the magnetized turbulence is small on the matter of linear power spectrum and becomes stronger due to non-linearity of other processes. It is conventional to derive the cosmological effects of a seed magnetic field by its spectral shape and the smoothed value of magnetic field at a given scale.

The different possibilities for the observed magnetic field amplification range from a MHD dynamo to the adiabatic gravitational compression of magnetic field lines during structure formation (e.g. see Refs. [143] and [144]). Both require initial magnetic seeds with different amplitude and correlation length. The simplest way to increase the magnetic field strength is gravitational compression under the constraint of flux-freezing that gives for a spherical collapse a magnetic field strength proportional to the gas density. The strength of cosmic magnetic field preserved through the magnetic flux conservation increases when the pre-galactic gas collapsed. The dynamo-amplification scenario is supported by the alignment of the galactic fields (see Ref. [141]). The dynamo mechanism amplifies seed fields by the cyclonic turbulent motion of ionized gas combined to the rotation of the galaxy. The small-scale dynamo converts turbulent energy into magnetic energy up to approximation equipartition in terms of the induction equation. The non-linear growth leads to an exponential amplification and the formation of larger-scale magnetic fields with strengths in the order of  $0.1 \times 10^{-9}G$  from the small-scale fields.

A primordial origin is favoured by significant magnetic fields in the intergalactic space, in high redshift systems, in proto-galactic clouds, in early Universe and possible imprints in the CMB power spectrum (e.g. see Refs. [145] and [146]). Observations of magnetic fields in quasars support the efficient conversion by small-scale dynamo of turbulent into strong magnetic energy during the formation of first stars and proto-galaxies (see Ref. [116]). The scenario of dynamo amplification requires an initial seed fields to operate which may have a post- or pre- recombination origin (see Ref. [147]). The strength requirement for the dynamo varies between  $10^{-12}G$  and  $10^{-34}G$ . The efficient astrophysical small-scale dynamo action may compensate the initially weak seed fields on very short time scales by rapid exponentially amplification in the presence of turbulence. The discovery of the proposed primordial magnetic fields would have profound insights into the fundamental problems of the early Universe such as matter-antimatter asymmetry.

### 1.4.3 Magnetogenesis

The cosmological magnetogenesis is assumed to be before recombination in a lot of studies (e.g. Refs. [120]; [148] and [149]). The magnetic fields are generated by cosmological perturbations with scales from  $100 AU$  to the horizon scale. Early magnetogenesis faces problems in both strength and size of primordial fields to account for present day observations. The possible generation processes are nonlinear cosmological perturbations during the radiation-dominated era : phase transitions and breaking conformal invariance during inflationary epoch. The existence of defects in the Standard Model have application to the cosmological electromagnetic field generation.

The magnetic fields generated in the phase transition satisfy the causality condition where the maximal correlation length can not exceed the Hubble radius at the generation time. During cosmological phase transitions, primordial magnetic fields generation can be considered as an injection of magnetic energy to cosmological plasma at a given scale. During the radiation dominated epoch, it is at most comparable to the radiation energy density (see Ref. [150]). The dominant contribution to the magnetic energy density and length scale can be generated from the MHD processes driven by turbulence. The resulting power spectrum and the correlation length of the magnetic field at small wave-numbers has the form of a power-law supported by a phenomenological decay (see Ref. [151]). The comoving length corresponding to the Hubble radius at generation is inversely proportional to the corresponding phase transition temperature which is  $T = 0.15 GeV$  for QCD phase transition and  $T = 100 GeV$  for EW phase transition (e.g. see Refs. [152]; [153] and [154]). The maximal allowed magnetic energy density injected in the phase transition plasma is determined by the temperature and very weakly on the number of relativistic degrees of freedom at the moment when the primordial magnetic field is generated. During the QCD phase transition, the generated strength of magnetic field could reach  $10^{-9}G$  with present day correlation length of  $50 kpc$ . During the EW phase transition, the magnetic fields strength can reach  $10^{-10}G$  with correlation length of  $0.3 kpc$ . The energy density and correlation scale of the magnetic fields depend on their evolution from the cosmological magnetogenesis in phase transition epoch up to the present day epoch.

The gravitationally coupled electrodynamics can generate cosmological primordial magnetic fields during inflation (see Ref. [155]). The coupling is between curvature terms and Maxwell tensor in the Lagrangian representing photon propagation in a curved background. This coupling breaks the conformal invariance of Maxwell's equations in flat backgrounds. Several proposals have been given to break the conformal invariance of the theory : coupling the electromagnetic fields to a non-conformal-covariant charged field, coupling the electromagnetic fields to gravity by either gauge non-invariant terms or gauge invariant terms in the Lagrangian, invoking effects due to the quantum conformal anomaly, or breaking the conformal invariance by non-zero expectation values of flat directions (see Refs. [156]; [155] and [157]). Magnetic fields, generated between inflation and recombination, have small coherence lengths and can not seed galactic dynamo and the required coherence length for dynamo is  $10 kpc$ . Inflation is naturally creating super-horizon correlations and gives solution to the scale problem. Inflation can provide large scale coherence length, but the magnetic field will be weak to sustain the dynamo after an epoch of de Sitter expansion. But, the strength problem remain unsolved, the magnetic field that survives the inflation epoch are weaker than  $10^{-50}G$ . Another field called curvaton could be the completion of the model to obtain strong magnetic fields and the primordial curvature mode in a subsequent era during inflation, producing magnetic seed fields  $10^{-30}G$  (see Ref. [158]). The scalar metric fluctuations would be correlated with the produced large scale magnetic fields after a coupling of electromagnetism to inflation. The direct coupling of electromagnetism to inflation could lead to acoustic signature in

CMB.

Several exotic mechanisms propose modifications in standard model or classical theories to explain magnetic fields generation. The extended versions of classical Maxwell's theory care about electromagnetic fields in cosmological contexts (see Ref. [159]). The behaviour of electromagnetic fields with a low energy regime and wavelengths larger than the solar system radius is still not clear as the case of cosmic magnetic fields. In an expanding Universe, quantum electromagnetic fields found difficulties when trying to impose Lorentz condition. An extended electromagnetic theory eliminating Lorentz condition would allow the scalar states and preserve at the same time the dynamics of ordinary transverse photons. An effective current is then introduced in the usual Maxwell's equations allowing the generation of cosmic magnetic fields from the galactic scales to the Hubble radius. The spontaneous breaking of gauge symmetry and the subsequent development of a charge imbalance was considered as another mechanism of generation of primordial magnetic fields (see Ref. [160]). Experimental constraints, based on the dispersion from pulsar signals, limit the photon charge to be  $5 \times 10^{-30}e$ , or a less restrictive laboratory constraint  $8 \times 10^{-15}e$  (see Ref. [161]). The analysis of the luminosity evolution of red giants in globular clusters leads to a constraint on the charge of neutrinos of  $2 \times 10^{-14}e$  (see Ref. [162]). BBN rules out charges greater than  $10^{-10}e$  for particles with masses less than  $1 \text{ MeV}$ . The presence of a non-zero charge density would break the isotropy of the Universe through the creation of currents and electromagnetic fields. It is possible to constrain the presence of an overall charge asymmetry by the CMB measurements of the isotropy of the Universe.

#### 1.4.4 Primordial magnetic fields constrains

The matter perturbations in the Universe are affected by primordial magnetic field independently to the particular magnetogenesis scenario that assumes the generation prior to recombination (see Ref. [163]). The primordial magnetic fields generated in the radiation-dominated era are usually assumed to have stochastic nature to preserve the global isotropy of the model. The CMB anisotropies from a stochastic primordial magnetic field can be in several ways : Magnetic stress-energy perturbs the metric by the primordial magnetic fields energy density through the Einstein equations, Lorentz force deflects moving electrons and protons coupled to photons and the small-scale fields can alter the recombination history and the distance to last scattering from the enhanced small scale baryonic inhomogeneities (e.g. Ref. [164]). The magnetized matter perturbations generate a power spectrum with different shape compared to standard  $\Lambda$ CDM model by fully non-Gaussian contribution with a non-zero higher statistical moments (see Ref. [165]). CMB temperature anisotropies can provide limits the primordial magnetic fields from their imprints in the CMB power spectrum. A uniform magnetic field with large strength value leads to models incompatible with the high isotropy on large scales of the Universe observed in CMB. Constraining the cosmic magnetic fields from anisotropies at high multi-poles is not a straightforward extension where its dominant contribution is polluted by extragalactic contamination and secondary anisotropies such as Sunyaev-Zeldovich. The South Pole Telescope data are contaminated by some unresolved point sources and by the Sunyaev Zeldovich effect due to galaxy clusters (see Ref. [166]). The CMB anisotropies give an upper limit on vorticity that is translated into lower limits on the present value of cosmic magnetic fields. Current CMB anisotropies lead to upper limits on the amplitude of a stochastic background of primordial magnetic fields generated before nucleosynthesis. The measurable characteristics of observed magnetic fields differentiate the astrophysical or cosmological origin of these fields. Primordial magnetic fields

have certain constraints from nucleosynthesis and CMB : current limits on strength are between  $10^{-9}G$  for homogeneous fields and  $10^{-6}G$  for random fields (e.g. Ref. [167]). A different method to limit the primordial magnetic fields is to limit its total energy density by considering the several cosmological signatures: halos abundance, thermal Sunyaev Zel-dovich effect, mass dispersion that leave detectable signature on LSS statistics, the cluster number density and Lyman- $\alpha$  data giving limits between  $1.5 \times 10^{-9}G$  and  $4.5 \times 10^{-9}G$  (see Ref. [168]).

At a given direction on the sky, the CMB is characterized by its intensity and two additional Stokes parameters, their values depend on the choice of the coordinate axes, qualifying its linear polarization (For standard references see Refs. [169] and [170]). To interpret the polarization maps, it has become customary to separate them to parity-even (E-modes) and parity-odd (B-modes) patterns of observed combinations of Stokes parameters. The E-modes, generated by the existence of intensity fluctuations at last scattering, are observed to be consistent with the spectrum of temperature anisotropies. The B-modes would not be generated at last scattering unless there were gravitational waves or cosmic defects that are sources of metric perturbations of parity-odd components (e.g. Ref. [171]). The weak lensing of CMB photons by large scale structures along the line of sight distorts the polarization patterns generating B-modes. Through the Faraday rotation at or just after the last scattering, primordial magnetic fields can create B-modes from E-modes in CMB with a characteristic spectrum. The spatially dependent Faraday rotation couples off-diagonal CMB modes producing additional non-Gaussian signature in the CMB polarization (e.g. see Refs. [172] and [173]). The mode-coupling correlations between the E and B type polarization and between the temperature and the B-mode help to distinguish and probe the primordial magnetic fields from other sources of B-modes. These possible cross correlation results when the magnetic field, with cosmological relevant strengths, is generated during inflation.

Element abundances in the early Universe are important observables to determine the feature of the physical processes at the epoch of big bang nucleosynthesis (BBN). Since the final nuclear abundances of BBN depend on when the respective reactions becomes ineffective, the energy densities of the Universe influence the abundance of the elements produced in BBN. The total energy density in the radiation dominated era is the sum of the radiation density and the primordial magnetic field energy density neglecting the energy density of matter. Considering the primordial magnetic energy density, the cosmic expansion rate is larger than that of the standard BBN (see Ref. [174]). The primordial magnetic fields affect the BBN through their direct effects on the rate of weak reactions and the cosmic expansion rate by its energy density as their dominant effect. The effect of primordial magnetic field on the cosmic expansion rate increases the abundances of  ${}^4He$ ,  $D$  and  ${}^3He$  and decreases that of  ${}^7Li$  for baryon to photon ratio around the WMAP estimation for Standard BBN (see Ref. [175]). The primordial deuterium abundance is derived by observing the Lyman- $\alpha$  absorption system of the quasars (see Ref. [176]). The primordial magnetic field strength can be constrained by observational constraints on the abundance of light elements and the value of the baryon to photon ratio by BBN calculation including their effects. The primordial magnetic field, in all the possible generation scenarios, should satisfy BBN bounds. The total energy density of the magnetic field should not be greater than 10% of the radiation energy density given an effective magnetic field strength  $8.4 \times 10^{-7}G$  compatible with the extremely small values for causal fields (e.g. Ref. [177]). For causally-generated magnetic fields, there is significant magnetic power only on small scales and it could be as strong as  $10^{-6}G$  to  $10^{-7}G$  close to the bound imposed by the BBN.

The high isotropy of CMB supports that our Universe at recombination was extremely

smooth and gravitational instabilities seem to form this structure around us. The  $\Lambda$ CDM model is the current concordance scenario, but excludes magnetic fields and has large number of free parameters. The primordial magnetic fields are expected to affect the structure formation scenario (e.g. Ref. [178]). The Magnetic Lorentz force generates the density inhomogeneities in the matter distribution. Magnetism affects both the local and the long-range gravitational field by energy density. The anisotropic nature of fields makes it a source of shear distortions and gravitational waves. The ideal MHD approximation looks at the effects of the magnetic Lorentz force on density inhomogeneities in the magnetised structure formation. The presence of magnetic field generates the density perturbations and increases the oscillation frequency and the effective Jeans length and therefore domain where these inhomogeneities can not grow.

## 1.5 Cosmic rays

In this section, we present the phenomenology of cosmic rays, experimental efforts to detect those particle. The most important topic in this field is ultra high energy cosmic rays and enigmatic observations of such particle beyond an expected cut off.

### 1.5.1 Observations

The phenomenology of Cosmic Rays (CR) remains partially revealed over their spectrum, origin and composition. Observational techniques divide the CR spectrum into pieces (e.g. see Refs. [179] and [180]) : low-energy CR, solar-modulated CR, CR in the GeV range, TeV range, accessible to satellite, balloon-borne or ground-based experiments, region of the knee, around the ankle, in the GZK range, up to super-GZK CR or Ultra-High-Energy Cosmic Rays (UHECR). Observations techniques tracks particles created after the interaction of CR with atmosphere using water tanks to record Cerenkov light emitted as relativistic shower particles traverse the water, as well as a set of detectors to record the fluorescent light emitted nitrogen molecules excited by the shower particles as they traverse the atmosphere (see Refs. [181] and [182]). The largest arrays probing highest energies are AGASA in Japan, covering  $100 \text{ km}^2$  with surface detectors (e.g. Ref. [183]). The Pierre Auger Observatory (PAO) in Argentina uses combined ground array and air fluorescence detector, covering  $3000 \text{ km}^2$  (see Ref. [184]). The High Resolution Fly's Eye (HiRes) uses a pure air fluorescence technique (e.g. Ref. [185]). The study of cosmic ray spectrum at extreme energies exhibits significant structure reflecting their origins and propagation (e.g. Ref. [186]). The spectrum should be expected up to the highest energies depending on the source distribution, the extragalactic magnetic field, the source spectrum and composition. The CR spectrum can be described by series of power laws with important reported structures: no structure reported in the spectrum at low energy, a spectral feature called the knee at intermediate around  $3 \times 10^{15} \text{ eV}$  energies with spectral index from  $-2.7$  to  $-3.0$ , a second knee reported by a number of experiments near  $3 \times 10^{17} \text{ eV}$ , an ankle structure reported near energies of  $3 - 5 \times 10^{18} \text{ eV}$  consist of the spectral index of  $-3.3$  and the spectrum flattens above  $10^{18.5} \text{ eV}$  has an approximately  $E^{-2.7}$  spectrum up to the highest observed energies which dominate the falling galactic population.

The only astrophysical motivated distinction is between origins : galactic cosmic rays (GCR) and extragalactic cosmic rays (EGCR) with an unknown energy range of the transition from GCR and EGCR. CR above  $10^{18} - 10^{19} \text{ eV}$  can be from extragalactic unknown sources with energy spectrum that extends up to  $3 \times 10^{20} \text{ eV}$  beyond an expected cut-off (see Ref. [187]). The extragalactic cosmic ray spectrum shape carries information about

galactic evolution as measured by cosmic ray luminosity. From the observational point of view, two roads were followed to pinpoint the GCR/EGCR transition energy : one relying on the spectrum in the change of slope and the other on the composition from the heavy to light transition (see Ref. [188]). The spectral ankle structure is the natural feature where such transition shows up from GCR to EGCR, but not yet established firmly. The composition of the CR does not give much information on the GCR sources which are compatible with the standard interstellar medium, except for the  $^{22}\text{Ne}$  abundance that is much higher among the GCR (e.g. see Ref. [189]). The  $^{22}\text{Ne}$  is produced by very massive stars arguing that CR originates from regions where massive stars are concentrated. A heavy composition, mostly composed of Fe nuclei, could exhibit structure due to nuclear fragmentation. At sufficiently large distances, an initially heavy flux would turn into a light composition dominated by protons. A conclusion has been proposed in the composition, presented by the HiRes collaboration, tentatively showing a transition from heavy to light primary nuclei at energy around  $5 \times 10^{17} \text{eV}$  which could be identified with second knee feature that to be confirmed (see Ref. [190]).

The anisotropy studies provide that the galactic component would become more and more anisotropic as the energy increases and the CR confinement by galactic magnetic fields becomes less effective. No clear indication of a meaningful anisotropy in the CR angular distribution has been obtained and can not be easily used to reveal their sources from the diffusive transport up to a few  $10^{18} \text{eV}$  (see Ref. [191]). The extragalactic incoming flux of CR should be more isotropic in high energy even if the extragalactic fields are low related to the large distance of sources. The highest energy CR above  $10^{20} \text{eV}$  are produced outside the galaxy without doubt, or at least outside the disk, where the galactic magnetic fields can not confine them and their arrival direction pattern does not reflect the galactic structure. The highest energy CR would not be confined in the disks and halos would thus propagate throughout the Universe, while lower energy ones would be confined for some time and increase their density depending on the size and magnetic field of each individual galaxy.

Another important question in cosmic rays studies is the processes creating such high energy particles. The diffusive shock mechanism from supernovae remnants accelerates the GCR up to energy of  $10^{15} \text{eV}$ , but does not work well at high energy at the end of spectrum (e.g. see Refs. [192] and [193]). An important problem of the standard diffusive shock acceleration of isolated supernovae remains that protons can hardly be pushed up to energies higher than few  $10^{14} \text{eV}$  below the knee spectrum. A natural solution of the light elements abundance problem in GCR could be obtained within the so-called super-bubble model which are large galactic structures blown by the joint activity of many massive stars and the explosion of tens of supernovae. The energetically motivated connection between SN and GCR does actually point towards super-bubbles than isolated SN accounting for the acceleration of CR. These super-bubbles may be the source of most of the GCR, up to energies of order of  $10^{17} \text{eV}$  for protons, and up to the ankle for Fe nuclei. The super-bubbles can be important possibility in accelerating CR where a unique type of sources producing CR with spectrum in  $E^{-2.3}$  could account for all the observed CR (see Ref. [194]). Sources of CR up to the ankle spectrum remain unknown that can be related to bend of the charged particle trajectories in the galactic magnetic field and the CR do not point back to their sources.

### 1.5.2 UHECR Cut-off

The defined cut-off was independently calculated in 1966 by Greisen (see Ref. [195]) and by Zatsepin and Kuzmin (see Ref. [196]) (GZK) pointing out that cosmic rays degrade

in energy over cosmological distances. Cosmic rays beyond a certain threshold energy would have an inelastic interaction with the CMB radiation in form of a photo-pion production. The GZK effect is based on the cosmic ray flux being composed of protons. This interaction is greatly enhanced through the excitation of the  $\Delta^+$  ( $1232 \text{ MeV}$ ) resonance

$$\gamma + p \longrightarrow \Delta^+ \longrightarrow p + \pi^0, \quad (1.66)$$

$$\gamma + p \longrightarrow \Delta^+ \longrightarrow n + \pi^+. \quad (1.67)$$

The computation of the interaction threshold is based on the special theory of relativity and particle physics. For the proton with mass  $M$ , momentum  $\vec{p}$  and energy  $E$ , and the CMB photons momentum  $\vec{q}$ ; the square of centre-of-momentum system energy ( $E_{cms}$ ) is given by

$$E_{cms}^2 = (E + q)^2 - (\vec{p} - \vec{q})^2, \quad (1.68)$$

$$E_{cms}^2 = M^2 + 2q(E - |\vec{p}| \cos \theta), \quad (1.69)$$

where  $\theta$  is the angle between the proton and CMB photon directions.

To cosmic rays at very high velocity, CMB photons appear to be blue-shifted by the Doppler Effect up to gamma ray energies. The centre of momentum system energy can be at least equal to the sum of proton (or neutron) and pion masses. The interaction threshold energy ( $E_{threshold}$ ) is then

$$E_{threshold} = 5.96[y(1 - \cos \theta)]^{-1} 10^{20} eV. \quad (1.70)$$

The CMB energy could be represented by  $q = ykT$  where  $kT = 2.35 \times 10^{-4} eV$ . For head on collisions, we can put ( $\cos \theta = -1$ ) and  $y = 5$  resulting in  $E_{threshold} = 6 \times 10^{19} eV$ . The interaction cross section near threshold is  $\sigma = 2 \times 10^{-28} \text{ cm}^2$ . The total CMB photon density is  $\rho = 400 \text{ cm}^{-3}$  (e.g. Ref. [197]). The collision mean free path would be then  $\lambda = \frac{1}{\rho\sigma} = 4.1 \text{ Mpc}$  and for the 10% of photons with  $y > 5$ , the mean free path would be of order  $50 \text{ Mpc}$ . Less than 20% of protons survive with energy above  $3 \times 10^{20} eV$  limiting the propagation distance to about  $18 - 60 \text{ Mpc}$  (e.g. Ref. [198]). A secondary minimum near  $3 \times 10^{18} eV$  develop because of the  $e^+e^-$  production of protons on the CMB photons with additional energy loss. As the mean free path for this process is few Mpc, proton of initial energy  $10^{20} eV$  is virtually impossible to travel distances greater than  $50 - 100 \text{ Mpc}$  without losing a large fraction of its energy. Only nearby sources (closer than about  $50 \text{ Mpc}$ ) could produce protons which would escape the GZK mechanism due to lack of interaction length. The distance forms the boundary of the so-called 'GZK sphere'.

The main problem in the UHECR phenomenology remains the absence of a GZK feature above  $10^{20} eV$ . Many of the pioneering ground array experiments such as Volcano Ranch, Haverah Park and AGASA seemed to see a continuing flux of particles beyond the GZK energy cut-off (see Ref. [199]). More than 20 cosmic rays have been observed with nominal energies at or above  $10^{20} \pm 30\% eV$  with record Fly's Eye event having  $3.2 \times 10^{20} eV$ . The GZK suppression break point is at  $5.62 \times 10^{19} eV$  in the spectrum. The GZK predictions are consistent with observations in five sigma significance given the apparent discrepancy between the current observational results and the poor available statistics. But, none of the post-GZK events pointed firmly to any astrophysical source within the local GZK sphere which should be expected if higher energy UHECRs are not attenuated. Unresolved trans-GZK events are the fundamental questions concerning the composition/charge of the primaries and how the distribution of arrival directions is related to the spatial distribution of sources. The Hillas condition and other properties of sources capable of accelerating protons to these high energies, do not match to any

sources within  $50 Mpc$  that somehow explain the origin of the observed UHECR (e.g. see Refs. [200] and [201]).

With no distance information available for cosmic ray events, statistical analysis of the arrival directions of cosmic ray induced air-showers is necessarily restricted to two dimensional tests. The two point correlation function is an effective and commonly used statistic to measure departures from homogeneity of an observed distribution of points separated by an angle (see Ref. [202]). It represent only the lowest order term in a Taylor series expansion of the characteristic function of the probability distribution. Small scale angular anisotropies in the distribution of galaxies are associated with localized spatial inhomogeneities. This is similarly true for UHECR if they originate from sources embedded in a matter distribution. The clustering of UHECR arrival directions into doublets and triplets was analysed with the Monte Carlo simulations (e.g. Ref. [203]). Investigations of AGASA data of 92 events have found statistically significant clustering on small scales for an opening angle of  $3^\circ$ , but with no apparent clustering or anisotropy on large scales on angular scales of  $4^\circ$  to  $5^\circ$ . The observed configuration of 4 doublets for an angle  $2.5^\circ$  has a probability of less than 0.1% to occur due to random projection. The observed anisotropy and correlation with the super-galactic plane may be related to a source distribution residing within the Local super-cluster. The energies partitions found are consistent with certain expectations of regimes where GZK or magnetic fields effects change their relative importance. The three energy distributions may possess the following properties : cosmic rays with energy  $E < 5 \times 10^{19} eV$  of a primary distribution largely unaffected by GZK losses, proton primaries with  $5 - 8 \times 10^{19} eV$  energy that lost energy through the GZK effect and trans-GZK primaries of unknown composition and origin with energies  $E > 8 \times 10^{19} eV$  that may or may not be losing energy through GZK effect (e.g. Ref. [204]). The presence of three distinct energy-partitioned events could reflect possible changes in primary composition, different source distributions, differing levels of GZK losses, or deflection effects of magnetic fields. The GZK paradox is the apparent lack of suitable astrophysical sources of the observed high energy cosmic rays with energy  $E > 5 \times 10^{19} eV$  (UHECRs). No correlation has been found between the arrival direction of high energy cosmic rays and the most likely sites of origin for these particles namely, AGN at distances less than  $60 Mpc$ . The angular distribution of GRB or AGN sources does not match to that of the arrival directions of UHECR, leading to the absence of identifiable sources.

The ultra-high-energy nuclei and photons lose energy even more readily. The relevant process, for establishing the limit on the maximum energy of photons that can reach us from distant sources, is electron-positron pair production/absorption due to interactions with the Far Infrared Background radiations (FIBR) (see Ref. [205]). For the photons from Markarian 501, FIBR absorption should become efficient around  $10 TeV$  (see Ref. [206]). Higher energy photons should collide with FIBR photons, disappearing into an electron-positron pair, and should not be able to reach observatories. Photons with energies as high as  $24 TeV$  are observed from Markarian 501(a BL Lac object at  $157 Mpc$ ). With respect to the Markarian 501 paradox, there have been clear identification of the particles as photons and clear identification of Markarian 501 as the source. The satisfactory level of accuracy of the FIBR measurement is significant for establishing the Markarian 501 paradox that depends on the density of FIBR ( $0.005 eV$ ). Another anomalous observation of UHECR is the longitudinal development of the showers (see Ref. [207]). The kinematic rules for the production of particles and particle theories can predict some features of the longitudinal development of the showers as the probability distribution of the maximum depth. Experimental data on the air shower produced by ultra-high energy hadronic primaries appear to be in disagreement with these predictions. The analysis

suggests that the ultra-high-energy neutral pions are more stable than low-energy ones or the available phase space for decay in two photons was becoming smaller.

## 1.6 Numerical simulations in cosmology and astrophysics

Most problems in astrophysics are multi-variant and non-linear in nature and only the power of computational resources could get us useful data about them. Magnetohydrodynamic simulations are taking more interest lately. Cosmological magnetic fields are simulated from primordial seed fields to galactic outflows models (e.g. Ref. [208]). Several codes are developed and available to simulate the evolution of the Universe in both cases with and without magnetic fields. Those codes are using two main approaches to solve hydro-dynamical equations :

1. Smoothed Particle Hydrodynamics (SPH) (see Refs. [209] and [210]) or Lagrangian hydrodynamics where particles are used to approximate the behaviour of continuum dynamics of fluids such as GADGET (see Ref. [211]);
2. Adaptive Mech Refinement (AMR) (see Ref. [212]) or Eulerian hydrodynamics where the simulation box is divided to several subsections and the partial differential equations of hydrodynamics evolutions are solved using several methods of finite volume discretization of fluid dynamics (see Ref. [213]) such as RAMSES (see Ref. [214]).

Within the Lagrangian approach, other codes were developed such as: Hydra [215], Gasoline [216] or GrapeSPH [217]. Within Eulerian approach, the following codes were developed : NIRVANA [218], FLASH [219], ZEUS [220], ART [221], Athena [222], Pencil Code [223], Heracles [224], Orion [225], Pluto [226], CASTRO [227], GAMER [228]. Many problems in numerical analysis are often limited to pre-determined quantified grids as in the Cartesian plane which constitute the computational grid, or 'mesh'. Adaptive mesh refinement is a method of adapting the accuracy of a solution within certain sensitive or turbulent regions of simulation. This is done dynamically and during the time the solution is being calculated. The AMR function allows us to achieve higher resolutions more efficiently by only fully resolving areas of interest, designated by baryon and particle over-densities. Each of those codes are now in use to tackle down several cosmological and astrophysical problems. Each code has its method having its strong and weak points.

Using large computational resources, important simulations were done using those codes and their datasets (at least for some of them) are available. Besides the original Millennium (see Ref. [229]) and Millennium II (see Ref. [230]) simulations, we find also simulations like Illustris simulations [231], MICE [232], Bolshoi and Multidark [233], DarkSky simulations [234] and Q Continuum simulation [235]. Those simulations give us a detailed picture that allow the study of magnetic fields origins and possible evolution processes responsible for current observed state. Those simulations are finished by creating and comparing synthetic to real observations. Subjects studies range from galaxy formation and clusters formation (e.g. Refs. [236] and [237]), recreation of local observable Universe and galaxies distributions with redshift catalogues similar to the ones observed (e.g. Ref. [238]; [239]; [240]; [241] and [242]), satellite galaxies (e.g. Ref. [243] and [244]), observations done with variant light bandwidths (see Ref. [245]), and of course and as discussed above cosmic magnetic fields studies (e.g. Ref. [246]; [247] and [248]). Different processes like feedbacks of stellar formation, Active Galactic Nuclei or

supernovae and black holes are included to make those simulations the closest possible to real Universe evolution (e.g. Ref. [249] and [250]). Such simulations are done now to recreate local and global observations of magnetic fields by creating and comparing synthetic to real observations. Those simulations are helping us to evaluate observations made like Faraday rotation measurements, the analysis methods used and new ways to extract reliable data from them (e.g. Ref. [208]).

## 1.7 Chapter conclusions

The phenomenon of paradox can be defined as an unacceptable conclusion resulting from an acceptable model of inference and from acceptable initial presuppositions. The different types of astrophysical paradoxes are the paradoxes of physics according to their structure defining the functional aim of creating paradoxes. The astrophysical paradoxes cover a wide spectrum of physical branches used to formulate and solve astrophysical phenomena. According to the manner of their establishing and the valid previous knowledge, a certain phenomenon called paradoxical can be paradox of assumption and paradox of paradigm. Paradox of assumption can be related to the inaccurate initial supposition in the process of explaining a physical phenomenon within the same paradigm where the deductive analysis is based upon the assumption leading to the conclusion contradictory to the actual condition of the physical system. Paradox of paradigm exists within the framework of a paradox, when the paradigm is changed the paradox is gone. such phenomena should studied with both analytical and numerical methods. My point in doing the analytic calculations is to understand the physics of the cosmological phenomena. On the other hand, observation needs accurate calculations which must be done numerically. So, the main recommendation is to use numerical codes to obtain significant and reliable results in the complex problems found in cosmological and astrophysical context.

# Chapter 2

## SCOPE: Constraining cosmological parameters using Boltzmann equations

Cosmological parameters estimation is a major goal of modern cosmology studies. We search for the combination creating the best fitting of observational data to theoretical models. For SNIa, we compare data with redshift-distance relation. For CMB data, we fit the power spectrum of anisotropies. Cosmological parameters are impacting both cases by the expansion rate of the Universe. In those data analysis, we use Monte Carlo methods to get maximum likelihood. In those methods, random combinations of cosmological parameters are generated which follow conditions to converge toward best fitting. At the end, regions of, for example, the  $(\Omega_{m0}, \Omega_{\Lambda0})$  plan are highlighted and believed to contain the searched combination describing the Universe.

We consider in this chapter the recombination era of early Universe. We are interested in densities of chemical composition like electrons, protons and hydrogen atoms. Those densities evolution are described by Boltzmann equations. Those equations are affected by the expansion of the Universe and thus by cosmological parameters values. We develop a new code which computes the evolution of free electron densities using numerical integration. Then, a physical constrain is presented on cosmological parameters via their impact on those densities evolution. Those constrains could help as prior bounds to cosmological parameters estimations from observational data.

### 2.1 Recombination era and densities evolution

**Boltzmann equation** describes the evolution of the phase-space density of a particle. This gives the probability of finding the particle in some volume. The Boltzmann equation states that (see Ref. [251])

$$L[f] = C[f], \quad (2.1)$$

where  $f$  is the one-particle distribution function. The operator  $L[f]$  acting on  $f$  is similar to the convective derivative used in fluid dynamics and is also called **Liouville operator**.  $C[f]$  is **collision operator**, i.e. a functional of  $f$  describing the interactions among the particles constituting the system under investigation and that may alter the phase-space density. If interactions are absent, Boltzmann equation is collisionless, also called **Vlasov equation** (see Ref. [252]). On the other hand, when the interaction rate is extremely high, i.e. it is much larger than than the Hubble rate. This equation represents **chemical equilibrium** and is also known as **Saha equation** (e.g. Ref. [253]).

For most interesting applications, we need to investigate interactions of two particles (1, 2) resulting to (3, 4) such as

$$1 + 2 \longleftrightarrow 3 + 4. \quad (2.2)$$

This reaction can describe scattering or annihilation and is suitable for discussing BBN, recombination and calculating the expected relic abundance of CDM. Let us take the particle 1 as reference and let us focus on its Boltzmann equation (see Ref. [251])

$$a^{-3} \frac{\partial(n_1 a^3)}{\partial t} = n_1^{(0)} n_2^{(0)} \langle \sigma \nu \rangle \left[ \frac{n_3 n_4}{n_3^{(0)} n_4^{(0)}} - \frac{n_1 n_2}{n_1^{(0)} n_2^{(0)}} \right], \quad (2.3)$$

where

$$\langle \sigma \nu \rangle = \frac{1}{n_1^{(0)} n_2^{(0)}} \int \int \int \int \frac{d^3 \vec{p}_1}{(2\pi)^3 2E_1} \frac{d^3 \vec{p}_2}{(2\pi)^3 2E_2} \frac{d^3 \vec{p}_3}{(2\pi)^3 2E_3} \frac{d^3 \vec{p}_4}{(2\pi)^3 2E_4} (2\pi)^4 \delta^4(P_1 + P_2 - P_3 - P_4) |M|^2 \exp(-(E_1 + E_2)/T). \quad (2.4)$$

Boltzmann equation is used to compute the evolution of free electron fraction in the cosmological Hydrogen recombination. The evolution equation can be applied after the end of Helium recombination and the beginning of the Hydrogen recombination until the re-ionization. For the recombination process, the interaction involve (e, p) resulting in (H,  $\gamma$ ) and Boltzmann evolution of the free electron fraction  $X_e$  defined as

$$X_e = \frac{n_e}{n_p + n_H} = \frac{n_e}{n_p^{(0)}}, \quad (2.5)$$

would be given by

$$\frac{\partial X_e}{\partial t} = C_r [(1 - X_e)\beta - n_b \alpha^{(2)} X_e^2]. \quad (2.6)$$

The parameters of this equation are

$$\beta = \left(\frac{m_e T}{2\pi}\right)^{3/2} e^{-B_1/T} \alpha^{(2)}, \quad (2.7)$$

$$\alpha^{(2)} = \frac{64\pi}{(27\pi)^{1/2}} \frac{e^4}{m_e^2} \left(\frac{T}{B_1}\right)^{-1/2} \phi_2, \quad (2.8)$$

$$\phi_2(t < 6000K) \approx 0.448 \ln\left(\frac{B_1}{T}\right), \quad (2.9)$$

and

$$C_r = \frac{\Lambda_\alpha + \Lambda_{2s-1s}}{\Lambda_\alpha + \Lambda_{2s-1s} + \beta^{(2)}} \quad (2.10)$$

where baryon number density  $n_b$ , the collision ionization rate  $\beta$  (see Eq. 2.7), the recombination rate  $\alpha^{(2)}$  (see Eq. 2.8) and the reduction factor  $C_r$  (see Eq. 2.10). This factor  $C_r$  is just the ratio of the net decay rate to the sum of the decay and ionization rates from the  $n = 2$  level. The free electron fraction evolution equation was first studied by Peebles (1968) (see Ref. [70]). Cosmological parameters affect the evolution of this equation in two parts : The first one is in baryon number density  $n_b$  related to the baryon density parameter and the second one is in the conversion of equation to be in function of the scale factor (see Eq. 2.11). We write then

$$\frac{\partial X_e}{\partial a} = \left[\frac{da}{dt}\right]^{-1} C_r [(1 - X_e)\beta - n_b \alpha^{(2)} X_e^2], \quad (2.11)$$

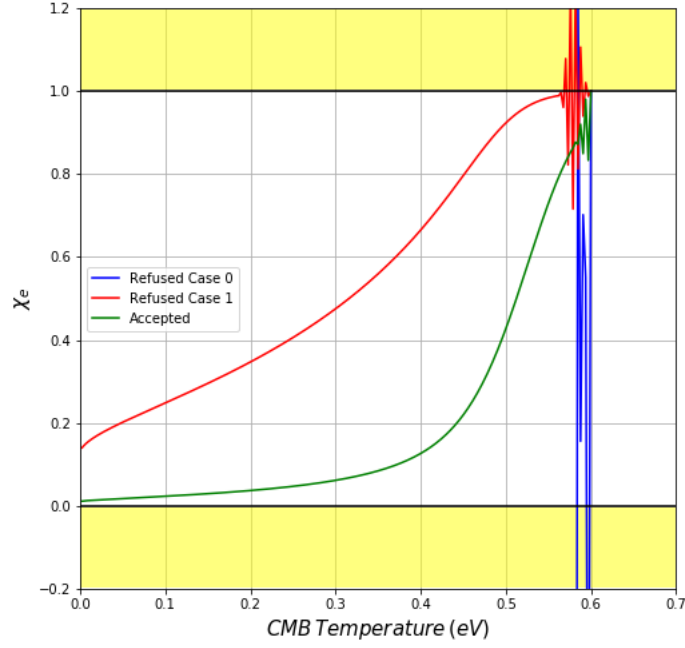


Figure 2.1: Free electron fraction evolutions: the three possible cases.

where

$$\frac{da}{dt} = \frac{3.24 \times 10^{-18}}{a} (\Omega_{\Lambda 0} h^2 a^4 + (\Omega_{dm0} + \Omega_{b0}) h^2 a + \Omega_{r0} h^2)^{1/2}. \quad (2.12)$$

The free electron fraction evolution equation based on the Boltzmann equation is physically well argued. This equation is independent of models of perturbations : the different gauges of metric perturbation and the inflation parameters and models. Eq. 2.11 describes the evolution of free electron fraction in term of the Universe's scale factor, making the impact of cosmological parameters on this fraction evolution more clear. Due to the complexity of the expression, straightforward analytical solution could not be found and a numerical integration is more convenient. It is imperative to get physically meaningful values all along this integration. For instance, the number densities are by definition positive quantities and then their fraction must be positive too. Moreover, our model of the Universe is based on charge symmetry. Recombination era starts with equal numbers density of protons and electrons. Then, the fraction evolution should not exceed one in any time during the integration. Some combinations of cosmological parameters values could lead the fraction evolution to violate one of these two conditions. Any Universe described with such combinations is incoherent with the physics of this equation and its existence is not possible.

## 2.2 Code algorithm

As discussed in the previous chapter, numerical calculations are used to determine the epoch of recombination from Boltzmann equations. Similarly, a C++ code was written to constrain the cosmological parameters combinations through the free electron fraction evolution. The code is labelled SCOPE "Simulation for COsmological Parameters Estimation". For each set of cosmological parameters, the numerical integration is carried from the start of recombination. At this start, the free electron fraction is set to be 1

which means that the Universe plasma is completely ionized. The integration is done by incrementation with fixed scale factor step. The concept of the recombination is more neutral hydrogen atoms form, then we expect that the fraction of free electron to drop in all this era. But, the integrated free electron fraction equation considers also the recombination to higher levels effects. At each step, the fraction is checked for the two conditions discussed above. If one of them was violated at any time before the end of recombination era, the set is considered as physically inconsistent. Cases where the fraction becomes negative are labelled as "refused case 0". Cases where the fraction exceeds one are labelled as "refused case 1". Only when the evolution is within the accepted interval from the start to the end of recombination era, we consider this combination as "accepted". Our Universe would be then one of these possible Universes described by accepted combinations (see Fig. 2.1). To determine which of these combinations fits our Universe, the analysis of cosmological data like CMB or supernovae is required. Then, our code determines only whether or not a combination of cosmological parameters values could be consistent with our knowledge of recombination era and its processes.

To have more physical significance, the code is set to accept inputs on recombination start and end as CMB temperatures ( $T_{Start}^{CMB}$  and  $T_{End}^{CMB}$ ). The algorithm then converts the two CMB temperatures to scale factor limits of the integration. The CMB temperature at the start of recombination is believed to be  $0.25 eV$  and to be  $0.0023 eV$  at the re-ionization (see Refs. [70] and [254]). We take the present day CMB temperature to be  $2.348 \cdot 10^{-4} eV$  (see Ref. [255]). It is used to compute photon contribution to density parameter of relativistic particles. The next input is the number of iterations ( $N_{Iterations}$ ) between these two limits. We determine then the scale factor step of the integration. The cosmological parameters examined are generated using the random generators of C++ libraries and are identified by  $N_{Parameters}^{cosmological} = 4$ . In some variations of the simulations, we simulated Universes containing baryon matter with/without dark matter and with/without dark energy ( $N_{Parameters}^{cosmological} = 3 - dm$ ,  $N_{Parameters}^{cosmological} = 3 - de$ ). The generation process could be done beforehand or during the simulation. The cosmological parameters considered are : Hubble constant and density parameters of baryon, dark matter and dark energy. The two different contributions to the evolution equation of the baryon matter impose the generation of baryon and dark matter contribution separately rather than density parameter for all matter. Density parameter of relativistic neutrinos is also considered in some simulations in which case  $N_{Parameters}^{cosmological} = 5$ . In those simulations, this density parameter is fixed in some simulations and is generated randomly in others. When the contribution of neutrinos is fixed, present day neutrino density parameter that contributes to density parameter of relativistic particles is provided to the code as input. The only condition on the generated combinations is that they describe a flat Universe. Then, the sum of density parameters of baryon, dark matter, dark energy and relativistic particles must be one. Helium fraction is also introduced as one of the evolution equation parameters. This helium abundance  $Y_p$  converts the number density of baryons to number density of free electrons at the decoupling epoch and it is given by  $n_e = (1 - Y_p)n_b$ , since helium recombines earlier than the epoch of photon decoupling (see Ref. [70]). The integration is then done from the scale factor value representing the start of recombination. The simulation is immediately interrupted when one of the two conditions are violated. The simulation is repeated for the number of combinations given as input. Three files are generated at the end of the simulation containing the lists of "accepted", "refused case 0" and "refused case 1".

Table 2.1: Input parameters for simulations done using SCOPE code.

Sim	$T_{Start}^{CMB}$	$T_{End}^{CMB}$	$Y_{Helium}$	$N_{Iterations}$	$N_{Parameters}^{cosmological}$	$N_{pairs}^{accepted}$
001	0.25	0.0023	0.24	10000	4	876
047	0.25	0.0023	0.24	50000	4	3679
019	0.25	0.0023	0.24	100000	4	7400
018	0.25	0.0023	0.23	30000	4	2493
002	0.25	0.0050	0.24	100000	4	9228
003	0.25	0.0012	0.24	100000	4	3889
004	0.25	0.0006	0.24	500000	4	1455
005	0.25	0.0002348	0.24	500000	4	1474
021	0.25	0.0002348	0.75	1000000	3-dm	5044
013	0.5	0.0023	0.24	50000	4	880
017	0.4	0.0023	0.24	40000	4	1566
046	0.4	0.0023	0.24	50000	4	1912
035	0.5	0.0002348	0	1000000	3-dm	2512
020	0.25	0.0023	0.24	50000	4	3891
042	1	0.0023	0.24	500000	5	134
044	0.6	0.0023	0.24	50000	5	666
040	0.5	0.0023	0.24	50000	5	9335
041	0.25	0.0023	0.24	100000	5	4722
043	13.6	0.0002348	0.24	1000000	5	262

Table 2.2: Input parameters for special simulations done using SCOPE code given inconsistent accepted combinations.

Sim	$T_{Start}^{CMB}$	$T_{End}^{CMB}$	$Y_{Helium}$	$N_{Iterations}$	$N_{Parameters}^{cosmological}$	$N_{pairs}^{accepted}$
007	13.6	0.0023	0.24	1000000	4	1
009	13.6	0.0002348	0.24	1000000	4	1
014	0.75	0.0023	0.24	75000	4	1
015	0.6	0.0023	0.24	100000	4	1
049	0.6	0.0023	0.24	50000	4	1
016	0.55	0.0023	0.24	50000	4	1
006	1	0.0023	0.24	1000000	4	1
010	1	0.0023	0.76	100000	4	1
008	1	0.0002348	0.24	1000000	4	1
022	1	0.0002348	0	1000000	3-dm	30
023	1	0.0002348	0	1000000	3-de	30
024	1	0.0002348	0	1000000	4	1
029	1	0.0002348	1	1000000	3-dm	30
030	1	0.0002348	0.25	1000000	3-dm	30
031	1	0.0002348	0.5	1000000	3-dm	30
032	1	0.0002348	0.75	1000000	3-dm	30
033	1	0.0002348	0.99	1000000	3-dm	30
034	0.75	0.0002348	1	1000000	3-dm	30
011	1	0.0023	0.76	1000000	4	1
012	13.6	0.0002348	0.76	1000000	4	1

## 2.3 First results and discussions

SCOPE simulations could take from several minutes to several hours depending on the number of iterations and the number of combinations tested (see Table 2.1). The precision of the integration is changed using the number of iterations. The number of combinations tested was fixed to 1000000. From all simulations done, some configurations of the CMB temperature of the start and end of recombination resulted in another type of inconsistent combinations (see Table 2.2). Those simulations don't violate the two conditions, but they are not for possible Universes as the baryon density is null.

To represent data, multiple scatter plots are created in each single figure. Each scatter plot represents the accepted (or refused in some plots) pairs of two cosmological parameters as given by the simulation. The plots show the ranges of all cosmological parameters simulated. Each simulation had a unique pattern corresponding to parameters configurations (see Fig. 2.2, Fig. 2.3, Fig. 2.4, Fig. 2.5 and Fig. 2.6). The common observation of our simulations is that accepted combinations are dispersed over regions of cosmological parameters pairs. This dispersion makes that in closest neighbour of an accepted combination; we find refused combination of one or both cases (see Fig. 2.7, Fig. 2.8 and Fig. 2.9).

The tendency for baryon density parameter is for lower values less than 0.01. For Hubble constant, the tendency is for higher values more than 0.5. In the opposite, all intervals between 0 and 1 are possible for dark matter and dark energy density parameters or even for neutrinos density parameter. The sum of dark matter and dark energy density parameters are close to one, as shown in their corresponding plan. This is related to the fact that we simulated only combinations describing flat Universes. The tendency of baryon and relativistic particles to have very weak contribution. Then, the deviation from 1 is weak of the sum of dark energy and dark matter density parameters. Only when we consider neutrinos contributions to be highly variate than this tendency is changed and all values become possible. Doing simulations using higher number of iterations, then better integration precision, increase the number of accepted combinations and widen the range where we find them (see Fig. 2.10).

The two temperatures of the start and end of recombination era are strongly related to cosmological parameters. When these two SCOPE inputs change, the accepted intervals of the cosmological parameters change. When we fix the start of the recombination to  $0.25 eV$  and change the temperature at the end, we find more accepted cases and wider ranges for higher temperatures at the end of recombination (or the start of reionization) (see Fig. 2.11). These temperatures, around  $0.005 eV$ , are related to shorter recombination era. Similar results are obtained when fixing the end of recombination to  $0.0023 eV$  and changing the start of recombination. More accepted cases are present with lower temperatures at the start of recombination (see Fig. 2.12).

## 2.4 Application on Neutrinos : massive vs. relativistic

Massive and relativistic neutrinos contribute to different parts in Eq. 2.11. The relativistic neutrinos contribute to density parameter of relativistic particles as described in Eq. ???. But, massive neutrinos contribute to density parameter of dark matter (see Ref. [256]). Considering neutrinos as relativistic and as massive in two time simulation allows measuring cosmological parameters evolution for both neutrino types. Relativistic neutrinos contribution to  $\Omega_{r0}h^2$  vanishes with the existence of massive neutrinos. The

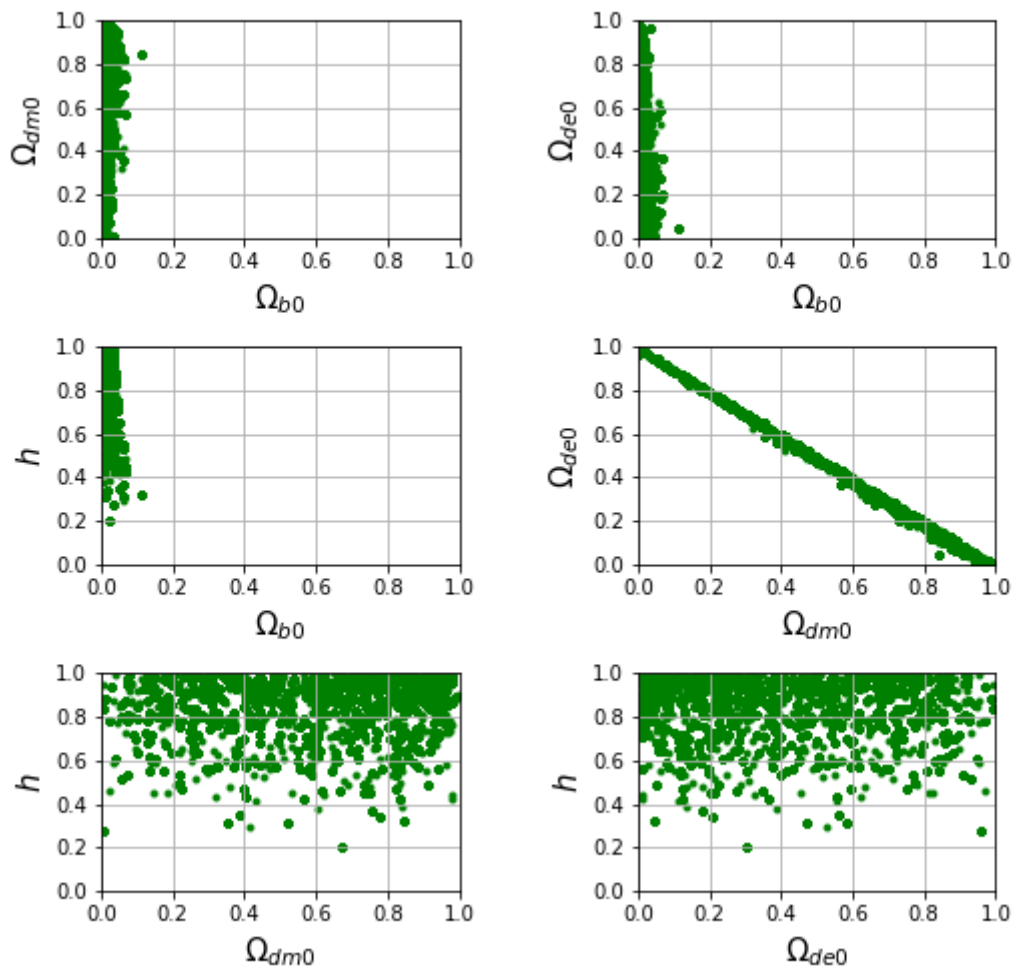


Figure 2.2: Accepted combinations of all cosmological parameters for simulation Sim.002.

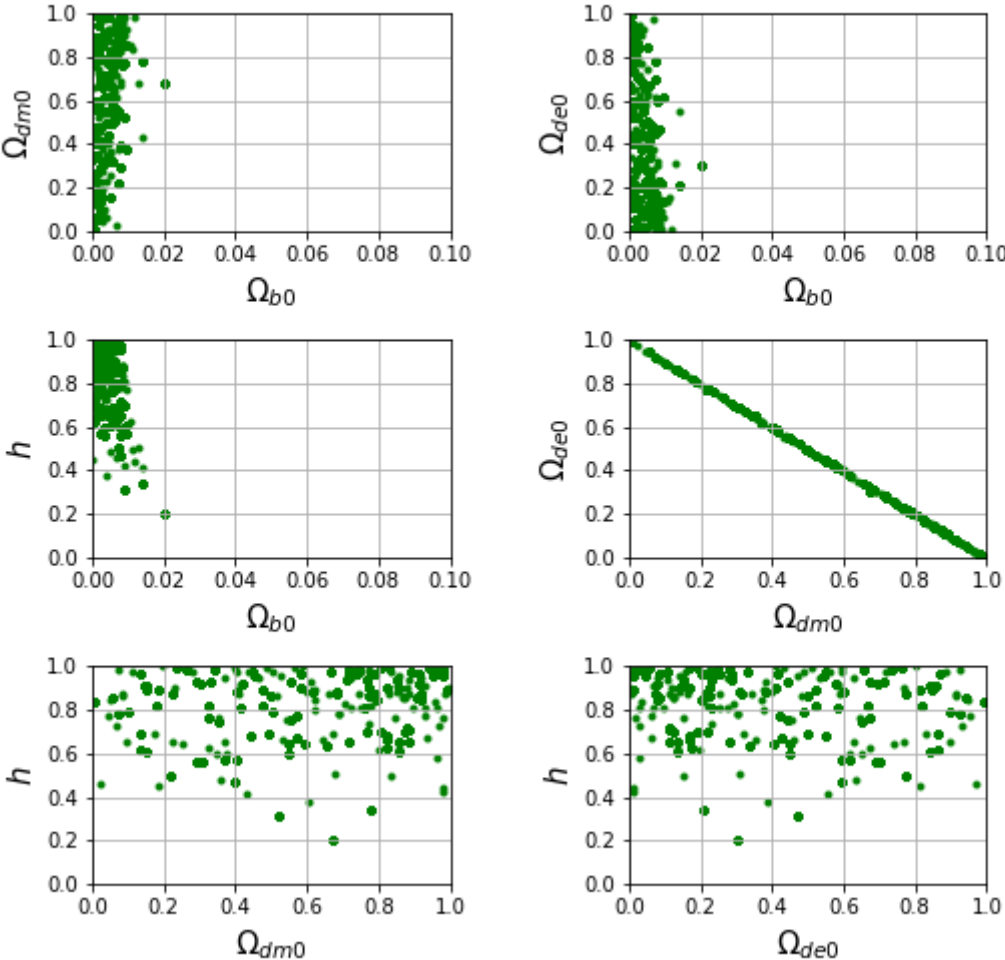


Figure 2.3: Accepted combinations of all cosmological parameters for simulation Sim.020.

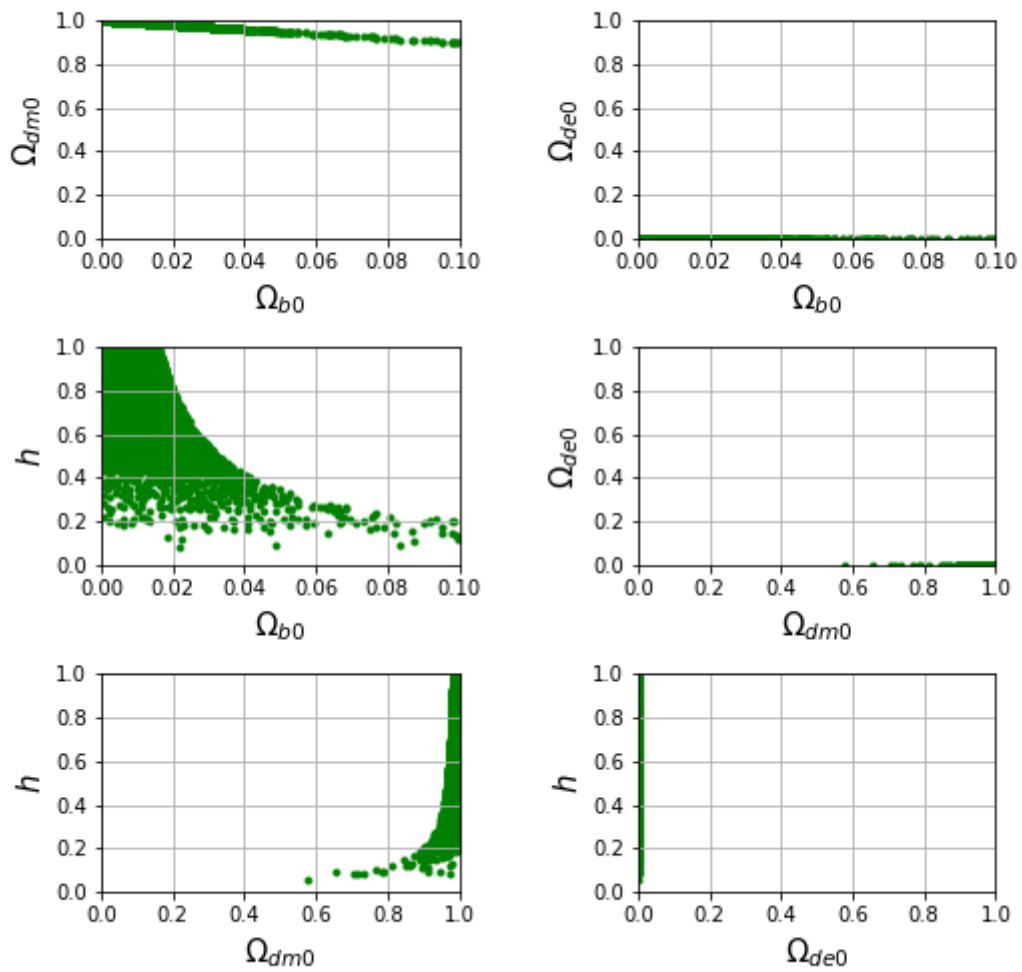


Figure 2.4: Accepted combinations of all cosmological parameters for simulation Sim.021 (with no dark energy in the Universe).

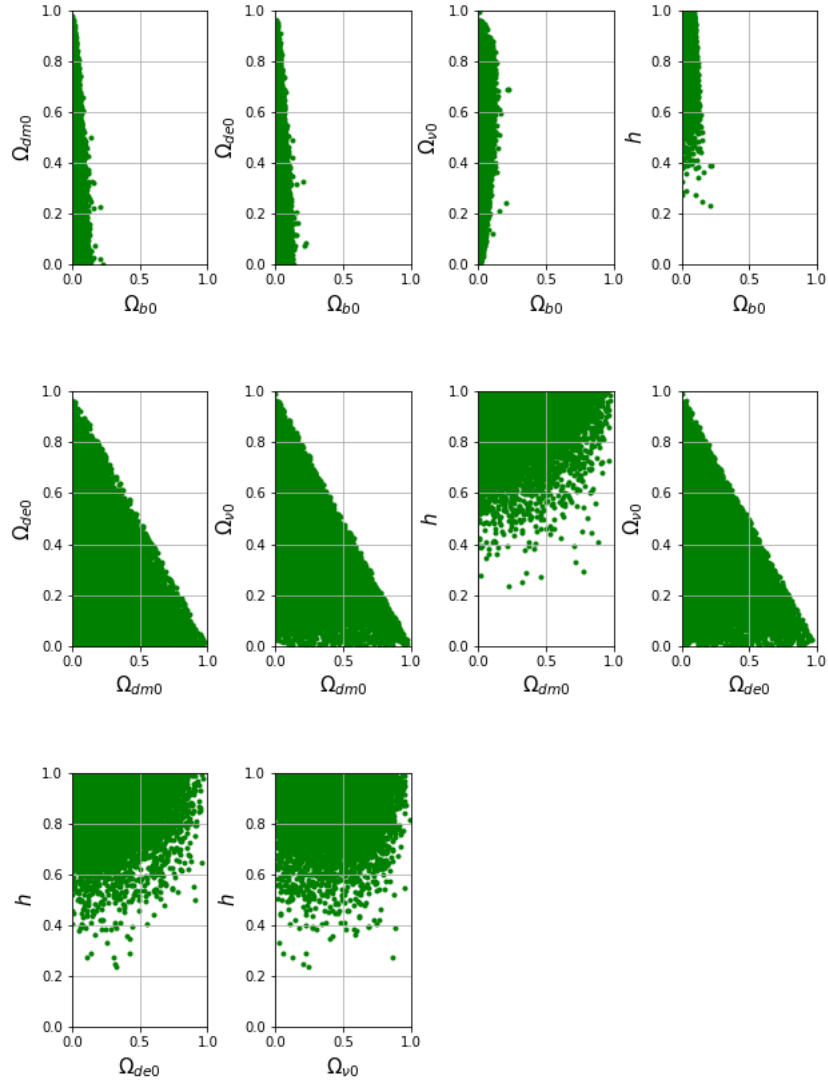


Figure 2.5: Accepted combinations of all cosmological parameters for simulation Sim.040 (with relativistic neutrinos density parameter simulated).

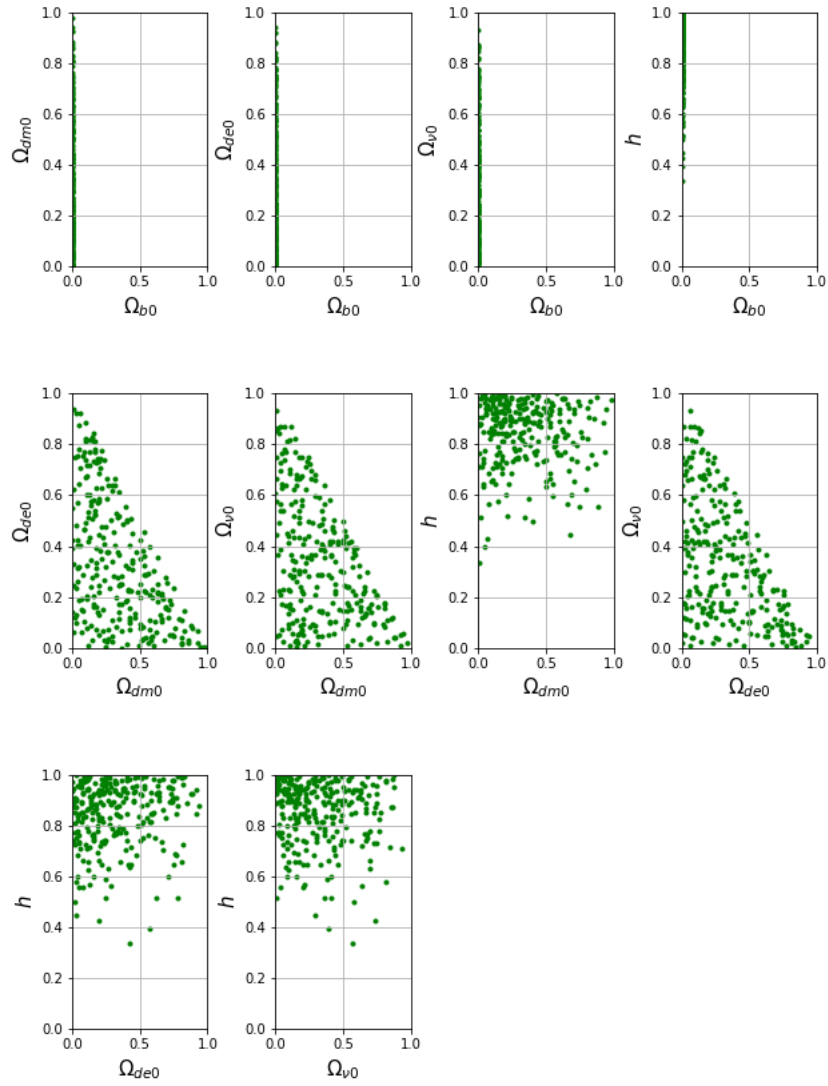


Figure 2.6: Accepted combinations of all cosmological parameters for simulation Sim.043 (with relativistic neutrinos density parameter simulated).

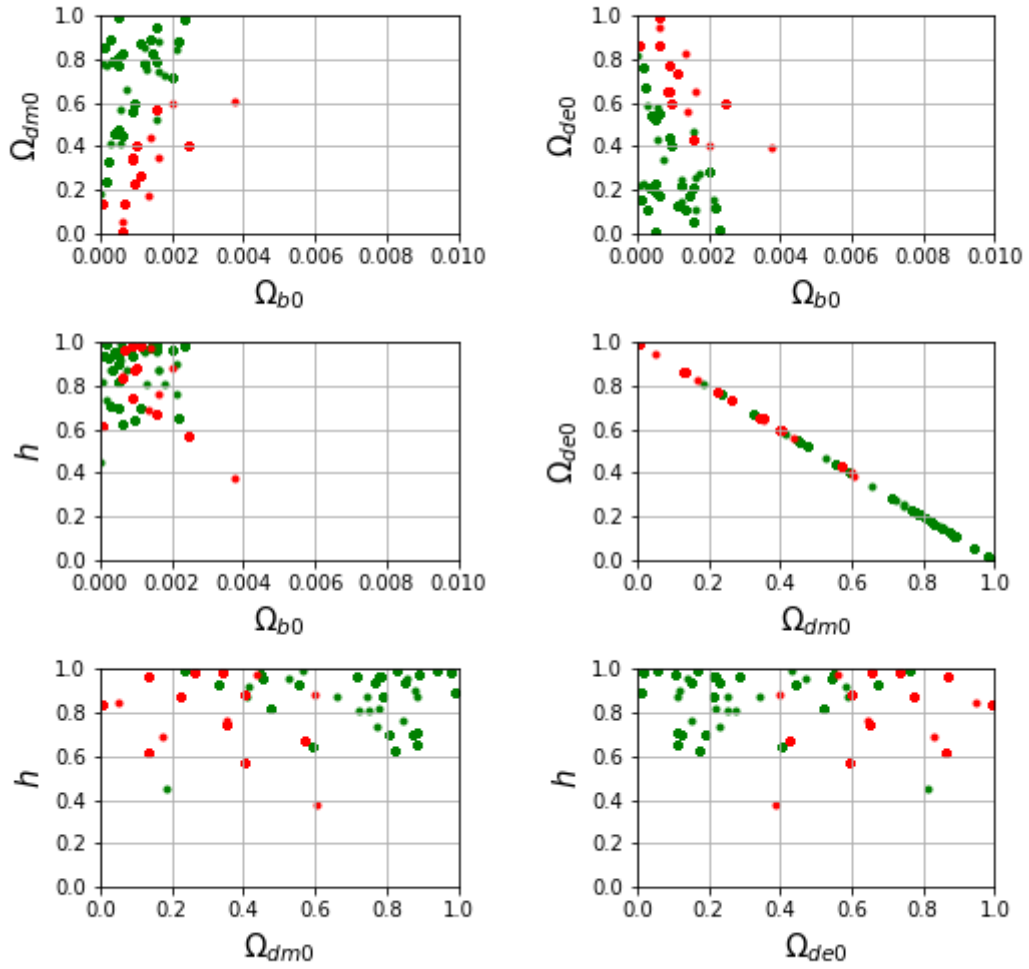


Figure 2.7: Accepted vs refused case 1 combinations of all cosmological parameters for simulation Sim.013.

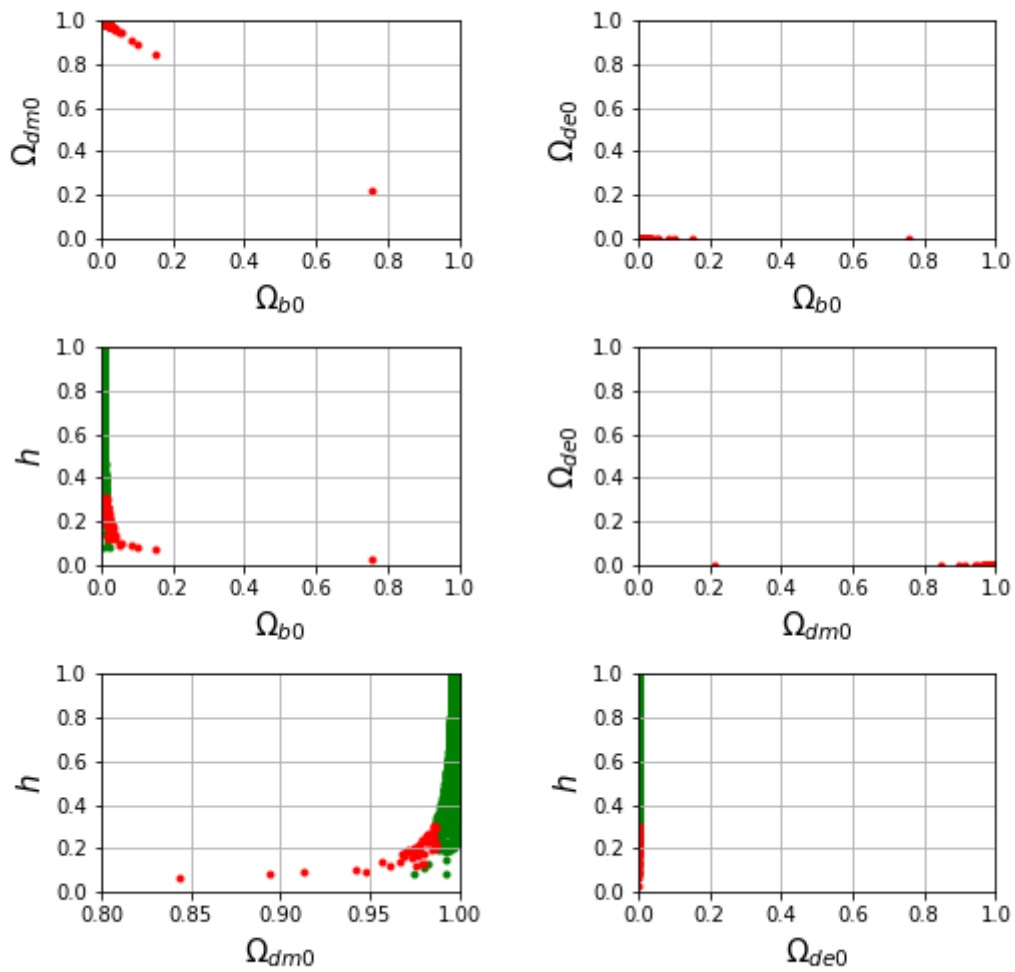


Figure 2.8: Accepted vs refused case 1 combinations of all cosmological parameters for simulation Sim.035.

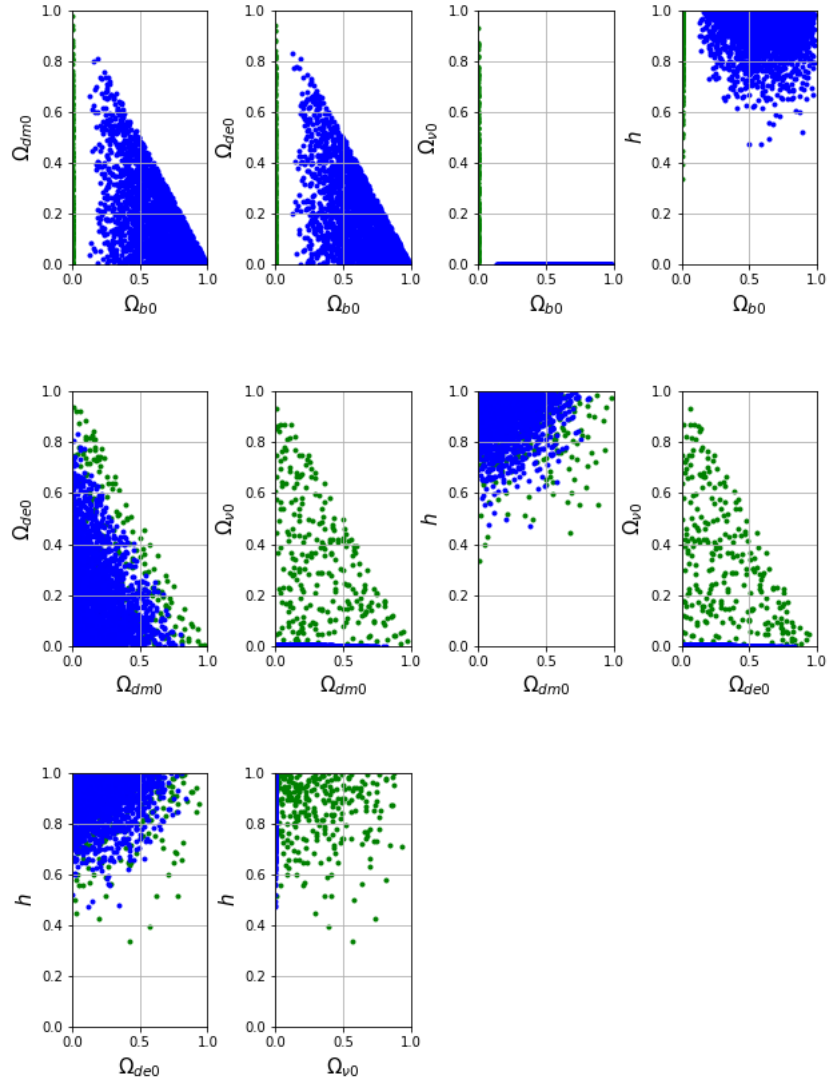


Figure 2.9: Accepted vs refused case 0 combinations of all cosmological parameters for simulation Sim.043 (with relativistic neutrinos density parameter simulated).

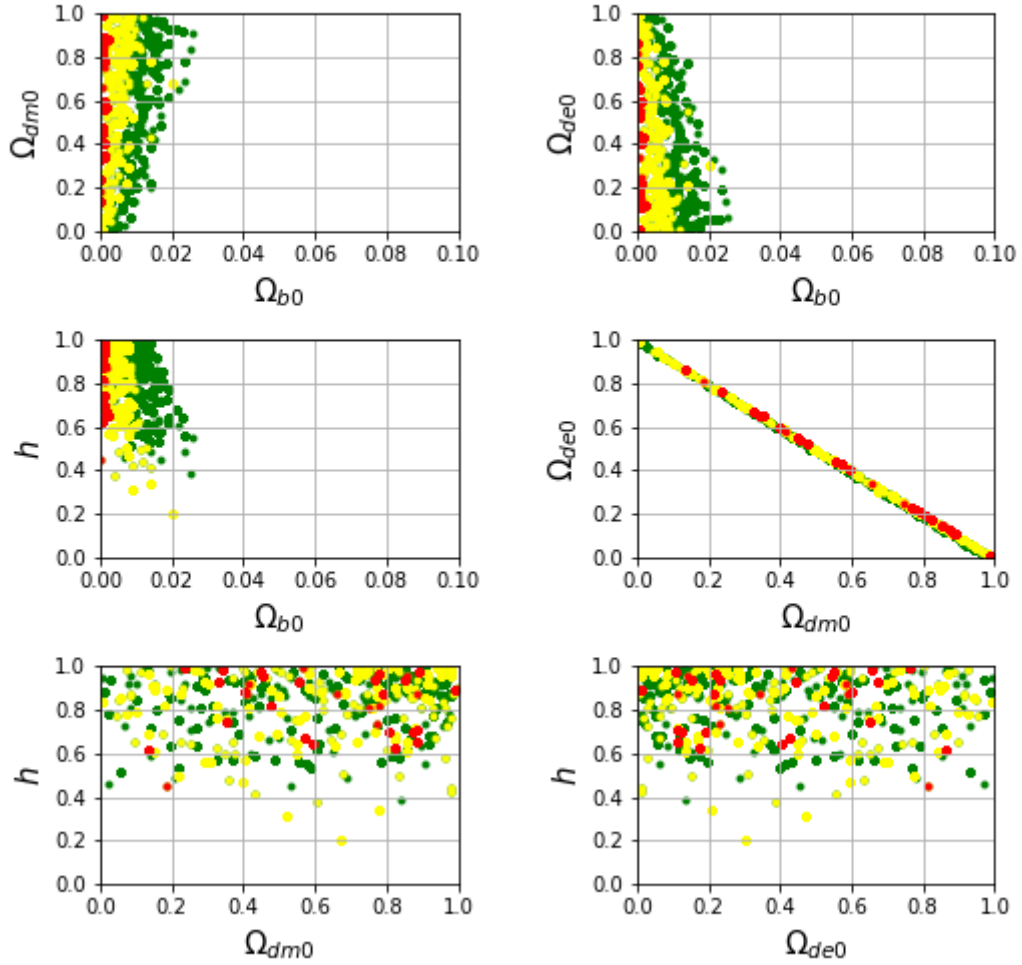


Figure 2.10: Accepted combinations of all cosmological parameters for simulations with different iteration number : green points represent data from simulation Sim.019 with  $N_{Iterations} = 10^5$ , yellow points are for data from simulation Sim.047 with  $N_{Iterations} = 5 \times 10^4$  and red points represents data from simulation Sim.001 with  $N_{Iterations} = 10^4$ .

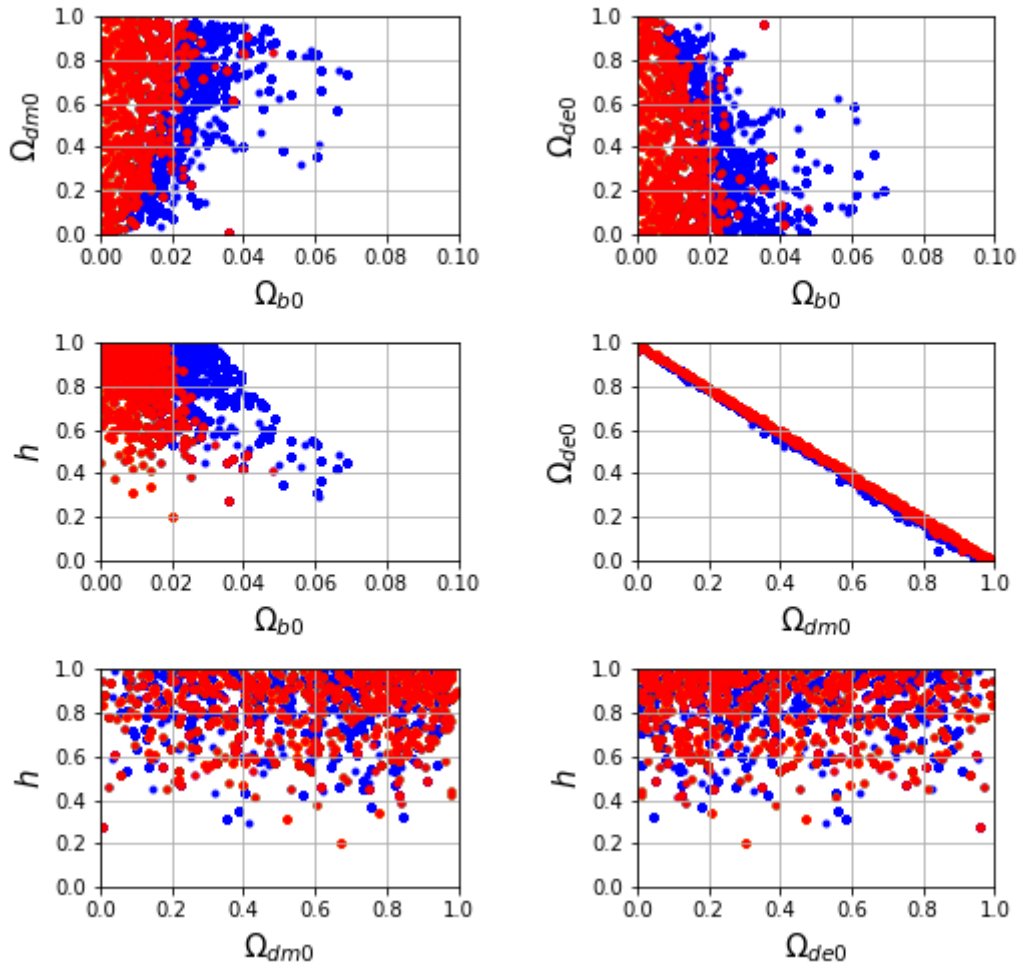


Figure 2.11: Accepted combinations of all cosmological parameters for simulations with different CMB temperature at the end of recombination : blue points represent data from simulation Sim.002 with  $T_{End}^{CMB} = 0.005 eV$  and red points represents data from simulation Sim.004 with  $T_{End}^{CMB} = 0.0006 eV$ .

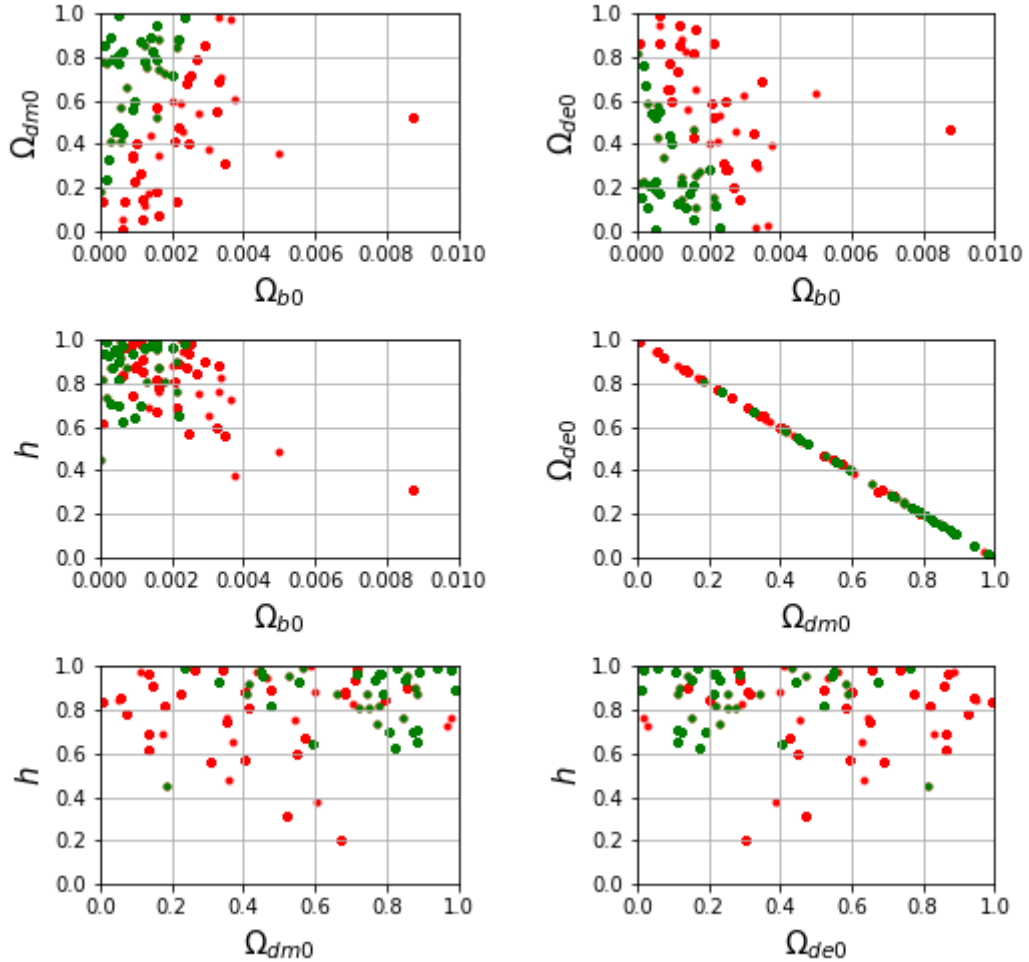


Figure 2.12: Accepted combinations of all cosmological parameters for simulations with different CMB temperature at the start of recombination : red points represent data from simulation Sim.046 with  $T_{Start}^{CMB} = 0.04 eV$  and green points represents data from simulation Sim.013 with  $T_{Start}^{CMB} = 0.05 eV$ .

contribution of these neutrinos would be then considered as part of the total dark matter density parameter. The difference in the dark matter contribution in two cases is considered as an allowed massive neutrino contribution. This difference could be used to infer the total mass of neutrinos species using (see Ref. [257])

$$\Omega_{\nu 0} h^2 = \frac{\sum_i m_i}{93 eV}. \quad (2.13)$$

Such SCOPE simulations are performed for different CMB temperatures at the start and end of recombination, and have resulted in the following results for cosmological parameters :

1. Dark matter cosmological parameter mean was greater for the massive neutrino case. This predicted compartment reflects that the neutrino contribution in the case of vanishing relativistic contribution is added in the dark matter compartment raising its contribution.
2. The unpredicted behaviour is that the allowed massive neutrino contribution is greater for large recombination eras corresponding to earlier recombination start.
3. The neutrino masses computed (using Eq. 2.13) challenges the lower limits  $0.05 eV$  from neutrino experiments and upper limits  $0.6 eV$  from the structure formation and their relation to recombination era (see Ref. [257]).

Neutrino mass newly discovered influences the scale factor of equivalence between matter and radiation. The estimated mass falls between expected bounds. From our results, this estimated mass could be used to infer or bound recombination era start and end additionally to equivalence era. Further simulations and development of our code should be done to explore this possibility. Those results were presented by Abdelali and Mebarki (2013) (see Ref. [258]).

## 2.5 Chapter conclusions

Some developments could be made to SCOPE code in order to obtain more reliable results. First and within the actual code, the accepted ranges of the free electron fraction can be made more restrained to smaller fractions at the end of iteration corresponding to the beginning of the re-ionization era. Also, the choice of two edges of the iteration : CMB temperature at the start and the end of recombination must be related to physical processes before and after the recombination era corresponding to more complex evolution of the Universe. We can add them to the list of parameters generated randomly to evaluate more the relation between them and other cosmological parameters. Second, Boltzmann evolution equations used are founded on both the FLRW spacetime for the evolution of flat Universe and standard Quantum Electro-Dynamics (QED) theory for the interaction of the recombination process. Then, the implementation of non standard theories can result in different evolution patterns and different constrains on the cosmological parameters. Another development of the code is possible from the Boltzmann Einstein equations (see Ref. [259]). The goal is to constrain the optical depth and then the estimation of cosmological parameters from CMB anisotropies through these equations. Also, we consider in this analysis only recombination of Hydrogen atoms. But, we should consider also high levels as heavy Hydrogen atoms (D, T) and all levels of Helium atoms as they contribute to free electron densities. Finally, SCOPE could be made as part of more complicated code for CMB estimations of cosmological parameters. This

allows the verification of cosmological parameters combinations before the search for best fitting when analysing observational data.

Our developed code SCOPE had allowed us to study the evolution of free electron densities around recombination. SCOPE gives a theoretical estimation with little and defined inputs. The code results are independent of the measure errors and secondary contaminations which affect the CMB estimations of cosmological parameters. SCOPE is used to determine the physically accepted combinations of cosmological parameters. The most important results are that we could not identify a whole region of cosmological parameters (for example  $\Omega_{m0}$ ,  $\Omega_{\Lambda0}$ ) plan as possibly containing the real Universe combinations. It may contain combinations that are refused when studied by our code as they don't verify the physical conditions on free electron densities evolution. We could use these bounds for future studies of cosmological parameters estimations. We found tight relation with CMB temperature in the start and end of recombination era with accepted ranges of cosmological parameters. We use this code to study neutrinos contribution to the Universe energy densities both as relativistic and as massive. More mass for neutrinos are allowed to exist from our study results. The approach of this chapter allowed us to get bounds (i.e. forbidden combinations) on cosmological parameters but didn't give us estimations on their real values as it didn't compare with cosmological data. A more developed method should be used if we want to estimate cosmological parameters and study impacts of different bias effects on their estimations.

# Chapter 3

## Curvature conservation of primordial magnetic fields

Cosmic magnetic fields are key components of the Universe and affecting various scales from star formation to structure formation. There is more and more observational evidence of its existence in all observable scales. But, their generation and structure are still unsolved questions. In some scenarios, magnetic fields are generated in early eras of cosmic history before creation of CMB. These primordial magnetic fields (PMF) are believed to be random, weak and driven by charged particles currents. Thus, they may lose strength or even vanish during recombination when the Universe became mostly neutral.

We consider in this chapter the impacts of spacetime curvature in PMF evolution. This curvature could preserve those primordial fields through and after recombination. It could also form a structure to these fields. The latter could leave observable impacts in CMB photons polarisations via Faraday rotations or other effects depending on magnetic fields. We solve Maxwell's equations in curved expanding spacetime to find analytical models representing the conserved primordial magnetic fields.

### 3.1 P.M.F. evolution through recombination

After a magnetic field is generated in pre-recombination era, the total energy density originating from the magnetic field is conserved in the adiabatic Universe and affects the cosmic expansion (see Ref. [260]). The evolution of the primordial magnetic field is a complex process affected by MHD turbulence responsible for the generation of the fluid perturbations. To account for the expansion, all physical quantities are rescaled in terms of their co-moving values which include effects of the expansion to the MHD equations retaining their conventional flat spacetime form with the conformal invariance. The strength of the frozen-in primordial large-scale magnetic field is proportional to an inverse square of the scale factor. The evolution process of the magnetic energy density, the correlation length and magnetic helicity strongly depends on initial physical conditions of the primordial plasma. These processes result in the equipartition between magnetic and kinetic energy densities. The initial values of correlation length and magnetic field strength at the temperature of magnetogenesis, with the two scaling indices, fully determine the large-scale magnetic field decay and the final configuration of the magnetic field. The decay of cosmological MHD turbulence occurs with the cooling of the Universe and the increase of magnetic correlation length up to a temperature of  $1\text{ eV}$  of the Universe (e.g. Ref. [261]).

The usual assumption is that the magnetic fields are affected during cosmic recombination by a sharp drop in ionization. The study of the behaviour of the magnetic field and

fluid motion around the recombination is a good test of this assumption (see Ref. [262]). Combining Maxwell equations to the fluid equations of electron, proton and neutral hydrogen includes the effect of recombination. The study of the relative velocity between protons and electrons estimates the residual ionization rate. The presence of magnetic fields leads to difference of motions between the charged particles and neutral hydrogen that do not feel the Lorentz force. The neutral hydrogen acts as an effective electric resistivity giving diffusion of magnetic fields in a non-linear effect. Then, recombination increases the effective electric resistivity. The ionization rate after recombination would be small enough for magneto-hydrodynamic to be a valid approximation due to residual charged particles and for a conservation of co-moving magnetic fields. The evolution of magnetic fields at cosmological scales is not affected by recombination with a required residual ionization much smaller than the standard value. The conservation of magnetic fields by mean of the conservation of electric current gives an acceleration of the relative velocity (e.g. Ref. [120]). An acceleration of protons and electrons in the process of recombination is shown and preserve the electric current and then the magnetic field. The acceleration of the relative velocity is proportional to the recombination rate and inversely proportional to the baryon density. The charged particles are accelerated to compensate for the decrease in their number densities and maintain the electric current. The magnetic field survive through cosmic recombination is an assumption that seems valid.

The evolution of primordial magnetic fields in post-recombination is expressed in form of Maxwell's equations. Several analyses had considered the interaction of the electromagnetic radiation with the curvature of spacetime (see Ref. [264]). The electromagnetic fields when interacting with the curvature of spacetime can be considered as small perturbations and scatter, forming tails manifested as a partial backscattering of a localized source of curvature (see Ref. [263]). To investigate these fields, their components are considered as measured by a standard observer. Different methods exist to consider the Maxwell's equations in curved spacetime : spherical components (e.g. Ref. [265]), higher order Green's function (e.g. Ref. [266]) or Skrotskii method (e.g. Ref. [267]). Maxwell's equations in curved spacetime can be written in a non-covariant form formally equivalent to Maxwell's equations in flat Cartesian spacetime. In this case, a macroscopic medium with electric and magnetic properties related to the background curvature is deduced (see Ref. [268]).

## 3.2 New evolution equations

Maxwell's equations are differential equations expressed initially in Minkowski spacetime. These equations take into account the electric  $\vec{E}$  and magnetic  $\vec{B}$  components forming the electromagnetic tensor  $F^{\mu\nu}$ . They give the generation and propagation of electromagnetic fields from an electric current  $J^\mu$ . In order to preserve the covariance of all physical equations, the partial derivations ( $\partial_\mu$ ) of the flat spacetime equations are replaced by covariant derivatives ( $D_\mu$ ). Electrodynamics equations in a curved spacetime take then the following form

$$D_\mu F^{\mu\nu} = J^\nu \quad (3.1)$$

and

$$D_\alpha F_{\mu\nu} + D_\nu F_{\alpha\mu} + D_\mu F_{\nu\alpha} = 0 \quad (3.2)$$

The covariant derivatives of a tensor ( $F^{\mu\nu}$ ) are defined to take the form given by

$$D_\alpha F^{\mu\nu} = \partial_\alpha F^{\mu\nu} + \Gamma_{\alpha\beta}^\mu F^{\beta\nu} + \Gamma_{\alpha\beta}^\nu F^{\mu\beta}, \quad (3.3)$$

where  $\Gamma_{\alpha\beta}^\mu$  are the Christoffel symbols and are calculated from the spacetime metric  $g_{\mu\nu}$ .

In our study, we consider a new scenario of cosmic magnetic fields in the curved expanding FLRW spacetime. This approach concentrates on the field evolution regardless of magnetogenesis processes and is considering vanishing electric currents ( $J^\mu = 0$ ). We also neglect the electric fields ( $\vec{E} = \vec{0}$ ). In our interpretation of Maxwell's equations in curved spacetime, the curvature preserves magnetic fields after the end of magnetogenesis processes and affects the evolution of these fields. Terms of the form ( $\Gamma_{\alpha\beta}^\mu F^{\beta\nu}$ ) act like pseudo-currents. In order to investigate this case, the electromagnetic tensor is defined with new form using coordinate transformations. We start from its definition in Minkowski spacetime

$$F_{\mu\nu}^{spherical} = \frac{\partial x^\alpha}{\partial x'^\mu} \frac{\partial x^\beta}{\partial x'^\nu} F_{\alpha\beta}^{Cartesian}, \quad (3.4)$$

where  $x^\alpha$  represent cartesian coordinates and  $x'^\mu$  represent spherical coordinates. Initially, the electromagnetic tensor  $F_{\mu\nu}$  of flat spacetime is given in spherical coordinates by

$$F_{\mu\nu}^{spherical} = \begin{pmatrix} 0 & E_1 & RE_2 & R \sin \theta E_3 \\ -E_1 & 0 & -RB_3 & R \sin \theta B_2 \\ -RE_2 & RB_3 & 0 & -R^2 \sin \theta B_1 \\ -R \sin \theta E_3 & -R \sin \theta B_2 & R^2 \sin \theta B_1 & 0 \end{pmatrix}, \quad (3.5)$$

where ( $E_i, B_j$  with  $i, j = 1, 2, 3$ ) are the electric and magnetic components in the spherical coordinates. The flat FLRW Universe could be seen as a flat spacetime expressed in spherical coordinates with a time dependent  $R$  coordinate. Then, the scale factor  $a(t)$  is introduced to provide the expansion in the spacetime

$$F_{\mu\nu} = \begin{pmatrix} 0 & 0 & 0 & 0 \\ 0 & 0 & -a(t)rB_3 & a(t)r \sin \theta B_2 \\ 0 & a(t)rB_3 & 0 & -a^2(t)r^2 \sin \theta B_1 \\ 0 & -a(t)r \sin \theta B_2 & a^2(t)r^2 \sin \theta B_1 & 0 \end{pmatrix} \quad (3.6)$$

where  $r$  is the dimensionless comoving coordinate given by relation ( $R = a(t)r$ ) and we neglect electric fields. This approach to define the electromagnetic tensor is different from previous studies. In those studies, they considered the electric and magnetic components of these fields as measured by a standard observer. But the evolution of both methods is given by Maxwell's equations. The physical and measurable strength of electromagnetic fields are defined as the scalar ( $F_{\alpha\beta}F^{\alpha\beta}$ ) given by

$$F_{\alpha\beta}F^{\alpha\beta} = \vec{E}^2/c^2 + \vec{B}^2. \quad (3.7)$$

And this definition is not affected by initial definition of the electromagnetic tensor. The new proposed definition of the electromagnetic tensor make the resolution of Maxwell's equations easier, illustrating the role of curvature as a pseudo-current in the preservation of magnetic fields.

### 3.3 Analytical solutions

When replacing the electromagnetic tensor defined in Eq. 3.6 in Maxwell's equations, the non vanishing equations are given as follows

$$\frac{\partial}{\partial t}(a^2(t)B_1(t, r, \theta, \phi)) = 0, \quad (3.8)$$

$$\frac{\partial}{\partial t}(a(t)B_2(t, r, \theta, \phi)) = 0, \quad (3.9)$$

$$\frac{\partial}{\partial t}(a(t)B_3(t, r, \theta, \phi)) = 0, \quad (3.10)$$

$$\frac{\partial}{\partial \phi}(B_3) + \frac{a(t) \sin \theta}{r} \frac{\partial}{\partial r}(r^2 B_1) + \frac{\partial}{\partial \theta}(\sin \theta B_2) = 0, \quad (3.11)$$

$$\frac{\partial}{\partial \theta}(\sin \theta B_3) - \frac{\partial}{\partial \phi}(B_2) = 0, \quad (3.12)$$

$$\sin \theta \left( B_3 + r \frac{\partial}{\partial r}(B_3) \right) - \frac{\partial}{\partial \phi}(a(t)B_1) = 0 \quad (3.13)$$

and

$$\left( B_2 + r \frac{\partial}{\partial r}(B_2) \right) - \frac{\partial}{\partial \theta}(a(t)B_1) = 0 \quad (3.14)$$

where  $(B_i, i = 1, 2, 3)$  are functions of the coordinates  $(B_i = B_i(t, r, \theta, \phi))$ . In the first step, a straightforward solution of the first three Eqs. (3.8 - 3.10) is given by

$$B_1(t, r, \theta, \phi) = a^{-2}(t)B_{11}(r, \theta, \phi), \quad (3.15)$$

$$B_2(t, r, \theta, \phi) = a^{-1}(t)B_{22}(r, \theta, \phi) \quad (3.16)$$

and

$$B_3(t, r, \theta, \phi) = a^{-1}(t)B_{33}(r, \theta, \phi). \quad (3.17)$$

These solutions express the temporal evolution of these cosmic magnetic fields.

Functions  $(B_{ii}, i = 1, 2, 3)$  represent the spatial  $(r, \theta, \phi)$  dependence of magnetic field components. Eqs. (3.11 - 3.14) are given after the first step to be

$$\frac{\partial}{\partial \phi}(B_{33}) + \frac{\sin \theta}{r} \frac{\partial}{\partial r}(r^2 B_{11}) + \frac{\partial}{\partial \theta}(\sin \theta B_{22}) = 0, \quad (3.18)$$

$$\frac{\partial}{\partial \phi}(B_{22}) = \frac{\partial}{\partial \theta}(\sin \theta B_{33}), \quad (3.19)$$

$$\frac{\partial}{\partial \phi}(B_{11}) = \sin \theta \left( B_{33} + r \frac{\partial}{\partial r}(B_{33}) \right) \quad (3.20)$$

and

$$\frac{\partial}{\partial \theta}(B_{11}) = \left( B_{22} + r \frac{\partial}{\partial r}(B_{22}) \right). \quad (3.21)$$

These equations are not all independent. For instance, if we differentiate Eq. 3.21 partially to  $\phi$  and then we replace  $\frac{\partial}{\partial \phi}(B_{22})$  from Eq. 3.19, it is the same result with the differentiate of Eq. 3.20 partially to  $\theta$ . Then, we continue only with Eqs. (3.18 - 3.20). We differentiate first Eq. 3.18 to  $\phi$ , then replacing  $\frac{\partial}{\partial \phi}(B_{11})$  and  $\frac{\partial}{\partial \phi}(B_{22})$ , which results in

$$\frac{\partial^2}{\partial \phi^2}(B_{33}) + \frac{\sin^2 \theta}{r} \frac{\partial}{\partial r}(r^2 B_{33} + r^3 \frac{\partial}{\partial r}(B_{33})) + \frac{\partial}{\partial \theta}(\sin \theta \frac{\partial}{\partial \theta}(\sin \theta B_{33})) = 0. \quad (3.22)$$

This last equation is a second order differential equation of  $B_{33}(r, \theta, \phi)$ . It could be solved by a technique of separation of variables. In this method, a function of several coordinates is decomposed to the product of a number of functions

$$B_{33}(r, \theta, \phi) = f_1(r)f_2(\theta)f_3(\phi), \quad (3.23)$$

CHAPTER 3. CURVATURE CONSERVATION OF PRIMORDIAL MAGNETIC  
FIELDS

with only one coordinate by adding constants in each separation. Quantum mechanics equations are mainly solved by this method. After replacing this expression, the equation to solve is given now by

$$\begin{aligned} & f_1(r)f_2(\theta)\frac{\partial^2}{\partial\phi^2}(f_3(\phi)) \\ & + f_2(\theta)f_3(\phi)\frac{\sin^2\theta}{r}\frac{\partial}{\partial r}(r^2f_1(r) + r^3\frac{\partial}{\partial r}(f_1(r))) \\ & + f_1(r)f_3(\phi)\frac{\partial}{\partial\theta}(\sin\theta\frac{\partial}{\partial\theta}(\sin\theta f_2(\theta))) = 0. \end{aligned} \quad (3.24)$$

Then, the separation of variables split this equation

$$\begin{aligned} & \frac{1}{f_3(\phi)}\frac{\partial^2}{\partial\phi^2}(f_3(\phi)) + \frac{1}{f_1(r)}\frac{\sin^2\theta}{r}\frac{\partial}{\partial r}(r^2f_1(r) + r^3\frac{\partial}{\partial r}(f_1(r))) \\ & + \frac{1}{f_2(\theta)}\frac{\partial}{\partial\theta}(\sin\theta\frac{\partial}{\partial\theta}(\sin\theta f_2(\theta))) = 0, \end{aligned} \quad (3.25)$$

to be

$$\frac{1}{f_3(\phi)}\frac{\partial^2}{\partial\phi^2}(f_3(\phi)) = -C^2, \quad (3.26)$$

$$\frac{1}{f_1(r)}\frac{\sin^2\theta}{r}\frac{\partial}{\partial r}(r^2f_1(r) + r^3\frac{\partial}{\partial r}(f_1(r))) = 0 \quad (3.27)$$

and

$$\frac{1}{f_2(\theta)}\frac{\partial}{\partial\theta}(\sin\theta\frac{\partial}{\partial\theta}(\sin\theta f_2(\theta))) = +C^2, \quad (3.28)$$

where  $C$  is a constant of separation. Then, the new three equations to solve are given then by

$$\frac{\partial^2}{\partial\phi^2}(f_3(\phi)) + C^2f_3(\phi) = 0, \quad (3.29)$$

$$r^3\frac{\partial}{\partial r}(f_1(r)) + r^2f_1(r) - D = 0 \quad (3.30)$$

and

$$\frac{\partial}{\partial\theta}(\sin\theta\frac{\partial}{\partial\theta}(\sin\theta f_2(\theta))) - C^2f_2(\theta) = 0, \quad (3.31)$$

where  $D$  is also a constant. Manually and using symbolic solvers such as Maple and Mathematica, one could find the following solutions

$$f_1(r) = \frac{K_{11}}{r} - \frac{D}{r^2}, \quad (3.32)$$

$$f_2(\theta) = K_{21}\frac{e^{-\sqrt{C^2}\tanh^{-1}(\cos\theta)}}{\sqrt{\sin^2\theta}} + K_{22}\frac{e^{\sqrt{C^2}\tanh^{-1}(\cos\theta)}}{\sqrt{C^2}\sqrt{\sin^2\theta}} \quad (3.33)$$

and

$$f_3(\phi) = K_{31}\cos(C\phi + K_{32}), \quad (3.34)$$

where  $K_{ij}$  are integration constants determined from the initial conditions. Replacing these Eqs. (3.32 - 3.34) in Eq. 3.23 gives us the expression of  $B_{33}(r, \theta, \phi)$ . Finally, the expressions of  $B_{22}(r, \theta, \phi)$  and  $B_{11}(r, \theta, \phi)$  is then obtained by the integration of Eqs. 3.19 and 3.20. Then, we obtain a complete and analytical solution of cosmic magnetic fields

evolution in flat FLRW spacetime. The measurable strength of the magnetic fields, as defined in Eq. 3.7, in the expanding flat FLRW Universe has the form

$$B^2 = F_{\alpha\beta}F^{\alpha\beta} = B_1^2 + \frac{1}{a^2(t)}(B_2^2 + B_3^2). \quad (3.35)$$

From the solutions expressed in Eqs. (3.15 - 3.17 and 3.35), we give the evolution of the physical strength of these cosmic magnetic fields in the cosmic time as follows

$$B^2 = \frac{1}{a^4(t)}[B_{11}^2(r, \theta, \phi) + B_{22}^2(r, \theta, \phi) + B_{33}^2(r, \theta, \phi)]. \quad (3.36)$$

### 3.4 Discussions and impacts on CMB anisotropies

The initial assumption on a null electric current is consistent with the evolution of these fields at late period of recombination and just after it ends as the Universe was almost completely neutral. The temporal evolution of the cosmic magnetic fields depend inversely on the square of the scale factor ( $a(t)$ ). The spatial configuration of these fields does not change in the cosmic evolution. Then, the evolution of these cosmic magnetic fields requires the existence of non vanishing initial fields. Maxwell's equations in the flat spacetime impose that a temporal depending magnetic field ( $\frac{\partial}{\partial t}\vec{B} \neq \vec{0}$ ) have to be associated with a non vanishing electric field. The cosmic magnetic fields are temporal depending in despite of the vanishing electric field. This is possible from the characteristics of Maxwell's equations in the curved expanding spacetime. These solutions found supports the hypothesis that the curvature of the FLRW Universe affects and preserves the cosmic magnetic fields evolution.

To find the initial magnetic fields, we should get back to cosmic history. The cosmological magnetogenesis of primordial magnetic fields is usually assumed to be in the pre-recombination epoch. The high conductivity of the Universe in the ideal MHD limit impose a vanishing electric fields. The strength of the frozen-in primordial large-scale magnetic field is proportional to an inverse square of the scale factor provided by the conservation of the magnetic flux and energy density in an adiabatic expansion of the Universe. The evolution of the primordial magnetic field is a complex process affected by Magneto-Hydrodynamics MHD turbulence, responsible for the generation of the fluid perturbations, and by the expansion of the Universe. The magnetic fields survive through cosmic recombination by mean of the conservation of electric current gives an acceleration of the relative velocity of protons and electrons.

The cosmic magnetic fields introduced in this new approach seem to hold with these characteristics of the primordial magnetic fields. The primordial magnetic fields that survive the cosmic recombination can be the initial magnetic fields to feed these cosmic fields. The vanishing electric fields in the new scenario conditions preserve the high conductivity of the Universe. In our scenario, no magnetogenesis process is active after recombination era which is consistent with the common models of magnetogenesis. This magnetic flux conservation is not preserved in some analysis of the electromagnetic radiation propagation in curved spacetime. But in our scenario, the temporal evolution of the strength preserve the magnetic flux conservation as given in Eq. 3.36.

A characteristic of this new scenario is that the cosmic magnetic fields are preserved by the curvature of the expanding spacetime. This is supported by the temporal evolution of the physical strength of these fields unlike the conservation of magnetic fields through electric currents around recombination. An important other characteristic of this scenario is that the preserved cosmic magnetic fields from the primordial ones has as

spatial configuration unlike the stochastic nature assumed for the primordial fields. The curvature should then impose a smoothness on these fields power spectrum. These fields have signatures on CMB which are distinguished other effects in both the CMB temperature anisotropies and B-mode polarizations. The final CMB temperature anisotropies are model dependent through the temporal evolution of the scale factor, the time of recombination and the age of the Universe. This two properties could help to identify these preserved magnetic fields. But, the number of anisotropies sources and complexity of overlapping signals could be challenging. Moreover, the analytical solution presented could represent only partially the real state of the primordial magnetic fields. From the randomness of these fields, the preserved signal could be the sum of several configurations of our solution with each time a different set of  $K_{ij}$  (see Eqs. 3.32, 3.33 and 3.34). This could add more complexity to our analysis of CMB observations in our research to identify the preserved fields characteristics. Those results were first presented by Abdelali and Mebarki (2013) (see Ref. [269]).

### 3.5 Chapter conclusions

Our solutions to Maxwell's equations within curved spacetime have showed us that with initial seeds the curvature could conserve primordial magnetic fields through and specially after recombination. The conserved fields leave impacts on CMB temperature and polarisations. Those signatures could be overlapped with other effects impacts. The correlation between temperature and polarisation signatures could help us to identify those magnetic fields and estimate their strengths. The structure of those conserved magnetic fields can be smoothed by curvature and can be also complex.

The strength and structure could be only identified from the analysis of observational data such as CMB. Their impacts could also be so weak and lost with other effects signatures. For instance, more recent magnetic fields generated around galaxies and within clusters have also similar impacts on CMB photons in temperature and polarisation. Those recent magnetic fields are related to complex genesis and evolution processes and must be studied by numerical methods. The analytical approach could not provide significant insights to those complex evolutions of those processes. The signature from primordial magnetic fields conserved with curvature and the recently generated complicate further more the analysis of CMB anisotropies and the extraction of cosmological parameters.

# Chapter 4

## Magnetically induced redshift effect

Light from its far emitters in the Universe to observer encounter several processes like dispersion, scattering and absorption in the cosmic environment. These processes differ from a source to another and from a direction to another depending on local inhomogeneities. But, the most important effect is redshift representing a main interest in cosmological observations and interpretations. Possible effects causing this shift in light wavelength are variants. The most considered in astrophysical studies, let call them conventional, are : cosmological, Doppler Effect and gravitational redshifts. But, more effects could exist and produce similar effect on data.

This chapter starts by an overview of conventional and exotic redshift effects. Then, a new redshift effect is presented which is based on gravitational interaction between photons and background magnetic fields. The presentation is then followed by a discussion of its importance and possible measurable impacts in astrophysical and cosmological data.

### 4.1 Conventional redshifts

Along with cosmological redshift (presented in a previous chapter), Doppler effect is a redshift caused by relative motion between observer and light source. The relativistic Doppler effect is different from the non-relativistic Doppler effect as it includes the time dilation effect of special relativity. We give Doppler effect redshift ( $z_D$ ) with

$$(1 + z_D) = \frac{\nu_E}{\nu_O} = \sqrt{\frac{1 + \beta}{1 - \beta}}, \quad (4.1)$$

where  $\nu_E$  and  $\nu_O$  are light frequency in emitter and observer respectively.  $\beta$  is the longitudinal projection of velocity of emitter on the line-of-sight in the observer rest frame. Doppler effect can produce negative redshifts, i.e. blueshifts, if the emitter has negative values of  $\beta$ . This is the case when the longitudinal projection of velocity of the emitter is directed toward the observer.

Gravitational redshift is created when light travels between two points of different gravitational potential. In this relativistic process, photons emitted from a source that is in a gravitational field ( $\phi_E$ ) are reduced in frequency, or redshifted, when observed in a region at a higher gravitational potential ( $\phi_O$ ) compared to emitter. The effect could be also a blueshift if we switch the situation and the photon is observed in a region of lower gravitational potential. For a weak gravitational potential, we get the line element defined as

$$ds^2 = \left(1 + \frac{2\phi}{c^2}\right) c^2 dt^2 - \left(1 - \frac{2\phi}{c^2}\right) d\sigma^2, \quad (4.2)$$

where

$$d\sigma^2 = dr^2 + r^2 d\theta^2 + r^2 \sin^2 \theta d\psi^2. \quad (4.3)$$

The ratio of the photon's frequency measured by emitter and observer is proportional to the ratio of metric element ( $g_{00}$ ) expressed as follows

$$(1 + z_G) = \frac{\nu_E}{\nu_O} = \sqrt{\frac{g_{00}(O)}{g_{00}(E)}} = \sqrt{\frac{(1 + \frac{2\phi_O}{c^2})}{(1 + \frac{2\phi_E}{c^2})}}. \quad (4.4)$$

After a Taylor expansion of this last expression, we get the simplified form of gravitational redshift  $z_G$  for weak gravitational potential to be

$$(1 + z_G) = \frac{\phi_O - \phi_E}{c^2}, \quad (4.5)$$

where we neglected higher order terms.

These are most common effects causing redshifts (or blueshifts) in the observed light of distant sources. The observed redshift  $z_{Obs}$  is a combination of all those effects : cosmological, Doppler and gravitational. The final redshift measured by an observer is then giving by

$$(1 + z_{Obs}) = (1 + z_C)(1 + z_D)(1 + z_G)(1 + z_{NC}), \quad (4.6)$$

where  $z_{NC}$  stands for any other kind of redshift effects (of non cosmological nature) which could affect the travelling photon.

Both Doppler and gravitational redshifts can cause noticeable differences between observed redshift and cosmological redshift of an extragalactic object. Those effects were thought to be negligible for objects in Hubble flow. But if not considered, those deviations create a biased results when taking the observed redshift as created only by cosmological expansion. A number of articles have investigated the cosmological parameters bias caused by gravitational redshifts (e.g. Refs. [3]; [4] and [270]). Inhomogeneities of the local Universe is creating differences in the cosmic gravitational potential in observer and emitter which leave its impacts as redshift or blueshift on light travelling between these two points. Taking redshifts measured as caused purely from cosmological expansion without eliminating the gravitational redshift contribution obviously impact the results of cosmological parameters fits. The introduction of any new redshift effect adds to the possible bias and deviations that could be predicted.

In the study of Wojtak, Davis and Wiis (2015) (see Ref. [271] hereafter WDW15), they use numerical simulations data to reconstruct the gravitational potential across the local Universe and then estimated the resulting gravitational redshift affecting observations. They estimated  $2 \times 10^{-5}$  additional shift for observed galaxies' redshifts measured by an observer galaxy similar to ours. They applied such a shift to supernovae data by adding or subtracting a fixed value from all supernovae redshifts. And they estimated a shift from the flat model of the Universe indicated by their estimations of cosmological parameters using those altered supernovae data.

A recent work of Calcino and Davis (2017) (see Ref. [5]) had used new statistical methods to evaluate the redshift bias  $\Delta z$  by adding it as a nuisance parameter in cosmological parameters estimations analysis. This had allowed them to estimate the possible contribution of all effects' bias affecting supernovae data. The result was  $2.6 \times 10^{-4}$  which is higher than the estimation of WDW15 from gravitational redshifts. Their explanation was that possibly more contributions of gravitational redshifts or measurement errors were responsible of the difference of bias estimations. One could also say that this is possibly an indication or even evidence of new effect contribution that must not be blamed on measurement errors. More should be done to investigate possible new effects that may be responsible of this bias.

## 4.2 Exotic redshift effects

Some non conventional effects from several models could in theory cause light frequency shift, but they are not verified experimentally. Others are proved in laboratory but for rare conditions and then could be dismissed from cosmic conditions. Here are some examples of those exotic effects. In some theoretical formulation, every motion in homogeneous mass filled space is feeling a viscous-like force. The energy loss rate may be equal to photons redshift in an expanding Universe (e.g. Ref. [272]). Another possible redshift effect is an energy loss of photons by an excitation and relaxation of vacuum by  $e^-e^+$  pairs (e.g. Ref. [273]). If the external magnetic field is so strong, the vacuum polarization effect would be significant causing dispersions, reflection, refraction and splitting of X-rays. Redshifts could be also caused by particle interactions creating an overall index of refraction of the Universe with cumulative effects of these interactions over long distances (e.g. Ref. [274]). In other theoretical formulation, we could predict redshift from interactions with hypothetical gravitons background (e.g. Ref. [275]). Some, if not all, of those effects are aiming to support the steady Universe hypothesis (e.g. Ref. [276]; [277]; [278] and [279]).

Several redshift effects were predicted with coherent foundations and even proved in laboratory but for rare conditions. For example, effects from optical origins, anomalous spectral behaviour was proved by experiment for polychromatic light completely or partially coherent in simple double-slit (see Ref. [280]) and in modified Mach-Zehnder interferometers (see Ref. [281]). Observations showed redshifts in positions and blueshifts in other positions of the interference field. In astrophysical context, not all existing phenomena give significant contribution. For example, magnetic fields have some theoretical effects causing redshifts related to moments and polarizations. A photon can create an electron-positron pair and their energy is altered by magnetic fields (e.g. Refs. [282] and [283]). The interaction of light with this background makes the photon exhibits a tiny magnetic moment which is also interpreted as a redshift in the same form of gravitational effect. This effect is important around strong magnetic fields sources like Magnetars (e.g. Refs. [284] and [285]). But, this type of effects is not verified experimentally. And, it is insignificant in cosmological context as the verified magnetic fields in observations are so weak.

Wolf effect has been described as a redshift mechanism. This effect occurs in several closely related phenomena in radiation physics, with analogous effects occurring in the scattering of light. It was first predicted by E. Wolf in 1987 (e.g. Ref. [286]) and subsequently confirmed in the laboratory by Bocko et al. (1987) (see Ref. [287]) and Faklis and Morris (1988) (see Ref. [288]). This effect is predicting correlation induced spectral changes. It can be used as an attempt to explain both the broadening and spectral lines shifts of astronomical objects, rather than using explanations like Doppler Effect and environmental conditions in line of sight. This explanation is applicable on discordant redshifts of galaxy - quasar associations. Under certain conditions, the shift may be distortion free. Even if it is built on simple models for AGN and quasi stellar objects (QSO or quasar), the theory of this effect is extensively tested as certain aspects of this phenomenon (e.g. Refs. [289] and [290]). The effect of coherence and especially in phase singularities had shown spectral shifts as redshifts and blueshifts and it is reported in several experimental observations (e.g. Refs. [291] and [292]). For two vacuum separated light sources interacting, the Wolf effect cannot produce shifts greater than the line width of the source spectral line. This comes from the fact that it is a position-dependent change in the distribution of the source spectrum, not an effect where new frequencies may be generated. However, when interacting with a medium, in combination with effects such as Brillouin scattering it may produce distorted shifts greater than the line width

of the source. Under suitably controlled scenarios, it may even be possible to roughly mimic Doppler redshifts. These scenarios are not for sure replicated in cosmological environments.

### 4.3 New magnetically induced redshift : mathematical formalism

The mechanism of our redshift effect starts with photons travelling through external (or background) magnetic fields. The gravitational interaction of electromagnetic waves with these external static magnetic fields is studied using Einstein general relativity equations (see equation 8.14 in Ref. [293])

$$R_{\mu\nu} - \frac{1}{2}g_{\mu\nu}R = -\kappa T_{\mu\nu}, \quad (4.7)$$

where  $\kappa = \frac{8\pi G}{c^4}$  with  $G$  is the gravitational constant and  $c$  the speed of light.  $R$  is the curvature scalar computed from Ricci tensor which is  $R_{\alpha\beta} = R^{\gamma}_{\alpha\beta\gamma}$  and  $R^{\rho}_{\alpha\beta\gamma}$  is Riemann tensor. The left hand side represents the Einstein tensor computed from the space-time metric  $g_{\mu\nu}$ . The right hand side represents the energy momentum tensor of the studied source of space-time curvature. The energy of electromagnetic fields is weak, but still curves space-time. Then, the linear approximation of Einstein equations is used, starting from a metric having a weak perturbation  $h_{\mu\nu}$  to Minkowski metric  $\eta_{\mu\nu}$  which takes then the following form

$$g_{\mu\nu} = \eta_{\mu\nu} + h_{\mu\nu}. \quad (4.8)$$

In the first order of the approximation, Einstein equations are expressed in term of this weak metric perturbation as

$$\partial_{\alpha}\partial^{\alpha}\bar{h}_{\mu\nu} + \eta_{\mu\nu}\partial_{\alpha}\partial_{\beta}\bar{h}^{\alpha\beta} - \partial_{\nu}\partial_{\alpha}\bar{h}_{\mu}^{\alpha} - \partial_{\mu}\partial_{\alpha}\bar{h}_{\nu}^{\alpha} = -2\kappa T_{\mu\nu}, \quad (4.9)$$

where

$$\bar{h}_{\mu\nu} = h_{\mu\nu} - \frac{1}{2}\eta_{\mu\nu}h^{\alpha}_{\alpha}. \quad (4.10)$$

We choose to consider solutions verifying the transverse-traceless gauge which simplifies Einstein equations even further to

$$\partial_{\alpha}\partial^{\alpha}\bar{h}_{\mu\nu} = -2\kappa T_{\mu\nu}, \quad (4.11)$$

where  $\partial_{\beta}\bar{h}^{\alpha\beta} = 0$ ,  $h^{\alpha}_{\alpha} = 0$  and  $\bar{h}_{\mu\nu} = h_{\mu\nu}$ . These differential equations are wave equations with source function which have a general solution and special solution. The general solution is just the usual gravitational waves with their two polarisations. We are interested in the special solution related to our studied source which is the electromagnetic fields in our case. After the special solution of these equations is found, we check if these gravitational waves described by this metric perturbation are physical radiations carrying energy. The second order Einstein tensor represents the energy momentum tensor of emitted gravitational waves (see Ref. [293]) which could be written as

$$t_{\mu\nu}(h_{\rho\sigma}) = \frac{1}{\kappa}\langle (R_{\mu\nu} - \frac{1}{2}g_{\mu\nu}R)^{(2)} \rangle, \quad (4.12)$$

where  $\langle \dots \rangle$  denotes an average over a small region at each point in space-time and  $^{(2)}$  denotes the second order in the perturbation expansion. In the transverse-traceless gauge, this energy-momentum tensor in vacuo is reduced to

$$t_{\mu\nu}(h_{\rho\sigma}) = \frac{1}{4\kappa}\langle (\partial_{\mu}h_{\rho\sigma})\partial_{\nu}h^{\rho\sigma} \rangle. \quad (4.13)$$

Thus, any physical gravitational radiation should have non vanishing energy momentum tensor  $t_{\mu\nu}$ .

The energy momentum tensor is given for electromagnetic fields expressed in function of the electromagnetic field tensor  $F_{\mu\nu}$  as

$$T_{\mu\nu}^{(EM)} = -\frac{1}{\mu_0} \left( F_{\mu\alpha} F_{\nu\beta} g^{\alpha\beta} - \frac{1}{4} g_{\mu\nu} F_{\alpha\beta} F^{\alpha\beta} \right), \quad (4.14)$$

where

$$F^{\mu\nu} = \begin{pmatrix} 0 & -E^1/c & -E^2/c & -E^3/c \\ E^1/c & 0 & -B^3 & B^2 \\ E^2/c & B^3 & 0 & -B^1 \\ E^3/c & -B^2 & B^1 & 0 \end{pmatrix}, \quad (4.15)$$

$\mu_0$  is the permeability of free space,  $B^i$   $i = 1..3$  are magnetic fields components and  $E^i$   $i = 1..3$  are electric fields components. The electromagnetic fields are composed of a plane monochromatic electromagnetic wave given by its electric field  $\vec{E}$  ( $E_0 \cos(k(t-z))$ , 0, 0) and magnetic field  $\vec{B}$  (0,  $\frac{E_0}{c} \cos(k(t-z))$ , 0). The electromagnetic wave is propagating along the z-axis. We study the propagation of this electromagnetic wave in 3 regions of space depending on the existing constant magnetic field  $\vec{B}_{ext}$  as follows: the first ( $z < 0$ ) and the last region ( $z > l$ ) have no external magnetic fields, only the second region ( $0 < z < l$ ) has constant magnetic field, where  $l$  represent the coherent length where the constant magnetic field exists. The magnetic fields are perpendicular to the direction of propagation along x-axis  $\vec{B}_{ext}$  ( $B_x$ , 0, 0). The electromagnetic tensor of these fields in this second region of space is given by

$$F^{\mu\nu} = \frac{E_0 \cos(k(t-z))}{c} \begin{pmatrix} 0 & -1 & 0 & 0 \\ 1 & 0 & 0 & 1 \\ 0 & 0 & 0 & 0 \\ 0 & -1 & 0 & 0 \end{pmatrix} + B_x \begin{pmatrix} 0 & 0 & 0 & 0 \\ 0 & 0 & 0 & 0 \\ 0 & 0 & 0 & -1 \\ 0 & 0 & 1 & 0 \end{pmatrix}. \quad (4.16)$$

For this second region, we can distinguish three parts of the electromagnetic energy momentum tensor: the first is static related only to constant magnetic fields, second part is related only to the electromagnetic wave and the third part is proportional to both magnetic fields and electromagnetic wave. This tensor has the following form

$$T_{\mu\nu}^{(EM)} = \frac{B_x^2}{2\mu_0} \begin{pmatrix} 1 & 0 & 0 & 0 \\ 0 & -1 & 0 & 0 \\ 0 & 0 & 1 & 0 \\ 0 & 0 & 0 & 1 \end{pmatrix} + \frac{E_0^2 \cos^2(k(t-z))}{\mu_0 c^2} \begin{pmatrix} 1 & 0 & 0 & -1 \\ 0 & 0 & 0 & 0 \\ 0 & 0 & 0 & 0 \\ -1 & 0 & 0 & 1 \end{pmatrix} + \frac{B_x E_0 \cos(k(t-z))}{\mu_0 c} \begin{pmatrix} 0 & 0 & 0 & 0 \\ 0 & 0 & -1 & 0 \\ 0 & -1 & 0 & 0 \\ 0 & 0 & 0 & 0 \end{pmatrix}. \quad (4.17)$$

In the first and third regions, only the terms related to electromagnetic wave is not vanishing. After replacing this tensor in Eq. 4.11, we solve the gravitational equations to find the perturbation metric. We have rewritten the perturbation metric to three parts according to the three parts of  $T_{\mu\nu}^{(EM)}$  as follows

$$\begin{aligned}
 \bar{h}_{\mu\nu} &= \bar{h}_{\mu\nu}^{(I)} + \bar{h}_{\mu\nu}^{(II)} + \bar{h}_{\mu\nu}^{(III)} \\
 &= f^{(I)}(t, z) \begin{pmatrix} 1 & 0 & 0 & 0 \\ 0 & -1 & 0 & 0 \\ 0 & 0 & 1 & 0 \\ 0 & 0 & 0 & 1 \end{pmatrix} \\
 &+ f^{(II)}(t, z) \begin{pmatrix} 1 & 0 & 0 & -1 \\ 0 & 0 & 0 & 0 \\ 0 & 0 & 0 & 0 \\ -1 & 0 & 0 & 1 \end{pmatrix} \\
 &+ f^{(III)}(t, z) \begin{pmatrix} 0 & 0 & 0 & 0 \\ 0 & 0 & -1 & 0 \\ 0 & -1 & 0 & 0 \\ 0 & 0 & 0 & 0 \end{pmatrix}.
 \end{aligned} \tag{4.18}$$

This reduces our equations to three simple wave equations with source terms. The general solution to these equations represents the ordinary gravitational waves propagating in vacuum. We are interested to the special solutions related to our electromagnetic fields. After a straightforward operation (see Appendix A for detailed solutions), we find that the two first parts produces non physical gravitational radiations with vanishing energy momentum tensor and violate the traceless transverse gauge. These two parts are related to pure magnetic field and pure electromagnetic wave contributions. This is the same situation in first and last region where only pure electromagnetic wave contributions exists. We find that the physical radiations ( $h_{\mu\nu}^{(III)}$ ) given by

$$h_{\mu\nu}^{(III)} = \frac{-2\kappa E_0 B_x}{\mu_0 c} \frac{z}{2k} \sin(k(t-z)) \begin{pmatrix} 0 & 0 & 0 & 0 \\ 0 & 0 & -1 & 0 \\ 0 & -1 & 0 & 0 \\ 0 & 0 & 0 & 0 \end{pmatrix}, \tag{4.19}$$

has a non vanishing energy momentum tensor and doesn't violate the traceless transverse gauge. It is related to cross terms between constant magnetic fields and the propagating electromagnetic wave. The gravitational radiation created by this term has one of the two known polarizations of gravitational waves. This solution verify the continuity conditions at the boundaries. First between region 1 and 2 at  $z = 0$ ,  $h_{\mu\nu}^{(III)}$  vanishes indicating that these gravitational waves are generated only from the interaction of incident electromagnetic waves with the magnetic fields background. This process doesn't require an initial or incident gravitational waves to occur which are not hypothesized in our scenario in the first place. Between region 2 and 3 at  $z = l$ ,  $h_{\mu\nu}^{(III)}$  start to have a constant amplitude for these gravitational waves. These waves propagate then as any other ordinary gravitational waves in vacuum. We have the non vanishing elements of energy momentum tensor for the radiated gravitational waves as follows

$$t_{00} = \frac{\kappa}{4\mu_0^2 c^2} B_x^2 E_0^2 z^2, \tag{4.20}$$

$$t_{33} = \frac{\kappa}{4\mu_0^2 c^2} \frac{B_x^2 E_0^2}{k^2} (k^2 z^2 + 1) \quad (4.21)$$

and

$$t_{03} = -\frac{\kappa}{4\mu_0^2 c^2} B_x^2 E_0^2 z^2. \quad (4.22)$$

Thus, gravitational waves created by electromagnetic waves in vacuum without the existence of magnetic fields have null energy momentum tensor. This is the case in first and last regions. Only within the second region with magnetic fields, the electromagnetic wave creates a physical gravitational radiation carrying energy. We expect an energy loss of the radiating system which is photons in our case. In the case of pulsar binary, we observed a loss in rotation period when radiating gravitational waves and we observe a spin-up of binary systems. In analogy, the radiation of gravitational waves makes the electromagnetic wave lose energy expressed as frequency drop or redshift. The radiated energy carried by gravitational waves is calculated from their energy momentum tensor components (see Ref. [293]) as follows

$$\frac{dE}{dt} = -L_{GW} = -\int \int F(\vec{n}) dS, \quad (4.23)$$

where the right hand side contains the gravitational waves energy flux. It is calculated from the energy momentum tensor as follows

$$F(\vec{n}) = -ct^{0k} n_k, \quad (4.24)$$

where

$$[n_\mu] = [1, 0, 0, -1]. \quad (4.25)$$

When replacing the tensor elements, we find

$$\frac{dE}{cdt} = -\int \int \frac{\kappa}{4\mu_0^2 c^2} B_x^2 E_0^2 z^2 dx dy, \quad (4.26)$$

where  $E$  represent the energy of the photon. Poynting vector represent the power density vector associated with an electromagnetic field. The time average over the oscillation period of Poynting vector is called the flux density, irradiance or intensity of light wave  $I$  (see Ref. [294]) which is given for a plane monochromatic light wave as

$$I = \frac{E_0^2}{2\mu_0 c}. \quad (4.27)$$

In another hand, the energy of light is carried by discrete particles called photons in the perspective of quantum mechanics. If the light has a frequency of  $\nu$ , then the photon's energy is  $h\nu$ . The intensity of the light is equal to the number of photons  $F$  crossing a unit area, in a unit time, multiplied by the energy of an individual photon

$$I = Fh\nu. \quad (4.28)$$

When considering in our case of a light wave propagating in z-axis, it could be seen as a beam of single photons travelling only along z-axis. We introduce a delta function in  $F$  to describe this propagation mathematically:  $\delta(x)$  impose the photon to exist only in  $x = 0$  and  $\delta(y)$  impose the photon to exist only in  $y = 0$  representing a propagation of photon particle along z-axis. Then, the number of photons  $F$  is

$$F = \delta(x)\delta(y) \frac{\text{photon}}{m^2 s}. \quad (4.29)$$

From the last three equations, we could then put

$$\frac{E_0^2}{2\mu_0 c} = h\nu\delta(x)\delta(y) \quad (4.30)$$

when we replace each term and simplify Eq. 4.26, we find the following differential equation, after replacing  $cdt = dz$  as the propagation is along the z-axis

$$\frac{d\nu}{dz} = \frac{-\kappa}{2\mu_0 c} B_x^2 \nu z^2 \int \int \delta(x)\delta(y) dx dy \quad (4.31)$$

which we integrate to find

$$\ln\left(\frac{\nu}{\nu_0}\right) = \frac{-\kappa}{6\mu_0 c} B_x^2 l^3 \quad (4.32)$$

and

$$(1 + z_{MIR}) = \left(\frac{\nu_0}{\nu}\right) = \exp\left(\frac{\kappa}{6\mu_0 c} B_x^2 l^3\right), \quad (4.33)$$

where  $\nu_0$  is the initial frequency of the photon,  $\nu$  is the frequency of the photon when leaving the second region and  $l$  is the coherent length of the magnetic field where the magnetic field is constant (represent here the length of the second region along  $z$  axis). This final result  $z_{MIR}$  represents the redshift that a photon suffer when propagating within constant magnetic field and radiating gravitational waves (i.e. Magnetically Induced Redshift (MIR) effect see Ref. [295]). It could appear that the right hand side of Eq. 4.32 has the dimension of time (seconds in SI units). But, it is worth to notice that a dimension of  $s^{-1}$  remains after replacing the number of photons  $F$  and simplifying its dimensions in Eq. 4.31. This ensures that the right hand side of Eq. 4.32 is dimensionless.

## 4.4 Discussion of the new effect and possible implications

We compare in this section our redshift effect to similar effects found in the literature and discuss the existence and the significance of its contribution in astrophysical and cosmological data. We present arguments in favour of the method used in the following chapters to estimate our redshift effect contribution. For the steps leading to radiated gravitational waves energy-momentum tensor (see Eq. 4.22), our results are not different from some previous papers (see Ref. [296]) but with different interpretation. In a theorized phenomenon known as Gertsenshtein effect, light passing through an external magnetic field produces a gravitational wave via wave resonance. This idea was predicted in the pioneer papers of Gertsenshtein (1962) (see Ref. [297]) and Zeldovich (see Ref. [298]) with applications to some astrophysical phenomena. This effect was reviewed by Kolosnitsyn and Rudenko (2015) (see Ref. [299]). Recently, more cosmological implications of such effect were investigated such as impacts in CMB and the existence of high frequency gravitational waves background (HFGW) (see Refs. [300]; [301] and [302]). Even some experimental application were formulated as the design of detectors to observe very High frequency gravitational waves HFGW using reverse Gertsenshtein effect where gravitons are converted to photons (e.g. Ref. [303]). In this theorized Gertsenshtein effect, light passing through an external magnetic field produces a gravitational wave via wave resonance. Some components of energy momentum tensor of those gravitational waves are used as a probability of the conversion between photons and gravitons. The interaction between represent an important topic in gravitational cosmology affecting various phenomena such as appearance of binary systems (see Ref. [304]).

Gertsenshtein effect has some weak points in its conception and especially its interpretation of the final state. The conversion in quantum level of a spin 2 particle to a spin 1 particle could have a spin violation. The energy momentum tensor of the photon loses energy randomly in this effect indicating a non continuum and a non conservation of energy. Such effect has non observational data supporting it until now and no analogue effects to compare with it. There is no theoretical foundations that justify the interpretation of the energy momentum tensor elements of gravitational waves as probabilities of conversion. And there is no effect that made such interpretation and has experimental or observational evidence. In our effect, those gravitational waves carries energy radiated from the electromagnetic wave resulting in a redshift for the photon. The new effect has mainly two strong foundations that differentiate it from the Gertsenshtein effect. First, we have a continuity of the energy momentum tensor of both radiations. Second, this effect is built in analogy with binary system prediction which was confirmed by Hulse-Taylor observations (e.g. Refs. [305]; [306] and [307]). These reasons make our effect more coherent. Then, we investigate its existence in cosmic conditions and significance.

Several redshift effects have very special conditions to occur. Then, they may not be suited for cosmological cases explanations. In the case of our effect, the only condition needed to have a redshift is the existence of magnetic field in the photon's trajectory. The existence of CMF has more and more observational evidence (e.g. Refs. [116]; [117]; [118] and [119]). The Faraday rotation measurements indicate dynamically significant magnetic fields in several observations of galaxies, clusters and recently even in inter-clusters voids. These magnetic fields have a magnitude ranging from  $10^{-9}G$  to  $10^{-6}G$ . Even if their existence is proven, magnetogenesis processes and evolution are still an open question (see Refs. [138]; [137]; [141] and [142]). The measurable characteristics of the observed magnetic fields differentiate the astrophysical or cosmological origin of these fields. These CMF provide the conditions for the contribution of our effect to exist in cosmological data.

The contributions of our effect are related to magnetic fields strengths and the size of the space where they exist. Our redshift effect could be described by the following equation

$$(1 + z_{MIR}) = \exp \left( 0.0269192 \left( \frac{B}{1\mu G} \right)^2 \left( \frac{dl}{100kpc} \right)^3 \right). \quad (4.34)$$

To recreate such effect in laboratory on Earth, we have done estimations on hypothetical experiment using Laser Interferometer Gravitational-Wave Observatory (LIGO) observatory. If we use the laser beams that travels along LIGO arms and to produce a shift in the wavelength of this light ray of  $10^{-4}$ , we need to apply all along this arm of  $4km$  a magnetic field of  $7.28 \times 10^{+18}G$ . This magnetic fields are not found even in magnetars that are famous by their extremely powerful magnetic fields of  $10^{12}$  to  $10^{15}G$ . The strongest magnetic fields created by mankind on Earth is about  $91.4T = 9.14 \times 10^5G$  at the High Magnetic Field Laboratory Dresden (HZDR) in 2011, making such an experiment inconceivable. Wolf effect was proved experimentally but with no observational evidence to explain abnormal astrophysical cases leaving them without clear explanation.

To prove the significance and estimate the impact of our effect, the study focuses on cosmological and astrophysical data. We present estimations for some magnetic fields strengths with possible corresponding coherent lengths in Table 4.1. Magnetic fields in our solar system or in interstellar medium are strong enough but don't have large space for the photons to accumulate noticeable redshifts from our effect. Redshifts from this effect exist but are insignificant against other effects or even measurements errors. Interstellar magnetic fields can cause possibly non noticeable redshifts. But, at large scales of extragalactic and galactic mediums, magnetic fields are weak with ranges from

Table 4.1: Estimations of our redshift effect for several magnetic fields strengths and corresponding coherent lengths of different cosmic scales.

Magnetic Field (B)	Coherent Length (dl)	$Z_{MIR}$
$10^{-6}G$	1 <i>kpc</i>	$2.69 \cdot 10^{-8}$
$10^{-9}G$	1 <i>Mpc</i>	$2.69 \cdot 10^{-5}$
$10^{-12}G$	1 <i>Gpc</i>	$2.71 \cdot 10^{-2}$
$10^{-3}G$	1 <i>pc</i>	$2.69 \cdot 10^{-11}$
$10^{-6}G$	100 <i>kpc</i>	$2.71 \cdot 10^{-2}$

$10^{-9}$  to  $10^{-6}G$  but spread at large distances and have noticeable impacts on cosmological data. A magnetic field with strength of  $10^{-6}G$  and a coherent length of 100 *kpc* produces a  $Z_{MIR}$  redshift of  $2.71 \times 10^{-2}$ . We can conclude that only astrophysical and cosmological scales are the ones to have noticeable contributions from our effect. Cosmic magnetic fields constant over coherent lengths of 1 *Mpc* have a weaker strength in order of *nG* as shown by observations. Then, accumulation of our redshift effect should have significant but not inexplicably and unobserved high contributions to the total redshift of a distant extragalactic object. Observed redshifts are hardly (if not impossible in some cases) broken to their individual effect contributions especially if those contributions are in comparable ranges. Then, the contribution of our effect is mis-interpreted as caused by Doppler Effect. This affects current models recreating the kinematic evolution of local and global structure formations. The wrong interpretation of our effect contributions as gravitational redshifts would result in over-estimation of gravitational potentials and then of dark matter composition of clusters and the whole Universe. Considering our effect contributions as cosmological redshifts is creating bias in cosmological parameters estimations and could account for additional estimations found by Calcino and Davis (2017) (see Ref. [5]).

## 4.5 Chapter conclusions

Recent studies had shown evidence of non-cosmological and non-Doppler contributions to observed redshifts of extra-galactic objects. Gravitational redshifts are responsible of just part of those contributions. We introduce a new magnetically induced redshift effect which could be the origin of the rest of redshift bias observed. This new effect is caused by a gravitational interaction of photons with cosmic magnetic fields producing gravitational waves and manifested as redshift. The main implications could be that contributions from different non cosmological redshift effects could be easily confused. This creates biased cosmological parameters estimations and over-estimation of dark matter composition of galaxies and clusters and even could change our perspective on the accelerated expansion of the Universe. Confusing contributions from our effect and Doppler Effect could affect numerical models constructed of structure formation in term of peculiar motion of galaxies.

Large scale surveys of extragalactic radio sources have important but not clear potential to investigate intergalactic magnetic fields. Techniques to discriminate Faraday rotations contributions are very ambiguous about estimations degeneracy and possibility of over-estimations of each part (see Refs. [128] and [129]). Several limitations make the creation of a reliable and detailed all sky map a very challenging or impossible task. Moreover in the case of Faraday rotations, measurements need cosmological redshifts to make estimations. In the existence of our effect, observed redshifts are deviated by unknown amounts from cosmological value. Then, the estimates done using observed redshifts as

reliable indicators of cosmological redshifts are biased. This is adding more doubts on estimations of cosmic magnetic fields strength. The estimation of our redshift effect impact on observations is not then feasible using current observational data on cosmic magnetic fields. Another method must be developed to estimate the magnetically induced redshift effect impacts. Magneto-hydrodynamic simulations are taking more interest lately as they present new insights about the multi-variant and non-linear astrophysical questions. We need to use numerical simulations data to make impacts estimations of our new magnetically induced redshift. Some of available magneto-hydrodynamic simulations are limited in access and their outputs are not configured in the appropriate setting to our study. To see the bias and deviations of cosmological parameters, we need to create a complete synthetic observation : cosmological distances and redshifts along with Doppler, gravitational and the new magnetically induced redshift effect.

# Chapter 5

## RPC - Interpolation from observed Redshift

Redshifts of extragalactic objects are determined directly by spectroscopic methods or via photometric means. The observed values represent the total shift of wavelengths that a photon had suffered from all possible effects. Contributions from non cosmological origins, such as our magnetically induced redshift, are making the observed redshift a not reliable indicator of cosmological redshift which represents just a part of the observed value. In our observations, we have very limited knowledge of environmental conditions in which light had travelled. We measure the final compilation of all the trajectory events overlapping on the initial state of the photon. It is challenging to decrypt the final observed state of the photon, to identify each individual effect contribution. In our case, we want to find the cosmological redshift of this extragalactic object from observed value. This could be possible if we can estimate other effects contributions.

We present in this chapter a probabilistic way to interpolate cosmological contributions from observed redshifts. This is achieved by proposing a model of cosmic conditions in which photons could travelled. This model describes mainly line of sight magnetic fields. The analysis of obtained results would give us the possible contribution of our redshift effect and thus the possible cosmological contribution depending on the trajectory magnetic fields model.

### 5.1 Magnetic fields models in cosmic environment

In previous chapters, we presented the state of the art in observations and theories on cosmic magnetic fields. The accumulated measurements had shown its existence in various astrophysical scales. The Extra-Galactic Magnetic Fields (EGMF) that has a large scale structure may have mean fields in the  $\mu G$  range. But, its origin and evolution is still enigmatic. The surveys present only a two dimensional view of the Universe. We need to probe their three dimensional structure to be able to understand these fields, their origins and impacts. For the cosmic scale, the involved processes are so varied and the resulting picture is highly complex. For this reason, we need to cut some levels of resolution when studying cosmic scales such as extra-galactic phenomena. This is achieved by putting simple mathematical models to describe even more complex processes giving an approximate but the most accurate picture possible. Two models arise for the structure of the EGMF:

1. *Randomly Oriented Patches* where the EGMF consists of domains of constant but randomly oriented field such the ferromagnetic materials (e.g. Ref. [308]);

2. *Sheets and Voids* where the scale structure of the EGMF consists of randomly oriented sheets of field associated with the filamentary concentrations observed in the matter distribution separated by relative voids (see Ref. [309]).

Observations of high redshift clusters provide strong evidence that the density of matter is small and the sheets and voids are largely in place with no scaling of the magnetic field strength and electron density in the sheet void model or average over voids. The EGMF is of order a few tenths  $\mu G$  at least in the local super-cluster with the sheets and voids model (see Ref. [310]). A  $\mu G$  field corresponds approximately to equipartition between the magnetic energy, the gravitational and thermal energies of the super-cluster.

The abundance of magnetic fields in cosmic environment makes their inclusion in any global or even local scale study imperative. In a past chapter, we introduced our prediction on new redshift effect generated in the existence of such fields. It is obvious to reconsider our interpretation of observed redshifts of extra-galactic objects. Even with the possible elimination of gravitational and Doppler effect contributions from the observed amounts, the resulting value of redshift is not of pure cosmological origin. Then, its interpretation as distance indicator is biased. New methods to estimate and eliminate the magnetically induced redshift contribution from observed redshift must be developed. We use current models of extra-galactic magnetic fields and numerical methods to study this problem. This method is presented in the following section.

## 5.2 Code algorithm

When dealing with an extra-galactic object, its redshift is a high valuable indicator especially that it represents the cosmic time when light had left the source. We explained in the previous chapter that observed redshift could be the combination of contributions from cosmological and our magnetically induced redshifts. For several objects having the same distance to observer, their cosmological redshift is the same and is dependent to their distance through Hubble law. From the randomness of magnetic fields, each path is different resulting in different contribution of our magnetically induced redshift. Then, their observed redshifts would not be equal. In the opposite, two objects with the same observed redshift could be in different distances having different cosmological redshifts. Then, we have an uncertainty on the contribution of each effect to the observed redshift. A method is needed to estimate the noise or bias created from our new redshift effect. As only observed redshift is available of a distant light source, a probabilistic approach could be the unique method to determine each effect contribution, especially cosmological redshift. Then for each observed value, we could only identify an interval of probable cosmological redshifts. For each cosmological redshift, we could also predict a range of possible observed redshifts. A main difficulty in this approach is to represent magnetic fields distribution along paths travelled by light. We choose to use patch model for cosmic magnetic fields where the Universe is a succession of small regions (patches) of random lengths and magnetic fields strength within them.

A C++ code was written to perform the probabilistic study of the relation between observed and cosmological redshifts correspondingly to cosmic magnetic fields. This code is labelled "Redshift Project Code" or RPC and represents a first approach to our probabilistic study. This code creates a simplified simulation of the propagation of photons within magnetic fields through cosmological distances. The hypothetical cosmic environment of the simulation is based as follows :

1. The space from the source to the observer is filled by magnetic fields;

2. This space could be decomposed to a succession of small patches;
3. Each patch have a random length;
4. The transverse magnetic field magnitude within each patch is constant and with a random value.

In this framework, we used then a model of Randomly Oriented Patches or ferromagnet like space. It is proposed theoretically and a simple one to implement in our first approach to the problem.

RPC generates randomly a number of patches which consists together a path travelled by light. The length of each patch is computed from the length mean ( $l_0$ ) and two random numbers. The first ( $r_1$ ) is used to decide whether the patch is longer or smaller than the mean. The second ( $r_2$ ) represents the amount of the difference from the mean. The length of each patch is given by

$$L = \begin{cases} l_0(1 + l_{ran}r_2) & \text{for } 0 < r_1 < 0.5, \\ l_0(1 - l_{ran}r_2) & \text{for } 0.5 < r_1 < 1. \end{cases} \quad (5.1)$$

The transverse magnetic field at each patch is also computed from a mean ( $b_0$ ) and a random number. ( $r_3$ ) can be taken as a sin of an angle between the photon propagation direction and the magnetic field vector. The strength of magnetic field at each patch is given by

$$B_{\perp} = b_0 r_3. \quad (5.2)$$

These three random numbers are generated by the code and are restrained between (0, 1). By this configuration, each patch is different from another and each path consisting of a section of patches is also unique. This is handy when trying to quantify the impact of random magnetic fields on observed redshift. At the end of this simulation, the goal is to find the possible contributions of both cosmological and magnetically induced redshifts which led to a certain observed value. We are aiming to estimate the non cosmological redshift effects with different cosmic magnetic fields configurations. This could help us to make predictions on the real cosmological redshift contribution of an observed redshift value.

RPC runs by following these steps :

1. After each patch generated and travelled, the photon is redshifted from cosmological and non cosmological effects.
2. The sum of these patches' lengths represent the distance travelled by light and is converted to cosmological redshift using Hubble law.
3. For each patch, the magnetically induced redshifts are computed and their product represents the total contribution of our effect to the observed redshift.
4. After each patch, the generation of these patches could be interrupted if a limit, given as input, is reached either for cosmological or observed redshift.
5. The code saves the results when it reaches this value within a margin error and starts over for another path. Otherwise, the code continues to another patch.

From the basic inputs and the random parameters generated for each patch, we compute the magnetically induced redshift by

$$(1 + Z_{MIR}) = \exp\left(\frac{\kappa}{12\mu_0 c} \sum_n B_{\perp n}^2 L_n^3\right), \quad (5.3)$$

and cosmological redshift using

$$Z_C = \left[ \frac{H_0}{c} \sum_n L_n \right] + \frac{1+q_0}{2} \left[ \frac{H_0}{c} \sum_n L_n \right]^2 \quad (5.4)$$

where  $\kappa$  is the gravitational constant in Einstein's equations,  $\mu_0$  is the permeability of free space and  $c$  is the speed of light. Eq. 5.4 represents an inverse form of Eq. 1.54 taking first and second order of Taylor expansion. The index (  $n$  ) represent the  $n^{th}$  patch that the photon has passed. After a number of patches, the final equations of the magnetically induced and cosmological redshifts are given by

$$(1 + Z_{MIR}) = \exp(0.027b_0^2l_0^3 \sum_n r_{3,n}^2 (1 \pm l_{ran}r_{2,n})^3), \quad (5.5)$$

and

$$Z_C = \left[ 0.33 \times 10^{-4} h l_0 \sum_n (1 \pm l_{ran}r_{2,n}) \right] + \frac{1+q_0}{2} \left[ 0.33 \times 10^{-4} h l_0 \sum_n (1 \pm l_{ran}r_{2,n}) \right]^2. \quad (5.6)$$

The simulated observed redshift is given by equation

$$(1 + Z_{Obs}) = (1 + Z_C) \times (1 + Z_{MIR}). \quad (5.7)$$

To run the code, several inputs should be set for the simulation which are :

1. magnetic strength mean (  $b_0$  ) in  $\mu G$ , mean of patches length (  $l_0$  ) in  $100 \text{ kpc}$  and randomness parameter  $l_{ran}$  for the generation algorithm of patches;
2. Hubble parameter (  $h$  ) in  $100 \text{ km} \times \text{Mpc}^{-1} \times \text{s}^{-1}$  and deceleration parameter (  $q_0$  ) describing the expansion of the Universe;
3. the observed value we aim to evaluate and the accepted error of the simulated observed redshift
4. the number of paths simulated to run and accepted cases wanted.

The output is a text file containing lists of the observed redshift, the simulated observed redshift, the simulated observed redshift error, the cosmological redshift and an index value of each path which represents the ratio of the observed redshifts on cosmological one. The total paths simulated are representing the possible dispersion from the cosmological redshift for a given fixed value of observed redshift. The analysis of the results should give us the possible relation between the deviation from cosmological redshift and magnetic field configurations.

### 5.3 Results and discussions

Several simulations were done by varying patches parameters. We set the generation limit to a single value of cosmological and observed redshift, then to a row of values covering a range of cosmological and observed redshifts. The common results of these simulations

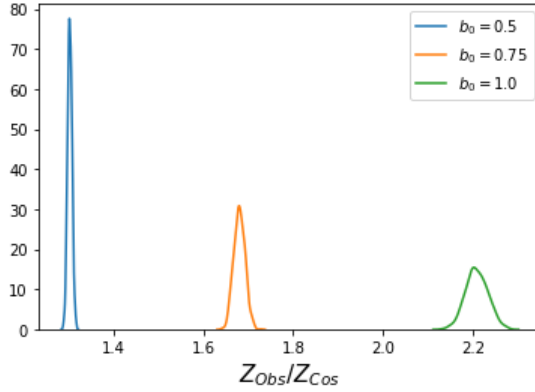


Figure 5.1: Probability distribution dependence to magnetic fields means  $b_0$ . The mean patch length is  $l_0 = 0.1$  and the observed redshift is  $Z_{Obs} = 0.01$  for the 3 simulations represented.

done confirm the uncertainty in the determination of cosmological redshift from a measured value of redshift. This uncertainty is represented by a probability distribution of a range of possible cosmological redshift. The distributions are represented using python's seaborn package functions. The function "seaborn.kdeplot" Fit and plot an univariate or bivariate kernel density estimations. Then, it converts the data to smoothed density distributions instead of representing data in the form of histograms. This probability distribution is highly related to the magnetic fields model's parameters. When studying these parameters impacts, we first vary only one each time, fixing others. The impact of each parameter could be summarized as follows :

1. Higher magnetic fields means induce a higher amplification with larger dispersion (see Fig. 5.1);
2. Higher patch length means create similar impact with higher amplification but with even larger dispersion (see Fig. 5.2);
3. For the randomness parameter of patches lengths, lower values are causing higher amplifications and more dispersion of the probability distribution (see Fig. 5.3).

When converting distances to cosmological redshifts, we use first and second order approximation of the Hubble law. The Hubble constant is set for all simulations to  $70 \text{ km s}^{-1} \text{ Mpc}^{-1}$ . For deceleration parameter, we use zero to keep first order approximation and  $-0.6$  when using second order approximation (see Ref. [311]). The impact on probability distribution is not significant especially as we study weak redshifts where first order approximation is sufficient (see Fig. 5.4 and Fig. 5.5).

The number of paths generated is also varied. We have done simulations with 1000, 10000 and 20000 path and the results of the amplification are similar in all of them (see Fig. 5.6). The impact of a certain magnetic model on redshift amplification for different observed redshifts is also studied (see Fig. 5.7, 5.8, 5.9, 5.10, and Fig. 5.11). The possible amplification is always bigger and more dispersed for higher observed values. This effect is studied using a row of observed redshift values instead of single values (see Fig. 5.12 and Fig. 5.13). Higher magnetic fields and patches mean lengths cause a larger divergence of possible cosmological redshifts from observed values.

The same behaviour is reproduced when fixing the cosmological redshifts and studying the possible observed redshifts (see Fig. 5.14 and Fig. 5.15). The divergence is always

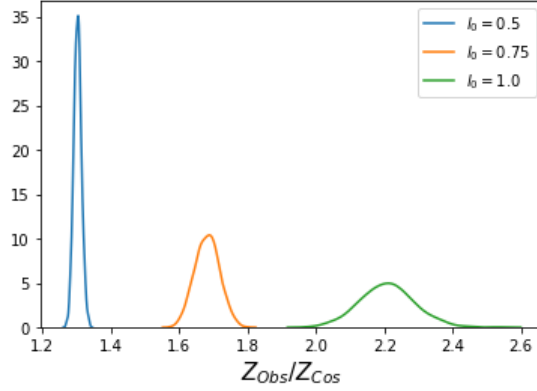


Figure 5.2: Probability distribution dependence to patches lengths mean  $l_0$ . The magnetic fields mean is  $b_0 = 0.1$  and the observed redshift is  $Z_{Obs} = 0.01$  for the 3 simulations represented.

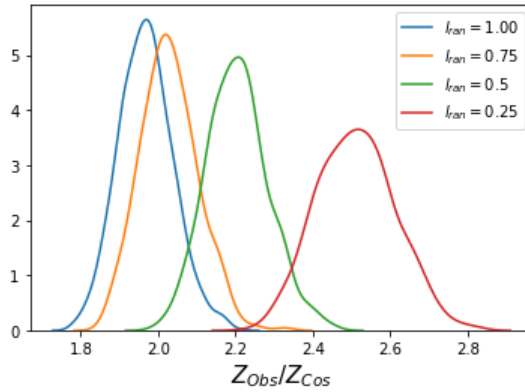


Figure 5.3: Probability distribution dependence to patches randomness parameter  $l_{ran}$ . The mean patch length is  $l_0 = 1.0$ , magnetic fields mean is  $b_0 = 0.1$ , the observed redshift is  $Z_{Obs} = 0.01$  and deceleration parameter is  $q_0 = -0.6$  for the 4 simulations represented.

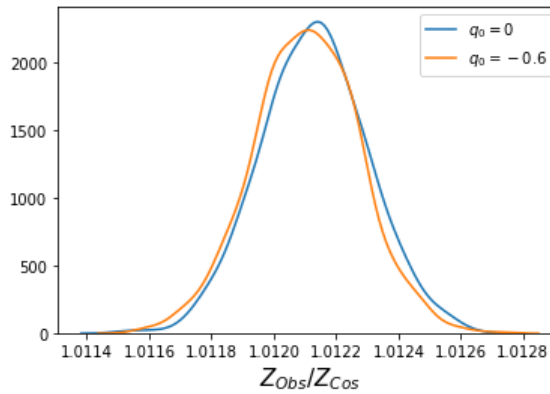


Figure 5.4: Probability distribution dependence to deceleration parameter  $q_0$ . The mean patch length is  $l_0 = 0.1$ , magnetic fields mean is  $b_0 = 0.1$  and the observed redshift is  $Z_{Obs} = 0.01$  for both simulations represented.

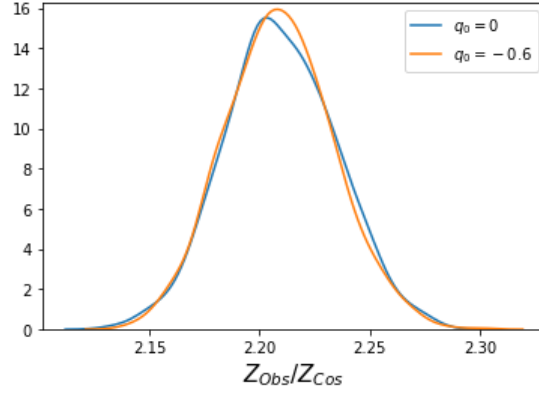


Figure 5.5: Probability distribution dependence to deceleration parameter  $q_0$ . The mean patch length is  $l_0 = 0.1$ , magnetic fields mean is  $b_0 = 1.0$  and the observed redshift is  $Z_{Obs} = 0.01$  for both simulations represented.

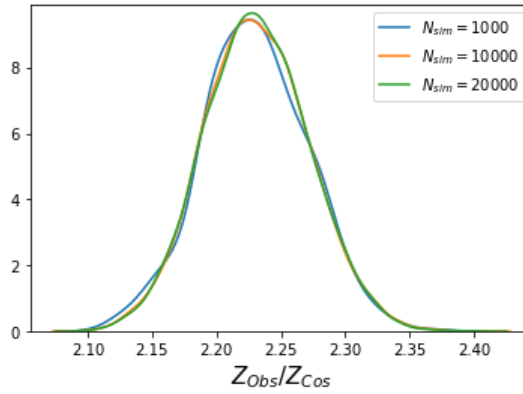


Figure 5.6: Probability distribution dependence to number of paths simulated done  $N_{sim}$ . The mean patch length is  $l_0 = 1.0$ , magnetic fields mean is  $b_0 = 0.1$ , deceleration parameter is  $q_0 = -0.6$  and the observed redshift is  $Z_{Obs} = 0.04$  for the 3 simulations represented.

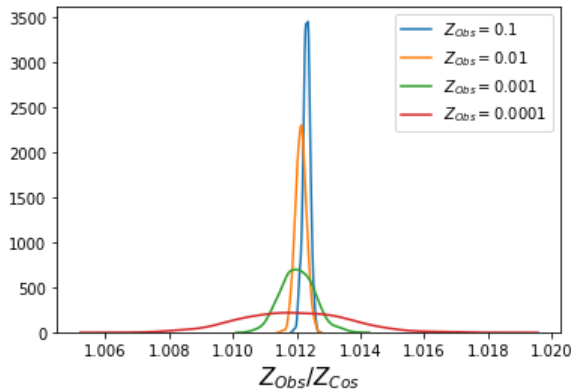


Figure 5.7: Probability distribution dependence to observed redshift  $Z_{Obs}$ . The mean patch length is  $l_0 = 0.1$  and magnetic fields mean is  $b_0 = 0.1$  for the 4 simulations represented.

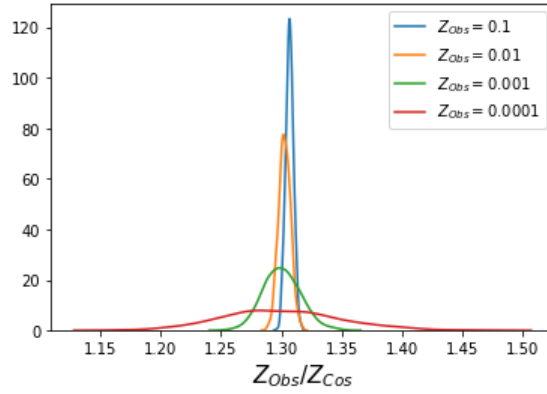


Figure 5.8: Probability distribution dependence to observed redshift  $Z_{Obs}$ . The mean patch length is  $l_0 = 0.1$  and magnetic fields mean is  $b_0 = 0.5$  for the 4 simulations represented.

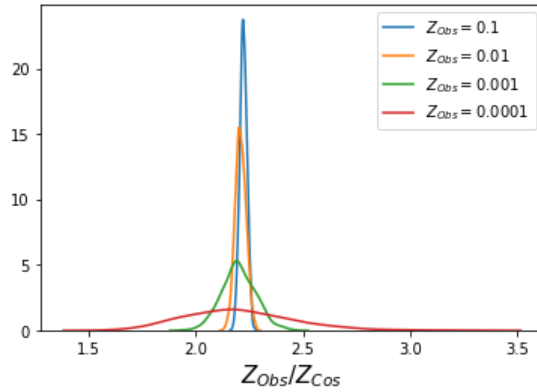


Figure 5.9: Probability distribution dependence to observed redshift  $Z_{Obs}$ . The mean patch length is  $l_0 = 0.1$  and magnetic fields mean is  $b_0 = 1.0$  for the 4 simulations represented.

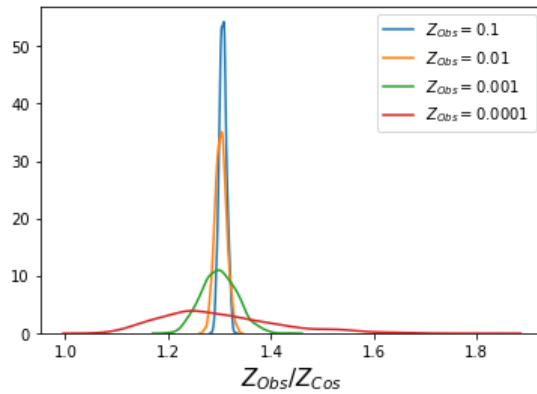


Figure 5.10: Probability distribution dependence to observed redshift  $Z_{Obs}$ . The mean patch length is  $l_0 = 0.5$  and magnetic fields mean is  $b_0 = 0.1$  for the 4 simulations represented.

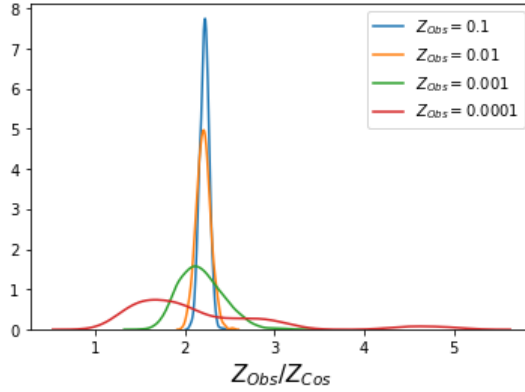


Figure 5.11: Probability distribution dependence to observed redshift  $Z_{Obs}$ . The mean patch length is  $l_0 = 1.0$  and magnetic fields mean is  $b_0 = 0.1$  for the 4 simulations represented.

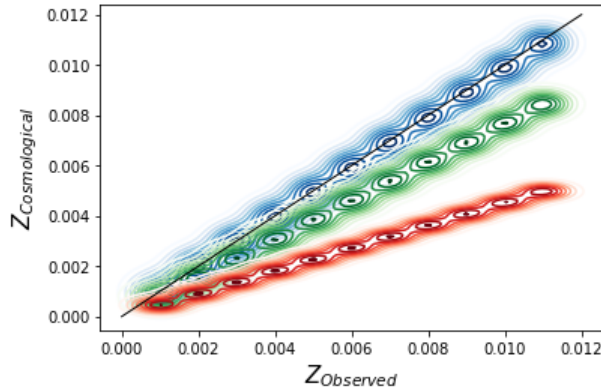


Figure 5.12: Probability densities for several observed redshift values  $Z_{Obs}$ . Simulations done for mean patch length  $l_0 = 0.1$  and magnetic fields mean  $b_0 = 0.1$  (in blue),  $b_0 = 0.5$  (in green) and  $b_0 = 1.0$  (in red).

larger for stronger magnetic fields and longer patches with less randomness in their lengths. Our redshift effect contribution is higher with stronger magnetic fields and longer patches explaining the higher amplification. Less randomness generates longer patches more frequently, which stabilizes the resulting amplification and results in less divergence. These results create a high uncertainty in observed redshifts interpretation. The model describing the real state of cosmic magnetic fields has also an important impact on the correction of our understanding and perception of observed redshifts and astrophysical objects real distances.

## 5.4 Chapter conclusions

Using the approach presented in this chapter, we could identify the cosmological part of observed redshifts. This identification is dependent of the magnetic field model parameters assumed. We could determine the dependence of redshift amplification to each model parameters. This amplification is higher for stronger magnetic strength and longer patches. The uncertainty in the determination of our effect contribution is related to the amplification dispersion. This dispersion is dependent mainly to the randomness in

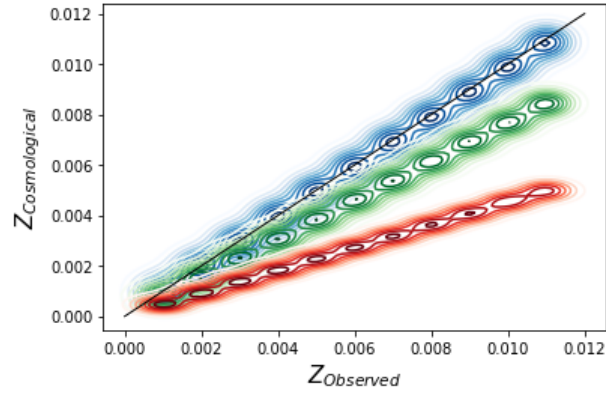


Figure 5.13: Probability densities for several observed redshift values  $Z_{Obs}$ . Simulations done for magnetic fields mean  $b_0 = 0.1$  and mean patch length  $l_0 = 0.1$  (in blue),  $l_0 = 0.5$  (in green) and  $l_0 = 1.0$  (in red).

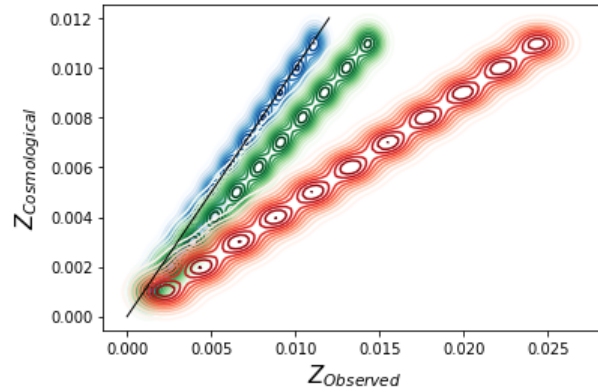


Figure 5.14: Probability densities for several cosmological redshift values  $Z_{Cos}$ . Simulations done for mean patch length  $l_0 = 0.1$  and magnetic fields mean  $b_0 = 0.1$  (in blue),  $b_0 = 0.5$  (in green) and  $b_0 = 1.0$  (in red).

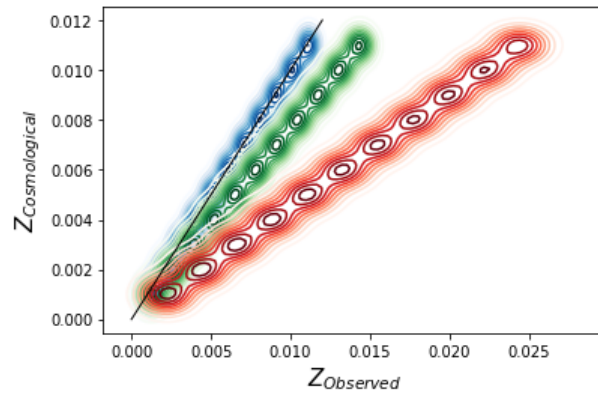


Figure 5.15: Probability densities for several cosmological redshift values  $Z_{Cos}$ . Simulations done for magnetic fields mean  $b_0 = 0.1$  and mean patch length  $l_0 = 0.1$  (in blue),  $l_0 = 0.5$  (in green) and  $l_0 = 1.0$  (in red).

patches length. The probable value of cosmological redshift is highly dependent to the model parameters. Those unknown parameters of the model are magnetic field mean and coherent length. Those parameters must be determined by observational techniques. But, those techniques could be biased by the same effects which we want to constrain. Cosmic magnetic fields are studied for example by Faraday rotation measurements. The estimations are also dependent of cosmological redshifts which we want to find in the first place.

This approach of interpolation is also neglecting other non cosmological redshift effects contributions such as Doppler or gravitational redshifts. These effects have been proved to have non negligible contributions and must be considered. This approach uses a model of magnetic field which is totally randomized. But, observations of magnetic fields around galaxies, for example, have confirmed a strength and configuration depending of the galaxy type and size. The inter-cluster magnetic fields are also related to cosmic history of structure formation and have specific configuration. This simple model used here could not replicate it. This is also making the signature of our MIR position dependent. The particular observed galaxy and its position in space would have a specific magnetic field and thus signature of MIR in the observed redshift. The observed redshift could be the same but for different cosmological redshift from different magnetic fields parameters. We should then change the model parameters for each particular case. Those models are then not reliable.

The code could be have more developments and applications. RPC can be adapted to more real configurations of magnetic fields in magnitude and patches length. New configurations can test the randomness of cosmic magnetic fields described by this approach. RPC simulations with all-sky maps of the cosmic magnetic fields can re-create these maps and identify galaxies' actual cosmological redshifts. These new maps have serious implications on our view to the Universe and several astrophysical processes. We can use RPC principle to study some anomalous redshift cases related to a magnetic field presence. Stephan Quintet and galaxy-quasar associations are some of these candidate cases where distances estimations give contradicting information to redshift interpretation. An extension of cosmic ray propagation code with RPC can show new results, constrains and implications of the ultra-high energy cosmic rays and the GZK cut-off. The coupling of the two codes would be on the magnetic configuration of simulations boxes.

From the above, we need a more appropriate method to study MIR impacts on observed redshifts. This approach should consider the complex process leading to the creation of galaxies in different regions of the cosmos and the hierarchy evolution of magnetic fields in all the Universe. This would make our results more significant and limit free parameters. Moreover, we should consider other non cosmological redshift effects namely Doppler and gravitational. Such a complete study would make interpolation of observational data more efficient.

# Chapter 6

## Possible explanation of trans-GZK events of UHECR

Determining distances to celestial objects is a key task in astronomy and astrophysics. This is a difficult mission as we only have a 2 dimensional view of the cosmos around us. These distances and their accuracy are very important to understand and interpret astrophysical processes observed. From the brightness of stars and supernovae and other indicators, we could determine distances to some objects. Those distances are redshift independent. For other cases, we must use Hubble law to determine distances from redshift which are redshift dependent distances. The redshift used should be from cosmological origin. As explained before, observed redshifts are the result of overlapping contributions from several effects affecting light. Both gravitational and Doppler effects are deviating observed redshifts toward higher values in some cases and toward lower values in others. But, our MIR effect is causing always a deviation toward higher observed redshifts.

In those cases where our effect has a significant contribution, the redshift indicated distances would tend to be overestimated. This makes the observer to believe that the light source is more distant than it is really. This could create paradoxical cases when trying to explain astrophysical phenomena using those wrong assumptions on objects distances. In this chapter, we consider the paradoxical observations of trans-GZK events of UHECR. In this case, potential sources capable of accelerating those particles up to those extreme energies are believed to exist far outside the GZK sphere. We approach this problem as an assumption paradox where the overestimation of those sources distances could created an apparent violation of GZK cut-off. To study this problem, we use a forward tracking of UHECR. We check if our MIR could make these sources of observed trans-GZK events appear much distant then GZK distance. The study is done using an extended version of CRPROPA code to compute our effect impacts on observed redshifts of UHECR sources.

### 6.1 Proposed explanation to GZK violation

The GZK paradox is based upon the difference between a theoretical perspective and results of an actual experiment. Several models are proposed to account for the acceleration of UHECR and the violation of the GZK cut off. There are a number of suppositions about the causes of the GZK paradox : an instrument error (AGASA observations), an incorrect interpretation, cosmic rays coming from distant local sources of vague origin, or Heavier nuclei possibly circumventing the GZK limit. Possible models include : Magnetic fields deflection, Deformed dispersion relation, Super-symmetric particles or Relic super-heavy particles. There is currently no preferred scenario for these UHECR where

the very energetic astrophysical sources such as Gamma Rays Bursts (GRB) or Active Galactic Nuclei (AGN) do not seem able to produce particles of a few  $10^{20}eV$ . The PAO experiment in the Southern Hemisphere has found a possible correlation with AGNs in the Veron catalogue with  $z$  less than 0.18 and with cosmic ray energies above  $5.62 \times 10^{19}eV$  (see Ref. [312]). Two plausible sources are MCG 8-11-11 (aka UGC 03374) at a distance of  $62 - 124 Mpc$  and AGN 3C 147 at a distance of  $1200 Mpc$ , but are highly unlikely sources of primary protons.

GZK violation is based on the assumption that UHECR and photons from the same source should arrive from the same general direction and with only a moderate arrival time difference. The coincidence of an observed UHECR and its astrophysical source depend on angular deflection of UHECR being small. Angular deflection and time delay between UHECR and photons are underestimated to few degrees or less by the generally assumed  $nG$  extragalactic magnetic fields. One solution to the GZK paradox is to assume the energetic particles are isotropized in the Inter-Galactic Medium by tangled magnetic fields, effectively randomizing their observed arrival direction by a diffusive propagation (see Ref. [313]). To apply diffusive propagation for the Fly's Eye particle, the requirement for the magnetic fields is  $B_{\mu G, \lambda Mpc} > 0.3$ . The Extra-Galactic Magnetic Fields with a large scale structure may have mean fields in the  $\mu G$  range. UHECR experience large deflections in such fields. With a diffusive propagation, the observed UHECR could be produced by sources within the GZK distance which are not in the direction of the UHECR arrivals. AGN or GRB active in the local super-cluster in the past 10-100 million years can account for the observed UHECR flux without contradicting the GZK distance limit (see Ref. [314]). The particular spectra of magnetic inhomogeneities could fit the observed spectrum and angular distribution of CR above  $10^{19}eV$ . AGN or GRB capable of accelerating UHECR to required energies must satisfy the Hillas acceleration condition and two additional constraints : their effective number and the observed flux of UHECR (see Ref. [315]). Independently of the nature of the UHECRs sources and of the magnetic fields which may deflect or confine them, 'low energy' UHECR protons ( $5 \times 10^{18} - 3.16 \times 10^{19}eV$ ) with path lengths up to a few  $Gpc$  contribute to the flux at Earth. While 'high energy' UHECR protons ( $> 10^{20}eV$ ), only reach Earth if their path length is of order few  $10's Mpc$  or less. This straightforward explanation that survives the analysis is that most UHECR reaching detectors come from a single unusually powerful AGN at a distance of a few Mpc. The M87 at  $18 Mpc$  that has been proposed as a possible single source of UHECR is too far away for the magnetic diffusive propagation (e.g. Ref. [316]). The nearby powerful radio galaxy Centaurus A (NGC5128, at  $3.4 Mpc$ ) proves to be an excellent candidate source of most UHECR observed. Cen A satisfy the Hillas criterion for acceleration of UHECR and can be considered as the only acceptable if the UHECR propagate diffusively requiring a magnetic field, probably in the few-tenth  $\mu G$  range.

The GZK prediction could be seen as the first test of special relativity approaching the Planck scale at which we might see the effects of a quantum theory of gravity. The Planck-scale deformation of the relativistic dispersion relation can explain some experimental paradoxes that presently confront astrophysics : observation of cosmic rays above the expected GZK limit, observations of multi-TeV photons from Markarian 501 and studies of longitudinal development of the air showers produced by ultra-high-energy hadronic particles (see Ref. [317]). The three experimental paradoxes involve the kinematic rules for particle production in a continuum classical spacetime, but the different relevant particle-production processes are at different energy scales. The quantum gravity literature has discussed several mechanisms for the emergence of deformed dispersion relations : the deformed symmetries of a quantum version of (quasi-) flat spacetime, properties of the spacetime foam background, or from the presence of more ordinary backgrounds like string

theory or non-commutative geometry (e.g. Ref. [318]). The deformed dispersion relation advocated in the spacetime foam phenomenological scheme can be the key ingredient for the solution of these three paradoxes. For the energy  $E$ , momentum  $p$  and mass  $m$  of a particle, the Planck length  $L_p$  correction to the dispersion relation can be

$$E^2 = f(E, p, m, L_p) = p^2 c^2 + m^2 c^4 - L_p m E \quad (6.1)$$

This deformed dispersion relation, having no free parameters, would affect the development and the kinematics of particle-production processes. The limit of very small (say vanishing) Planck length of the new threshold describes the conventional energy. The correction term turns out to be significant for the ultra high energy. Even at energies of  $3 \times 10^{20} eV$ , the photo-pion production on the CMB photons would be still not possible, providing an explanation for the observed cosmic rays of such high energies (see Ref. [317]). The Markarian 501 paradox can be explained in a completely analogous manner where the correction term is sufficient to forbid electron-positron pair production even above  $20 TeV$  from FIBR photons. The particle-decay process is affected by the deformed dispersion relation through the reduction of the available phase space. The pion decay related to the available phase space would inhabit an increasing in the lifetime and appear more stable affecting the air shower development.

The properties of new particle physics that could account for UHECR observations can be tightly constrained. A hadron with mass of order a few  $GeV$  and lifetime greater than a week can travel from distant sources of  $100 Mpc$  to  $1 Gpc$  without energy loss and yet produce an air shower consistent with observations. There is a possibility for the exotic UHECR from cosmological distant sources that can be transmitted with properties necessary to evade the GZK bound and interact like an ordinary hadron (e.g. Ref. [319]). This required particle is found in an interesting class of super-symmetric theories with very light gluino. The gluino lifetime which is long compared with the strong interaction time scale binds with quarks, antiquarks and/or gluons to make color singlet hadrons called  $R$  hadrons. The lightest  $R$  hadron with nonzero baryon number is the  $(udsg^*)$  bound, quasi-stable state designated  $S^0$  that could be the origin of UHECR. The neutral hadron with mass larger than a few times the proton mass would have a long enough mean free path in the CMB to evade the GZK bound. The GZK cut-off for this particle is at higher energy than for protons and this particle can come from appropriate accelerators at cosmological distances and point to these sources with no deflection in the magnetic fields. The lifetime is compatible with the required one to travel  $100 Mpc$  with such high energies. The GZK bound is several times higher than for protons by a factor of  $2.7 - 7.5$ .

The highest energy cosmic rays above the GZK cut-off may also be produced in decays of primordial super-heavy long-lived  $X$  particles (see Ref. [320]). The mass of the  $X$  particles has to be very large up to  $10^{13} GeV$  to produce cosmic rays of energies up to  $10^{20} eV$ . The lifetime can not be much smaller than the age of the Universe, up to  $10^{10} yr$  and act as a cold dark matter. The  $X$  particles can be produced in the right amount by usual collision and decay processes with a required reheating temperature after inflation. The super-heavy long-lived relics of the big bang particles are produced from vacuum fluctuations during inflation. The new cut-off of the UHECR and the shape of the spectrum beyond GZK cut-off predicted below  $10^{22} eV$  would be determined by QCD quark/gluon fragmentation. The observation of UHECR can probe the spectrum of elementary particles in its super-heavy range.

Other exotic theoretical ideas were proposed such as hadronization of quarks, the Z-burst, or structure defect models (e.g. Ref. [321]). Other models of astrophysical sources include : magnetars,  $eV$  neutrinos, Lorentz invariance violation, light gluino-containing baryons or sources from the galactic dark matter. There was no reliable model firmly

established with the available data set and remains as a current problem of astrophysics. They appear to give a satisfactory accounting of the spectrum around GZK energy, but have a wrong spectrum shape below this energy. The cosmic ray paradox is well established in the sense that there can be no doubt; the cosmic rays with energies beyond the GZK limit are observed. But, margins of uncertainty are in the identification of UHECR as protons and the identification of the possible sources.

## 6.2 New explanation using our MIR effect

In the previous chapter, we introduced GZK cut-off. We explained that for an event to be considered as a violation of this cut-off, it must fulfill three conditions :

1. The cosmic ray particle was a proton from the source to observer;
2. The final energy when entering Earth's atmosphere is higher than  $50 EeV$ ;
3. The source distance from the observer is higher than  $100 Mpc$ .

If an event doesn't have one of these conditions, it doesn't represent a violation of our understanding to special relativity and quantum field theories. For real events observed, the final arrival energy is determined by studying the showers formed after the interaction with Earth's atmosphere. Then, these energies are confirmed by measurements. The ambiguity on these observations come from particle type and source. Even the observation of primary protons with ultra high energies does not represent the paradoxical character of GZK phenomenon, but the absence of coherent sources of UHECR within the GZK sphere. It is challenging to interpolate the type of the particle and its origin from the current data. But, the possible sources that could accelerate the initial particle to these ultra-high energies are believed to be outside the GZK sphere.

For some possible sources, their distances are indicated by redshift. By the introduction of our new redshift effect, we showed that redshift-dependent distance estimations could have bias toward higher values. This is making the light source to appear much distant than it is really. The magnetic fields of the acceleration sites of UHECR, such as AGN, with the intergalactic magnetic fields can indicate a significant contribution of the magnetically induced redshift. Our effect is currently not considered when analysing and interpreting astrophysical data specially when estimating distances from observed redshifts. The recalibration of the observed redshift may affect significantly estimated distances. It is then possible that some potential sources of UHECR are more close than we believe and may even exist within GZK sphere. In this case, observation cosmic rays with energies equal or higher to  $50 EeV$  is not puzzling any more. Propagated particles, even protons, wouldn't have enough distance to interact with CMB photons. Consequently, any such events represent only an apparent violation of the cut-off and doesn't represent actual trans-GZK events. This apparent violation is then the result of mis-interpretation of sources' distances.

As explained in the previous chapters, the current cosmological data doesn't allow to test our hypothesis for real sources, especially when considering the 8complex mechanisms of cosmic rays propagations. The appropriate method to test our new hypothesis is to perform numerical simulations on UHECR propagations. In such simulations, several parameters of cosmic ray propagation are known : the actual sources, initial and final particles types and energies and the magnetic fields within the simulation box. All such information are missing for real observed cases. We perform forward tracking of generated UHECR from sources to fixed observer. All possible interactions, type changing and

Table 6.1: Common input parameters for simulations done using Extended CRPROPA code.

<b>Magnetic Field</b>	
Model	Kolmogoroff
Step ( $Mpc$ )	0.5
Spectral Index	-3.66
$K_{min}$	0.03125
$K_{max}$	0.5
<b>Interactions</b>	
Model	Sophia
Infrared and optical background	off
MaxStep ( $Mpc$ )	100
<b>Integrator</b>	
Model	Cash-Karp RK
Epsilon	1.e-5
MinStep ( $Mpc$ )	1e-4
<b>Observers</b>	
Number	1
Radius ( $Mpc$ )	0.2
Position	center of simulation box

energy loss are computed during the propagation. For confirmed observations and from information available, we need to compute both cosmological (real) and apparent distances to sources from observer. Then, if a proton is observed with energy higher than  $50 EeV$ , this event is considered to be possible GZK violation. If the cosmological distance is higher than  $100 Mpc$ , we have a real violation. We don't expect to have such cases, as the physics implemented in the model and code won't permit it. If the apparent distance is higher than  $100 Mpc$  and is considered by the observer as real, then this observer concludes wrongly that it is a trans-GZK event. The existence of such apparent trans-GZK events in our simulations data would provide the credibility to our hypothesis. This explanation was first presented by Mebarki and Abdelali (2014) (see Ref. [322]).

### 6.3 Extended CRPROPA code and simulations done

The forward tracking of UHECR is performed using CRPROPA code version 2.0 (see Ref. [323])<sup>1</sup>. For each observed event, an extension added to the code computes the two additional simulation outputs related to our hypothesis testing. This extension doesn't need any more inputs. First, the commands added compute the real source distance from the distance between source and observer within the simulation box. This cosmological distance is converted to cosmological redshift using Hubble law. The Hubble constant and deceleration parameter are fixed to  $70 km s^{-1} Mpc^{-1}$  and  $-0.6$  respectively. The magnetically induced redshift is computed from the magnetic field within the light path from source to observer. Then, the observed redshift of the UHECR source's light is estimated and converted to redshift-dependent distance or apparent distance using Hubble law (see Eq. 1.54). Both estimated distances are found in the simulation outputs along with particle initial and final type, energy and position.

Table 6.1 summaries the common parameters of simulations done. The configurations

<sup>1</sup><https://github.com/CRPropa/CRPropa2>

Table 6.2: Input parameters for simulations done using Extended CRPROPA code. "SP" stands for energies generated in power law where  $\alpha = 1$  and  $Rigidity = 100 EeV$ . In other simulations,  $E_{Initial}$  (in  $EeV$ ) use "Monochromatic" energies for generated particles.  $X_{max}$  (in  $Mpc$ ) represents the simulations box side size.  $B_{RMS}$  (in  $\mu G$ ) is the mean magnetic field strength used when generating cosmic magnetic fields within the simulation box. MaxTime is the maximum time a trajectory is followed expressed in  $Mpc$ .

Sim	MaxTime	$X_{max}$	$B_{RMS}$	$E_{Initial}$	Initial Species	$N_{sources}$
001	100	100	0.002	1000	$Mg$	500
002	100	100	0.002	100	$Mg$	500
003	70	60	0.020	100	$P$	300
004	70	60	0.002	100	$P$	300
005	70	160	0.002	100	$P$	800
006	70	160	0.020	100	$P$	800
007	100	100	0.002	SP	$Mg$	500
016	70	60	0.002	100	$P$	300
030	100	100	0.002	SP	$Mg$	1
032	100	100	0.002	1000	$Mg$	1

of simulations done are those of 3-Dimensional source distribution with the environment of Large Scale Structure "LSS" and only one observer is always considered in the centre of the simulation box. For particle interactions, the simulations are done using Sophia libraries (see Ref. [324]) with no infrared or optical backgrounds. The only interactions considered are with CMB photons.

The integration of magnetic field interaction is done with Runge-Kutta integrator (see Ref. [325]). Magnetic fields are generated within the simulation using a Kolmogoroff turbulence model (see Ref. [326]). To record only interesting events, we set the minimum energy; below this trajectories are abandoned, to be  $40 EeV$ . Some configurations are varied from a simulation to another to test their effects on observed events (see Table 6.2). For the simulation box size, we use  $60 Mpc$ ,  $100 Mpc$  and  $160 Mpc$ . For the distributions of sources, we use unique source in fixed position in some simulations and multiple sources distributed randomly and uniformly within the simulation box. The mean magnetic fields used are  $0.002 \mu G$  and  $0.020 \mu G$ . The initial particles type injected in the beginning of the simulation are proton and Magnesium atoms. The initial energies are monochromatic at  $1000 EeV$  and  $100 EeV$  in most simulations and power law in few cases. To get a significant number of observations, we generate for each simulation  $10^6$  particle to follow their trajectories. For this reason, each simulation take several hours to end.

## 6.4 First results and discussions

The results of all simulations done are analysed and the most common result is that no real trans-GZK events are observed. Figure 6.1 represents a scatter plot of all observed events. This figure helps to identify the real from apparent trans-GZK events. For this purpose for particles with final energy higher than  $50 EeV$ , source cosmological distances higher than  $100 Mpc$  are coloured in red as any such event would represent a real violation of GZK cut-off. If the apparent distance is longer than  $100 Mpc$ , then it represents only an apparent violation and this region of the plot is coloured in yellow. No observed particle with final energy higher than  $50 EeV$  has real source distance than  $100 Mpc$ . The detailed data of our simulations show us that none of these events have a travelled distance higher

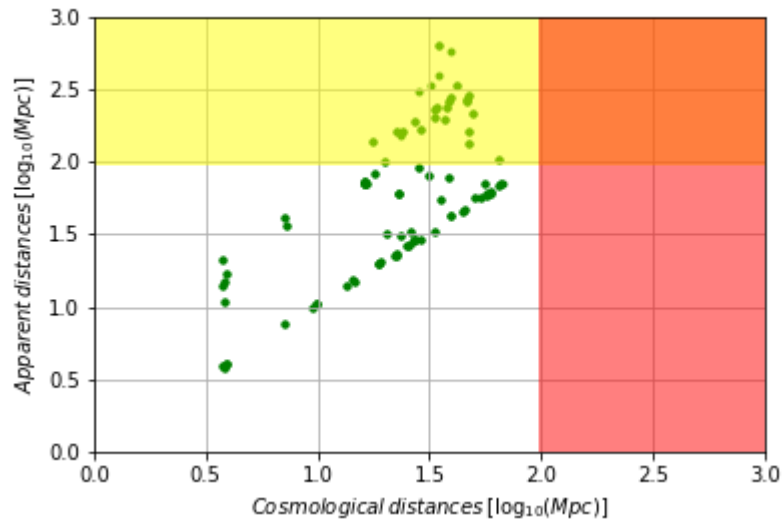


Figure 6.1: Apparent vs cosmological distance for all simulations observed particles with final energy higher than 50  $EeV$ .

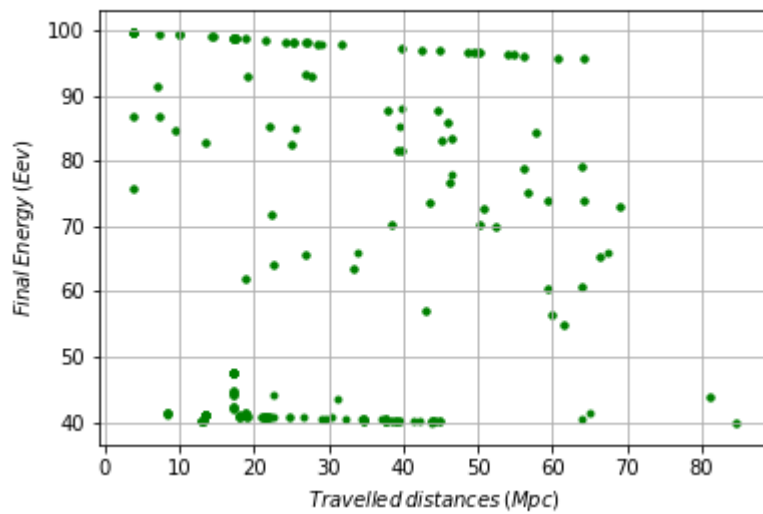


Figure 6.2: Final Energy vs Travelled distances for all simulations observed particles.

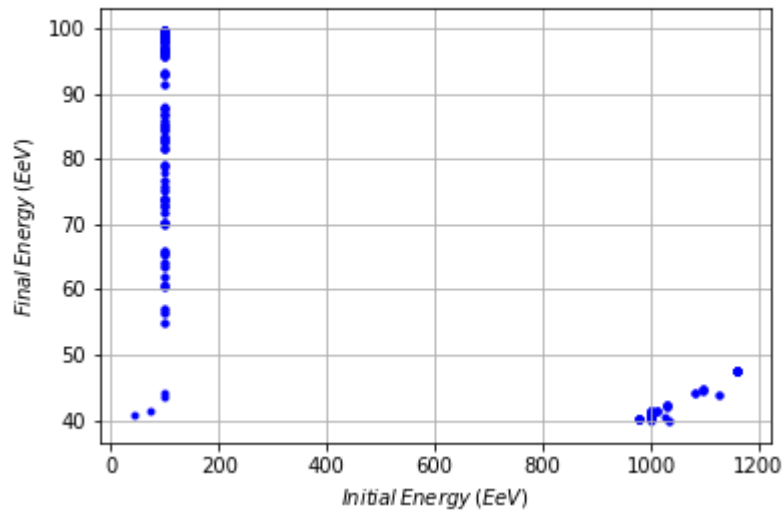


Figure 6.3: Final energy vs Initial energy for all simulations' observed particles.

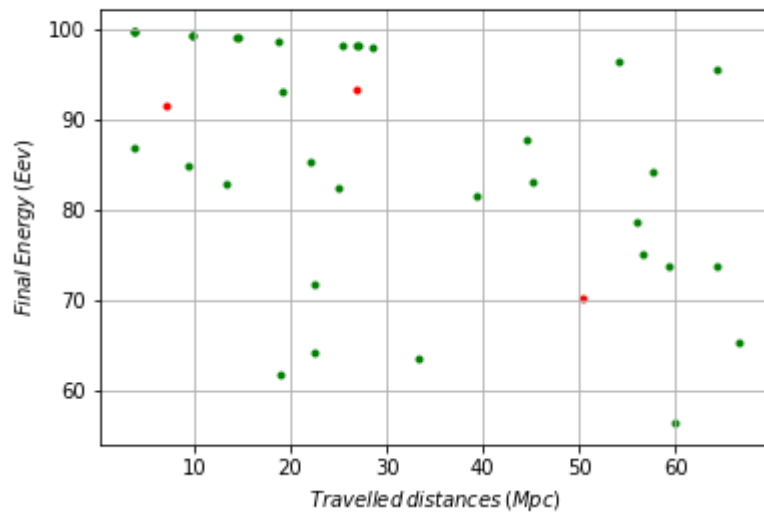


Figure 6.4: Final Energy vs Travelled distances for simulation Sim.016. Green points represent protons and red points represents neutrons.

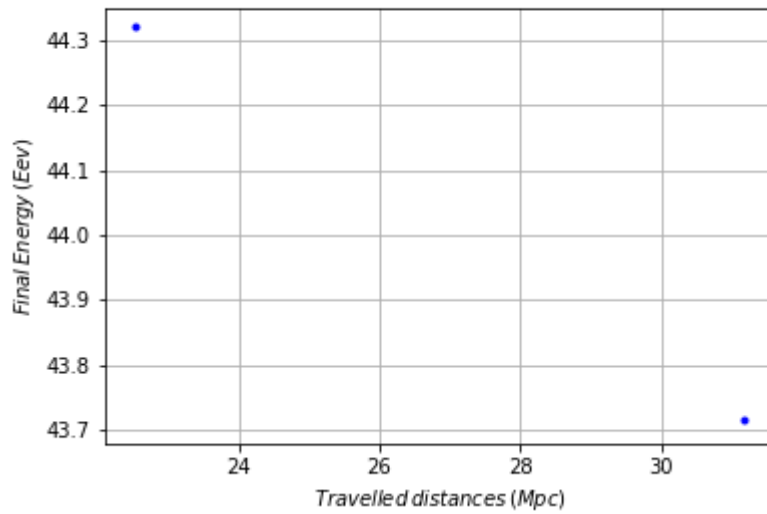


Figure 6.5: Final Energy vs Travelled distances for simulation Sim.002. The blue points represent Boron  ${}^1_5B$ .

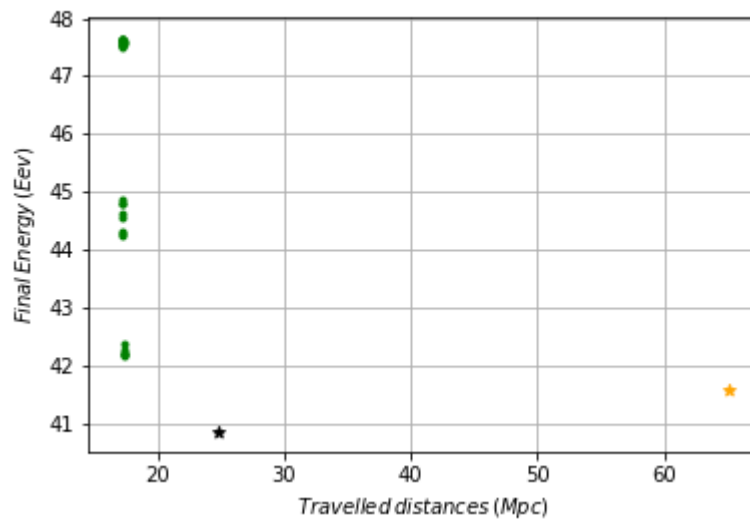


Figure 6.6: Final Energy vs Travelled distances for simulation Sim.030. Green points represent protons, the black star represents Magnesium  ${}^{24}_{12}Mg$  and the orange star represents Nitrogen  ${}^{17}_7N$ .

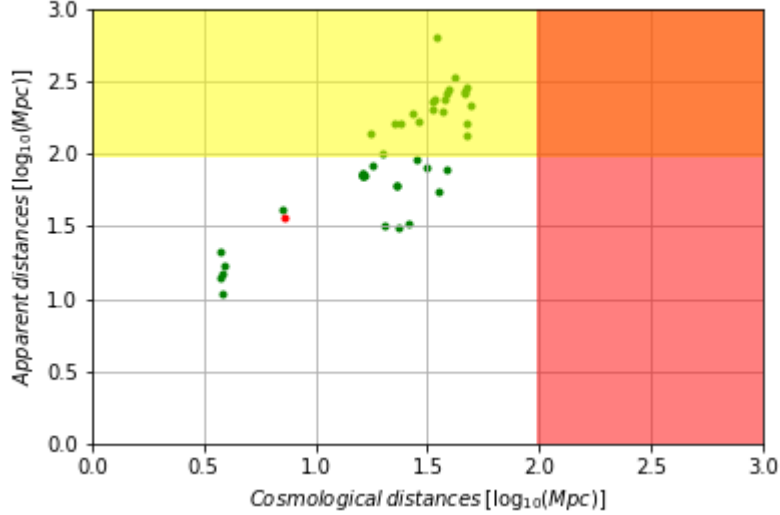


Figure 6.7: Apparent vs cosmological distance for observed particles of simulation Sim.003 with final energy higher than  $50 EeV$ . Green points represent protons and red points represents neutrons.

than  $100 Mpc$  (see Fig. 6.2). The correlation between initial and final energies of all observed events are represented in figure 6.3.

Most observed particles are protons with some other particle types such as neutrons, Boron  $^{11}B$ , Nitrogen  $^{17}N$  and even Magnesium  $^{24}Mg$  atoms which had travelled to observer. Some protons and even neutrons had energy higher than  $50 EeV$  (see Fig. 6.4), but all heavier atoms had less than  $50 EeV$  (see Fig. 6.5 and Fig. 6.6). These heavier atoms observed as final particles as resulted in simulations started with Magnesium as initial particles. The most important result is that several of these observed cases had an apparent violation of GZK cut off with apparent distances higher than  $100 Mpc$ . The only particles appearing to be trans-GZK events are protons (see Fig. 6.7, Fig. 6.8 and Fig. 6.9). The initial particles creating those interesting events are protons (see Table 6.3).

The impact of magnetic fields is clear in those events. The deviation induced by magnetic fields in propagated particles is represented by the angle between the source direction and the direction of arrival. For higher magnetic fields means, we observe higher deviations and more apparent trans-GZK events as illustrated in figures 6.10 and 6.11. This correlation comes from the fact that both phenomena depends on magnetic fields strength. The apparent distance has the contribution of our magnetically induced redshift. The higher deviations are related to electromagnetic interaction between these charged particles and fields which is more intense for stronger magnetic fields (see Fig. 6.12). The impact of initial energies on deviation angles is represented in figure 6.13 and shows dependence even it is not as high as of deviation angles and magnetic fields. The number of apparent trans-GZK events is related to the bias created by our effect in observed redshifts which is higher for stronger magnetic fields. Then, with strong magnetic fields ( $0.02 \mu G$ ), we have a possibility for the initial particle to be a proton. For weaker magnetic fields, the most probable is that apparent trans-GZK events could be from heavier atoms like Magnesium in our simulations.

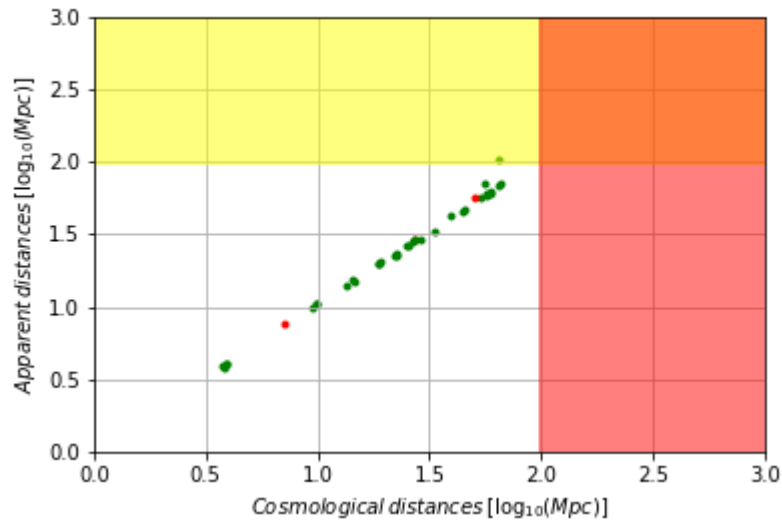


Figure 6.8: Apparent vs cosmological distance for observed particles of simulation Sim.004 with final energy higher than  $50 EeV$ . Green points represent protons and red points represents neutrons.

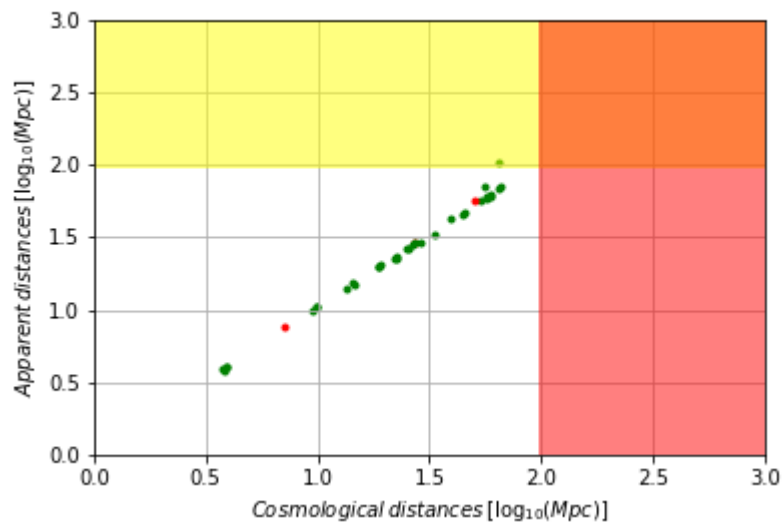


Figure 6.9: Apparent vs cosmological distance for observed particles of simulation Sim.016 with final energy higher than  $50 EeV$ . Green points represent protons and red points represents neutrons.

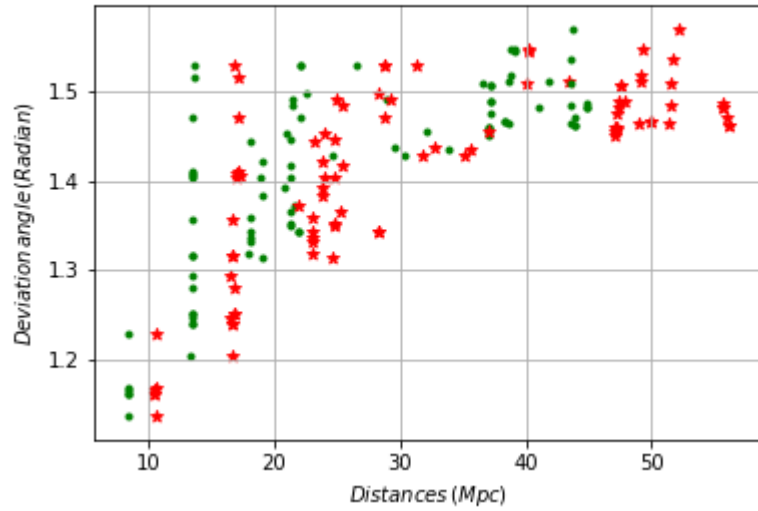


Figure 6.10: Deviation angles vs Distances for observed particles of simulation Sim.001. Green points represent the cosmological distance of the particle's source and red stars represents the apparent distance of this source.

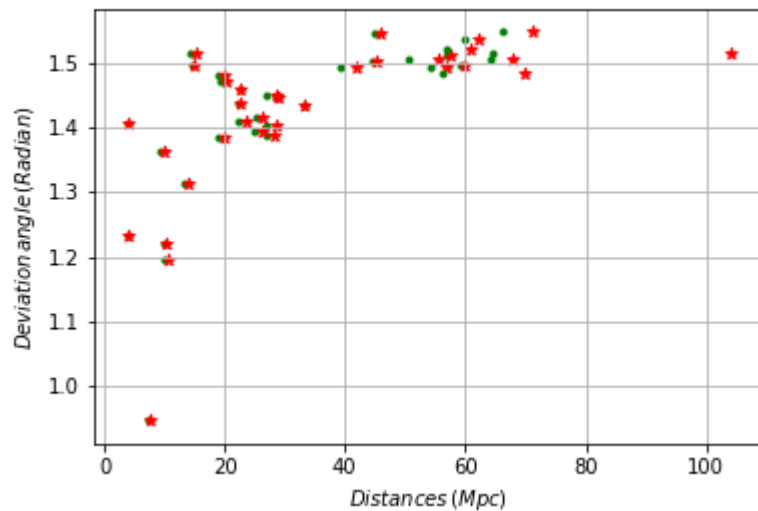


Figure 6.11: Deviation angles vs Distances for observed particles of simulation Sim.004. Green points represent the cosmological distance of the particle's source and red stars represents the apparent distance of this source.

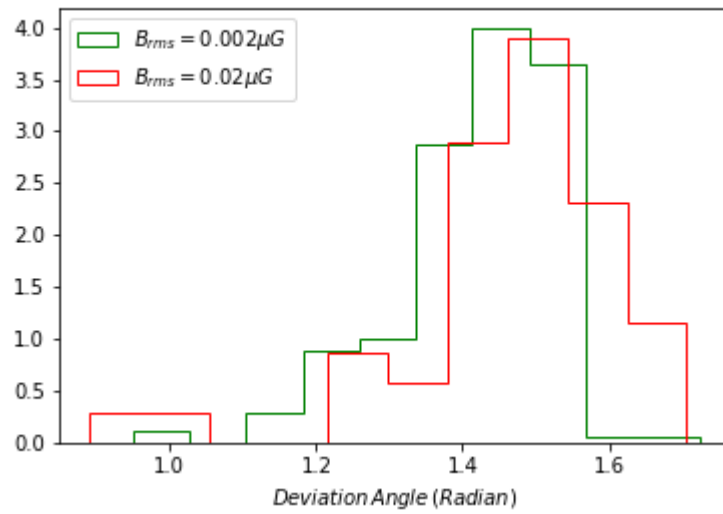


Figure 6.12: Deviation angles histogram for observed particles of simulations with magnetic fields means  $0.002 \mu G$  and  $0.02 \mu G$ .

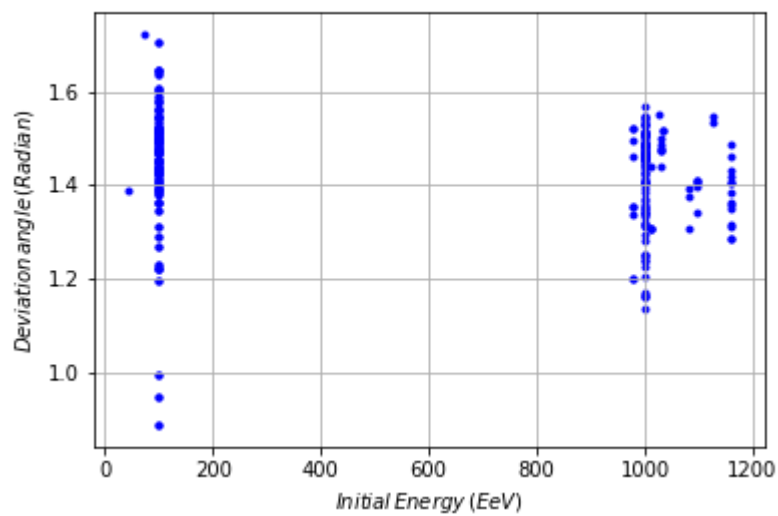


Figure 6.13: Deviation angles vs Initial energies for observed particles of all simulations.

Table 6.3: All events observed in simulations done by Extended CRPROPA code. These events have final energy  $E_{Final}$  (in EeV) higher than  $50 EeV$  and apparent distance  $D_{Apparent}$  (in  $Mpc$ ) higher than  $100 Mpc$ . The value '1001' represent a proton.  $E_{Initial}$  is the initial energy of the particle at the start of propagation in  $EeV$ .  $D_{Cos}$  is the cosmological distance of particle source in  $Mpc$ .

Sim	Initial particle	$E_{Initial}$	Final particle	$E_{Final}$	$D_{Cos}$	$D_{Apparent}$
003	1001	100.00	1001	86.07	17.47	135.44
003	1001	100.00	1001	69.93	47.35	132.31
003	1001	100.00	1001	96.59	27.36	191.83
003	1001	100.00	1001	96.62	33.94	232.94
003	1001	100.00	1001	96.26	47.81	284.94
003	1001	100.00	1001	87.85	33.03	200.51
003	1001	100.00	1001	81.62	34.43	636.24
003	1001	100.00	1001	92.85	22.40	159.22
003	1001	100.00	1001	72.72	46.03	263.39
003	1001	100.00	1001	76.69	38.96	275.85
003	1001	100.00	1001	70.23	37.39	232.94
003	1001	100.00	1001	65.53	24.08	161.89
003	1001	100.00	1001	79.25	33.13	230.81
003	1001	100.00	1001	97.28	28.88	168.89
003	1001	100.00	1001	97.10	36.73	195.56
003	1001	100.00	1001	96.57	46.10	264.67
003	1001	100.00	1001	96.17	38.91	260.64
003	1001	100.00	1001	96.68	41.83	337.02
003	1001	100.00	1001	60.35	49.12	217.68
003	1001	100.00	1001	73.05	47.73	163.06
004	1001	100.00	1001	73.86	64.36	104.00
006	1001	100.00	1001	77.92	39.39	573.07
006	1001	100.00	1001	84.98	23.34	149.47
006	1001	100.00	1001	87.97	34.54	395.22
006	1001	100.00	1001	98.02	28.24	304.81
006	1001	100.00	1001	65.90	32.15	333.62
016	1001	100.00	1001	73.86	64.36	104.00

## 6.5 Chapter conclusions

Simulations done with the extended CRPROPA code have shown us the possibility that GZK cut-off violation could be just an assumption paradox. Trans-GZK events are observed for sources within the GZK distance. But, their observed redshifts affected by our MIR are making sources to appear much distant outside the GZK sphere. So, even if those sources are identified, they would create a paradox as they appear outside the GZK-sphere. Those apparent trans-GZK events are observed in our simulations and may represent an explanation to the paradoxical observations in real observatories. The existence of such events is related to cosmic magnetic fields in environments of creation and propagation of particles and light from their sources. In our simulations, stronger magnetic fields of the order of  $20 nG$  allowed the bias of sources distances to higher values more than GZK distance of  $100 Mpc$ . Such magnetic fields create higher deviations making the identification of particles sources much challenging. Then, even if the high deviation angle is overcome and the source is identified, we would believe it exists outside the GZK sphere.

Those simulation results are giving clear indication on a possible explanation of UHECR paradox. More development in the study should be done to provide indications to overcome both the possible high deviation and distance estimation bias to solve the paradox of real observations. This would give more conclusive and significant results. Those developments would be in the environmental conditions of the simulation. Magnetic fields in those simulations are set manually and do not follow the complex evolution of the Universe. Galaxies sources positions are also generated randomly. In recent observational sources, cosmic magnetic fields are highly related to regions densities. Thus, the cosmic magnetic fields of nearby Universe are correlated to galaxies distributions. Moreover, the observed redshifts computed in those analysis considers only cosmological and MIR effects. For more realistic studies, Doppler and gravitational redshifts must be estimated. This couldn't be done within CRPROPA framework. The study of UHECR could be redone using results of more complex simulations. In those simulations, we will consider all processes governing the cosmic evolution. This will make magnetic fields, sources positions and observed redshifts more reliable and conclusions more significant.

# Chapter 7

## Cosmological simulations and synthetic observations

When we try to estimate our redshift effect contributions from actual CMF data, we find limitations preventing the construction of conclusive results. As most astrophysical and cosmological observations, indirect techniques are used to get information from light collected to estimate magnetic fields in galaxies and intergalactic medium. Another source of bias in CMF estimations is the impact of our effect on Faraday rotation measurements. When the source is more distant, Faraday rotation measurements are affected by the expansion of the Universe and the cosmological redshift  $z$  must be included. With our effect, observed redshifts are deviated from cosmological value by unknown amounts. Then, estimations are biased when done using observed redshifts as reliable indicators of cosmological redshifts. This is adding more doubts on cosmic magnetic fields estimations. All those limitations make the creation of a reliable and detailed all sky map a very challenging or impossible task. The estimation of our redshift effect impact on observations is not then feasible using current observational data on cosmic magnetic fields. Another method should be used to estimate magnetically induced redshift impacts.

### 7.1 Need for cosmological simulations

The only method to make reliable estimations is to use numerical simulations. Those simulations give us full control of initial conditions of the synthetic Universe. We have data of 4 dimensional evolutions of all key fields such as density, temperature, gravitational potential and magnetic fields. The analysis of those simulations outputs get us new insights about several astrophysical questions. This is then the reliable method which should be used to estimate our redshift effect contribution and possible impacts on cosmological data. The goal of our study is to estimate non cosmological bias of cosmological parameters especially from our new magnetically induced redshift. We need first to do numerical simulations data to create synthetic observations. Some of the available simulations do not simulate the evolution of magnetic fields which make them useless for our study. Other simulations following genesis and evolution of magnetic fields are also available but are limited in access.

Simulations needed should be configured to evaluate magnetic fields in the evolution of the Universe. We need to variate magnetic fields inputs in order to estimate properly impacts of our magnetically induced redshift effect. To evaluate the bias of cosmological parameters estimations, we need to create a complete synthetic observation. We have to do simulations which can give us possibility to synthesize cosmological distances and redshifts along with all non cosmological redshift contributions for each galaxy identified

relatively to an observer within this numerical Universe. From such synthetic observations, we could estimate impacts of all redshift effects and their possible bias on the cosmological parameters using redshift-distance relation similarly to methods used for SNIa data. To realise this, simulation outputs must be in a specific setting (i.e. specific redshifts intervals) which is not done in the actual publicly available simulations outputs. This is making a customized simulation a pressing need to complete the study of our new redshift effect's possible impacts.

The detailed data and specific outputs make it possible to calculate exact distance of astrophysical objects to observer and to compute the observed redshift from all contributing effects : cosmological, Doppler, gravitational and our new effect. It is a main difference to previous studies done with simulation outputs (e.g. WDW15) where they didn't consider cosmological redshift. In previous studies, observations were made from a single dataset taken in a fixed redshift - time (mostly present time  $z = 0.0$ ). But and as it is clear, observed haloes (galaxies) were in different positions, gravitational potentials and had relative velocities when light was emitted. All those are intrinsic to light source when looking to distance measurements, gravitational and Doppler redshifts. The deviations or errors of estimation from real values are not deniable and are higher for more distant objects. For our redshift effect, the problem is similar if not worse as the cosmic conditions in the path travelled by light have definitely changed as time passes.

For all those reasons and for the sake of accuracy, our synthetic observation is constructed from several datasets with a minimum distance that light can travel within each dataset. We use additional dataset outputs to map the basic fields' evolution of our simulated Universe. The ideal sure is to collect data of positions and light paths when the simulation is running in an inline analysis. For this possibility, we would have the exact situation on the path of light instantaneously. But, this method is more expensive in the amount of development in cosmological simulation code. Moreover, this method has a problem of recursive analysis. As the simulation is going along, we can't determine the exact time when light starts propagating and then start collecting data. We need to first, and at all simulation steps, find haloes and then check their observation in a location that is still in the future. This would be highly expensive in computation time in a problem (cosmological simulation) which is already resources needy. The closest possible method was to choose a minimum distance travelled by light within each dataset. This dataset is representing the state of the Universe in the time (redshift) interval between two data dumps. The changes that should be reported in such short redshift interval are negligible. Shorter intervals gives more accuracy to this approximation. This could be achieved with codes for cosmological simulation and synthetic observations. Our simulations are executed after determining the set of output datasets needed to construct the appropriate observation.

## 7.2 Customized cosmological simulations: code, common settings and variations

Our simulations are performed using AMR code ENZO (see Refs. [327] and [328])<sup>1</sup>. ENZO is a publically available code developed by an active community. It gives the possibility to simulate evolution of magnetic fields in cosmological context. ENZO is a highly parallel code that was used for multi-physics cosmological magneto-hydrodynamics (MHD) simulations along with other problems types implemented. It was used in several studies in both galactic scales on magnetized interstellar mediums (e.g. Ref. [329]) and cosmic scales

---

<sup>1</sup><http://enzo-project.org>

in clusters for shocks, cosmic rays and amplifications of primordial magnetic fields (e.g. Refs. [330] and [331]). It uses a particle-mesh N-body method to follow the dynamics of the Dark Matter and a variety of Riemann solvers to evolve the gas component. Our equilibrium cooling follows pre-computed tabulated cooling rates and cooling library which is implemented in **ENZO**. The time integration is carried out with 2nd order Runge-Kutta (RK) scheme (see Ref. [332]). Spatial reconstruction employs the piecewise linear method (PLM) (see Ref. [333]), and the flux at cell interfaces is computed with the Harten-Lax-van Leer (HLL) (see Ref. [334]) approximate Riemann solver. A maximum 50% of the Courant-Friedrichs-Lewy (CFL) timestep is used to advance any fluid element in the simulation (i.e. hydrodynamic CFL safety number of 0.5).

Within most simulations, we fix cosmological parameters to these values ( $\Omega_{b0} = 0.04$ ,  $\Omega_{m0} = 0.27$ ,  $\Omega_{\Lambda 0} = 0.73$ ,  $H_0 = 0.71$ ) and the initial redshift to  $z = 99$ . A separate code used before **ENZO** is (`inits.exe`) responsible of the preparation of the density and distribution of particles with their positions and velocities. This is done following a power spectrum equation form several models available. We choose for all simulations done to use the Eisenstein and Hu fitting model for initial particles densities and distributions having functions for low and moderate baryon fraction, including the case of one massive neutrino (see Ref. [335]). We fix  $\sigma_8$  by setting `PowerSpectrumSigma8` to 0.9. A random seed value (`PowerSpectrumRandomSeed`) is introduced to generate the distribution of matter of simulated Universe. This initial redshift, grid size, the simulation box size, the cosmological parameters are common parameters for both codes.

For **ENZO**, we define the rest of the simulation parameters such as : hydrodynamics or magneto-hydrodynamics model, cosmological initial magnetic field seed, star formation and feedback model and refinement options. As we are interested in the cosmic magnetic fields, we have chosen for all our simulation: The Dedner magneto-hydrodynamic method implemented in **ENZO** which was described in the paper of Dedner et al. (2002) (see Ref. [336] also Refs. [329] and [337] for implementation and test problems). The Dedner formulation of MHD equations uses hyperbolic divergence cleaning to preserve the  $div(\vec{B}) = 0$  condition. This method conserves the density, momentum, magnetic induction, and total energy density. In **ENZO**, only one method is implemented to seed magnetic fields. In this method, a 3 dimensional Cartesian framework is considered. Then and to seed magnetic fields, we could give a fixed vector of constant values. This method provides an homogeneous primordial magnetic field seeded to all initial simulation box cells. We have chosen several initial values to simulate but with the same vector configuration along a single axis of the simulation box. We set for all our simulations Global Schmidt Law (see Ref. [338]) for star formation and for star feedback.

Other simulation parameters are changed from a simulation to another to make comparisons between impacts of simulation conditions on each redshift effect contributions especially our effect. The random seed of the `inits.exe` code was changed to simulate different parts of the Universe. Feedbacks of supernovae and initial values of magnetic fields are changed along those several simulations. Those variations are done to check possible impacts of resolution, initial seeds and feedbacks on all simulations outcomes and specially magnetic fields and our redshift effect. Feedbacks like thermal and magnetic feedbacks are also used and tested to see impacts on magnetic fields evolutions. For the simulation box sizes, we have done simulation with  $20 Mpc h^{-1}$ ,  $40 Mpc h^{-1}$  and  $80 Mpc h^{-1}$ . The most useful initial grid size of the simulation is  $64^3$  and  $128^3$ . It is represented by parameters (`GridDims` and `TopGridDimensions`). We call initial grid size the number of root grid cells along each axis, which gives us the initial number of cells. Those grid sizes and simulation box sizes were the only possible as the accessible computational resources were from 1 core to 128 cores. This is making larger simulation boxes

and better resolutions very expensive in computational time. The AMR function allows us to achieve higher resolutions more efficiently by only fully resolving areas of interest, designated by baryon and particle over-densities. In our simulations, we set the ENZO parameter (`CellFlaggingMethod = 2 4`) which means that refinement is on baryon and dark matter mass. We set (`MinimumOverDensityForRefinement = 8.0 8.0`) which means that cells are refined when cell mass are 8 times the original cell mass. The refinement levels of 7, 6 and 5 allow for the finest cell size of around  $(5 \text{ kpc } h^{-1})^3$ . The simulations have taken several hours to several days. The whole set of simulations done with their analysis have took 5 months to be done. The biggest simulation is done with  $(20 \text{ Mpc } h^{-1})^3$  as box size and  $128^3$  as grid initial size for 28 hours in 128 cores making the total of 3584 core hours.

### 7.3 Synthetic observation: code and algorithm

The code YT is chosen for the construction of the synthetic observations. This code is also open source, developed and tested by active community. The YT code was presented as an analysis code which reads outputs from several simulations codes and creates synthetic observations (see Ref. [339])<sup>2</sup>. This code is chosen as it is already set to read and analyse ENZO datasets and it has some developed synthetic observations tools. This code is written with Python language making the development of the existing analysis and visualisation functions very easy and allowing fast extensions using available and well developed Python packages. To set of simulation outputs, a function in YT version 3.1 was implemented to prepare such output plan. After setting the Universe cosmological parameters, we choose the observer redshift which is in our case (present time  $z = 0.0$ ) and the expected maximum redshift. The function automatically determines the set of output datasets needed to construct the appropriate observation.

To create our needed synthetic observation, this task is done by new and old extended functions of the code YT version 3.1. A new class of functions called (`haloesLightRay`) is added to the code. Those functions had the role of observation construction using new features added and modifications in old YT functions. The main function of this class functions is to organize the flow of the analysis as follows :

1. After the initialisation of basic parameters, the list of output datasets is loaded from the biggest redshift to the lowest.
2. For each dataset, a previously implemented function of the code is called to search and determine haloes. This function is (`HaloCatalog`) and it uses a specific finder method to identify those haloes. We fix for all simulations the method to 'hop'. This method is implemented in YT-3.1 and described by Eisentein and Hu (1998) (see Ref. [340]).
3. For each halo of each dataset, we call a new function to check if this halo from this dataset could be observed in present time. This new function checks if a propagated light from that halo would reach the chosen observer in the chosen time, which is mostly present time,  $z = 0.0$ . In all our simulations analysis, we fix the observer position to the centre of simulation box. We want to have observed haloes from all sky directions. This position is not related to any halo of any dataset. The light is propagated at first for the two limits of the redshift interval representing the current dataset. If light from the higher redshift didn't reach the observer, the conclusion is that we observe this halo from another dataset with higher redshift.

---

<sup>2</sup><http://yt-project.org/>

If the light from both lower and higher redshift limits of the current dataset had passed the observer, this means that we observe now a newer picture of this halo represented by a dataset with lower redshift. Only if the light of the higher redshift had passed the observer and from the lower had not yet reached the observer, we conclude that the cosmological redshift of this halo is within those limits. We iterate then between them until we find the value which allows the light to start travelling from that halo and reaches the observer at present time. Only in this later case, this value represents the cosmological redshift and the halo is declared 'observable'.

4. The main function proceeds for an observable halo of the current dataset. We determine now the exact distance and other redshift contributions. Here, we call a modified version of a YT-3.1 function (`LightRay`). We have altered this function to allow the computation of our effect's parameters. This function was designed to collect data from cells in which a light ray propagates. But, light beams were generated randomly and can't be tracked from start to intermediate and end points. Moreover, the light is tracked only within the same dataset. We extend the features of this function to be able to follow light from several datasets with sequential points relating those datasets. The constructed light ray starts from the observable halo and proceed until it reaches the observer. The new changes done have allowed the total path to be divided to several smaller paths. In each one, light travels within different dataset until it reaches the exact location of the observer. The light when travelling stops in the first dataset at a certain point and proceeds from an equivalent point but in the following dataset. The small redshift intervals representing each dataset makes changes of those points unnoticeable. The function is also developed to collect magnetic fields all along the light ray path and calculate for each cell the magnetically induced redshift that light is expected to suffer. At the end of the propagation, the function returns : the exact distance travelled by light from the accumulation of cell sizes, our redshift effect detailed contributions of each cell and the final sum.
5. Now for this observable halo, we have distance, cosmological redshift and magnetically induced redshift. We need now to compute other effects' contributions. First, gravitational redshift is computed from the difference of gravitational potential between the emitter position and the observer position. The gravitational potential is one of the key fields in hydrodynamic equations integration when the simulation is running. ENZO code is providing an option where we could request that this potential is been recorded when datasets are dumped. This option is making the determination of gravitational redshift a straightforward operation. This method of analysis is more accurate than the one used in a previous work where publicly available data were used and the gravitational potential was not recorded. In WDW15 study, a reconstruction was needed to estimate gravitational potential and then the gravitational redshift. Our method uses the actual potential which was running within the simulation cutting the reconstruction and possible accumulation of numerical uncertainties. Those gravitational potentials are collected in the previous step with the (`LightRay`) function execution. The Doppler redshift is related to the velocity of this halo along the line-of-sight with the observer. For Doppler redshift, we project all star particles velocities to line-of-sight and then we calculate the mean as an estimation of the halo projected velocity to the line of sight. Then, this mean is used to evaluate Doppler redshift.
6. Finally, this analysis is done for each observable halo of each available dataset.

At the end of the analysis, a list of observed haloes is presented with their corresponding distance, cosmological, gravitational, Doppler and our new effect redshifts. Observed redshifts affected by our redshift effect contribution could be calculated. The step now is to analyse those data which represent a close mimic of supernovae type Ia data and then to estimate cosmological parameters.

This algorithm and preliminary results were firstly presented by Abdelali and Mebarki (2015) (see Ref. [341]). The results presented in the following chapters are the most accurate currently achieved. The analysis presented in the last points could be customized by several ways. Some other options could be used to allow better understanding and more data about those observed haloes. For example, this analysis could be limited for haloes having stars. Haloes that are only formed by dark matter and gas without stars are removed in all our simulations analysis. Haloes expected to have their light lensed by foreground haloes could be also eliminated before reaching the final haloes list. We check if the light of a halo would pass close to another halo sphere of the same or the following dataset in a line-of sight projection. Then, it is declared possible to be lensed or not. This method is not accurate enough but gives a first approximation to the problem of lensing. This option is then just in test. Additional data on each halo are collected such as the absorption lines of foreground dust and gas and redshifts of those lines. We could also estimate the spectral energy distribution of light of each halo. Those data could be used later to estimate photometric redshifts of those haloes. The analysis of the redshift distance data are now with statistical methods. In case we have high cosmological redshifts, data analysis would be sensitive to all cosmological parameters. Our simulations size allowed only weak cosmological redshifts to be reported, the data are only sensitive to Hubble constant.

## 7.4 Chapter conclusions

To estimate and then eliminate the gravitational and other redshift effects bias, we need a complete knowledge of the state of the local Universe : masses, positions, velocities, compositions ...etc. This information is difficult to reconstruct from the two dimensional picture that we have of the cosmos around us. The available data is mostly partial and affected by the same bias effects and technical limitations of other observations. For those reasons, cosmological simulations offer an ideal framework to study the evolution of the Universe. As this is a highly non linear process, numerical simulations give us a full control and access to the Universe parameters and key fields' evolution like : densities, temperature, gravitational potentials ...etc. Such simulations allow us to follow the evolution of Universes with different configurations and the construction of synthetic observations. This offers the possibility of estimation of several effects' contributions : conventional or new ones predicted by theory and their impacts on our view of the cosmos are waiting to be estimated.

# Chapter 8

## Simulations results

Our simulations are dedicated to study impacts of non cosmological redshift effects and specially our new magnetically induced redshift by studying synthetic observations which mimic supernovae type Ia data. We report our results starting by the catalogue of haloes, their redshifts and distances of a realised simulation labelled Sim.9. The data collected from this simulation are detailed for distances, positions in 2 dimensional all sky map, redshifts of all effects. The sim.9 is done with 128 cores and took more than 35 hours of simulation and analysis. The simulation has  $(20Mpc h^{-1})^3$  as box size,  $128^3$  as initial grid size and 5 levels of refinement. The simulation box of sim.9 is not big enough to allow high redshift observations. This simulation had 688 haloes observed but only 443 haloes had stars. The simulation had created 3468201 star particles. Just one halo is reported to be lensed by our lensing check method.

### 8.1 Possible misinterpretation of redshift deviations origins

To be able to visualize deviations of the observed redshift, we plot the data of haloes with stars on redshift - distance plan. We expect to see Hubble law between weak cosmological redshifts and corresponding distances of observed halos which is projected as a linear pattern. This behaviour is confirmed for all simulations done when we plot distance vs. cosmological redshift. This is a first confirmation that our method is correct. We represent then observed redshift to corresponding distances. In observed redshift, we distinguish two cases. The first observed redshift is computed from cosmological, Doppler and gravitational contributions. The second observed redshift takes into account our new redshift effect contribution. An observer in this synthetic (or in the real) Universe has a single observed redshift for each extragalactic object. This measured value has contributions from some or all non cosmological redshift effects mentioned above. By distinguishing these two cases, we can evaluate the impact of our effect separately. They represent the cases where our redshift is or isn't a real effect affecting photons.

Starting with the first kind of observed redshifts (see Fig. 8.1), we observe that some haloes have a slice deviation from the linear behaviour. Others have more deviations but always around linear pattern. An interesting part of the plot is where a group of haloes (galaxies) have large deviations raising above the linear pattern in the form of a "bump". Those haloes are expected to form a cluster and that the gravitational bounding between its members has created high potential difference between them and the observer. The large difference of gravitational potential of those haloes, one to another and to observer, has impacted their light with significant gravitational redshift causing an amplification of

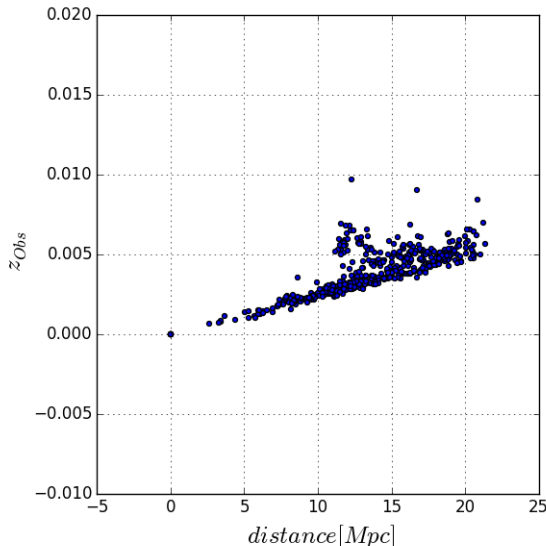


Figure 8.1: Sim.9 observed haloes' distances plotted vs. observed redshift (Cosmological + Doppler + gravitational).

their observed redshift. Such amplified redshift is observed in the form of this deviation from the linear behaviour of Hubble law of this cluster of galaxies. Such cases are also observed in real Universe data as was the case observed for Virgo cluster's galaxies. Their distances were measured by Cepheid variables using Hubble Space Telescope (see Ref. [342]) (see Fig. 8.4) credit to Keel (2007) (see Ref. [343]). The shape and difference between those galaxies points and the expected cosmological redshift distance relations is due primarily to gravitational potential at those haloes. The impact of the gravitational potential in the observer position is not significant. Different observer location and then with different gravitational potential measures changes in the size of the deviation but not the shape of the distribution of those galaxies points which is not as linear as we would expect.

The other important case is when we include the new redshift effect. When analysing this observed redshift plots (see Fig. 8.2), we notice similar behaviour of the previous plot : linear pattern and different deviations. The bump of the cluster previously observed in the first configuration is still present. Some few points are different from where they are in the previous plot. To be able to see better the differences, we plot both cases in the same diagram (see Fig. 8.3). We noticed 3 main differences :

1. We find new deviated points for more haloes which are not previously deviated.
2. We notice that some halo points have joined the cluster points.
3. Some of the cluster points have even more deviations to higher redshifts.

Those differences are really important and indicate us to the following possible ambiguities in our perception of such data :

1. The new halo points joining the cluster points could be confused as part of the cluster and influenced by its gravitational potential well even if they are not.
2. The additional deviation of the cluster halo points could be considered as created only by gravitational redshift causing biased estimation of the gravitational potential at this halo position.

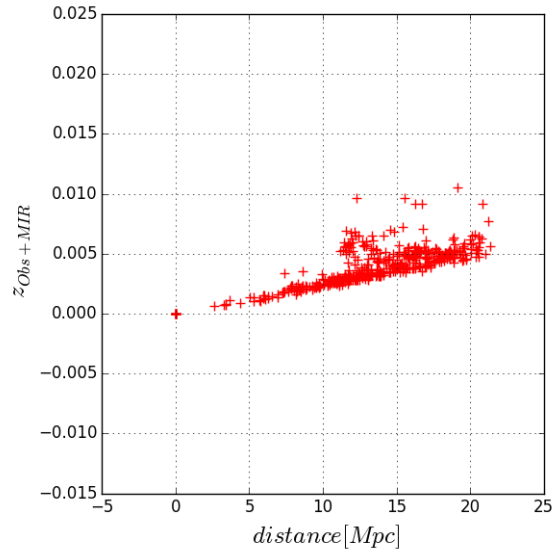


Figure 8.2: Sim.9 observed haloes' distances plotted vs. observed redshift (Cosmological + Doppler + gravitational + magnetically induced redshift).

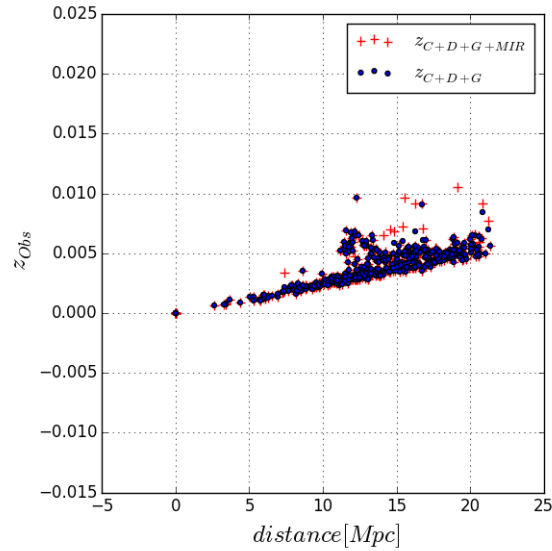


Figure 8.3: Sim.9 observed haloes' distances plotted vs. observed redshift of both cases without our effect (represented by points) and with our effect (represented with plus signs).

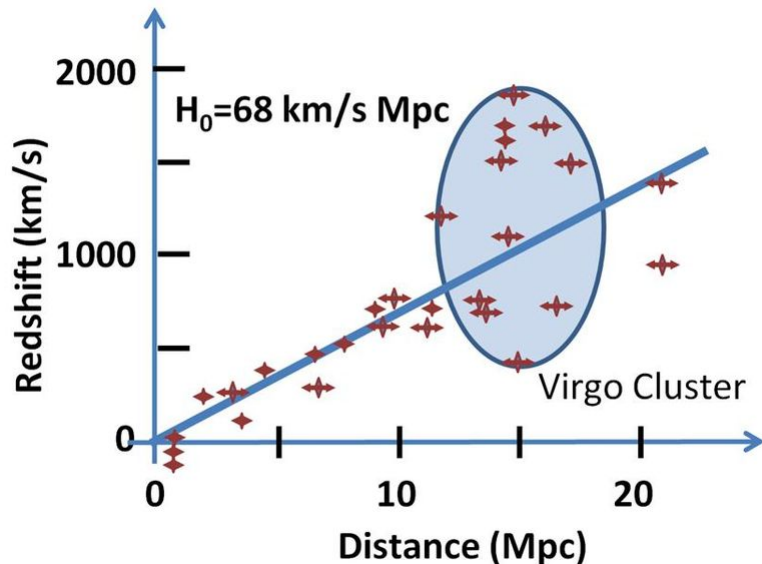


Figure 8.4: Redshifts vs. Distances of Virgo cluster measured by Cepheid variables using Hubble Space Telescope (see Ref. [342] credit to Keel (2007) see Ref. [343]).

3. The new points deviated could be considered to form a cluster or in influence of gravitational forces that don't exist.

Those possible confusions are due to the fact that observed redshift is hardly (if not impossible in most cases) broken to its individual effect contributions. Some of the observed deviations that are thought to be due gravitational or Doppler could be in part or even totally from our new redshift effect. This is true even in actual observations and estimations. And our simulation data has shown that clearly.

For the second possibility of ambiguity, it is highly probable and could not be ruled out. For the two others, it is possible that the similar distance and redshift (cosmological + gravitational) are not enough to consider a halo as part of a cluster. The same for points deviated only by the magnetically induced redshift, they could be separated by large angular differences, and exists in different parts of the sky and then of the Universe. So, the possibility of a confusion of haloes that are not in clusters or clusters which are only apparently gravitationally bounded is weak. To check this point further, we plot the all-sky map of all haloes observed filtered by the contribution of gravitational and magnetically induced redshifts in each halo case. The first map is for all haloes which their light suffers from additional redshift due gravitational cause more than  $10^{-3}$  (see Fig. 8.5). The second map is for all haloes which have additional redshift from our redshift effect more than  $10^{-4}$  (see Fig. 8.6). The two maps are plotted in the same all sky map to be compared (see Fig. 8.7). We notice first large number of points in constellation with high gravitational redshifts and have very low spatial differences indicating that those haloes are bounded gravitationally. Those haloes represent the cluster described above. Smaller such groups exist in different parts of the sky. For our redshift map, we report first single halo points which are highly separated from other haloes. Other haloes are in close constellations. Some of those haloes are a continuation of those found from gravitational redshift. They could, or could not, be part of the same cluster. The small spatial separation and the deviation from both gravitational and magnetic origins could be easily confused. Finally and even far from gravitationally bounded haloes, we notice that the magnetically induced deviations are also regrouped in constellations making the confusion between them and the real clusters bounded gravitationally possible. Those

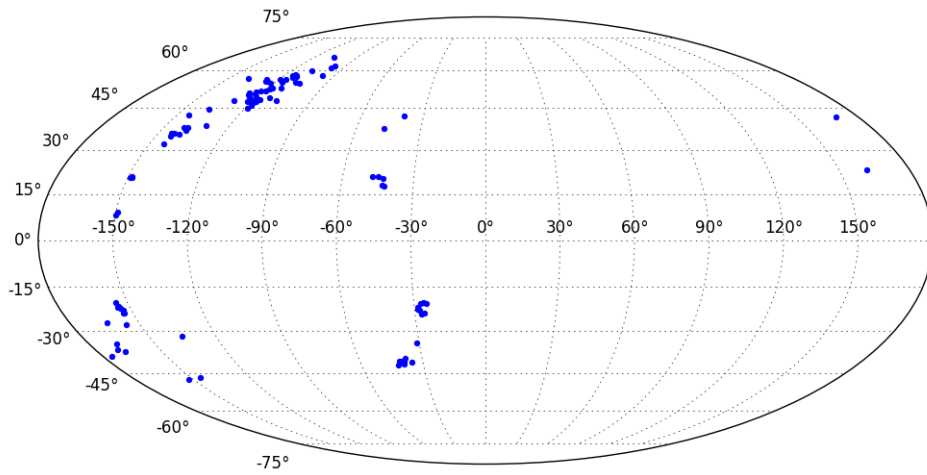


Figure 8.5: All-sky map of Sim.9 halos filtered by gravitational redshifts contributions higher than  $10^{-3}$ .

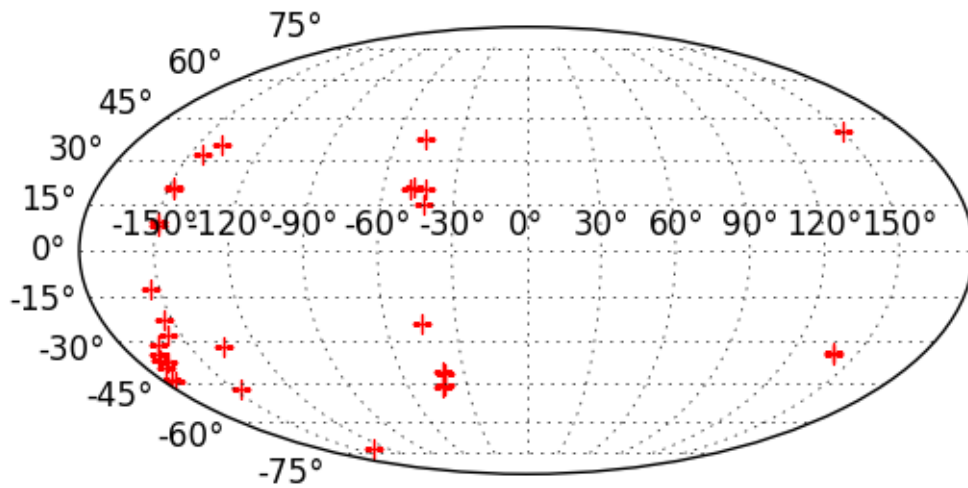


Figure 8.6: All-sky map of Sim.9 halos filtered by our effect redshifts contributions higher than  $10^{-4}$ .

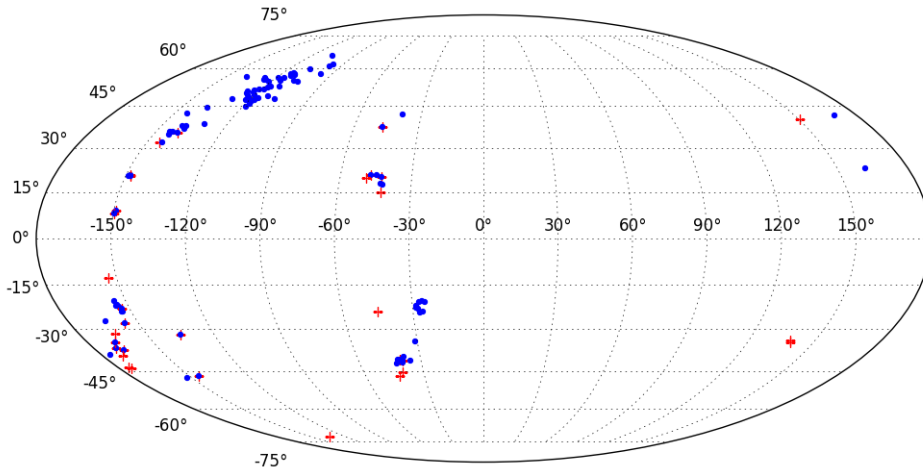


Figure 8.7: All-sky map of Sim.9 haloes filtered by gravitational redshifts contributions higher than  $10^{-3}$  (represented by points) and haloes with contribution from our effect contribution higher than  $10^{-4}$  (represented by plus signs).

remarks from all-sky map make it possible and not ruled out the confusion between the real members of clusters and other haloes deviated by our redshift effect. The possibility of apparent clusters bounding from our redshift amplification is possible too.

We have to do a cut in the data for our representation of redshift-distance plots and later in Hubble constant estimation. This cut is mainly caused by our redshift effect amplification only or combined with gravitational redshift contribution. Some cases have low deviations when we compute the contribution of our effect. And in other cases, the deviation is so large that we could not use those data as normal ones. We call those cases extreme cases and their number in the data is very variable from a simulation to another and especially the magnetic fields within the synthetic Universe of a simulation. For sim.9, those cases exist in small portion of the data. Those cases have to be eliminated for the redshift distance plots to have a plot in a representative scale. For Hubble constant estimation, the method is not even applicable on them. The used method considers low redshift converting the redshift distance relation to linear Hubble law. But, some of those extreme cases had a very high redshift. We do the cut for data in our redshifts exceeding 0.01. All haloes having an observed redshift affected by our effect exceeding that value are eliminated and its measurements not used in estimation. Those cases have important information and explanations that we detail in a following section. Only in the all-sky maps, those extreme cases are represented with the rest of haloes. The deviations from our redshift effect are highly related to magnetic fields and could cumulate contribution all along the way to observer. For this reason, it could reach very high contributions close to double the observed redshift or even more in some cases as its relation is exponential (see Eq. 4.33). The gravitational redshift in the other hand have a limited value. It reaches infinity only for a singularity which doesn't exist in our simulations. We found that at maximum and in present time : the gravitational redshift of a light travelling from the lowest to highest gravitational potential in our Universe couldn't exceed  $2 \times 10^{-2}$  (positive or negative related to who are the emitter and observer) (see Fig. 8.8). This is a confirmation of our method of computation of the gravitational redshift which is based on the assumption that we have weak gravitational potential.

We use histograms to have a better understanding of the distribution of different red-

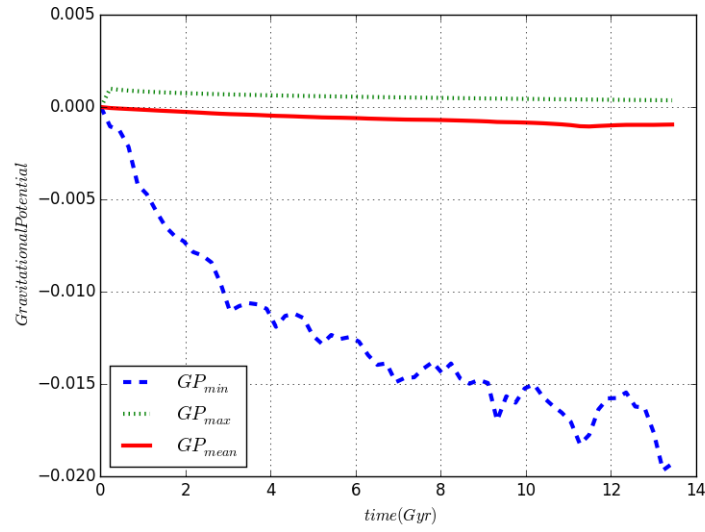


Figure 8.8: Maximum, mean and minimum gravitational potential evolution plotted vs. cosmic time for Sim.9.

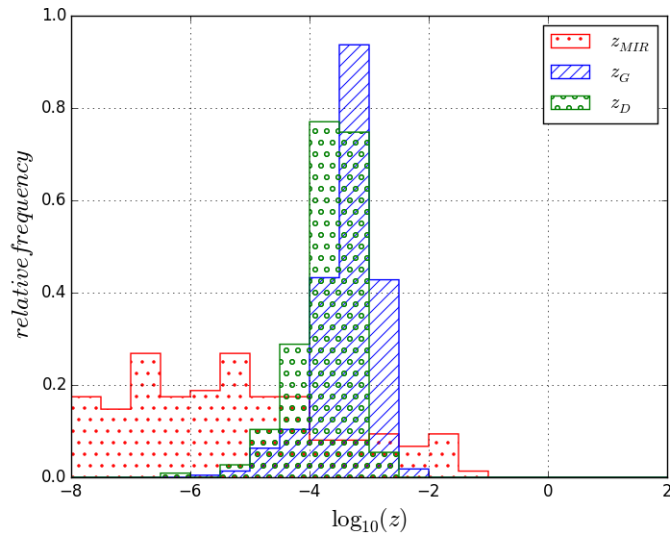


Figure 8.9: Histograms for each redshift effect contribution (Doppler, gravitational and magnetically induced) describing their distribution along several ranges for Sim.9.

shift effect of non cosmological cause. First, we take absolute values for gravitational and Doppler redshifts and then computed their decimal logarithm. To be better representative, histograms are drawn for the relative frequency not for the number of the haloes in each class. For our effect, all redshifts exceeding 1 are gathered in the last class. For sim.9, we notice that Doppler and gravitational redshifts are really close in distribution (see Fig. 8.9). Even if, Doppler is dominant near  $(10^{-4.5} - 10^{-4})$  and  $(10^{-4} - 10^{-3.5})$ . And gravitational redshift is dominant in both  $(10^{-3.5} - 10^{-3})$  and  $(10^{-3} - 10^{-2.5})$  classes. Those estimations for gravitational redshift are higher than previous works estimations that were around  $10^{-5}$  only (see WDW15 also Refs. [4] and [270]). This could be in partial for observer position but mainly of the specific simulated Universe on and to the fact that those estimations are from exact data of the simulation and not a reconstruction. For our redshift effect, we notice that it fills all classes from  $10^{-8}$  to  $10^{-1}$ . For cases with redshifts less than  $10^{-4.5}$ , the contribution of our effect is the only existing in this magnitude. But, it is dominated by Doppler and/or gravitational contributions to the total observed redshift when there is a contribution from one or both effects. For cases of redshifts from  $10^{-4.5}$  to  $10^{-2.5}$ , our redshift effect contribution could be easily confused and explained as a Doppler or/and gravitational in origin as explained in previous parts. Haloes, with mixed contributions or pure contribution from only our effect, could easily be interpreted mistakenly. From  $10^{-2.5}$  and more, our redshift effect is totally dominant. Those cases could be in our analysis of the data taken as abnormal or extreme or just hardware malfunction. But, we present in the following sections a more insight in those cases.

## 8.2 Impact on Hubble constant estimation

As we explained, the distance redshift relation is converged to Hubble law for lower redshifts. To compute Hubble constant from those data points, we used the Hubble law for each halo and we converted its redshift and distance to a Hubble constant for this halo. The Hubble constant values computed for each halo separately is then averaged to give a mean and a standard deviation.

We are now interested to impacts on Hubble constant estimation of those deviations of observed redshifts with and without the inclusion of our new magnetically induced redshift effect. After collecting Hubble constant values for all haloes, we present their means and standard deviations as estimation of Hubble constant of this synthetic Universe and from observations of this observer. First, we do the quantitative check of our method in synthetic observations construction and Hubble constant estimation. This check is done with cosmological redshifts. In all simulations, Hubble constant estimation for this check is the same as the value implemented in the start of our simulations which is  $(71 \text{ km/s/Mpc})$ . The difference is so weak and with very low standard deviation. This case is expected if the Universe is described by Einstein general relativity with FLRW space-time and we could somehow for real observations estimate and eliminate all contributions of non cosmological effects. This perfect picture is exactly what we have in our simulations and those synthetic observations. This behaviour is verified and replicated in all simulations done. This is a confirmation that our method is correct.

Now for the effect of deviations on Hubble constant, we start with observed redshift affected by our effect only. We report a biased higher Hubble constant with significant deviation. We then use observed redshift affected by Doppler and gravitational redshifts and we report a bias in Hubble constant and a higher mean value with significant standard deviation. Last, we use observed redshift influenced by all effects. We find the biggest mean between all cases and even higher standard deviation. We notice a similarity between

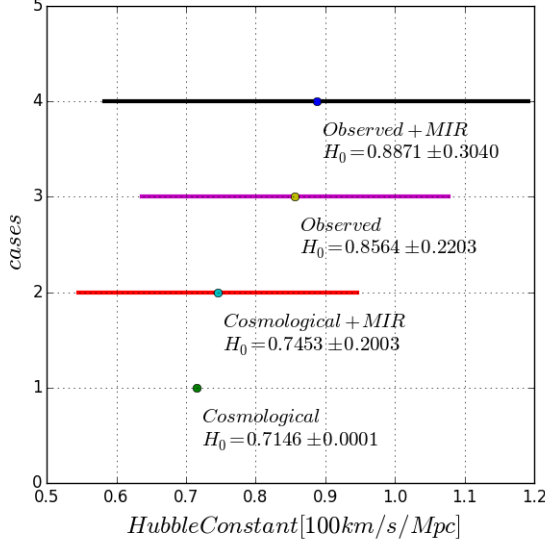


Figure 8.10: Hubble constant estimations of Sim.9 data for all cases of non cosmological redshifts effects bias.

Table 8.1: angular position, each redshift effect contribution and observed redshifts for important abnormal cases in Sim.9.

Halo Id.	$\theta$	$\phi$	$d_L$ ( $Mpc$ )	$z_C$ $\times 10^{-3}$	$z_D$ $\times 10^{-4}$	$z_G$ $\times 10^{-4}$	$z_{MIR}$	$z_{C+MIR}$ $\times 10^{-3}$	$z_{Obs}$ $\times 10^{-3}$	$z_{Obs+MIR}$ $\times 10^{-3}$
71	0.527	-2.59	16.07	3.83	1.43	9.18	$1.74 \times 10^{-5}$	3.84	4.89	4.91
139	0.520	-2.58	14.74	3.51	5.98	8.93	$4.98 \times 10^{-9}$	3.51	5.01	5.01
243	0.560	-2.49	15.45	3.68	1.61	10.00	$1.03 \times 10^{-7}$	3.68	4.85	4.85
169	0.558	-2.51	15.82	3.76	0.27	9.68	$1.03 \times 10^{-4}$	3.87	4.76	4.87
303	0.548	-2.50	15.88	3.78	-1.53	9.32	$1.84 \times 10^{-6}$	3.78	4.56	4.56

the second and third cases, at least in standard deviations and with close means. This is another reason in favour of the possibility of confusion between impacts of two effects, gravitational and our magnetically induced, on redshift data and parameters estimation. The combination of both effects produces obviously higher bias and deviation from real Hubble constant value. To better see differences of those cases estimation, we plot all cases in the same diagram (see Fig. 8.10).

### 8.3 Compact galaxy groups and galaxy-quasar associations : Synthetic equivalent examples

A particularly interesting configurations are found in all-sky map of sim.9 (see Fig. 8.11). These two configurations remind us of similar ones in real observations. This situation found in two cases reminds us of similar ones in real observations (see Fig. 8.12 and Fig. 8.13). The first is a combination of two haloes (galaxies) (71, 139) which are separated by small solid angle (we labelled those haloes by their position in our observed haloes list). These haloes are at different distances (16.07  $Mpc$ , 14.74  $Mpc$  respectively) which make one a background (71) and the other one a foreground (139). When analysing their corresponding redshifts compositions (see Table 8.1), we find that cosmological redshifts are normal and correspondent to the distance order. When we consider the contribution of Doppler and gravitational redshifts, we find that their contribution had produced an amplification making us believe that they are more distant from observer. The difference

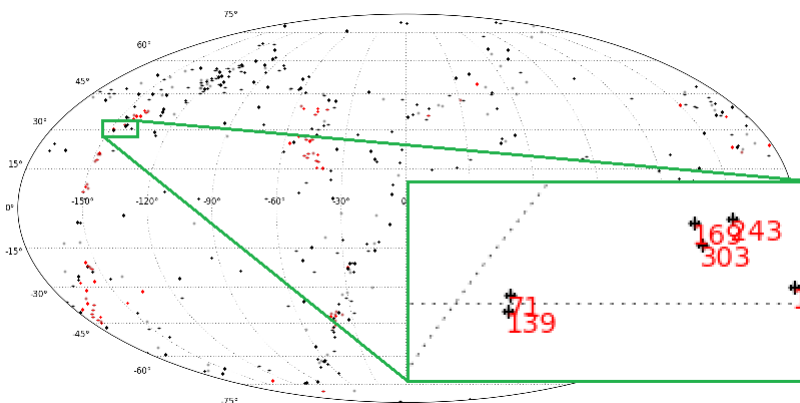


Figure 8.11: Special cases found in Sim.9 and their position in all-sky map with small angular separation.

between them is almost the same giving a close indication of the real distance between both galaxies. But, the magnetically induced redshift is imposing more amplification of the observed redshift of the background galaxy. When tracing the location of main contributions, we find the main one at a distance corresponding to the foreground galaxy. The reason is that light of the background galaxy travels from its source and have small amplifications occurring all along its way. Until it reaches the space around the foreground galaxy, it gets this large contribution (see Fig. 8.14). Even if the contributions of the rest of the way to observer in matter of our new redshift effect are small, the harm is done and the background galaxy is observed with higher redshift. The difference in redshift between the first and second galaxy is now not corresponding to their difference in distances to observer. In absence of distance indicators such as Cepheid stars or supernova type Ia, the observer would conclude wrongly that the background galaxy is as much distant from the foreground as the redshift difference. In cases with stronger magnetic fields within the foreground galaxy, the amplification from our effect is stronger and cause more discordance with the real distance difference. The first case of associations found Sim.9 reminds us of galaxy-galaxy or galaxy-quasar associations like the case of Seyfert galaxy NGC 7603 (see Ref. [6]). We may conclude that the two objects (galaxy and quasar) are really close. The abnormal redshift difference is only amplification from the foreground-background configuration similar to this first case in our synthetic Universe.

In the second case, we have 3 galaxies with small solid angles between them (243, 169, 303). Those galaxies are really close to each other as their distances from observer are around  $15 Mpc$  ( $15.45 Mpc$ ,  $15.82 Mpc$ ,  $15.88 Mpc$  respectively). When analysing their redshifts contributions (see Table 8.1), we observe that one of three (303, the third in the real distance order) has negative Doppler redshift contribution and the two others have positive values. This is indicating that they are moving toward each other and that they are interacting gravitationally with each other especially with their small distances between them. All galaxies have amplifications in their observed redshift from our new redshift effect which are not noticeable. But, the second one (169) has the biggest deviation from its cosmological redshift and it is noticeable. This is mainly caused by two reasons. The first is (169) which is the resulting halo of two haloes merging together and has strong magnetic fields around them given first high contribution from our redshift effect. The second reason is that its light travels near a second region of strong magnetic fields from the foreground galaxy (243) and another merging haloes (see Fig. 8.15) getting more amplification.

If we consider redshifts affected only by our effect, the halo (169) would appear to

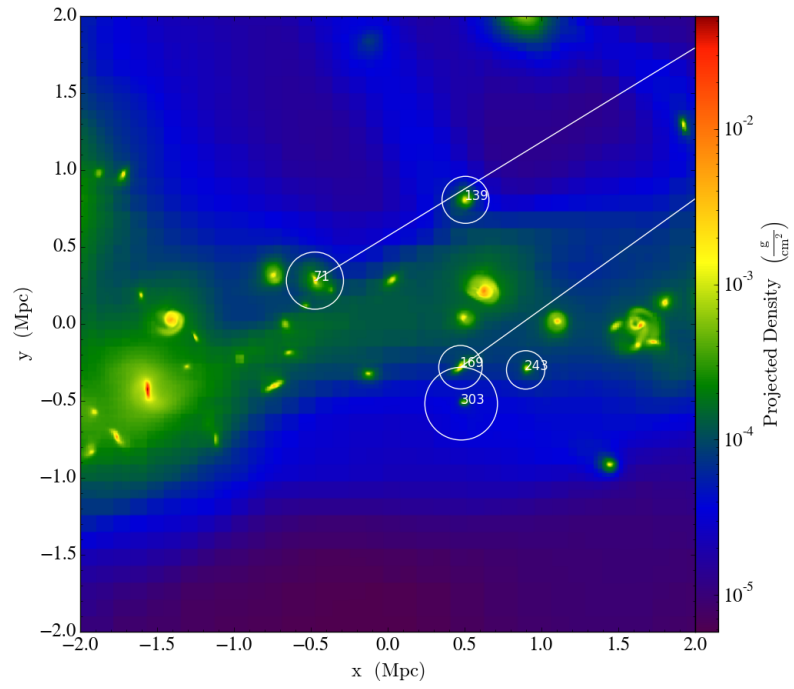


Figure 8.12: Density projection of Sim.9 annotated with the special cases positions and the light ray that will travels to observer.

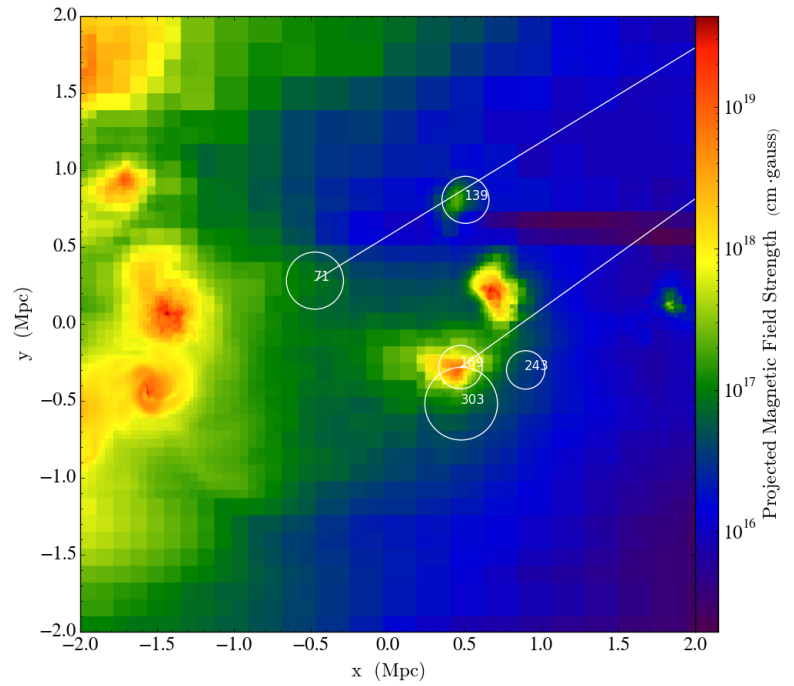


Figure 8.13: Magnetic fields projection of Sim.9 annotated with the special cases positions and the light ray that will travels to observer.

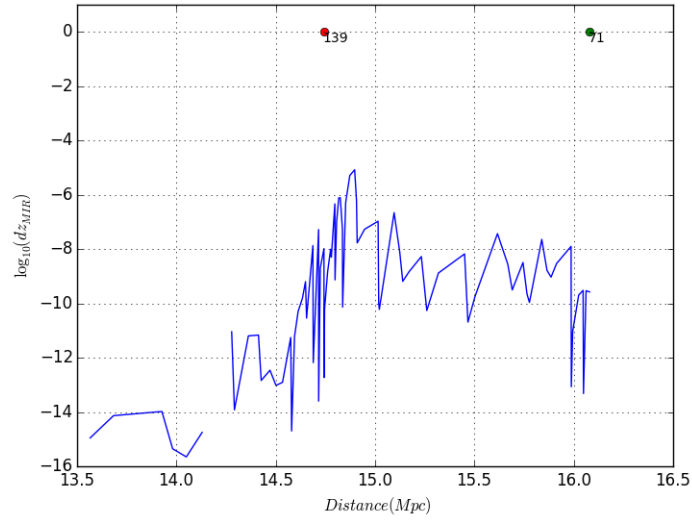


Figure 8.14: Our redshift effect elementary contributions for each simulation cell to the total redshift of the background galaxy 71 of Sim.9 plotted vs. distance to observer and annotated with positions of both galaxies positions.

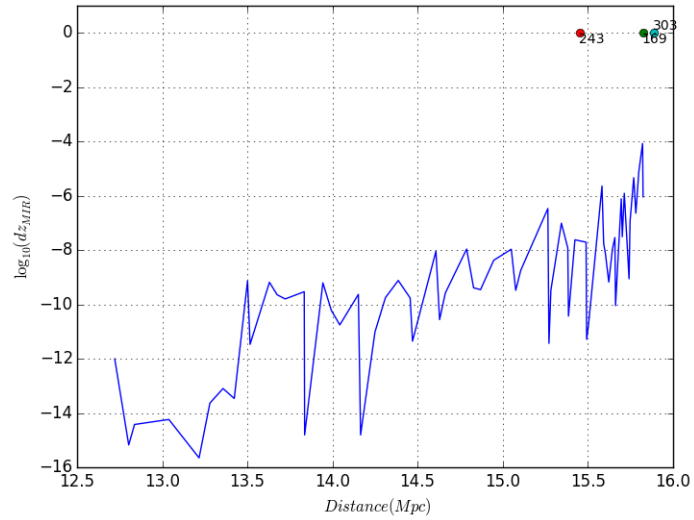


Figure 8.15: Our redshift effect elementary contributions for each simulation cell to the total redshift of the galaxy 169 of Sim.9 plotted vs. distance to observer and annotated with positions of all galaxies positions.

be the farthest one contradicting the real distance order. Moreover and if we consider redshifts affected only by Doppler and gravitational redshifts, the order is completely reversed: the closest (243) would appear to be the farthest and (303) would appear to be the closest. When we add our effect contribution, the order is again affected. All this distance order confusion is caused by conventional redshifts contributions and our effects adds more. If we don't have reliable distance indicators for an observed interacting cluster of galaxies, we are bounded to take redshifts as indicators of distances order and differences. The picture drawn from redshifts only could be completely biased as we illustrated here.

This case reminds us of the famous Stephen's Quintet (see Refs. [9]; [344]; [345]; [346]; [347] and [348]). The case described above has to change our perspective about Stephen's Quintet current and past configuration. Possibly the galaxy NCG 7320 is closer to the rest of the cluster. The high redshift of the rest of the cluster is a result of their light travelling within magnetically active regions of the interacting galaxies and getting amplified by our redshift effect. This foreground-background configuration can be an explanation of such observed abnormal redshifts. But, this should be taken carefully and not apply it as the rule without further examination.

## 8.4 Impacts on Stephan's quintet models

We could present another perspective of the second case discussed in the previous section. When comparing cosmological redshifts, the differences between galaxies are small and indicating the differences in distances. When adding the Doppler effect contribution, the differences are now reflecting mainly the radial velocities that caused the Doppler effect. This is giving us a good indication of the kinematics of the compact group. Adding the gravitational redshift contribution, as in  $z_{Obs}$ , affects slightly our perception. When the significant contribution from our effect is added, as in  $z_{Obs+MIR}$ , the differences between observed redshifts are no more indicative of the group members' motion. Redshift differences due to cosmological expansion could be seen as difference in Hubble flow and interpreted as velocity differences. Along with Doppler contributions, they represent the peculiar motion of group members to each other. But, differences from gravitational and especially from our magnetically induced effects could not and should not be interpreted as velocities differences. An observer that measures  $z_{Obs+MIR}$  and estimate that gravitational contribution is insignificant and do not consider our redshift effect contribution have an overestimation of velocities differences and an incorrect perception of the group kinematics.

The famous quintet has new observational evidence on its formation history presented by Duc, Cuillandre and Renaud (2018) (see Ref. [349]). The new indications suggest an older formation with a contribution of NCG 7317 to the successive collisions of group members. These indications call for new models and numerical simulations to recreate the formation scenario. When trying to reproduce formation scenario of Stephan's Quintet (SQ), Renaud, Appleton and Xu (2010) (see Ref. [350] hereafter RAX10) searched to recreate observed morphological features and the kinematics of the group. Models search to well-reproduce the velocity patterns of the group members existing in previous observational studies (see also Refs. [9] and [351]). Those measures provide only radial velocities and it is not possible to know repartition of those velocities for a given galaxy for recession and proper motion. In models proposed by RAX10 (see also Refs. [352] and [353]), a common recessional velocity is assumed to main group members: NGC 7319, NGC 7320c, NGC 7318b and NGC 7318a. The velocity differences represent the geometrical offset along the line-of-sight and a proper motion. At the start of each numerical simulation of

the quintet, the main galaxy NCG 7319 is assumed to be in the centre of the simulation box with no velocity. Other members are given different positions and velocities to reproduce, at the end of the simulation, the relative velocities of the galaxies. These velocities' estimations are actually measurements of redshifts interpreted as a combination of cosmological and Doppler redshifts. Then, the cosmological part of the redshift corresponds to recession motion and Doppler contribution corresponds to the peculiar motion. But, this interpretation is incorrectly neglecting gravitational and do not consider our magnetically induced redshift contributions.

But, we should consider gravitational and our new effect and the case found in our simulation is supporting this proposal. Observed redshifts of SQ members have similar effects contributions to those of the simulated compact group. The close positions of the quintet members create high gravitational potential and then significant gravitational redshift contributions. The complexity of the quintet induces different gravitational contributions to each member. In the paper of Nikiel-Wroczyński et al. (2013) (see Ref. [354]), they presented estimations quintet's magnetic fields from radio observations. Their observations had shown significant magnetic fields of  $6.4 \pm 1.1 \mu G$  as mean strength in the group area. This is supporting a significant contribution of our magnetically induced effect in observed redshifts of quintet's members. These fields are also shown to have different strengths and configuration over the quintet and could reach the strength of  $11.0 \pm 2.2 \mu G$  between NGC 7318a and NGC 7319. The differences in magnetic fields in quintet regions suggest different contributions from our redshift effect. Then, the observed redshift differences of SQ members are the result of several differences of all contributing effects. And similar to our simulated compact group, it could not reflect the exact radial velocity differences. This fact should be considered with the recent observation indications in the revisited SQ models.

The velocities of each member represent important parameters to recreate the interaction process. Our misinterpretation of redshift measurements of SQ members is creating incorrect estimation of velocities. Along with common cosmological redshift and Doppler effect contribution, these redshifts include the gravitational and magnetically induced effect contributions but are not considered by previous studies. These velocities are overestimated if the member is moving away from us and underestimated if it moves towards us. This is from the fact that our effect is biasing redshift always to higher values. Depending on the relative velocities of the galaxies, the final merger would involve all or only part of the members and could occur in more than a Hubble time. Until now, different studies suggested that the compact group has recent formation. Then, high velocities were needed to explain several morphological features creation. For instance, it was believed that the velocity of NCG 7318b should be high to separate it from the rest of the group in a small amount of time. Also, the perturbation effects of NCG 7318b is reduced due its high velocity and the short time of their interaction.

The evidence of an older SQ changes our understanding of the group formation scenario and questions members' believed high velocities. It could be an indirect evidence of our overestimation of these velocities affecting deeply our perception and creation of models. The role of NCG 7317 in the group history can be misinterpreted. A collision between this galaxy and NCG 7318b is already excluded by Duc, Cuillandre and Renaud (2018) (see Ref. [349]) because of the believed high radial velocity of NCG 7318b. The new observational evidence with our results should be the ground for future studies aiming to create formation scenarios. Our suggestion is that they recreate the redshift patterns of different group members and regions. This step will make the new models much accurate and reflecting the reality of the compact group present and historical evolution (see Ref. [295]).

## 8.5 Chapter conclusions

This first simulation has indicated a possible confusion of our effect contribution with other effects. All those contributions affect our perception of observations and Hubble constant estimations. The existence of abnormal cases in our synthetic data is used to explain similar cases in real observations. Other abnormal cases could exist in real Universe without being identified as so. All haloes in our simulations are identified and their distances and redshifts are calculated from the full data that we have from simulations datasets. Distances are exactly computed and redshifts are determined from the contributions of principal redshift effects: cosmological, Doppler, gravitational and the new magnetically induced effect which is not possible now for all observed galaxies. And to identify an extreme case, we need to know its redshift and distance with precision and see how far it is from the expected redshift-distance curve predicted theoretically. Distances to billions of galaxies are major labyrinth in our study of our observable Universe especially that supernovae are not observed in all galaxies. Even redshifts of those galaxies are not all easy to identify with spectroscopic method where we identify emission lines and estimate their shift from known wavelengths at rest. Photometric methods are used to estimate redshifts of some galaxies observed (e.g. Refs. [355] and [356]). This is making the identification of such cases a difficult task especially in absence of distance estimations. The cases such as galaxy-quasar association or Stephen's quintet are considered as abnormal because of physical connections which contradict the redshift differences. Some extreme deviations from redshift-distance relation could be present without been identified as deviations from the absence of parts of this relation; distance essentially or redshift or both. The analysis of further simulations is crucial to confirm these results and indicate possible new ones.

# Chapter 9

## Discussions

Several simulations sets (see Table 9.1 and Table 9.2) are done to study magnetic fields (see Table 9.3) and resulting redshifts from our new effect. Most of results described in the previous chapter are replicated. This information would help us to understand the synthetic observations data. Those data are presented in several forms to get full understanding of their content. Those methods of representation are described in the previous chapter with Sim.9 data.

### 9.1 Results confirmed by other simulations

Simulation sets have several common configurations described in a previous chapter. Other simulation parameters are changed like simulation box size, initial grid size, initial magnetic fields seeds, seeds methods and feedbacks to estimate impacts on the synthetic observations created. The first changes impacting observations are the random seeds. They create the initial densities distributions which result in the present time configuration of the simulated part of the Universe. This is represented by a parameter given to (`inits.exe`) code. When the synthetic observation is created at the end of the study, we get the list of observed halos projected in all-sky map as seen from the studied observer position. We presented these maps for the configurations used where all observed halos are plotted without any cut in the data (see Fig. 9.1, Fig. 9.2, Fig. 9.3 and Fig. 9.4).

As a general conclusion from all simulations done, stronger present time magnetic fields are related to high initial seed at the start of the simulation or a reset seed in closer time. The bias in Hubble constant is very variable from a simulation to another depending on the strength of the present time magnetic fields. Redshift deviations are observed also in more shifted points from the linear pattern in redshift - distances plots. We notice in overall changes between those plots in the number of halos represented. This is related to the resolution of the different simulations as better resolutions produces more stars by refinements and then more halos to be observed as we limited synthetic observations only for halos with stars. Another reason is the cut we do in our data, as explained before all halos exceeding 0.01 are then removed from distance-redshift plots and then from Hubble constant estimations. Another characterization of those plots is the existence in most of them of a bump representing a cluster of galaxies. Those galaxies are bounded gravitationally and then the gravitational redshift creates amplification in the observed redshift for both cases affected by our effect or not. The most important changes are in the deviations from our effect. For simulations with strong magnetic fields, our effect contributions are higher making the confusion on the observed redshift origin even more possible. We notice large differences from a simulation to another : from ones where it barely deviate one or two halos noticeably like in Sim.13 (see Fig. 9.5) or Sim.12 (see Fig.

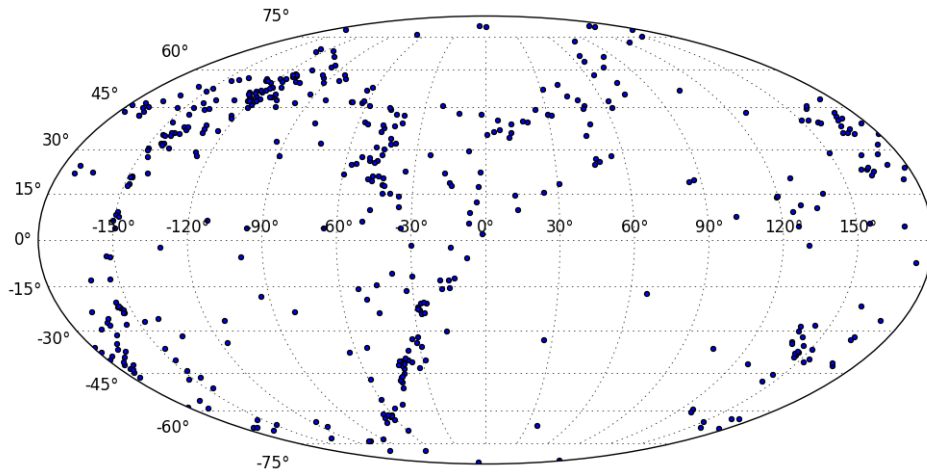


Figure 9.1: All-sky map for all observed halos of Sim.9.

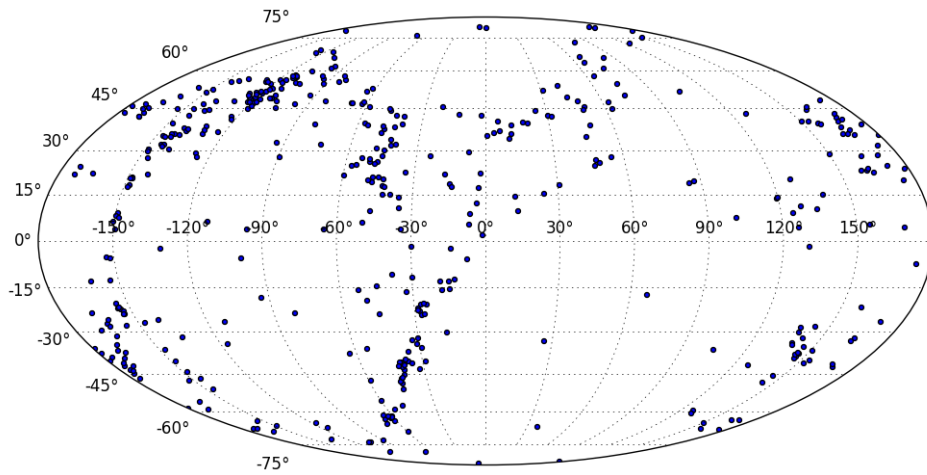


Figure 9.2: All-sky map for all observed halos of Sim.10.

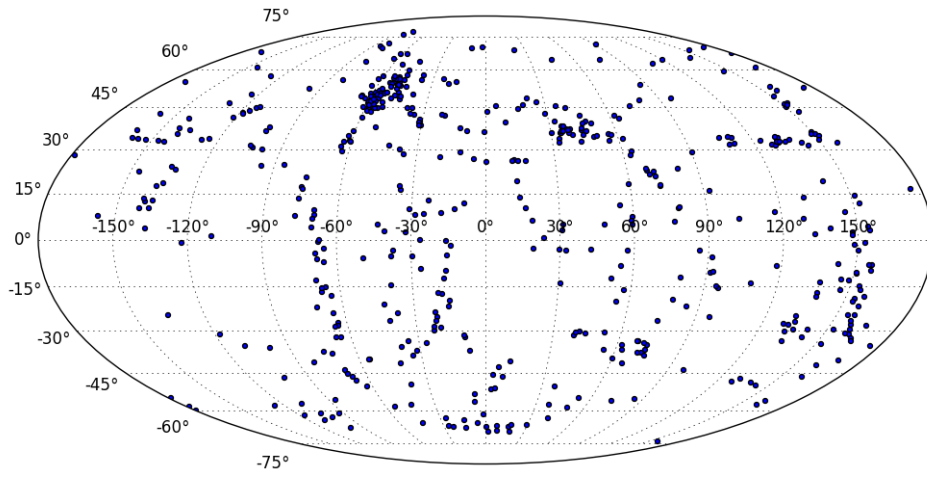


Figure 9.3: All-sky map for all observed halos of Sim.17.

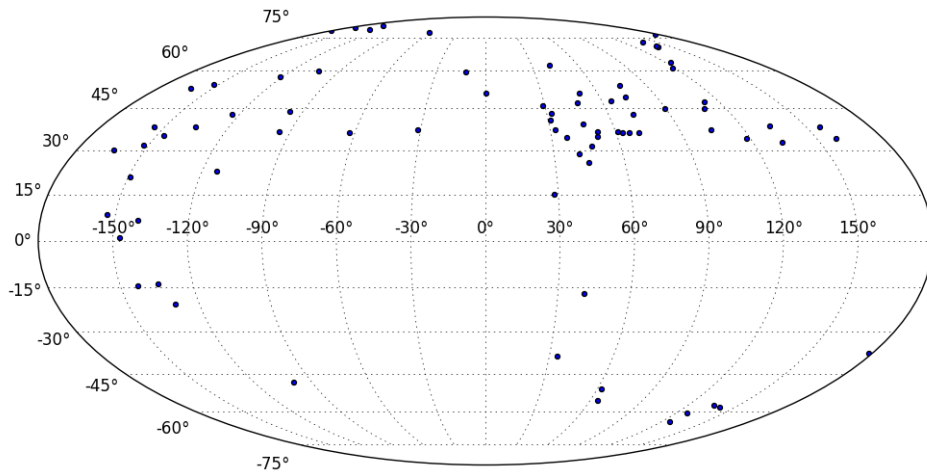


Figure 9.4: All-sky map for all observed halos of Sim.8.1.

Table 9.1: Mainly changed parameters in `inits.exe` parameter files of the simulations done. The parameters presented are: Parameter 1: `CosmologyComovingBoxSize`, Parameter 2: `PowerSpectrumRandomSeed` and Parameter 3: `GridDims - ParticleDims`.

Sim.	Parameter 1	Parameter 2	Parameter 3
2	20.0	-123456789	64
4	20.0	-123456789	64
5	20.0	-123456789	64
6	20.0	-123456789	64
9	20.0	-12345931	128
10	20.0	-123456789	128
12	20.0	-123456789	128
13	40.0	-123456789	128
14	20.0	-12345931	128
15	80.0	-123456789	128
16	160.0	-123456789	128
17	20.0	-987654321	128
18	20.0	-987654321	128
8.1	20.0	-10989041	64
8.5	20.0	-10989041	64
8.2	20.0	-10989041	64

Table 9.2: Mainly changed parameters in ENZO parameter files of the simulations done. The parameters presented are: Par. 1 : Normal/Restart, Par. 2 : TopGridDimensions, Par. 3 : `CosmologySimulationInitialUniformBField`, Par. 4 : `CosmologyComovingBoxSize`, Par. 5 : `ResetMagneticField`, Par. 6 : `ResetMagneticFieldAmplitude`, Par. 7 : Refinement, Par. 8 : `StarMakerTypeIaSNe` and par. 10 : `UseSupernovaSeedFieldSourceTerms`.

Sim.	Par. 1	Par. 2	Par. 3	Par. 4	Par. 5	Par. 6	Par. 7	Par. 8	Par. 9
2	N	64	2e-12	20.0	0	-	7	0	0
4	N	64	2e-15	20.0	0	-	6	0	0
5	N	64	2e-18	20.0	0	-	6	0	0
6	N	64	2e-21	20.0	0	-	6	0	0
9	N	128	2e-24	20.0	0	-	5	0	0
10	R (7)	128	-	20.0	1 (R17)	1e-9	5	0	0
12	R (7)	128	-	20.0	1 (R17)	1e-21	5	0	0
13	N	128	2e-21	40.0	0	-	5	0	0
14	R (9)	128	-	20.0	1 (R17)	1e-21	5	0	0
15	N	128	2e-21	80.0	0	-	5	0	0
16	N	128	2e-9	160.0	0	-	5	0	0
17	N	128	2e-21	20.0	0	-	5	0	0
18	R (17)	128	-	20.0	1 (R17)	1e-21	5	0	0
8.1	N	64	2e-24	20.0	0	-	5	0	0
8.5	N	64	2e-24	20.0	0	-	5	1	1
8.2	N	64	2e-24	20.0	0	-	5	1	0

Table 9.3: Magnetic fields outcomes (minimum, mean and maximum) of the simulations done represented by present day values all across the simulation boxes.

Sim.	Min.	Mean	Max.
2	1.088222e-16	4.333095e-06	6.106908e-03
4	1.312223e-19	5.935497e-06	3.886033e-03
5	1.302587e-22	1.657222e-06	2.644793e-03
6	1.302438e-25	6.289783e-07	2.214052e-03
9	1.019211e-28	1.360387e-06	1.404779e-03
10	8.119096e-132	1.325397e-07	5.372270e-04
12	0.000000e+00	2.586789e-08	5.421085e-04
13	4.593902e-26	1.559590e-07	1.055194e-03
14	9.446154e-22	2.599095e-08	5.467025e-04
15	1.522469e-25	8.154263e-22	5.777177e-19
16	8.418657e-14	3.295207e-10	7.756278e-08
17	1.182700e-25	2.681904e-06	2.744517e-03
18	2.100090e-21	6.896036e-09	5.590980e-05
8.1	2.077278e-28	1.669810e-08	6.008823e-05
8.5	2.159388e-28	5.330137e-19	3.763127e-16
8.2	9.883995e-29	3.353879e-15	1.058788e-11

9.6) or Sim.18 (see Fig. 9.7) to others where it has bigger and more deviations like in Sim.10 (see Fig. 9.8) or Sim.17 (see Fig. 9.9). When we compare present time magnetic fields contents of those two simulations, we find that stronger mean and maximum fields are related to the higher contributions of our redshift effect in the latter simulations with more deviations.

To better evaluate the difference of each redshift effect contribution from different simulations, we then plotted the histograms as explained for Sim.9. For Doppler and gravitational redshifts, the ranges ( $10^{-4}$  to  $10^{-3}$ ) are the most probable for those effects contributions. The difference from a simulation to another is which effect have the dominant contribution. Our redshift contributions fill higher classes in histograms near or even greater than Doppler and Gravitational redshifts contributions. For our effect, those simulations with weaker magnetic fields have very weak contributions for most halos and its contribution is dominated by conventional redshift contributions. For example, Sim.18 (see Fig. 9.10) have our effect contribution mainly for all halos in very weak ranges less than  $10^{-6}$  and very few in ranges where it could be confused to Doppler or gravitational effects. Other simulations with stronger magnetic fields have different distribution for our effect contribution. Simulations like Sim.13 (see Fig. 9.11) or Sim.17 (see Fig. 9.12) have halos with magnetically induced redshift in all ranges even in higher ones. In an interesting case, our redshift effect created an extreme contribution where observed redshifts are amplified to very high redshifts even to  $10^{+7}$  in one halo of Sim.17. Another important case is Sim.10 (see Fig. 9.13) where our effect almost mimics the distribution of Doppler and gravitational effects contributions making the confusion between contributions origins even more possible. They make the confusion between our effect contribution and gravitational redshift even more possible as confirmed by all-sky maps and histograms.

Talking about confusion and in our discussion on Sim.9, we describe the confusion between clusters members and halos with redshifts deviated by our effect and not by the gravitational potential well of the cluster. Those cases are represented with all sky maps filtered with different redshifts contributions mainly gravitational higher than  $10^{-3}$  and our effect higher than  $10^{-4}$ . Those maps presented re-affirm this possibility. Form the

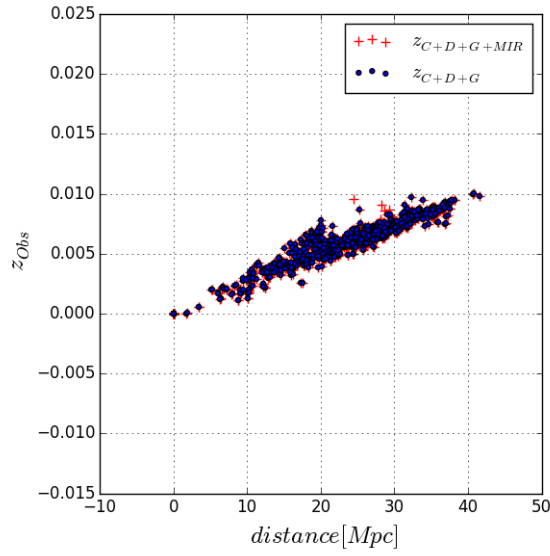


Figure 9.5: Both observed redshifts vs. distances of observed halos of Sim.13.

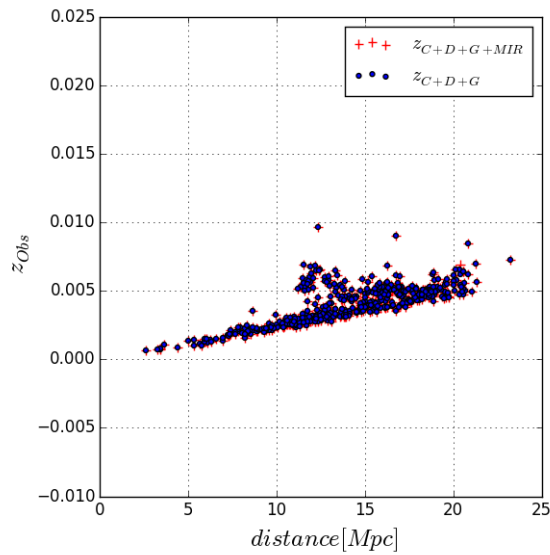


Figure 9.6: Both observed redshifts vs. distances of observed halos of Sim.12.

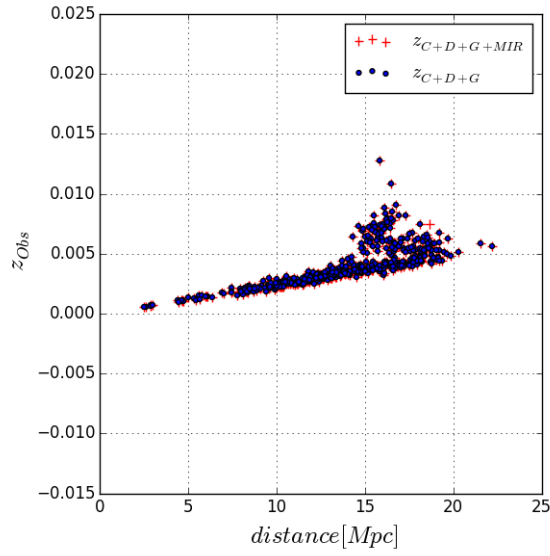


Figure 9.7: Both observed redshifts vs. distances of observed halos of Sim.18.

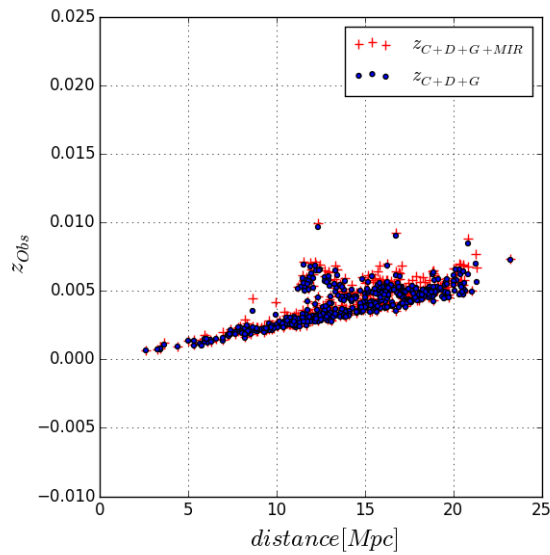


Figure 9.8: Both observed redshifts vs. distances of observed halos of Sim.10.

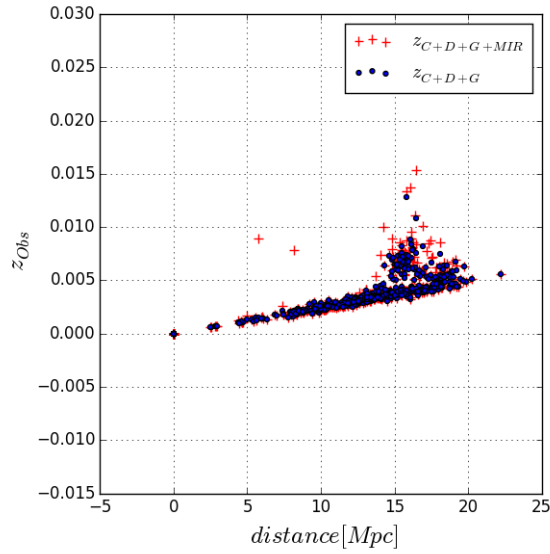


Figure 9.9: Both observed redshifts vs. distances of observed halos of Sim.17.

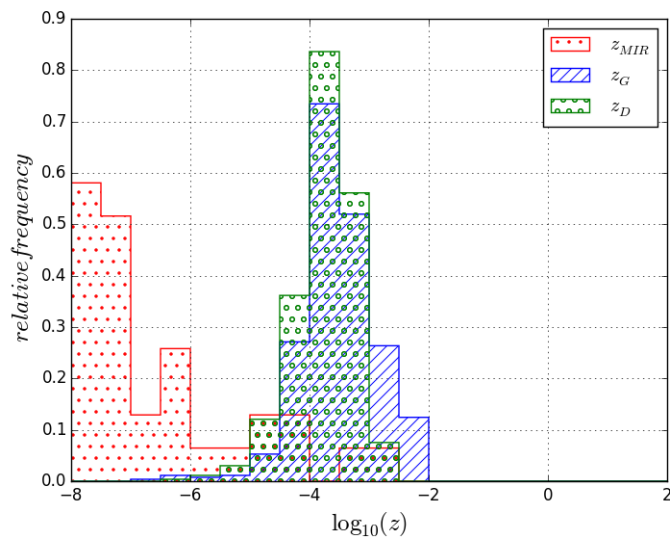


Figure 9.10: Histograms of different effects contributions of Sim.18 observed halos.

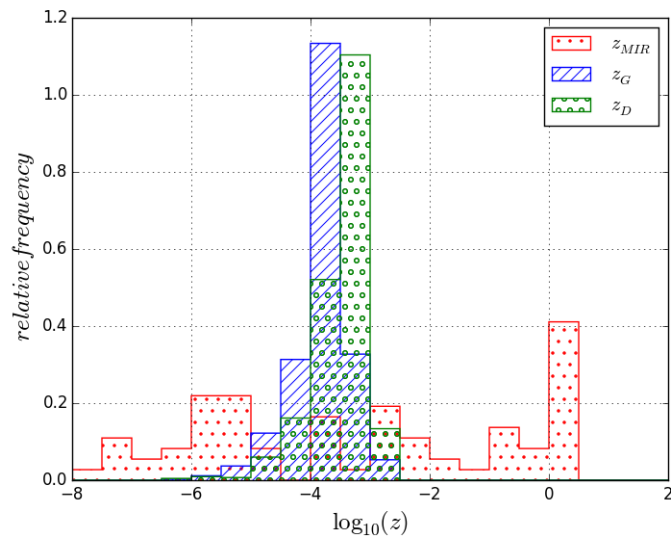


Figure 9.11: Histograms of different effects contributions of Sim.13 observed halos.

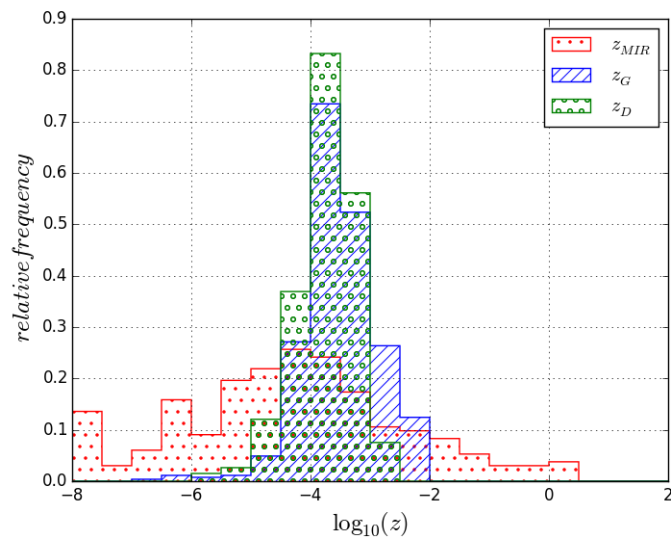


Figure 9.12: Histograms of different effects contributions of Sim.17 observed halos.

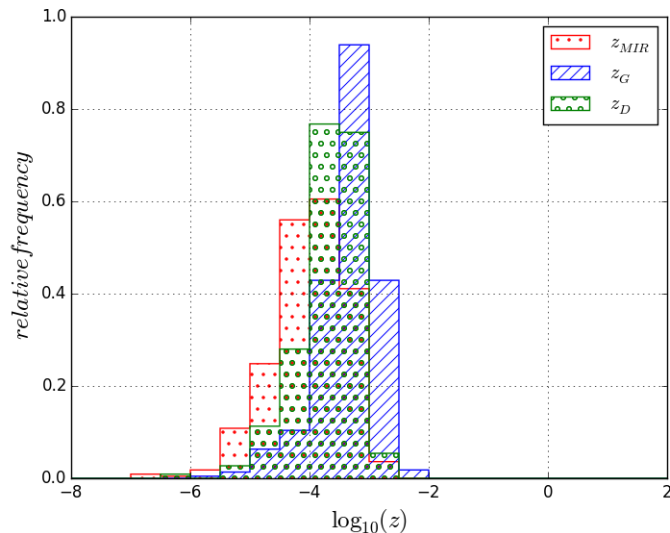


Figure 9.13: Histograms of different effects contributions of Sim.10 observed halos.

few found in Sim.13 (see Fig. 9.14) to more in Sim.17 (see Fig. 9.15) to large number in Sim.10 (see Fig. 9.16), all show constellations of galaxies with high contributions from our redshift effect and other close to each others from gravitational and our effect redshifts. This is giving stronger argument for cluster member's confusion or cluster not really bounded gravitationally or at least that the gravitational bound is over estimated.

All those representations lead to the main study goal which is to estimate impacts of those effects on cosmological parameters extracted from data. As we explained before, the only possible parameter estimated is Hubble constant. We plot for those simulations presented the Hubble constant estimations computed in the same way as Sim.9. We notice that Hubble constant from redshifts deviated from our effect has very variable bias: from slight deviation like in Sim.12 (see Fig. 9.17) and Sim.18 (see Fig. 9.18) to higher means and even higher standard deviations of Sim.10 (see Fig. 9.19), Sim.13 (see Fig. 9.20) and Sim.17 (see Fig. 9.21). In the first two cases, it is very close to cosmological estimation and the real value. But for the last three cases, it is almost the same as the deviations from Doppler and gravitational deviated redshifts making more possibility of confusion between them, if not for all haloes for some of them. For Hubble constant estimations, our redshift effect induces biased results in higher means and deviations compared to the real Hubble constant implemented in the simulation. Those results are very variable from a simulation to another depending on the strength of present time magnetic fields.

## 9.2 Magnetic field evolution with feedback models

We used time data dumps to study and follow magnetic fields evolutions within our simulations. Those datasets are recorded in equal time steps of  $0.22 \text{ Gyr}$ . For each dataset, we check key fields like : density, temperature, gravitational potential, star particles number and of course magnetic fields strength. For each of those fields, we compute 3 main indicators : maximum and minimum recorded across all dataset and the mean of the field weighted with cell mass. We then plot results versus time expressed in  $(\text{Gyr})$ . For magnetic field strength, we plot the decimal logarithm of the field strength expressed in  $(\text{Gauss})$ . In those plots, the evolution of the same indicator is represented for several configurations to compare differences. The different configurations compared in the case of magnetic fields are : initial seed field values, resolution and feedback settings. As a

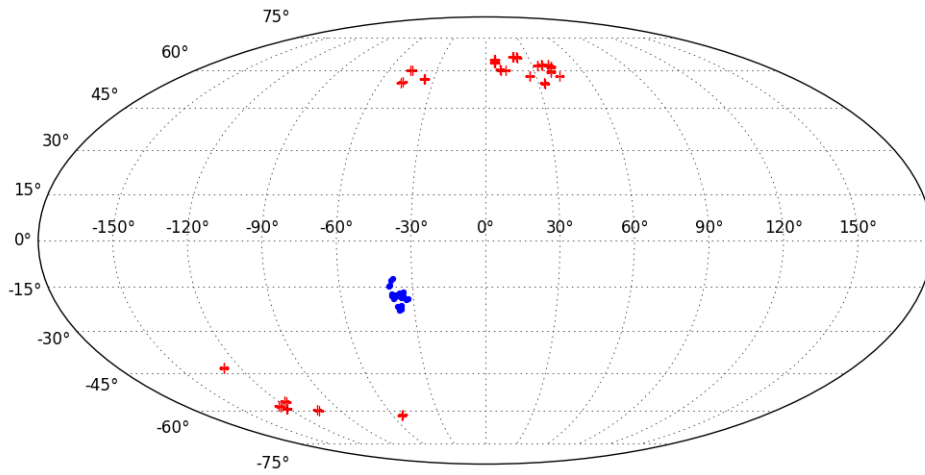


Figure 9.14: All-sky map of Sim.13 haloes filtered by MIR and gravitational redshifts contributions.

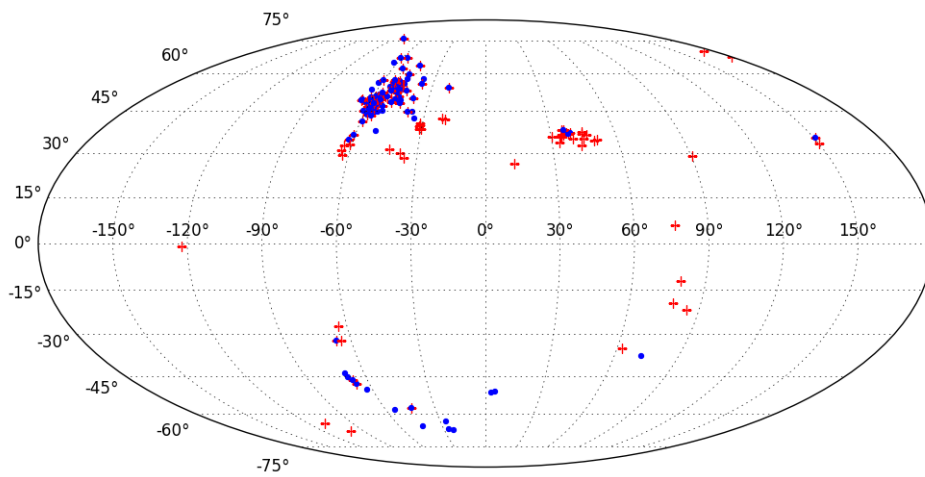


Figure 9.15: All-sky map of Sim.17 haloes filtered by MIR and gravitational redshifts contributions.

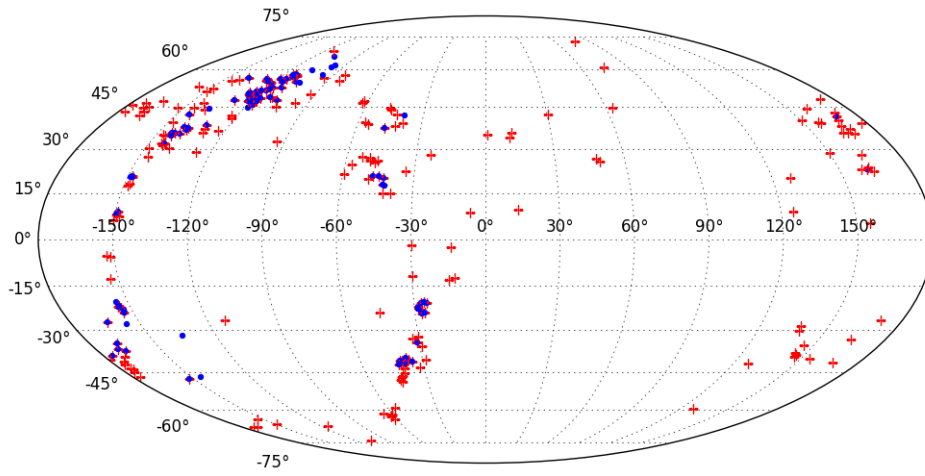


Figure 9.16: All-sky map of Sim.10 haloes filtered by MIR and gravitational redshifts contributions.

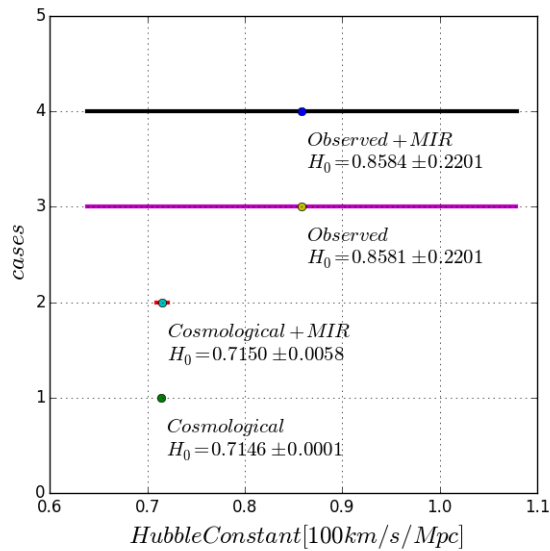


Figure 9.17: Hubble constant estimations of all deviations cases of Sim.12 data.

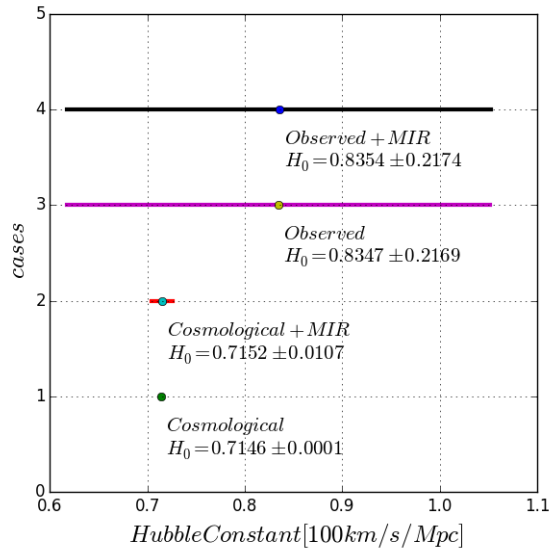


Figure 9.18: Hubble constant estimations of all deviations cases of Sim.18 data.

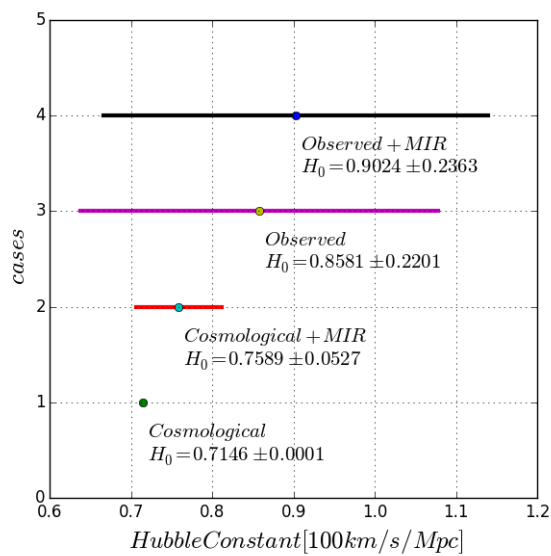


Figure 9.19: Hubble constant estimations of all deviations cases of Sim.10 data.

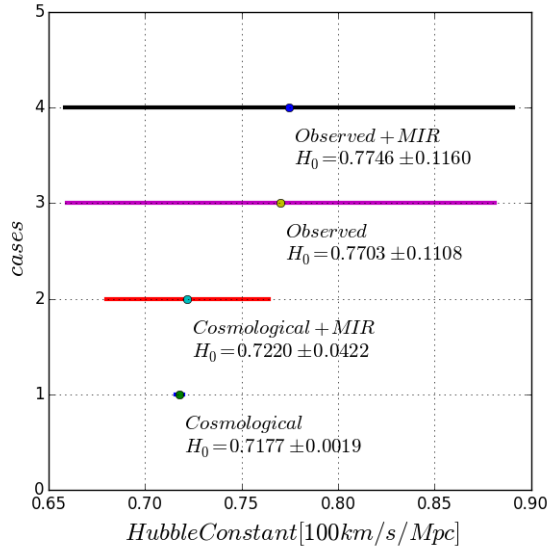


Figure 9.20: Hubble constant estimations of all deviations cases of Sim.13 data.

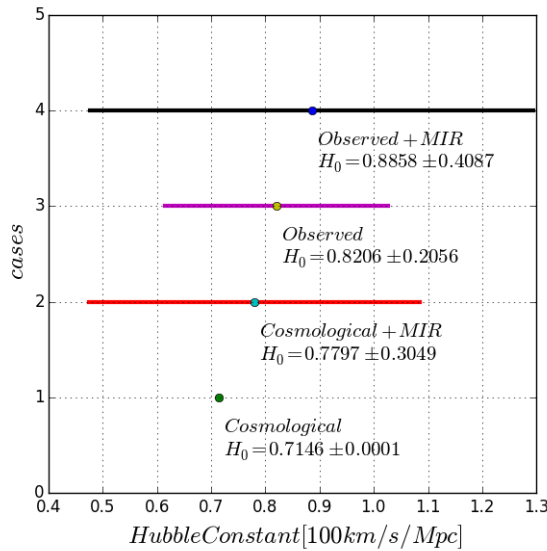


Figure 9.21: Hubble constant estimations of all deviations cases of Sim.17 data.

Table 9.4: Maximum and minimum cell side sizes (kpc/h) of the simulations done computed from box sizes, initial grid size and max levels of refinement.

Sim.	Min.	Max.
2	2.44	312.5
4	4.88	312.5
5	4.88	312.5
6	4.88	312.5
9	4.88	156.25
10	4.88	156.25
12	4.88	156.25
13	9.76	312.5
14	4.88	156.25
15	19.53	625
16	39.06	1250
17	4.88	156.25
18	4.88	156.25
8.1	9.76	312.5
8.5	9.76	312.5
8.2	9.76	312.5

general behaviour, the maximum strength of magnetic fields recover from a slice drop from initial seed value and continue until it reaches a maximum level where it stays until the present time. This stagnation of the maximum magnetic field is mainly around  $4 Gyr$  of the Universe age. The first set of configuration changes is initial magnetic seed. This behaviour is observed in the maximum (see Fig. 9.22) and mean (see Fig. 9.23) magnetic fields evolution. The minimum magnetic field of those cases (see Fig. 9.24) with different initial seed have a different behaviour. They are with the same difference of magnitude in their drop to lower and weaker magnetic fields.

The second of configurations change is in resolution. The resolution in our simulations is determined by the initial grid size, the maximum levels of refinements and the number of simulated dark matter particles. We set in our simulation the number of dark matter particles to be equal to initial grid size. The size of the simulation box side and the initial grid size are fixing the resulting minimal and maximum resolution. By the resolution, we mean the cell side length. The maximum cell size is computed by dividing the simulation box side size on grid size. The refinement is done when the density in a cell exceeds a threshold. ENZO code divides this cell to smaller cells by a fixed factor (which in our case by factor 2 and then the cell is divided to 8 smaller cells). Five levels of refinement with 2 as a factor of division would divide each cell initially created to  $32^3$  smaller cells in case that the density continues growing. The level of refinements allowed is fixed to 5 in most simulations. This is making the minimum cell side size to be computed by dividing the maximum size by 32 for our set of simulations. We would compare for this point 4 simulations : 2 with simulation box side of  $20 Mpc$  with two others of  $40 Mpc$  and  $80 Mpc$ . The initial grid size is of 64 and 128. Those simulations are labelled by Sim.6, Sim.9, Sim.13 and Sim.15. The maximum and minimum cell sizes in those simulations are reported in Table 9.4. We fix initial magnetic seed to  $10^{-21}G$  in all those simulations to verify only the impact of resolution. The results of magnetic fields maximum (see Fig. 9.25) and mean (see Fig. 9.26) evolution show quantitatively the expected behaviour that the resolution of the simulation is affecting the magnetic fields outcomes. The minimum magnetic fields (see Fig. 9.27) are technically the same in all those simulations.

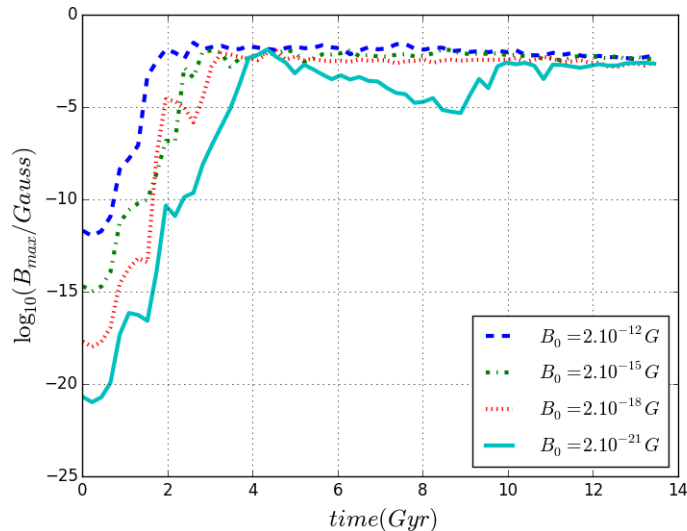


Figure 9.22: Maximum magnetic fields plotted vs. cosmic time for the first set of configurations changes of magnetic setting: initial values seeded.

The rise in magnetic field is related to the formation of denser regions, the formation of stars and the constellations of galaxies. The mean of magnetic fields are driven by the highest to maximum values of magnetic fields across simulation box. It has a similar behaviour to maximum fields even if the peak level reached is always lower 2 to 3 magnitude compared to level of the maximum magnetic fields. The minimum of magnetic fields has a similar behaviour in all configurations. It suffers a steady drop and loses 2 to 3 of the initial magnitude. The minimum magnetic fields are showing little informations. They are related to lower densities and they are not very differentiable for different configurations.

ENZO code has several star particle creation and feedback models implemented. It has also a feedback of thermal energy of supernovae type Ia and recently a new feedback of supernovae events is added : magnetic feedback (see Ref. [357]). The thermal feedback uses K. Nagamine's stellar feedback fitting formula (see Ref. [358]). We choose to test those feedback impacts on magnetic fields evolution. We have done basically 3 simulations : The first without any feedback of supernovae events (labelled Sim.8.1), the second with only thermal feedback (labelled Sim.8.2) and the last with both thermal and magnetic feedbacks (labelled Sim.8.5). The latter case has to be proceeded after changes in ENZO code which allows coupling of these two feedbacks. We have done light modifications to include the magnetic feedback of supernovae for the same supernovae events identified by the thermal feedback routines. Moreover, a slight error of units conversion between physical units and ENZO internal unit system is found and corrected in implemented functions by Butsky et al. (2017) (see Ref. [357]) for magnetic feedback of supernovae type Ia. Both feedbacks occurs separately but for the same cases and in the same positions. For the minimum of magnetic fields (see Fig. 9.28), they are barely different and have the same decaying behaviour. We notice a very important behaviour for the maximum (see Fig. 9.29) and the mean (see Fig. 9.30) of magnetic fields. The first simulation without any feedback has the strongest magnetic fields. The one with thermal feedback has lower maximum and mean magnetic fields. The last simulation with both feedbacks has even lower magnetic fields at the present time. We get those results even if all simulations had started with the same magnetic initial seed and had the same resolution (grid size - simulation box size - levels of refinement). The difference between the evolution patterns of the three is noticeable after 4 Gyr of the formation of the Universe. Before this

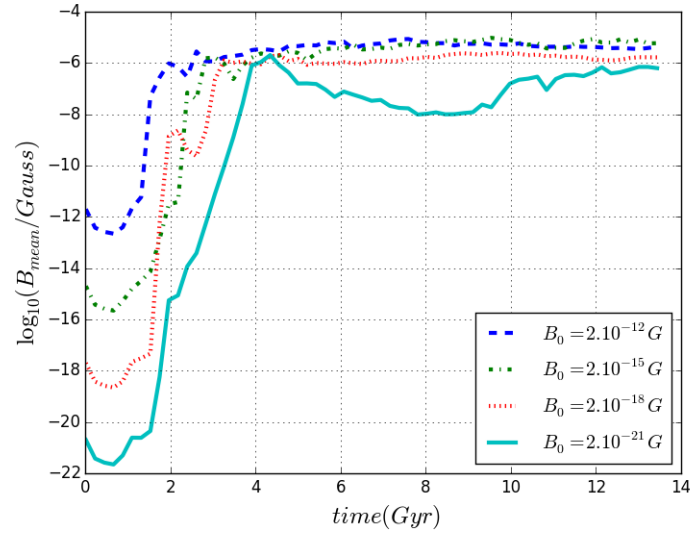


Figure 9.23: Mean magnetic fields plotted vs. cosmic time for the first set of configurations changes of magnetic setting: initial values seeded.

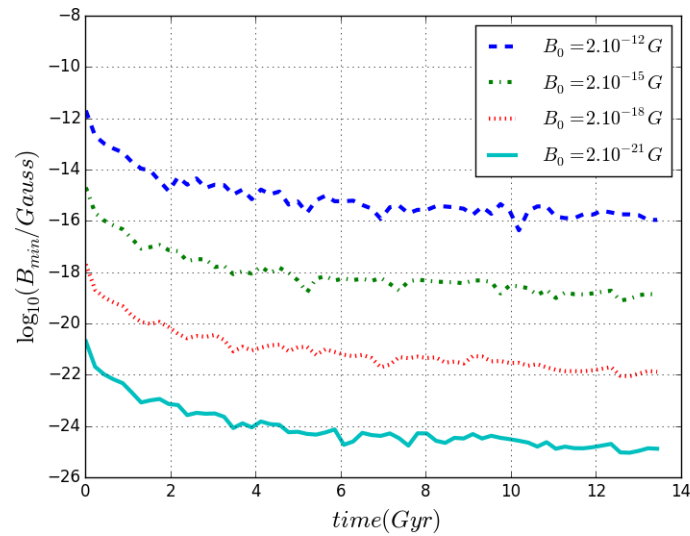


Figure 9.24: Minimum magnetic fields plotted vs. cosmic time for the first set of configurations changes of magnetic setting: initial values seeded.

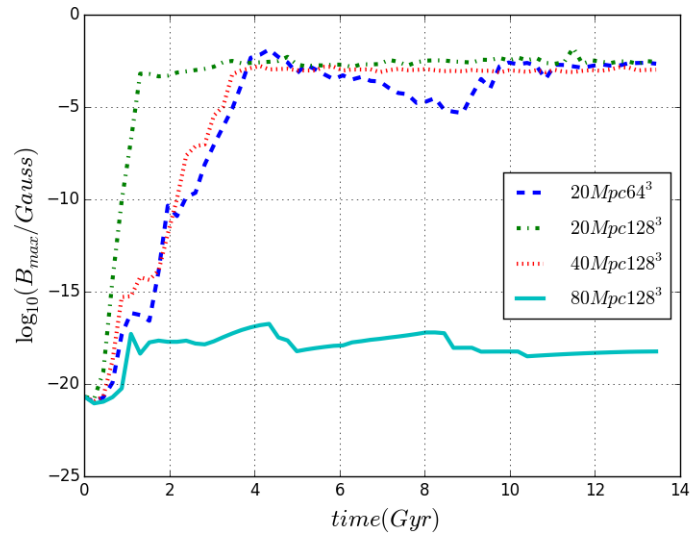


Figure 9.25: Maximum magnetic fields plotted vs. cosmic time for the second set of configurations changes of magnetic setting: simulation resolution.

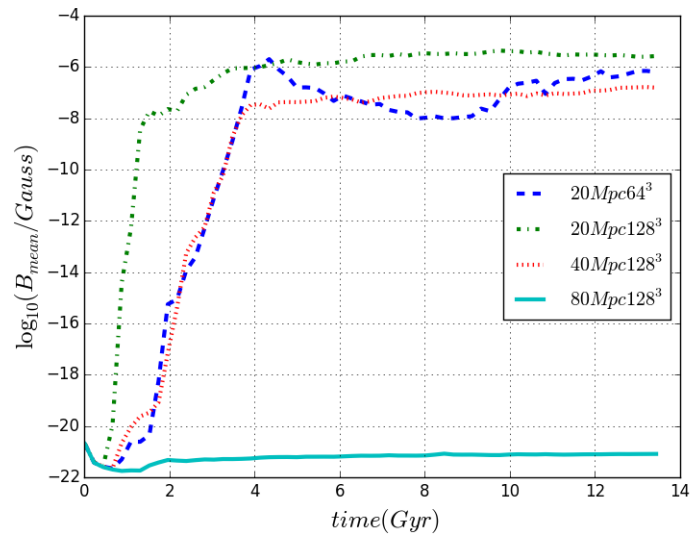


Figure 9.26: Mean magnetic fields plotted vs. cosmic time for the second set of configurations changes of magnetic setting: simulation resolution.

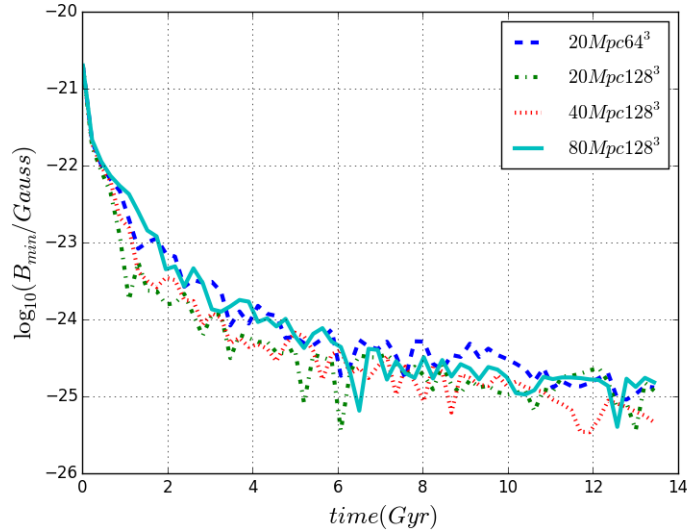


Figure 9.27: Minimum magnetic fields plotted vs. cosmic time for the second set of configurations changes of magnetic setting: simulation resolution.

time, densities are growing and star particles are forming. When supernovae explosions starts, feedbacks are triggered causing magnetic fields to be lower and lower to the present time. To see the cause of this lowering of magnetic fields, we check densities evolutions for those 3 simulations. The minimum densities of all simulations are not differentiable (see Fig. 9.31). We could see differences in maximum (see Fig. 9.32) and especially in mean (see Fig. 9.33) densities plots. We notice that densities are lower in simulations with feedbacks activated even with small differences. This is indicating that thermal and magnetic feedbacks are causing densities to be lower resulting in weaker magnetic fields. Supernovae are ejecting matter and energy making lower densities. The lower densities are not allowing amplification or maintain of high magnetic fields. The difference between the case without any feedback and with thermal feedback is several orders in magnitude. The same is true for the test magnetic feedback. This is indicating a very big importance of feedback models in the simulation of magnetic fields evolutions to recreate current state observations numerically.

### 9.3 Other magnetic field configurations tested

Several initial magnetic seed values are used in the start of each simulation. And despite of the large differences of magnitude, the difference in the present time is not so significant. This is observed in the maximum and mean magnetic fields evolution. Magnetic fields suffer from a drop after the start of our simulations to equilibrate with the densities and currents of charged elements like electrons, protons and others simulated species. The possible differences are small but still impact the evolution to our present day. The results of magnetic fields maximum and mean evolution show also quantitatively the expected behaviour which is that the simulation resolution is affecting the magnetic fields outcomes. Simulations with better resolution (smaller cell sizes) has stronger magnetic fields. Even if in some periods of the evolution, the difference isn't significant. This behaviour is present in all simulations especially in the case of the two simulations where the box size is the same and only grid size is higher.

A test method of magnetic fields resetting is tested. In this method, magnetic fields in certain redshift is reset across the simulation box by fixed new value for all cells in one

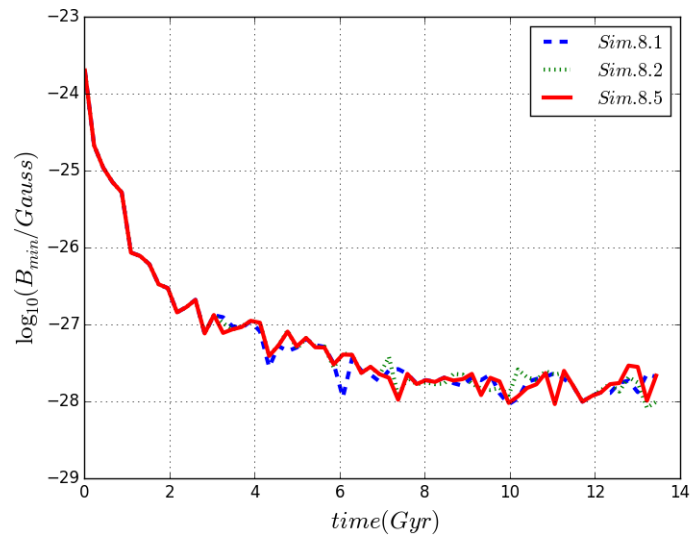


Figure 9.28: Minimum magnetic fields plotted vs. cosmic time for the last set of configurations changes of magnetic setting: feedbacks processes.

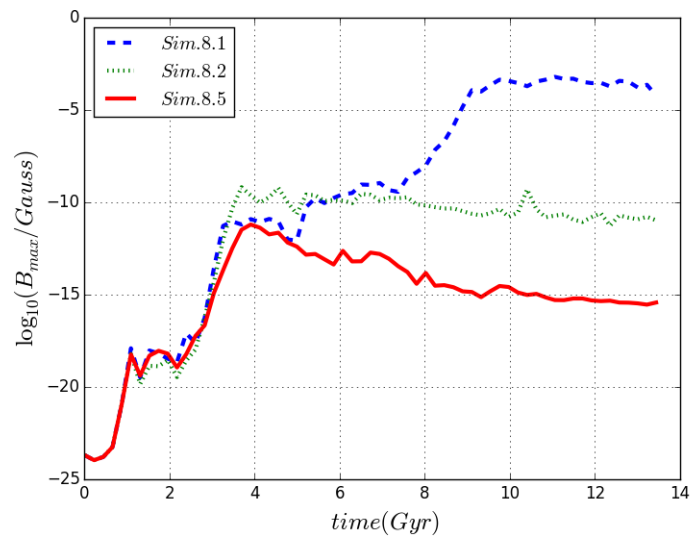


Figure 9.29: Maximum magnetic fields plotted vs. cosmic time for different feedback models.

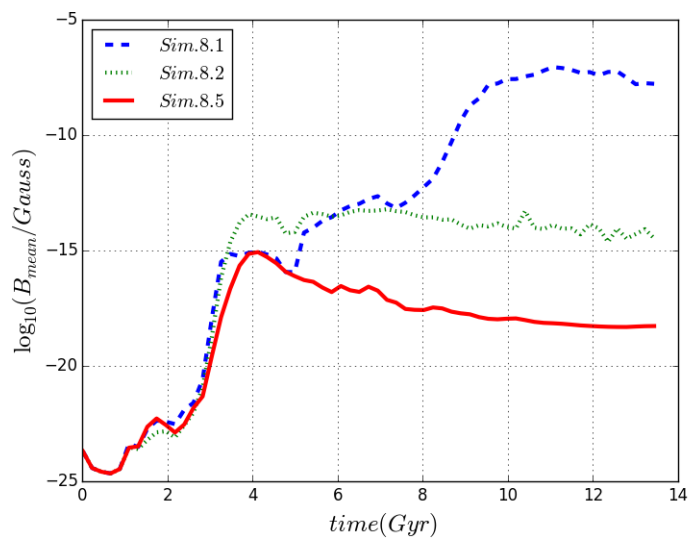


Figure 9.30: Mean magnetic fields plotted vs. cosmic time for different feedback models.

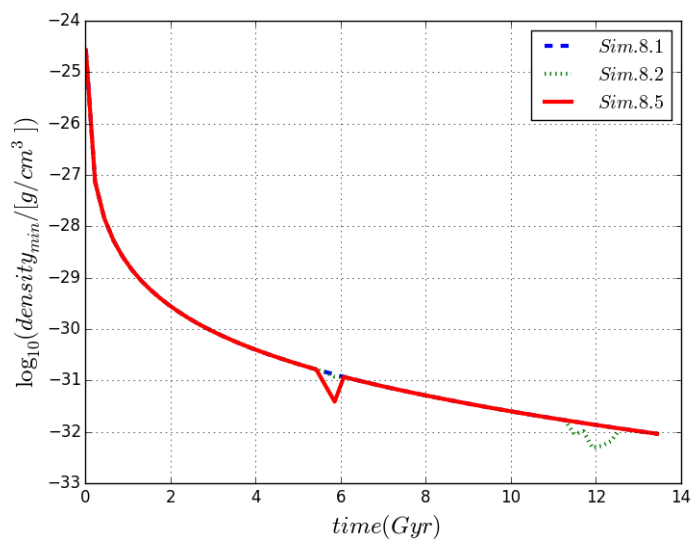


Figure 9.31: Minimum gas densities plotted vs. cosmic time for the last set of configurations changes of magnetic setting: feedbacks processes.

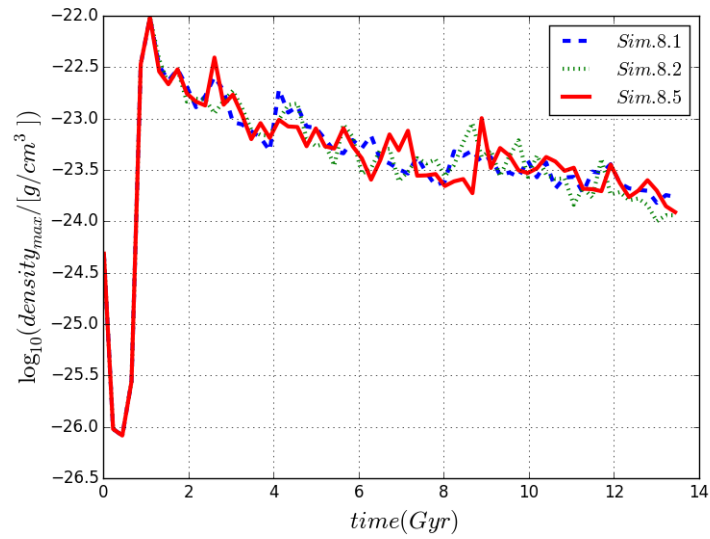


Figure 9.32: Maximum gas densities plotted vs. cosmic time for different feedback models.

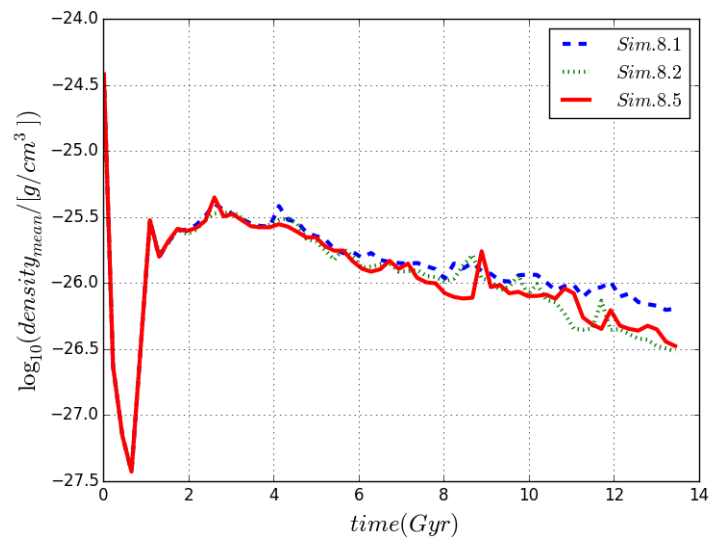


Figure 9.33: Mean gas densities plotted vs. cosmic time for different feedback models.

variation of this method and in another for only denser cells. This method is a test to see a possible impact of magnetic seed models on cosmological outcome. This method could mimic even with far resemblance the dynamo effect where magnetic fields are generated in local denser regions and spread across the Universe by turbulences of dynamo effect. Magnetic fields has a very big amplification in simulations done with a reset in only denser cells and in very close time to present time. Observations especially of our new redshift effect confirm this amplification. This is making a great ambiguity of the process responsible of the current magnetic fields observed : primordial seeds conserved and grown by turbulences or much new seed with great amplification all across the Universe.

The importance of the bias produced is related to CMF existing in the Universe. The history and the actual state of those magnetic fields are a multivariable problem. As shown in our simulations results, the same present state can be resulting from different past evolution paths. Different feedbacks effects can make two initially different magnetic fields configurations of the Universe to look the same at current time. All this is making the selection of initial magnetic fields and the real feedback processes shaping the Universe's state highly difficult. This is leaving a degeneracy of CMF patterns. When regarding the real Universe, the difficulty is bigger in the part of magnetic fields. As discussed above, the current observations on CMF is not able yet to : identify magnetic fields genesis processes, then its evolution and separate the contribution to our observations from galactic to extragalactic sources. Those estimations given must be taking with care. Those estimations are affected by our new redshift effect as described before, making it a self-referring problem. We need magnetic fields to eliminate this new effect contribution and get cosmological redshift. On the other hand, we need redshift in the estimation of magnetic fields.

## 9.4 Possible explanation of extra bias found in data

The previous sections' results are showing that our effect is responsible for an extra bias in Hubble constant when analysing weak redshift observations. Our data also show a higher gravitational redshift contributions than previously estimated. When considering both effects, we find higher Hubble constant estimations with larger deviations. To estimate all cosmological parameters, we need observations with higher redshifts as the case with supernovae data of joint light-curve analysis (JLA) sample data (see Ref. [359]) of the SNLS-SDSS collaborative. Higher redshifts represents longer distances travelled by photons. Those photons would suffer larger accumulation of our redshift effect contributions. If the impact of our effect on nearby galaxies observed redshifts is weak, the impact on more distant galaxies would be non negligible and on CMB photons even significant in the modest scenario. Our simulations results make it then possible that our effect is responsible for the unexplained bias estimated in results of Calcino and Davis (2017) (see Ref. [5]). They use new statistical methods to evaluate the redshift bias  $\Delta z$  by adding it as a nuisance parameter. This has allowed them to estimate the possible contribution of all effects' bias. The result is  $10^{-3}$  which is higher than the estimation of Wojtak, Davis and Wiis (2015) (see Ref. [271]) which is  $10^{-4}$  from gravitational redshifts. Their explanation is that possibly more contributions of gravitational redshifts or measurement errors were responsible of the difference of estimations. When analysing JLA data, the 740 SNIa have high redshift and relate to discussions on our redshift effect, we can say that this is possibly an indication or even evidence of new effect contribution which must not be blamed on measurement errors. The bias found could be from our effect only or with contribution of gravitational redshifts. Our effect could then present explanation to this yet unexplained bias.

To make the bridge from those synthetic Universes to the real ones, the Universe's real state that should be recreated is a maze. The evolution of the Universe and especially its magnetic fields are very important. Synthetic observations constructed would follow light travelling within several datasets representing billions of years of evolution. This evolution has its impact on the bias and deviations in observations. This is making the selection of the right evolution pattern highly significant and especially when larger simulations are done. The distances travelled by emitted photons are larger making the accumulations of the contribution of our redshift effect more significant, even if the impact on nearby galaxies is weak. This is creating the need for more simulations with all possible configurations : simulations with flat-open-or-closed Universes, several feedbacks effects and most importantly larger simulation boxes which allow for higher redshifts observations. The work to refine the observation contribution, to mimic better SNIa data must be done. The hope for confirmations from synthetic and real observations is higher and the possibility is real.

## 9.5 Extreme cases and supernovae data

After the discussion of extreme cases, a fair question would be where are such cases in observational data specially supernovae type Ia data? The extreme cases represent only a part of the data of each simulation done and are related to region in the cosmos with higher magnetic fields. These cases are rare in supernovae data due to feedbacks effects around the supernova. Our simulations data has proved that the thermal feedback creates weaker magnetic fields. Even the test magnetic feedback has created a similar effect. Then, galaxies hosting supernovae explosions should have magnetic fields around them less powerful than others resulting in lower contribution of our redshift effect. This makes the possibility of extreme case less and less. The situation that could produce an extreme amplification in redshift of a supernova is a background-foreground configuration. This is not a frequent situation but possible. Recently, a case of a supernova lensed to four images by a foreground galaxy is an example of this case (see Ref. [360]). Such cases will be challenging to decrypt. There is the lensing or dust absorptions and other effects altering data but still could have evidence supporting this possibility. A supernova explosion in background galaxy, for example, in Stephen's quintet would be interesting too. The difficult existence of extreme cases in supernova data is not making the contribution of our effect negligible. The magnetic fields around them are possibly weaker than needed to create very high redshift amplification, but still there is a contribution. Even with effects like supernovae feedbacks, the contribution of our redshift effect is present.

## 9.6 Implication on CMB studies

The impact of our redshift effect on CMB anisotropies is related to magnetic fields which the CMB photon has encountered from the moment of its last scattering to the moment of its observation. From its definition, this new magnetically induced redshift affects photons with all wavelengths without any cut-off or threshold. Our discussion of this redshift effect bias is until now on its impacts on synthetic data similar to supernovae type Ia data. But, cosmological parameters are estimated also from other methods such as CMB data. CMB measurements concern photons in microwave band and are also affected by our redshift. In theory, CMF exists in all cosmic history and in all scales with different configurations and origins. After the last scattering, CMB photons travelled then long distances within magnetic fields suffering from our effect redshifts. The long time

allowed the photon to interact with magnetic fields of very large parts of the Universe. This average the local differences and create an isotropic signature in CMB. The redshift of the monopole is indicating the time of last scattering of recombination. The isotropic signature that our effect may have on CMB contributes to the monopole redshift of CMB affects our estimation of the time of recombination.

Our redshift signature on CMB photons records magnetic fields from all eras of cosmic evolution. These cosmic magnetic fields are of different configurations and origins. Magnetic fields from early stages could be very random and very weak. Those magnetic fields suffer decreasing from recombination. The magnetic fields survival through cosmic recombination is an assumption that seems to be valid but, leave magnetic fields with very low strength. There is significant magnetic power only on small scales and it could be as strong as  $10^{-6}$  to  $10^{-7} G$  close to the bound imposed by BBN bounds. After the start of first dense objects formation like stars and galaxies, new magnetic fields grow from primordial ones that are amplified or from intrinsic one that are spread to all Universe regions. Those magnetic fields would also have their signature on the CMB photons redshifts. But, this time and specially the most recent and strong magnetic fields contribute to the higher orders of anisotropies multi-poles as the photons do not have the time to travel and average out the differences of magnetic fields in local Universe. Our redshift signature on CMB photons records magnetic fields from all eras of cosmic evolution. But, it is hard to be decrypted as it is overloaded with other signatures from the variety of effects creating CMB anisotropies. Again and with those impacts on CMB, this effect would have its impact on cosmological estimations creating bias and complicating the process of best-fitting extraction.

When trying to estimate impacts on CMB and with current resources, it's inconceivable to get a simulation which recreates the state of the entire Universe from at least the recombination time to current time. Our simulations can then track only signatures of magnetic fields in local Universe (within the simulation box). We create an all-sky map representing the redshifts of photons observed from all directions and travels from the same distance. The starting points of those photons represent a sphere centred by the observer. Those maps mimic the partial signature of local Universe magnetic fields on CMB photons reaching the observer from all directions. This is the situation found in Sim.9 data when we create and then plot the CMB all-sky observations affected by our new redshift from local Universe (the contained within the simulation box) (see Fig. 9.34). Most the sky pixels have redshift lower than  $10^{-9}$ . Those directions would have to accumulate with older and more distant contributions from our effect and other anisotropies effects to be noticeable. Few pixels have noticeable redshifts around  $10^{-6}$  and falls in the CMB anisotropies ranges. Fewer other pixels have larger redshifts up to  $10^{-3}$  which are caused for CMB photons travelling really close to haloes with strong magnetic fields. Those cases exist in real CMB data and may be blamed on foreground emissions of galaxies. Our effect makes it interesting to look back to those data removed from CMB analysis again.

When we represent CMB all-sky for other simulations, we find very variate impacts on CMB photons : Form highly redshifted to  $10^{-3}$  in simulations with strong present time magnetic fields, to low redshifts of  $10^{-9}$  in simulations with very weak magnetic fields. We find those with fewer pixels of high contribution like Sim.13 (see Fig. 9.35) and others with even more like Sim.10 (see Fig. 9.36). In the case of Sim.10, it could be used as a higher limit of magnetic fields existence of local Universe as we don't observe such big distortions in CMB maps, or we wait for more distant parts that could add isotropy to the observed maps making the monopole of CMB all-sky maps related to both cosmological and our redshift impacts. Sim.16 map (see Fig. 9.37) is interesting as anisotropies where tracked up to a sphere of  $107 Mpc$  and still be in the ranges of CMB anisotropies with

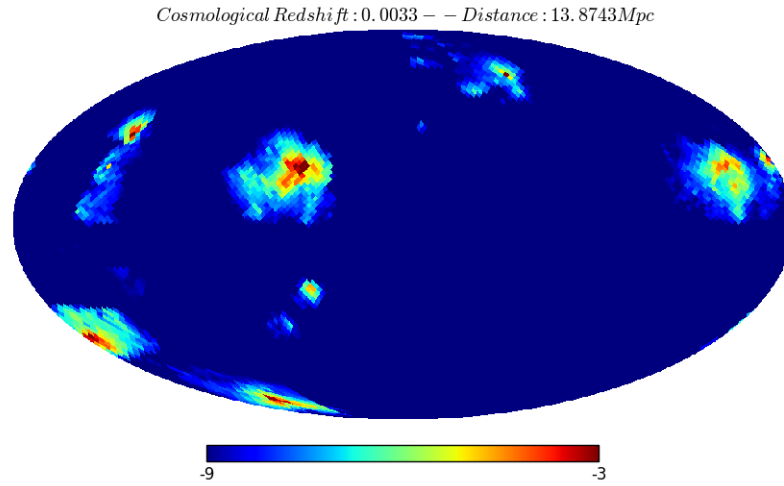


Figure 9.34: All-sky map of CMB anisotropies from our effect of the local Universe represented by a sphere around the observer inside the Sim.9 box. We represented the decimal logarithm of magnetically induced redshift.

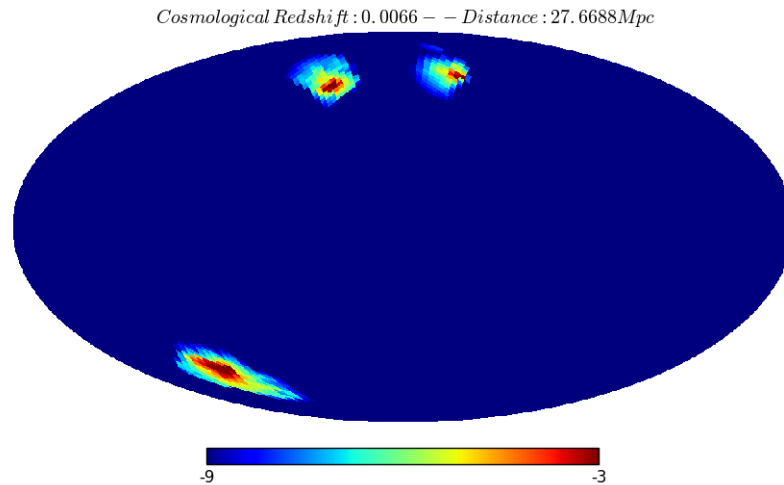


Figure 9.35: All-sky map of CMB anisotropies from our effect of the local Universe represented by a sphere around the observer inside the Sim.13 box.

few high contributions near halos.

We observe clearly in those maps magnetic fields in clusters and their resulting redshifts. This confirms the existence of such magnetic fields in clusters with concordance with other observations and simulations results. This signature also confirms our prediction on the local inhomogeneities of magnetic fields signature on CMB anisotropies. Such local impacts estimations are useful to make constrains on local magnetic fields from our redshift effects impacts on CMB. Anisotropies of CMB are very low in magnitude up to  $10^{-6}$ . So, contributions from our redshift effect on local Universe which are added to older contributions must not be so high or would be contradicting the CMB observations. With better resolutions, those maps are then very indicative on local magnetic fields. Moreover, we observe redshifts of very low orders to  $10^{-8}$  from our effect in simulations redshift effects histograms. Those cases are now very interesting in CMB anisotropies and accumulate with older contributions to affect CMB anisotropies.

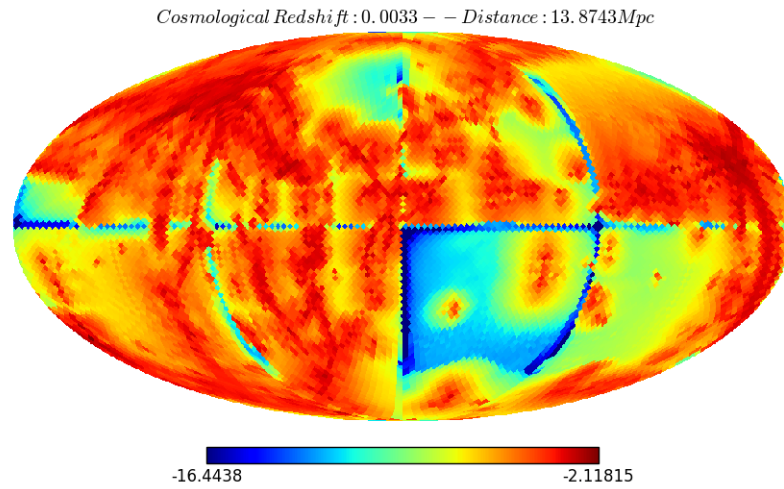


Figure 9.36: All-sky map of CMB anisotropies from our effect of the local Universe represented by a sphere around the observer inside the Sim.10 box.

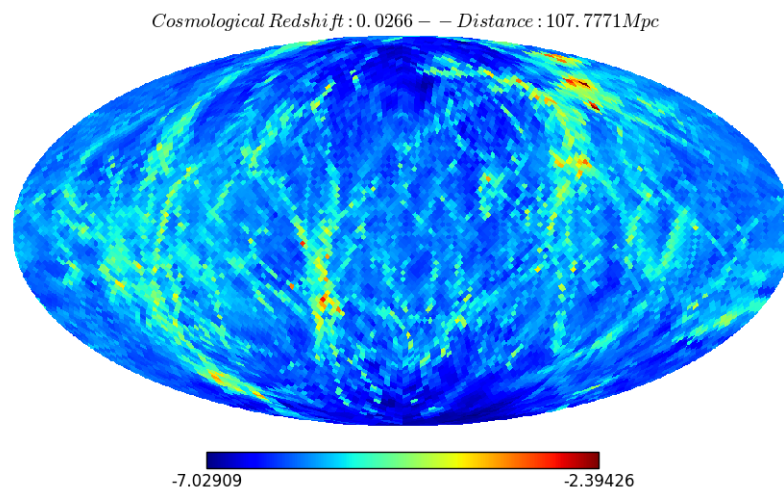


Figure 9.37: All-sky map of CMB anisotropies from our effect of the local Universe represented by a sphere around the observer inside the Sim.16 box.

## 9.7 Extreme Universe scenarios

Only cosmological models having analytical solutions were implemented in ENZO especially dust-only Friedmann models ( $\Omega_{r0} = 0, \Omega_{\Lambda0} = 0$ ) and spatially flat matter-only Lemaitre models ( $\Omega_{r0} = 0, \Omega_{m0} + \Omega_{\Lambda0} = 1$ ). First, we correct and add more models having analytical solutions. Then, we add a new and properly adjusted numerical implementation which is both precise and time efficient. The modified ENZO code is allowing us to follow the evolution of Universes with all possible  $(\Omega_{m0}, \Omega_{\Lambda0})$  configurations including cases where the Universe will eventually start to collapse (see Appendix B for more details on implementations). Even YT code is extended to be able to create observations in this scenario following the same principles. Some test simulations are already done with modified ENZO code in low resolution.

In those simulations, we found a more extreme scenario and strange possibility in which the illusion is more than few cases but much global. If the Universe is collapsing rather than expanding, nearby galaxies should have blueshifts not redshifts because the ratio of the scale factor is less than 1 as the Universe were larger in the past than now. When an isotropic magnetic fields exist with the appropriate strength and configuration, their impact as redshifts could deviate from blueshifts of nearby galaxies to reverse them to redshifts. It is challenging to find the appropriate configuration recreating the linear relation of Hubble law between redshifts and distances from a side with negative redshifts (blueshifts) to the positive redshifts. With the appropriate magnetic fields implemented at the start of those simulations, we could reverse lot of galaxies from blueshifts caused by the collapse of the Universe to redshifts by including the new redshift contribution. But, more work is to be done to adjust the corresponding magnetic fields evolution algorithms and configuration needed to make this scenario feasible. More simulations will be done for finer resolutions to check for such big claim.

A more moderate version of this scenario is corresponding to our Universe which is not flat or will not expand forever. The flatness observed is only from the bias caused as already argued by gravitational redshifts and now also by our new predicted redshift effect. The deviation from the flat model of the Universe are as big as the contribution from our effect. This scenario is also under intense investigation from simulations to synthetic observations creation with the extended versions of ENZO and YT. Two Universes with different configurations and composition with matter and dark energy and then with different fates could appear to be the same with the appropriate contribution from this new redshift effect. This makes our quest to find the real state of the Universe more complicated in data collection and even in cosmological parameters estimation techniques. The future results of both curious cases will be carefully analysed and presented correspondingly.

## 9.8 Chapter conclusions

We learn more about the evolution of magnetic fields in AMR configuration of ENZO code. We notice the effect of resolutions, initial seed and supernovae feedbacks on its resulting state. We could synthesize observations for the nearby Universe. This allows us to compare with existing works on gravitational redshifts bias and present new results concerning our new redshift effect. Impacts on estimations of Hubble constant is given and compared in several situations of magnetic fields. Some important extreme cases are noticed and interpreted as possible explanation of abnormal observations which contradicted intuitive understanding of seen configurations : single cases like Stephen's quintet and galaxy-quasar associations, dark galaxies in voids and possible global impact that

will make major shift in our understanding of the Universe around us. The possibility that the Universe may not be flat and may not even be expanding but collapsing is a big claim resulting from our simulations. Impacts on CMB measurements and SN Ia data are also discussed in light of our findings.

Our simulations have also limitations which must be discussed. The main ones are resolution and simulation box size. Those are technical limitations related to computational resources available in the time when those simulations were done. The simulation box size didn't allow us to get high redshift observations. Those observations would allow us to check the possible accumulation of our redshift effect contributions in those cases. The resources of our simulations didn't allow us to get the best evolution of the Universe for smaller cells. This is making key fields like magnetic fields inside smaller cells and inside haloes having low resolution and making our estimations inside haloes not very reliable. Having better resources in the future will make it possible to do more simulations : larger and with finer resolutions. Those simulations could help us to get more conclusive results about our redshifts effect impacts : bias on all cosmological parameters from SN Ia like data, signatures in CMB data, the real state of magnetic fields in the Universe and most importantly the real fate of our Universe. This will make it possible to respond to questions about the real composition of the cosmos and if the Universe is really flat or even really expanding. Simulations with non-flat configurations of  $(\Omega_{m0}, \Omega_{\Lambda0})$  must be done to respond to such big questions. The observations of higher redshift will improve the possibility to study cosmological parameters bias even from real data such as JLA data. Results from those simulations will allow us to synthesize deviations of observed redshifts by gravitational redshifts and our redshift effect. Introducing those deviations in the data, make us get estimates on bias produced. The synthetic deviations will be more realistic, if it is randomized for reach case alone and not a uniform insertion as done by WDW15. As we observed for our actual data, the deviations from gravitational or our effect are highly intrinsic to each halo and differ highly from a case to another. And the extreme cases of our redshift effect are clear examples.

# Conclusion

The approaches used in this thesis have giving important results in various current open problems in modern cosmology and astrophysics. Those approaches are new theoretical paradigm within standard theories such as Einstein's general relativity. For instance, new analytical solutions to Maxwell's equations in curved expanding spacetime have shown that primordial magnetic fields generated in pre-recombination era could be preserved at the end and after recombination. This preservation is due the curvature of spacetime acting like a pseudo-current and not from accelerated charged particles which suffer from a large drop in recombination weakening PMF. The conservation through spacetime curvature could give a homogeneity to the preserved fields. Our developed code SCOPE is used to study free electron fraction during recombination. The main result is indicating a tight relation of CMB temperatures at start and end of recombination era to accepted cosmological parameters ranges and even accepted neutrinos masses. This results was not considered in previous studies when fitting cosmological parameters from observational data especially that not all cosmological parameters combinations could be acceptable even a small change could result in non-physical combination.

In this thesis, the main result is a new redshift in photons travelling within external magnetic fields. The loss of energy of those photons is caused by the gravitational interaction between electromagnetic wave and the external magnetic field creating gravitational waves. This effect has no threshold energy or cut off to occur, making it affecting all our observations. First estimations of our effect contribution with different magnetic fields strengths and coherent lengths make the astrophysical and cosmic scales the most probable for noticeable impacts. The contributions of this effect in observed redshifts were not considered before in previous studies. Then, its contribution may have been misinterpreted as cosmological, Doppler or gravitational in origin. The developed code RPC was used as a first approach to the study of this effect impacts. It is found that observed redshift could not infer the exact cosmological contribution and only an interval of possible cosmological redshift could be estimated depending on models parameters of magnetic fields within nearby Universe. A much important application of this effect is done for the explanation of unexplained trans-GZK events. In our explanation, possible UHECR sources could exist within the GZK sphere, but the misinterpretation of observed redshifts and over-estimation of cosmic distances could make them appear to be out-side GZK sphere. Then, trans-GZK events could be only an apparent paradox caused by a mis-interpretation of our redshift effect contributions as cosmological in origin. This hypothesis is verified using extended versions of CRPROPA code, where we implemented a modular version of RPC.

From several weak points in previous simulations done with RPC and Extended-CRPROPA, a much developed method is used to have more reliable estimations of our effect impacts. Also, limitations in observational data of cosmic magnetic fields make the exact estimation of our effect impacts from current data not possible. The best framework to study our effect impacts and compare it to other non cosmological effects contributions is through customized numerical cosmological simulations. We choose ENZO code for those

## CONCLUSION

simulations and YT to create and analyse synthetic observations. Some extensions to both codes are done to provide the suited framework and create appropriate synthetic observations allowing us to estimate each redshift effect contribution. This makes our numerical study unique and more developed than previous studies. It allows us to create the closest recreation of extragalactic objects' redshift observations and distances estimations like supernovae type Ia data.

We have done several cosmological simulations changing several parameters like resolution, Universe's simulated matter distribution, initial magnetic fields, feedbacks and magnetic fields seeding methods.

The most important results of our simulations are :

1. Our redshift effect is shown to have a significant contribution comparable to Doppler and gravitational effects. This makes a possible misinterpretation of redshift origins. Another possibility is the over-estimation of gravitational potentials to account for redshifts which are partially caused by our effect. Related to a gravitational misinterpretation of redshift deviations from our effects, galaxies can be considered wrongly as members of clusters or forming clusters bounded gravitationally that don't exist.
2. The analysis of our synthetic observations which mimics supernovae data has shown that Hubble constant could be biased to higher values from impacts of our redshift effect. Recent analysis of supernovae data has pointed out that a bias exists in the data from non cosmological effects and that gravitational redshifts can not account for all the amount estimated. Our redshift effect could be then responsible for this bias according to our obtained results. Those results re-open the discussion on cosmological parameters estimations in general and Hubble constant in particular. The debate is no more about measurement uncertainties but on effects contributing to our data.
3. In more interesting cases, the contribution of our effect is so significant and may exceed the strongest gravitational redshift. Those cases may be blamed as measurement errors or considered as abnormal and discordant. Those cases are very important as they provide a possible explanation of complex cases such as Stephen' Quintet or even galaxy-quasar associations.
4. Our effect can leave impacts on CMB measurements which could be confused with other effects creating CMB anisotropies. Those impacts are biasing cosmological parameters from CMB data too.
5. In the extreme scenario of global impacts of our effect, our Universe may be collapsing and appear to be expanding. This is a big claim which is supported partially by our data. A more moderate scenario is that the Universe is not flat and the deviation biasing our understanding is created by our effect along with the gravitational redshift.
6. The importance of the bias produced is related to cosmic magnetic fields existing in the Universe. The history and the actual state of those magnetic fields are a multi-variable problem. Our simulations results had shown that the same present state can be resulting from different past evolution paths. This is leaving a degeneracy of CMF evolution patterns. Different feedback effects can make two initially different magnetic fields configurations of the Universe to look the same at current time. All this is making the selection of initial magnetic fields and the real feedback processes shaping the Universe's state highly difficult.

## CONCLUSION

7. The wrong interpretation of our effect contributions as gravitational redshifts would result in an over-estimation of gravitational potentials and then of dark matter composition of clusters and the whole Universe. Our simulations results add to uncertainties around dark matter in the universe similarly to previous simulations showing small scale anomalies of  $\Lambda$ CDM.
8. Contributions from our redshift effect are not considered in previous studies which could explain the discrepancy in cosmological parameters estimations especially as our effect affects SNIa data and CMB data differently.
9. In the synthetic observations constructed, a compact group of galaxies similar to SQ is found and gave new indications on SQ kinematics. The famous quintet has new observational evidence on its formation history. The velocities of each member represent important parameters to recreate the interaction process. Our misinterpretation of redshift measurements of SQ members is creating incorrect estimation of velocities. Confusing contributions from our effect and Doppler Effect is affecting numerical models constructed of structure formation in term of peculiar motion of galaxies. The evidence of an older SQ changes our understanding of the group formation scenario and questions members' believed high velocities. It could be an indirect evidence of our overestimation of these velocities affecting deeply our perception and creation of models. The new observational evidence with our results should be the ground for future studies aiming to create Stephan's Quintet formation scenarios. Our suggestion is that they recreate the redshift patterns of different group members and regions.

With our magnetically induced redshift effect, we give a potential explanation to abnormal redshift observations and to discrepancy in cosmological parameters estimations which are both currently unexplained. Our effect also makes new predictions and point out possible misinterpretations in both our understanding of local Universe and the cosmos as a whole. It is worth to mention that our simulations has their limitations which may impact possible estimations done. For instance, more simulations must be done with larger simulation box allowing us to make high redshift observations. Those observations will allow us to estimate impacts on all cosmological parameters from far extragalactic objects within the Hubble flow. Such simulations will allow us a better understanding of CMB anisotropies and make stringed constrains on local magnetic fields and inference of their evolutions, origins and seeds. Our redshift effect allowed us to make claims that must be verified like the Universe is not flat or even is collapsing and just appear from redshifts bias to be expanding. In the future studies, we will develop a better synthetic observations tools and apply them on larger simulations to have more insights and more conclusive results. More studies are under investigation. Even within standard theories, possible new effects could have noticeable impacts changing our perception to current data and our understanding of the Universe. Complex and unsolved questions don't need always exotic ideas and theories to be explained. Small details like an unconsidered effect, previously believed negligible, could then create big difference especially with accumulation effect.

# Appendix A

## Exact solutions to linearised Einstein equations

We present in this appendix the exact equations and solutions related to the new magnetically induced redshift discussed in a previous chapter. To study the propagation of electromagnetic waves within external magnetic fields, we start from Einstein equations in their linear approximation form. Applying the transverse traceless gauge, these equations are simplified as represented in Eq. 4.11. The energy momentum tensor of electromagnetic fields studied is giving by

$$T_{\mu\nu}^{(EM)} = \frac{E_0^2 \cos^2(k(t-z))}{\mu_0 c^2} \begin{pmatrix} 1 & 0 & 0 & -1 \\ 0 & 0 & 0 & 0 \\ 0 & 0 & 0 & 0 \\ -1 & 0 & 0 & 1 \end{pmatrix} + \frac{B_x^2}{2\mu_0} \begin{pmatrix} 1 & 0 & 0 & 0 \\ 0 & -1 & 0 & 0 \\ 0 & 0 & 1 & 0 \\ 0 & 0 & 0 & 1 \end{pmatrix} + \frac{B_x E_0 \cos(k(t-z))}{\mu_0 c} \begin{pmatrix} 0 & 0 & 0 & 0 \\ 0 & 0 & -1 & 0 \\ 0 & -1 & 0 & 0 \\ 0 & 0 & 0 & 0 \end{pmatrix} \quad (\text{A.1})$$

For simplicity, we could define three constant tensors as follows

$$T_{\mu\nu}^{(I)} = \begin{pmatrix} 1 & 0 & 0 & -1 \\ 0 & 0 & 0 & 0 \\ 0 & 0 & 0 & 0 \\ -1 & 0 & 0 & 1 \end{pmatrix}, \quad (\text{A.2})$$

$$T_{\mu\nu}^{(II)} = \begin{pmatrix} 1 & 0 & 0 & 0 \\ 0 & -1 & 0 & 0 \\ 0 & 0 & 1 & 0 \\ 0 & 0 & 0 & 1 \end{pmatrix} \quad (\text{A.3})$$

and

$$T_{\mu\nu}^{(III)} = \begin{pmatrix} 0 & 0 & 0 & 0 \\ 0 & 0 & -1 & 0 \\ 0 & -1 & 0 & 0 \\ 0 & 0 & 0 & 0 \end{pmatrix}. \quad (\text{A.4})$$

Then, we could easily put a general form of the perturbation metric given as

$$\bar{h}_{\mu\nu} = f^{(I)}(t, z)T_{\mu\nu}^{(I)} + f^{(II)}(t, z)T_{\mu\nu}^{(II)} + f^{(III)}(t, z)T_{\mu\nu}^{(III)}. \quad (\text{A.5})$$

Einstein equations are reduced to only three equations relative to each function  $f^{(II)}$

$$\begin{aligned}
 (\partial_t^2 - \partial_z^2)f^{(I)}(t, z) &= \frac{-2\kappa}{\mu_0 c^2} E_0^2 \cos^2(k(t - z)), \\
 (\partial_t^2 - \partial_z^2)f^{(II)}(t, z) &= \frac{-\kappa}{\mu_0} B_x^2, \\
 (\partial_t^2 - \partial_z^2)f^{(III)}(t, z) &= \frac{-2\kappa}{\mu_0 c} E_0 B_x \cos(k(t - z)).
 \end{aligned} \tag{A.6}$$

Or in a more ordered form as follows

$$\begin{aligned}
 (\partial_t^2 - \partial_z^2)f^{(I)}(t, z) &= \frac{-\kappa E_0^2}{\mu_0 c^2} (\cos(2k(t - z)) + 1), \\
 (\partial_t^2 - \partial_z^2)f^{(II)}(t, z) &= \frac{-\kappa B_x^2}{\mu_0}, \\
 (\partial_t^2 - \partial_z^2)f^{(III)}(t, z) &= \frac{-2\kappa E_0 B_x}{\mu_0 c} \cos(k(t - z)).
 \end{aligned} \tag{A.7}$$

Those equations are of the same form

$$(\partial_t^2 - \partial_z^2)f^{(i)}(t, z) = (A \cos(2k(t - z)) + B), \tag{A.8}$$

having a general solution as the following

$$f^{(i)}(t, z) = (A(\frac{z}{2k}) \sin(k(t - z)) + B(\frac{1}{2}z^2 + C_1 z + C_2)), \tag{A.9}$$

where  $A$  and  $B$  are constants determined from the integration. The solutions for our three functions are then giving by

$$\begin{aligned}
 f^{(I)}(t, z) &= \frac{-\kappa E_0^2}{\mu_0 c^2} \left( \frac{z}{4k} \sin(2k(t - z)) + (\frac{1}{2}z^2 + C_1 z + C_2) \right), \\
 f^{(II)}(t, z) &= \frac{-\kappa B_x^2}{\mu_0} (\frac{1}{2}z^2 + C_1 z + C_2), \\
 f^{(III)}(t, z) &= \frac{-2\kappa E_0 B_x}{\mu_0 c} \frac{z}{2k} \sin(k(t - z)).
 \end{aligned} \tag{A.10}$$

The combination of these three functions with the constant tensor gives the perturbation metric wanted.

# Appendix B

## Extended ENZO

We present in this appendix the internal functioning of an ENZO simulation, cosmological models implemented and our extensions and development of the code. The Universe evolution within an ENZO simulation is indicated mainly with cosmic time. Even if ENZO uses an internal time unit system, but the time is converted to physical units when needed. Two other indicators of the evolution are used scale factor and redshift. The scale factor  $a(t)$  used inside ENZO is the normalized scale factor. This scale factor is zero at the big bang and 1 in present time. And if the Universe had experienced only expansion, it would be always less or equal to one and we observe only cosmological redshifts. But if the Universe had started a collapse, this scale factor would be in some time of cosmic evolution be greater than 1 and we observe possibly cosmological blueshifts.

Redshift could be then calculated from this normalized scale factor. We need to compute redshift or equivalently scale factor from cosmic time inside ENZO for three main reasons : to apply the expansion in the grid sizes due to expansion, to verify the expansion steps with the maximum value giving as input to ENZO and finally to get outputs in the requested redshifts values. Thus, ENZO has two main functions allowing the computation of time from redshift and the computation of expansion factor (scale factor) from time. Then, we need a relation between time and scale factor from the FLRW spacetime. Starting from Friedmann equation and for each moment in Universe evolution described by time and scale factor, we could construct a relation of the form

$$H^2(t) = H_0^2(\Omega_{m0}a^{-3} + \Omega_{\Lambda0} + \Omega_{k0}a^{-2}), \quad (\text{B.1})$$

where  $\Omega_{r0} \sim 0$  and  $\Omega_{k0} = 1 - \Omega_{m0} - \Omega_{\Lambda0}$ . In all ENZO cosmological simulations, we consider that the Universe is dominated by matter or dark energy and the contribution of radiation is neglected. Using Hubble parameter definition

$$H(t) = \frac{\dot{a}(t)}{a(t)} = \frac{1}{a(t)} \frac{da(t)}{dt}, \quad (\text{B.2})$$

we could write

$$H_0 dt = \frac{da}{a} (\Omega_{m0}a^{-3} + \Omega_{k0}a^{-2} + \Omega_{\Lambda0})^{-1/2}. \quad (\text{B.3})$$

We integrated both sides from the big bang moment (time = 0, scale factor = 0) to the needed moment (time and scale factor). The right hand side integral is the most difficult as it has no general form and has analytical solutions for special configuration of the ( $\Omega_{m0}$  and  $\Omega_{\Lambda0}$ ) values.

Some of these solutions (models) are implemented models in ENZO which are mainly for dust-only Friedmann models ( $\Omega_{r0} = 0$ ,  $\Omega_{\Lambda0} = 0$ ) and spatially flat matter-only Lemaitre models ( $\Omega_{r0} = 0$ ,  $\Omega_{m0} + \Omega_{\Lambda0} = 1$ ). These models represents only points of two lines in

$(\Omega_{m0}, \Omega_{\Lambda0})$  plan : one for  $\Omega_{\Lambda0} = 0.0$  and the other for  $\Omega_{k0} = 0.0$ . Only 3 models are successfully implemented in ENZO which are

- Case 1 : for  $\Omega_{m0} = 1, \Omega_{\Lambda0} = 0$

$$a(t) = \left(\frac{3}{2}H_0t\right)^{2/3}$$

- Case 2 : for  $\Omega_{m0} < 1, \Omega_{\Lambda0} = 0$

$$a = \frac{\Omega_{m0}}{2(1 - \Omega_{m0})}(\cosh \psi - 1)$$

$$a = \frac{\Omega_{m0}}{2H_0(1 - \Omega_{m0})^{3/2}}(\sinh \psi - \psi)$$

- Case 4 : for  $\Omega_{r0} = 0, \Omega_{m0} + \Omega_{\Lambda0} = 1$

$$H_0t = \frac{2}{3\sqrt{\Omega_{\Lambda0}}}\sinh^{-1}\sqrt{a^3|\Omega_{\Lambda0}|/(1 - \Omega_{\Lambda0})}, \text{ if } \Omega_{\Lambda0} > 0$$

Another case (Case 3) was implemented in only one needed function with a slice sign error. We corrected and completed this case and we included a new one (Case 5) for negative dark energy

- Case 3: for  $\Omega_{m0} > 1, \Omega_{\Lambda0} = 0$

$$a = \frac{\Omega_{m0}}{2(\Omega_{m0} - 1)}(1 \cos \psi)$$

$$a = \frac{\Omega_{m0}}{2H_0(\Omega_{m0} - 1)^{3/2}}(\psi - \sin \psi)$$

$\psi$  varies over the range  $[0, \pi]$

- Case 5: for  $\Omega_{r0} = 0, \Omega_{m0} + \Omega_{\Lambda0} = 1$

$$H_0t = \frac{2}{3\sqrt{\Omega_{\Lambda0}}}\sin^{-1}\sqrt{a^3|\Omega_{\Lambda0}|/(1 - \Omega_{\Lambda0})}, \text{ if } \Omega_{\Lambda0} < 0$$

The most used case in cosmological simulations is case 4. As most cosmological data are indicating a flat accelerated expanding Universe, this is the only case which may be useful to implement. But, the recent studies are proposing a different idea of the Universe. There could be a bias from non cosmological effects on our data analysis and the Universe may not be flat or even in an extreme case not expanding but collapsing. This is giving a need for a more flexible implementation of time-redshift relation within cosmological simulation codes such as ENZO. Such an implementation allows the simulation of more possible  $(\Omega_{m0}, \Omega_{\Lambda0})$  configurations which may have a small deviation from a flat space-time or even completely in a different configuration.

We could develop in other special configurations more exact analytical solutions or approximate analytical solutions using Taylor expansions. But, those solutions do not cover the entire  $(\Omega_{m0}, \Omega_{\Lambda0})$  plan or are not efficient in computation time. We created

a numerical approach to the integration of the previous time-scale factor relation with special algorithm to be both precise and time efficient. First, we implemented separate functions to do the computations for this general case. The computation of the time from scale factor (redshift) is done by numerical integration on the right hand side of the previous Eq. B.3. We used trapezoidal numerical integration but with an adaptive integration step. The integration step is ranged from  $10^{-9}$  to  $10^{-5}$ . We choose the smallest step for biggest changes in the integrated function to avoid divergence. We use properties of integration and the fact that the evolution of the time is a monotonic function to cut time of computation. At the start of the simulation, we create a table of computed time - scale factor values which is used after during the simulation evolution.

When we need to compute time from scale factor, we compare the actual scale factor to all pre-computed values and we do integration only for the small interval between the closest value and the actual value. For the expansion factor computation, we use all the previous implemented measures and an additional setting. From the analytical relation of time to scale factor, we could not get a reverse function. We must solve an equation of the form  $t_{actual} - f(a_{actual}) = 0$ . We know from the monotonic behaviour of the function  $f(a)$  that the value needed  $a_{actual}$  is somewhere between ( $a_{min} = 0$ ) and ( $a_{max} = 1$ ) for expanding Universes. We must do several iterations of values between those two minimum and maximum values to find the needed value.

To get a faster conversion to this value, we used a simple algorithm. First, we compute time for the mean of the interval limits ( $a_{mean}$ ). Then, we decide according to the found value. If the time found is the same as  $t_{actual}$ , then this the needed scale factor ( $a_{actual} = a_{mean}$ ). If the difference is positive ( $t_{actual} - t(a_{mean}) > 0$ ), we set a new minimum to our expected interval equal to this mean and re-start again. If the difference is negative, we set a new maximum to our expected interval that is equal to this mean and re-start again. We continue in this pattern until we reach a mean verifying the check done in the second step. This allows us to get a fast conversion to the needed value. Those special configurations of the time-scale factor relation computation allows us also to get good precisions in the integration when compared to cases with exact analytic solutions, difference of about  $10^{-9}$  in time estimation, and the lowest possible computation cost.

To have the most developed implementation possible, we considered cases where the Universe will eventually collapse. If the simulation evolution is for the expanding era of the Universe, the computation is the same. If we continue until we reach the maximum expansion of the Universe and then we start the collapse, the new implemented functions are set to compute the maximum scale factor possible for each  $(\Omega_{m0}, \Omega_{\Lambda0})$  configuration. This maximum scale factor is related with a Universe stopping the expansion and reverse to a collapse which means that the Hubble constant at this moment would be null. From the definition of Hubble constant (see Eq. B.1), we could construct a third order polynomial of inverse scale factor. Using definition from Spiegel (1999) (see Ref. [361]), we could find a possible solution representing the maximum scale factor possible.

This solution must be real and less than or equal to 1 to give us a physically accepted scale factor. In those two possible cases the Universe had reached its maximum in the past and is collapsing now or it is now at its maximum. We specify the time of maximum scale factor as  $t_{max}$ . For the computation of times greater that  $t_{max}$ , we suppose symmetry of the time evolution function around  $t_{max}$ . Then, the scale factor of ( $t_{actual} > t_{max}$ ) and ( $t = 2 * t_{max} - t_{actual}$ ) is supposed to be equal and we then compute for the latter one in the same way described before. This method of computation allows us to do simulations of all possible configurations of  $(\Omega_{m0}, \Omega_{\Lambda0})$  plan and even for collapsing Universes. This represents our main contribution to ENZO development during the current work on magnetically induced redshift effect impacts.

# Appendix C

## Scientific contributions

### C.1 Papers and proceedings

- [304] Abdelali M. A., Mebarki N., 2012, AIP: Conference Proceedings, 1444, 413
- [269] Abdelali M. L., Mebarki N., 2014, Science & Technology A, 40, 105
- [258] Abdelali M. L., Mebarki N., 2015, J. Phys.: Conf. Ser., 593, 012013
- [322] Mebarki N., Abdelali M. L., 2017, On a possible solution to the UHECR GZK cut off, in Actes de Conference : Lumiere et astronomie Alger 22-23 decembre 2015, p. 54-58, ISBN 978-9947-0-4967-9
- [341] Abdelali M. L., Mebarki N., 2017, Impacts of a new non cosmological redshift effect on cosmological parameters estimation, in Actes de Conference : Lumiere et astronomie Alger 22-23 decembre 2015, p. 59-64, ISBN 978-9947-0-4967-9
- [295] Abdelali M. L., Mebarki N., 2019, Redshift effects implications on revised models of Stephan's quintet, Modern Physics Letters A, 1950342, DOI: 10.1142/S0217732319503425, arXiv:1806.02899v1 [gr-qc]

### C.2 Conferences

1. The 8th international conference on progress in theoretical physics, Constantine 2011
2. Conférence Internationale de Physique Subatomique et Application, Constantine 2013
3. 1st Franco-Algerian Workshop on Neutrino Physics, Constantine 2013
4. Journée Internationales de Physique de Constantine 2013
5. La conférence lumière et astronomie organisé par ATRST, Alger 2015
6. Several presentations as part of the internal seminars of LPMS activities

## New Alternative Explanation of the Astrometric Binary

M.A.Abdelali and N.Mebarki

*Laboratoire de Physique Mathématique et Subatomique  
Mentouri University, Constantine, Algeria*

**Abstract:** We want to give a new application of general relativity and precisely the gravitational waves. After studying and developing the explicit lensing and Doppler like effects of the circular polarised mode. A new explanation to the wavy motion of stars known as astrometric binary using the GW is presented and its applicability is discussed.

**Keywords:** Astrometric binary, Gravitational waves, Gravitational lensing, Doppler effect.

**PACS:** 97.80.Af, 04.30.-w, 95.85.Sz, 95.30.Sf, 43.28.Py

### INTRODUCTION

Far from the new theories that try to modify or change the relativistic theory of gravity, this work focus on one of the important predictions of general relativity (GR): gravitational waves (GW). To be more specific, we will study the lensing effect of GW in a very different way. This effect has attracted many physicists [1]-[6] and some of them propose to use it as a new method to detect GW satisfying a wave equation and their fundamental two polarisations in the traceless-transverse gauge [7]. Moreover, Hulse-Taylor has observed the predicted period decrease of a pulsar binary which has for the emitted waves the circular polarised mode. This confirm that this kind of polarisation modes exists really in nature. It is worth to mention that as far as we know, all the previous works do not take seriously these results and give an explicit expression of the light deviation. They do not discuss its application at least in our considered case and precise the main differences. The goal of this paper is to use the explicit expression of the circular polarised mode, solving the geodesics equation in the weak field approximation by taking into account the effect of these waves on the light beam trajectory. We study also the Doppler effect of these space-time perturbations and discuss these results in the astrometric binary [8]-[11] case and try to understand the strange wavy motion of a star that we did not see any companion (star or planets) using the known methods: spectroscopy, eclipsing, microlensing. In what follows, we define the astrometric binary and see what is the current explanation of the phenomena and the existing problems. We present our calculations for the gravitational lensing and Doppler like effects and finally discuss the results.

*The 8th International Conference on Progress in Theoretical Physics (ICPTP 2011)*  
AIP Conf. Proc. 1444, 413-418 (2012); doi: 10.1063/1.4715466  
© 2012 American Institute of Physics 978-0-7354-1040-4/\$30.00

413

This article is copyrighted as indicated in the article. Reuse of AIP content is subject to the terms at: <http://scitation.aip.org/termsconditions>. Downloaded to IP: 131.170.6.51 On: Fri, 14 Aug 2015 16:19:02

## NEW PRIMORDIAL MAGNETIC FIELD EVOLUTION AND SIGNATURE ON THE CMB SPECTRUM

M.A. ABDELALI AND N. MEBARKI

Laboratoire de Physique Mathématique et Physique Subatomique, , Frères Mentouri University, Constantine, Algeria

*Reçu le 11/04/2014 – Accepté le 11/11/2014*

### Abstract

A new scenario for a primordial magnetic field is proposed and its evolution is presented. Signatures on the cosmic microwave background spectrum are also discussed.

**Keywords:** *cosmology, redshift, cosmic microwave background, magnetic fields.*

### Résumé

Un nouveau scénario pour un champ magnétique primordial est proposé et son évolution est présentée. Des signatures sur le spectre du fond microonde cosmique sont aussi discutées.

**Mots clés:** *cosmologie, décalage vers le rouge, fond microonde cosmique, champs magnétiques.*

### ملخص

مستمد جديد للحقل المغناطيسي الأولي اقترح و تطوره قد طرح. أثار على طيف الخلفية الميكروموجية الكونية قد نوقشت أيضا.  
**الكلمات المفتاحية:** الكسولوجيا، الإنزياح نحو الأحمر، الخلفية الميكروموجية الكونية، حقل مغناطيسي.

## Simulation of the Free Electron Fraction for Cosmological Parameters and Possible Constraints on the Neutrinos

**M L Abdelali<sup>1</sup> and N Mebarki**  
Laboratoire de Physique Mathématique et Subatomique  
Mentouri University, Constantine, Algeria

E-mail: mabdelali@gmail.com

**Abstract.** A new simulation code to constrain the cosmological parameters and computes the free electron fraction evolution is presented. The code algorithm, inputs-outputs and possible preliminary results are also discussed.

### 1. Introduction

The evolution of the universe is controlled by the cosmological parameters which are principally constrained by observations of supernovae type Ia and cosmic microwave background (CMB) anisotropies. Codes, like CMBFAST, CMB-easy or CAMB, are developed to compute these parameters from the CMB anisotropies observations based on several experiments like WMAP, PLANCK or COBE [1]-[3]. These codes compute the cosmological fluid perturbations of the Einstein Boltzmann equations. To affine the cosmological parameters, the primary and secondary anisotropies have to be estimated including new theories like inflation. The code which we have developed uses new approach to constrain the cosmological parameters. This method is based on a theoretical estimation after the computation of a unique Boltzmann equation. The paper is organized as follows: In section 2, we present the code for the Simulation of free electron fraction for Cosmological Parameters Estimation (SCOPE) as well as its inputs and outputs. In section 3, the physical settings of the computed equation are discussed. In section 3, we show the possible constraints on neutrinos and finally, in the last section, we draw some of the preliminary results and conclusion.

### 2. SCOPE code, its inputs and outputs

The new code denoted by SCOPE (or Simulation of free electron fraction for Cosmological Parameters Estimation) [4]-[6] is a C<sup>++</sup> code based on a Monte Carlo algorithm. It has as an objective to constraint the cosmological parameters through a numerical computation of the free electron fraction. Its evolution is governed essentially by the Boltzmann equation. The main steps of the algorithm are:

- 1- Seed the principal cosmological parameters with randomly generated numbers;
- 2- Make a numerical integration of the evolution equation of the free electron fraction;
- 3- Check at all steps of integration the mathematical condition of the free electron fraction;
- 4- Do not take into account the combination if the condition is not valid;
- 5- Continue the integration until the acceptance of the combination;
- 6- Return to the first step until the needed number of cosmological parameters combinations.

<sup>1</sup> To whom any correspondence should be addressed.



## On a Possible Solution to the UHECR GZK Cut off

Noureddine Mebarki<sup>1\*</sup>, Mohamed Lamine Abdelali<sup>1</sup>

<sup>1</sup>Laboratoire de Physique Mathématique et Physique Subatomique, Université Frères Mentouri, Constantine, Algérie  
\*[nmebarki@yahoo.fr](mailto:nmebarki@yahoo.fr)

**Abstract:** A non cosmological redshift, generated by photon bremsstrahlung of high frequency gravitational waves in an external magnetic field, is studied. A recalibration of the cosmological parameters is discussed and a possible solution to the ultra high energy cosmic rays GZK cut is proposed.

**Key words :** Cosmic magnetic field, redshift, gravitational waves, cosmic rays.

### I. INTRODUCTION

From Hubble's observations of galaxies recession, the redshift of galaxies has made a revolution in our understanding to the universe. The Hubble law links two important quantities: the cosmological redshift and distance of the observed object (galaxies, quasars, or supernovae...). The distance recalibration has given more accurate determination of the cosmological distances and yields to a big change of Hubble Constant from 500km/s/Mpc as initial estimation, to around 70km/s/Mpc, the actual accepted value from the cosmic microwave background observations.

In this contribution, we investigate a new effect contributing to the total observed redshift of galaxies. The extra new redshift does not result from the universe expansion or the peculiar motion of galaxies. It is due to the photon radiation of high frequency gravitational waves in an external magnetic field. This effect will serve as an additional recalibration of the cosmological parameters improving our understanding to the universe and help to solve the ultra high energy cosmic rays (UHECR) GZK limit.

### II. BASIC FORMALISM

In what follows,  $(c, \kappa, \mu_0)$  stand for the speed of light, gravitational constant of Einstein equations

and the permeability of the vacuum respectively. We are interested in the light propagation through space-time and their gravitational interaction. In the Einstein's theory of gravity, the energy momentum tensor part includes the matter and electromagnetic fields contributions. We restrict our study to the vacuum case (absence of matter). The background is a flat space-time represented by a Minkowski metric  $(\eta_{\mu\nu})$ . We consider the weak linearized gravity (Ciufolini et al 2001, 2010), (Krasinski& Plebanski2006) where the curvature generated by the energy of the electromagnetic waves will be small enough to be a perturbation given by  $(h_{\mu\nu})$  in the first order approximation of the metric

$$g_{\mu\nu} = \eta_{\mu\nu} + h_{\mu\nu} \quad (1)$$

The Einstein equations will be rewritten as:

$$\partial_\alpha \partial^\alpha \bar{h}_{\mu\nu} + \eta_{\mu\nu} \partial_\alpha \partial^\alpha \bar{h}^{\alpha\beta} - (\partial_\mu \partial_\alpha \bar{h}^{\alpha\nu} + \partial_\nu \partial_\alpha \bar{h}^{\alpha\mu}) = -2T_{\mu\nu} \quad (2)$$

where  $\bar{h}_{\mu\nu}$  is given by

$$\bar{h}_{\mu\nu} = h_{\mu\nu} - \frac{1}{2} \eta_{\mu\nu} h^\alpha_\alpha.$$

in the traceless transverse gauge where:

$$\begin{aligned} \partial_\beta \bar{h}^{\alpha\beta} &= 0, \\ h^\alpha_\alpha &= 0 \end{aligned} \quad (3)$$

We define solutions of eqs. (2) as gravitational waves. We assign an energy-momentum tensor  $t_{\mu\nu}$  to the gravitational field itself just as we do for electromagnetism, or any other field theory. Physically, we accept that the gravitational radiation will carry a part of energy-momentum just as any

## Impacts of a New Non Cosmological Redshift Effect on Cosmological Parameters Estimation

Mohamed Lamine Abdelali<sup>1\*</sup>, Noureddine Mebarki<sup>1</sup>

<sup>1</sup>Laboratoire de Physique Mathématique et Physique Subatomique LPMPS,  
Université des Frères Mentouri, Constantine, Algeria  
[mabdelali1@gmail.com](mailto:mabdelali1@gmail.com)

**Abstract:** We present a new non cosmological redshift effect caused by the propagation of photons through cosmic magnetic fields. Its effect on cosmological parameters measurements is estimated via cosmological simulations done with modified versions of public codes ENZO YT. The added extensions are presented and the primary results are discussed.

**Keywords:** gravitational waves, redshift, cosmological simulations.

### I. INTRODUCTION

The observations of Hubble of the galaxies redshifts were the beginning of the modern cosmology and the dynamic view of the cosmos. The cumulated measures of this quantity show an expanding universe. The last observations of supernovae indicates, further more that the universe is in an accelerated expansion. The explanation of the cause of such accelerated expansion is the challenge of the modern cosmology. In the literature, it can be found several models that try to explain that acceleration. The most supported model uses dark energy; a new not known or demonstrated component of the universe. Lot of theoretical and experimental studies are in development to verify this theory.

All cosmological and astrophysical observations rely on cosmic objects redshift. This quantity describes the shift to lower wavelengths of emission and absorption lines within the light of distant objects. The three causes of redshift are gravitational, Doppler and cosmological. Gravitational redshift is the result of light travelling far from massive object. Doppler redshift is caused by the motion of an object with respect to the observer. Cosmological redshift is caused by the expansion or collapse of the universe. The latter is proportional to a fraction between the scale factor of the universe in the time of emission and at the observation. The scale factor is the indicator of the size of the universe predicted by the Einstein

equation solved in the case of dynamic universe considering the components of the universe: baryonic (everyday matter around us), dark matter and dark energy (both hypothetical and not confirmed experimentally). If the universe is expanding, as the general view tend to indicate, this fraction gives a shift to higher wavelengths; called redshift. If the universe had started to collapse, that fraction will give a shift to lower wavelengths; called blueshift. The observations of galaxies redshifts is simply a collection of these three kinds of redshifts.

In a previous work, we have predicted that photons when propagating in magnetic fields can radiate gravitational waves and be redshifted (Abdelali, Mebarki 2013). That prediction comes as an analogy of the binary stars case. In this case, the system loses energy by emitting gravitational waves. The system will change its period of rotation which is verified by observations of PSR1916+13 and lead Hulse and Taylor to get a Nobel Prize in 1993. The photons when propagating in an external magnetic field, as the cosmic magnetic fields, will radiate gravitational waves and should by analogy lose energy. To describe that effect, we had used Einstein's equations of general relativity with the energy momentum tensor of electromagnetic fields as source of space-time curvature. The electromagnetic fields are composed by external static magnetic fields and the electromagnetic waves of the propagating photons. The equations were linearized as the energy carried with these fields is weak. After solving those equations and estimating the energy carried by the generated gravitational waves, the new redshift is found to be proportional to the magnetic field strength 'B' and its coherent length 'L'.

$$z_{NC} = \text{Exp}(\alpha B^2 L^3) \quad (1)$$

1 Modern Physics Letters A  
 2 Vol. 33, No. 1 (2019) 1950342 (17 pages)  
 3 © World Scientific Publishing Company  
 4 DOI: 10.1142/S0217732319503425



5 **Redshift effect implications on revised models**  
 6 **of Stephan's quintet**

7 Mohamed Lamine Abdelali\* and Noureddine Mebarki  
 8 *Laboratoire de Physique Mathématique et Subatomique,*  
 9 *Université Frères Mentouri Constantine 1,*  
 10 *BP 325 Route de Ain El Bey, Constantine 25017, Algeria*  
 11 *\*mabdelali1@gmail.com*

12 Received 29 September 2018  
 13 Revised 27 July 2019  
 14 Accepted 1 August 2019  
 15 Published

16 Recent observations of Stephan's Quintet (SQ) gave new indications on its formation  
 17 scenario. Older formation and role of NCG 7317 should be considered in revised numer-  
 18 ical models of the compact group. Velocities of group members to recreate are estimated  
 19 from redshift measurements. Several effects contribute to observed redshifts and a new  
 20 effect is predicted to be the result of the gravitational interaction between photons and  
 21 constant magnetic fields creating gravitational waves. The energy carried by these waves  
 22 is manifested as redshifts of the photons. Cosmological simulation data are used to prove  
 23 the significant contribution of our effect. The analysis of synthetic observations created  
 24 from those simulations has shown that redshifts of SQ members could be misinterpreted  
 25 as caused only from Doppler Effect. The revised models of the group should consider  
 26 a new method to recreate the formation scenario based on redshift patterns and not  
 27 misestimated velocities.

28 *Keywords:* Magnetic fields; gravitational waves; redshift; Stephan's quintet; numerical  
 29 simulations.

30 PACS Nos.: 04.20.-q, 04.30.Db, 95.85.Sz, 98.62.Py

31 **1. Introduction**

32 The famous Stephen's Quintet (SQ) was subject of several previous studies (e.g. see  
 33 Refs. 1 and 2). This compact group of gravitationally interacting galaxies is a place  
 34 of interesting phenomena and a test field for various theories. Arp<sup>3</sup> believed that  
 35 the light from NCG 7320 is affected by non-Doppler effects making it appear to  
 36 be a foreground galaxy. Later observations indicated the role of NCG 7320c in the  
 formation scenario of SQ and gave evidence to the foreground position of NCG 7320.

1950342-1

# Bibliography

- [1] Riess A. G. et al., 2016, *Astrophys. J.*, 826, 56
- [2] Ade P. A. R. et al., 2016, *Astron. Astrophys.*, 594, A13
- [3] Sinclair B., Davis T. M., Haugbolle T., 2010, *Astrophys. J.*, 718, 1445
- [4] Sadeh I., Feng L. L., Lahav O., 2015, *Phys. Rev. Lett.*, 114, 071103
- [5] Calcino J., Davis T., 2017, *JCAP*, 01, 038
- [6] Lopez-Corredoira M., Gutierrez C. M., 2002, *Astron. Astrophys.*, 390, L15
- [7] Lopez-Corredoira M., Gutierrez C. M., 2006, *AIP Conf. Proc.*, 822, 75
- [8] Arp H. C., 2003, *Catalogue of discordant redshift associations*. Apeiron, Quebec, Canada
- [9] Sulentic J. W., Rosado M., Dultzin-Hacyan D., Verdes-Montenegro L., Trinchieri G., Xu C., Pietsch M., 2001, *Astron. J.*, 122, 2993
- [10] Arp H. C., 1973, *Astrophys. J.*, 183, 411
- [11] EAS, 2001, *Astron. Astrophys. Rev.*, 19, 45.
- [12] Xu Y. et al., 2015, *Astrophys. J.*, 801, 105
- [13] Leavitt H. S., Pickering E., 1912, *Harvard College Observatory Circular*, 173, 1
- [14] Hillebrandt W., Hoflich P., 1989, *Rep. Prog. Phys.*, 52, 1421
- [15] Burrows A., Goshy J., 1993, *Astrophys. J. Lett.*, 416, L75
- [16] Wang Y., 2009, *Phys. Rev.*, D80, 123525
- [17] Tully R. B., Fisher J. R., 1977, *Astron. Astrophys.*, 54, 661
- [18] Bonhomme N., Courtois H. M., Tully R. B., 2008, *Derivation of Distances with the Tully-Fisher Relation: The Antlia Cluster*, arXiv:0806.1140 [astro-ph]
- [19] An D., Terndrup D. M., Pinsonneault M. H., 2007, *Astrophys. J.*, 671, 1640
- [20] Mitchell R. C. et al., 2002, *Astrophys. J.*, 574, 293
- [21] Sakai S., 1999, Katsuhiko Sato, ed. *The Tip of the Red Giant Branch as a Population II Distance Indicator*. Proceedings of the 183rd symposium of the International Astronomical Union. Dordrecht, Boston: Kluwer Academic.
- [22] Oesch P. A. et al., 2016, *Astrophys. J.*, 819, 129

## BIBLIOGRAPHY

- [23] Hubble E., 1929, Proc. Nat. Acad. Sci., 15, 168
- [24] Williams R. E. et al., 1996, Astron. J., 112, 1335
- [25] Perlmutter S. et al., 1999, Astrophys. J., 517, 565
- [26] Riess A. G. et al., 1998, Astron. J., 116, 1009
- [27] Sofue Y., Tutui Y., Honma M., Tomita A., Takamiya T., Koda J., Takeda Y., 1999, Astrophys. J., 523, 136
- [28] Sofue Y., Rubin V., 2001, Ann. Rev. Astron. Astrophys., 39, 137
- [29] Rubin V. C., Ford W. K., 1970, Astrophys. J., 159, 379
- [30] Roberts M. S., Whitehurst R. N., 1975, Astrophys. J., 201, 327
- [31] Rubin V. C., Thonnard N., Ford W. K., 1980, Astrophys. J., 238, 471
- [32] Bosma A., 1981, Astron. J., 86, 1825
- [33] Hubble E. P., 1936, The Realm of the Nebulae. New Haven: Yale University Press. LCCN 36018182
- [34] Persic M., Salucci P., Stel F., 1996, Mon. Not. Roy. Astron. Soc., 281, 27
- [35] Zwicky F., 1933, Helvetica Physica Acta, 6, 110
- [36] Weinberg S., 2008, Cosmology, Oxford, UK: Oxford Univ. Pr.
- [37] Primack J. R., 1996 Dark Matter and Structure Formation in the Universe, Chapter 1 of Formation of Structure in the Universe, Proceedings of the Jerusalem Winter School 1996, edited by A. Dekel and J.P. Ostriker (Cambridge University Press). SCIPP/96-59 rev 7/97 Cite as: arXiv:astro-ph/9707285
- [38] Peebles J., Yu J., 1970, Astrophys. J., 162, 815
- [39] Dodelson S., 2017, Gravitational Lensing, Cambridge, UK: Cambridge University Press.
- [40] Clowe D., Bradac M., Gonzalez A. H., Markevitch M., Randall S. W., Jones C., Zaritsky D., 2006, Astrophys. J., 648, L109
- [41] Alpher R. A., Bethe H., Gamow G., 1948, Phys. Rev., D73, 803804
- [42] Penzias A. A., Wilson R. W., 1965, Astrophys. J., 142, 419
- [43] Smoot G. F. et al., 1992, Astrophys. J., 396, L1L5
- [44] Adam R. et al., 2016, Planck 2015 results. I. Overview of products and scientific results. Astron. Astrophys., 594, A1
- [45] Bouchet F. R. et al., 2011, COre (Cosmic Origins Explorer) A White Paper. arXiv:1102.2181 [astro-ph.CO]
- [46] de Bernardis P. et al., 2000, Nature, 404, 955

## BIBLIOGRAPHY

- [47] Piattella O., 2018, Lecture Notes in Cosmology. UNITEXT for Physics. Springer International Publishing DOI: 10.1007/978-3-319-95570-4 arXiv:1803.00070 [astro-ph.CO]
- [48] Wu K. K. S., Lahav O., Rees M. J., 1999, *Nature*, 397, 225
- [49] Sarkar S., Pandey B., 2016, *Mon. Not. Roy. Astron. Soc.*, 463(1), L12L16
- [50] Giblin J. T., Mertens J. B., Starkman G. D., 2016, *Astrophys. J.*, 833(2), 247
- [51] Friedmann A., 1922, *Z. Phys.*, 10, 377
- [52] Friedmann A., 1924, *Z. Phys.*, 21, 326
- [53] Robertson H. P., 1935, *Astrophys. J.*, 82, 284
- [54] Robertson H. P., 1936, *Astrophys. J.*, 83, 257
- [55] Walker A. G., 1937, *Proc. London Mathematical Soc.*, 2(1), 90127
- [56] Lemaitre G., 1931, *Mon. Not. Roy. Astron. Soc.*, 91, 490
- [57] Schutz B. F., 1985, *A First Course In General Relativity*. Cambridge, Uk: Univ. Pr.
- [58] Ade P. A. R. et al., 2016a, Planck 2015 results. XIII. Cosmological parameters. *Astron. Astrophys.*, 594, A13
- [59] Bertone G., Hooper D., 2016, *A History of Dark Matter*. FERMILAB-PUB-16-157-A, arXiv:1605.04909 [astro-ph.CO]
- [60] Profumo S., 2017, *An Introduction to Particle Dark Matter*. Advanced textbooks in physics. World Scientific.
- [61] Camarena D., Marra V., 2016, *Eur. Phys. J.*, C76(11), 644
- [62] Lesgourgues J., Pastor S., 2006, *Phys. Rept.*, 429, 307
- [63] Sandage A., 1962, *Astrophys. J.*, 136, 319
- [64] McVittie G. C., 1962, *Astrophys. J.*, 136, 334
- [65] Piattella O. F., Giani L., 2017, *Phys. Rev.*, D95(10), 101301
- [66] Hogg D. W., 1999, *Distance measures in cosmology*. arXiv:astro-ph/9905116
- [67] Etherington I. M. H., 1933, *On the Definition of Distance in General Relativity*. *Philosophical Magazine*, 15.
- [68] Aronson E. B., Hansen C. J., 1972, *Astrophys. J.*, 177, 145
- [69] Raychaudhuri A. K., 1979, *Theoretical cosmology*, Oxford, Clarendon Press; New York, Oxford University Press.
- [70] Peebles P. J. E., 1968, *Astrophys. J.*, 153, 1
- [71] Lindegren L., Perryman M. A. C., 1996, *Astron. Astrophys. Suppl. Ser.*, 116, 579
- [72] Conley A. et al., 2006, *Astrophys. J.*, 644, 1

## BIBLIOGRAPHY

- [73] Wang S., Hu Y., Li M., Li N., 2016, *Astron. Astrophys.*, 592, A101
- [74] Sandage A., 1958, *Astrophys. J.*, 127, 513
- [75] Tammann G. A., 1974, The Hubble Constant and the Deceleration Parameter. In: Longair M.S. (eds) *Confrontation of Cosmological Theories with Observational Data*. International Astronomical Union / Union Astronomique Internationale, vol 63. Springer, Dordrecht
- [76] de Vaucouleurs G., 1986, New Results on the Distance Scale and the Hubble Constant. In: Madore B.F., Tully R.B. (eds) *Galaxy Distances and Deviations from Universal Expansion*. NATO ASI Series (Series C: Mathematical and Physical Sciences), vol 180. Springer, Dordrecht
- [77] Tipler F. J., 1999, *Astrophys. J.*, 511, 546
- [78] Schmidt B. P. et al., 1998, *Astrophys. J.*, 507, 46
- [79] Koopmans L. V. E., Fassnacht C. D., 1999, *Astrophys. J.*, 527, 513
- [80] Reese E. D., 2004, Measuring the Hubble constant with Sunyaev-Zel'dovich effect, "Measuring and Modeling the Universe", from the Carnegie Observatories Centennial Symposia. Published by Cambridge University Press, as part of the Carnegie Observatories Astrophysics Series. Edited by W. L. Freedman, 2004, p. 138
- [81] Melnick J., Terlevich R., Moles M., 1988, *Mon. Not. Roy. Astron. Soc.*, 235, 297
- [82] Bernal J. L. et al., 2016, *JCAP*, 10, 019
- [83] Freedman W. L., Madore B. F., 2010, *Ann. Rev. Astron. Astrophys.*, 48, 673
- [84] Grieb J. N. et al., 2017, *Mon. Not. Roy. Astron. Soc.*, 467(2), 2085
- [85] Newman J. A., Ferrarese L., Stetson P. B., Maoz E., Zepf S. E., Davis M., Freedman W. L., Madore B. F., 2001, *Astrophys. J.*, 553, 562
- [86] Bonvin V. et al., 2017, *Mon. Not. Roy. Astron. Soc.*, 465(4), 4914
- [87] Abbott B. P. et al., 2017b, *Nature*, 551(7678), 8588
- [88] Rauscher B. J. et al., 2017, *PASP*, 129, 105003
- [89] Martin J., 2012, *Comptes Rendus Physique*, 13, 566
- [90] Zlatev I., Wang L.-M., Steinhardt P. J., 1999, *Phys. Rev. Lett.*, 82, 896
- [91] Amendola L., Tsujikawa S., 2010, *Dark energy: theory and observations*. Cambridge University Press.
- [92] Warren M. S., Abazajian K., Holz D. E., Teodoro L., 2006, *Astrophys. J.*, 646, 881
- [93] Bullock J. S., Boylan-Kolchin M., 2017, *Ann. Rev. Astron. Astrophys.*, 55, 343
- [94] Moore B., 1994, *Nature*, 370, 629
- [95] Klypin A. A., Kravtsov A. V., Valenzuela O., Prada F., 1999, *Astrophys. J.*, 522, 8292

## BIBLIOGRAPHY

- [96] Boylan-Kolchin M., Bullock J. S., Kaplinghat M., 2011, *Mon. Not. Roy. Astron. Soc.*, 415, L40
- [97] Kirby E. N., Bullock J. S., Boylan-Kolchin M., Kaplinghat M., Cohen J. G., 2014, *Mon. Not. Roy. Astron. Soc.*, 439(1), 1015
- [98] Spergel D. N., Steinhardt P. J., 2000, *Phys. Rev. Lett.*, 84, 3760
- [99] Vogelsberger M., Zavala J., Simpson C., Jenkins A., 2014, *Mon. Not. Roy. Astron. Soc.*, 444, 3684
- [100] Maccio A. V., Mainini R., Penzo C., Bonometto S. A., 2015, *Mon. Not. Roy. Astron. Soc.*, 453, 1371
- [101] Marra V., Amendola L., Sawicki I., Valkenburg W., 2013, *Phys. Rev. Lett.*, 110(24), 241305
- [102] Verde L., Protopapas P., Jimenez R., 2013, *Phys. Dark Univ.*, 2, 166
- [103] Battye R. A., Charnock T., Moss A., 2015, *Phys. Rev.*, D91(10), 103508
- [104] Abbott T. M. C. et al., 2017d, Dark Energy Survey Year 1 Results: Cosmological Constraints from Galaxy Clustering and Weak Lensing. FERMILAB-PUB-17-294-PPD, arXiv:1708.01530 [astro-ph.CO]
- [105] Valkenburg W., Marra V., Clarkson C., 2014, *Mon. Not. Roy. Astron. Soc.*, 438, L6L10
- [106] Schwarz D. J., Copi C. J., Huterer D., Starkman G. D., 2016, *Class. Quant. Grav.*, 33(18), 184001
- [107] Coc A., 2016, *J. Phys. Conf. Ser.*, 665(1), 012001
- [108] Abbott B. P. et al., 2016b, *Phys. Rev. Lett.*, 116(6), 061102
- [109] Abbott B. P. et al., 2016a, *Phys. Rev. Lett.*, 116(24), 241103
- [110] Silk J. et al., 2010, *Particle Dark Matter: Observations, Models and Searches*. Cambridge Univ. Press, Cambridge.
- [111] Dodelson S., Widrow L. M., 1994, *Phys. Rev. Lett.*, 72, 1720
- [112] Peccei R. D., Quinn H. R., 1977, *Phys. Rev. Lett.*, 38, 1440
- [113] Gaskins J. M., 2016, *Contemp. Phys.*, 57(4), 496
- [114] Liu J., Chen X., Ji X., 2017, *Nature Phys.*, 13(3), 212
- [115] Kollmeier J. A. et al., 2017, SDSS-V: Pioneering Panoptic Spectroscopy. arXiv:1711.03234 [astro-ph.GA]
- [116] Furlanetto S. R., Loeb A., 2001, *Astrophys. J.*, 556, 619
- [117] Frisch P. C., 2007, preprint(arXiv:0707.2970 [astro-ph])
- [118] Murase K., Takahashi K., Inoue S., Ichiki K., Nagataki S., 2008, *Astrophys. J.*, 686, L67

## BIBLIOGRAPHY

- [119] Anderson J., 2012, preprint(arXiv:1203.2467 [astro-ph.IM])
- [120] De Gouveia Dal Pino E. M., 2006, AIP Conf. Proc., 875, 289
- [121] Beck R., 2011, AIP Conf. Proc., 1381, 117
- [122] Pogosian L., Vachaspati T., Yadav A., 2013, Canadian J. Phys., 91, 451
- [123] Pogosian L., 2014, J. Phys.: Conf. Ser., 496, 012025
- [124] Schiffer P., 2011, PhD thesis, Aachen, Tech. Hochsch. Aachen
- [125] Taylor J. H., Cordes J. M., 1993, Astrophys. J., 411, 674
- [126] Vallee J. P., 2013, International J. Astron. Astrophys., 3, 99
- [127] Frick P., Sokoloff D., Stepanov R., Beck R., 2011, Mon. Not. Roy. Astron. Soc., 414, 2540
- [128] Akahori T., Gaensler B. M., Ryu D., 2014, Astrophys. J., 790, 123
- [129] Oppermanet N. et al., 2015, Astron. Astrophys., 575, A118
- [130] Durrer R., Neronov A., 2013, Astron. Astrophys. Rev., 21, 62
- [131] Kulsrud R. M., Zweibel E. G., 2008, Rept. Prog. Phys., 71, 0046091
- [132] Biermann L., 1950, Z. Naturf., A5, 65
- [133] Lazar M., Schlickeiser R., Wielebinski R., Poedts S., 2009, Astrophys. J., 693, 1133
- [134] Gregori G., Ravasio A., 2012, Nature, 481, 480
- [135] Xu H., Li H., Collins D. C., Li S., Norman M. L., 2009, Astrophys. J., 698, L14
- [136] Kandus A., Kunze K. E., Tsagas C. G., 2011, Phys. Rept., 505, 1
- [137] Kahniashvili T., Brandenburg A., Tevzadze A. G., 2016, Physica Scripta, 91, 104008
- [138] Grasso D., Rubinstein H. R., 2001, Phys. Rept., 348, 163
- [139] Somov B. V., 2012, Fundamentals of Cosmic Electrodynamics, Springer Science & Business Media.
- [140] Schober J., Schleicher D., Federrath C., Klessen R., Banerjee R., 2012, Phys. Rev. E., 85, 026303
- [141] Kulsrud R., Cowley S. C., Gruzinov A. V., Sudan R. N., 1997, Phys. Rep., 283, 213
- [142] Bassett B. A., Pollifrone G., Tsujikawa S., Viniegra F., 2001, Phys. Rev., D63, 103515
- [143] Zeldovich Y. B., Ruzmaikin A. A., Sokoloff D. D., 1980, Magnetic Fields in Astrophysics, Mc Graw Hill, New York.
- [144] Sur S., Federrath C., Schleicher D. R. G., Banerjee R., Klessen R. S., 2012, Mon. Not. Roy. Astron. Soc., 423, 3148
- [145] Jedamzik K., Katalinic V., Olinto A. V., 2000, Phys. Rev. Lett., 85, 700

## BIBLIOGRAPHY

- [146] Chluba J., Paoletti D., Finelli F., Rubio-Martín J. A., 2015, *Mon. Not. Roy. Astron. Soc.*, 451(2), 2244
- [147] Dolag K., Kachelriess M., Ostapchenko S., Tomas R., 2011, *Astrophys. J.*, 727, L4
- [148] Harrison E. R., 1973, *Phys. Rev. Lett.*, 30, 188
- [149] Kosowsky A., Loeb A., 1996, *Astrophys. J.*, 469, 1
- [150] Fleishman G. D., Toptygin I. N., 2013, *Cosmic Electrodynamics: Electrodynamics and Magnetic Hydrodynamics of Cosmic Plasmas*, Springer Science & Business Media.
- [151] Beck M. C., Beck A. M., Beck R., Dolag K., Strong A. W., Nielaba P., 2016, *JCAP*, 05, 056
- [152] Bonometto S. A., Pantano O., 1993, *Phys. Rep.*, 228, 175
- [153] Cheng B., Olinto A., 1994, *Phys. Rev.*, D50, 2421
- [154] Kahniashvili T., Tevzadze A. G., Ratra B., 2011, *Astrophys. J.*, 726, 78
- [155] Turner M. S., Widrow L. M., 1988, *Phys. Rev.*, D37, 2743
- [156] Dolgov A., Silk J., 1993, *Phys. Rev.*, D47, 3144
- [157] Ashoorioon A., Mann R. B., 2005, *Phys. Rev.*, D71, 103509
- [158] Bartolo N., Matarrese S., Riotto A., Vaihkonen A., 2007, *Phys. Rev.*, D76, 061302
- [159] Harmuth H. F., Barrett T. W., Meffert B., 2001, *Modified Maxwell Equations in Quantum Electrodynamics*, World Scientific.
- [160] Leggett A. J., Sols F., 1991, *Foundations of Physics*, 21(3), 353
- [161] Caprini C., Ferreira P. G., 2005, *JCAP*, 02, 006
- [162] Altherr T., Salati P., 1994, *Nuclear Physics B*, 421(3), 662
- [163] Harrison E. R., 1970, *Mon. Not. Roy. Astron. Soc.*, 147, 279
- [164] Miyamoto K., Sekiguchi T., Tashiro H., Yokoyama S., 2014, *Phys. Rev.*, D89(6), 063508
- [165] Tsagas C. G., Maartens R., 2000, *Phys. Rev.*, D61, 083519
- [166] Saro A. et al., 2014, *Mon. Not. Roy. Astron. Soc.*, 440, 2610
- [167] Zucca A., Li Y., Pogosian L., 2017, *Phys. Rev.*, D95, 063506
- [168] Kahniashvili T., Tevzadze A. G., Sethi S. K., Pandey K., Ratra B., 2010, *Phys. Rev.*, D82, 083005
- [169] Jackson J. D., 1998, *Classical Electrodynamics*, 3rd Edition. Wiley-VCH.
- [170] Griffiths D. J., 2017, *Introduction to Electrodynamics*, Cambridge, UK: Cambridge University Press.

## BIBLIOGRAPHY

- [171] Kamionkowski M., Kosowsky A., Stebbins A., 1997, *Phys. Rev. Lett.*, 78, 2058
- [172] Fenu E., Pitrou C., Maartens R., 2011, *Mon. Not. Roy. Astron. Soc.*, 414, 2354
- [173] Seshadri T. R., Subramanian K., 2001, *Phys. Rev. Lett.*, 87, 101301
- [174] Kawasaki M., Kusakabe M., 2012, *Phys. Rev.*, D86, 063003
- [175] Cuoco A., Iocco F., Mangano G., Miele G., Pisanti O., Serpico P. D., 2004, *Int. J. Mod. Phys. A*, 19, 4431
- [176] Noterdaeme P., Lopez S., Dumont V., Ledoux C., Molaro P., Petitjean P., 2012, *Astron. Astrophys.*, 542, L33
- [177] Hogan C. J., 1983, *Phys. Rev. Lett.*, 51, 1488
- [178] Widrow L. M., Ryu D., Schleicher D. R. G., Subramanian K., Tsagas C. G., Treumann R. A., 2012, *Space Sci. Rev.*, 166, 37
- [179] Gaisser T. K., 1990, *Cosmic Rays and Particle Physics*, Cambridge University Press, Cambridge.
- [180] Nagano M., Watson A. A., 2000, *Rev. Mod. Phys.*, 72, 689
- [181] Pierre Auger Collaboration, 2008a, *Nuclear Instruments and Methods in Physics Research A*, 586, 409
- [182] Pierre Auger Collaboration, 2010, *Nucl. Instrum. Meth. A*, 620, 227
- [183] Yoshida S. et al., 1995, *Astropart. Phys.*, 3, 105
- [184] Pierre Auger Collaboration, 2008b, *Phys. Rev. Lett.*, 101, 061101
- [185] Abbasi R. U. et al., 2008, (HiRes Collaboration), *Phys. Rev. Lett.*, 100, 101101
- [186] Blumer J., Engel R., Horandel J. R., 2009, *Progress in Particle and Nuclear Physics*, 63, 293
- [187] Aloisio R., 2006, Galactic and extragalactic cosmic rays, *Frontier Objects in Astrophysics and Particle Physics*, Vulcano Workshop 2008, held 22-27, 2006 in Vulcano, Italy. Edited by F. Giovannelli and G. Mannocchi., p.429
- [188] Allard D., Parizot E., Olinto A. V., 2007, *Astropart. Phys.*, 27, 61
- [189] Lemoine M., Vangioni-Flam E., Casse M., 1998, *Astrophys. J.*, 499, 735
- [190] Bird D. J. et al., 1995, *Astrophys. J.*, 441, 144
- [191] Abreu P. et al., 2010, *Astropart. Phys.*, 34, 314
- [192] Bell A. R., Lucek S. G., 2001, *Mon. Not. Roy. Astron. Soc.*, 321, 433
- [193] Ginzburg V. L., Syrovatskii, 1964, *Soviet Physics (JETP)*, 18, 245
- [194] Carroll B. W., Ostlie D. A., 1996, *An introduction to modern astrophysics*, Addison-Wesley Publishing Company, inc.
- [195] Greisen K., 1966, *Phys. Rev. Lett.*, 16, 748

## BIBLIOGRAPHY

- [196] Zatsepin G. T., Kuzmin V. A., 1966, *Pisma Zh. Eksp. Teor. Fiz.*, 4, 114
- [197] Kneiske T. M., Bretz T., Mannheim K., Hartmann D. H., 2004, *Astron. Astrophys.*, 413, 807815
- [198] Lemoine M., 2013, *J. Phys. Conf. Ser.*, 409(1), 012007
- [199] Kampert K.-H. et al., 2017, (Pierre Auger Collaboration), *AIP Conf. Proc.*, 1852, 040001
- [200] Hillas A.M., 1984, *Ann. Rev. Astron. Astrophys.*, 22, 425
- [201] Anchordoqui L., Paul T., Reucroft S., Swain J., 2003, *Int. J. Mod. Phys. A*, 18, 2229
- [202] Tinyakov P. G., Tkachev I. I., 2001, *Journal of Experimental and Theoretical Physics Letters*, 74, 1
- [203] Evans N. W., Ferrer F., Sarkar S., 2003, *Phys. Rev.*, D67, 103005
- [204] Yoshiguchi H., Nagataki S., Sato K., 2003, *Astrophys. J.*, 592, 311
- [205] Franceschini A., Rodighiero G., Vaccari M., 2008, *Astron. Astrophys.*, 487, 837
- [206] Samuelson F. W. et al., 1998, *Astrophys. J.*, 501, L17
- [207] Baus C., Engel R., Pierog T., Ulrich R., Unger M., 2011, *ICRC 2011 Conf. Proc.* (icrc2011.ihep.ac.cn)
- [208] Stasyszyn F., Nuza S. E., Dolag K., Beck R., Donnert J., 2010, *Mon. Not. Roy. Astron. Soc.*, 408, 684
- [209] Gingold R. A., Monaghan J. J., 1977, *Mon. Not. Roy. Astron. Soc.*, 181, 375
- [210] Lucy L.B., 1977, *Astrophys. J.*, 82, 1013
- [211] Springel V., 2005, *Mon. Not. Roy. Astron. Soc.*, 364, 1105
- [212] O'Shea B., Bryan G., Bordner J., Norman M., Abel T., Harkness R., Kritsuk A., 2005, *Lect. Notes Comput. Sci. Eng.*, 41, 341
- [213] Springel V., 2014, preprint(arXiv:1412.5187 [astro-ph.GA])
- [214] Teyssier R., 2002, *Astron. Astrophys.*, 385, 337
- [215] Pearce F. R., Couchman H. M. P., 1997, *New Astron.*, 2, 411
- [216] Wadsley J.W., Stadel J., Quinn T., 2004, *New Astron.*, 9, 137
- [217] Matthias S., 1996, *Mon. Not. Roy. Astron. Soc.*, 278, 1005
- [218] Ziegler U., 2005, *Astron. Astrophys.*, 435, 385
- [219] Mignone A., Plewa T., Bodo G., 2005, *Astrophys. J.*, 160, 199
- [220] Hayes J. et al., 2006, *Astrophys. J. Suppl.*, 165, 188
- [221] Kravtsov A., Klypin A., Homan Y., 2002, *Astrophys. J.*, 571, 563

## BIBLIOGRAPHY

- [222] Stone J. et al., 2008, *Astrophys. J. Suppl.*, 178, 137
- [223] Brandenburg A., Dobler W., 2002, *Comput. Phys. Comm.*, 147, 471
- [224] Gonzalez M., Audit E., Huynh P., 2007, *Astron. Astrophys.*, 464, 429
- [225] Krumholz M. R., Klein R. I., McKee C. F., Bolstad J., 2007, *Astrophys. J.*, 667, 626
- [226] Mignone A. et al., 2007, *Astrophys. J. Suppl.*, 170, 228
- [227] Almgren A. et al., 2010, *Astrophys. J.*, 715, 1221
- [228] Schive H., Tsai Y., Chiueh T., 2010, *Astrophys. J.*, 186, 457
- [229] Springel V. et al., 2005, *Nature*, 435, 629
- [230] Boylan-Kolchin M., Springel V., White S. D. M., Jenkins A., Lemson G., 2009, *Mon. Not. Roy. Astron. Soc.*, 398, 1150
- [231] Vogelsberger M. et al., 2014, *Mon. Not. Roy. Astron. Soc.*, 444, 1518
- [232] Fosalba P., Gaztanaga E., Castander F. J., M. Crocce M., 2015, *Mon. Not. Roy. Astron. Soc.*, 447, 1319
- [233] Prada F., Klypin A. A., Cuesta A. J., Betancort-Rijo J. E., Primack J., 2012, *Mon. Not. Roy. Astron. Soc.*, 423, 3018
- [234] Skillman S. W., Warren M. S., Turk M. J., Wechsler R. H., Holz D. E., Sutter P. M., 2014, preprint(arXiv:1407.2600 [astro-ph.CO])
- [235] Heitmann K. et al., 2015, *Astrophys. J. Suppl.*, 219, 34
- [236] Mathis H., Lemson G., Springel V., Kauffmann G., White S. D. N., Eldar A., Dekel A., 2002, *Mon. Not. Roy. Astron. Soc.*, 333, 739
- [237] Manfred K., 2008, PhD thesis, LMU Munchen: Faculty of Physics
- [238] Knebe A. et al., 2013, *Mon. Not. Roy. Astron. Soc.*, 428, 2039
- [239] Merson I. A. et al., 2013, *Mon. Not. Roy. Astron. Soc.*, 429, 556
- [240] Shattow G. M., Croton D. J., 2015, *Mon. Not. Roy. Astron. Soc.*, 452, 1779
- [241] Ford . B. et al., 2016, *Mon. Not. Roy. Astron. Soc.*, 459, 1745
- [242] Marulli F., Veropalumbo A., Moscardini L., Cimatti A., Dolag K., 2017, *Astron. Astrophys.*, 599, A106
- [243] Tempel E., Guo Q., Kipper R., Libeskind N. I., 2015, *Mon. Not. Roy. Astron. Soc.*, 450, 2727
- [244] Libeskind N. I., Hoffman Y., Tully R. B., Courtois H. M., Pomaredo D., Gottlober S., Steinmetz M., 2015, *Mon. Not. Roy. Astron. Soc.*, 452, 1052
- [245] Burns J. O., Skillman S. W., 2011, *Memorie della Societa Astronomica Italiana*, 82, 615

## BIBLIOGRAPHY

- [246] Dolag K., Bartelmann M., Lesch H., 1999, *Astron. Astrophys.*, 348, 351
- [247] Dolag K., Grasso D., Springel V., Tkachev I., 2004, *J. Korean Astron. Soc.*, 37, 427
- [248] Fromang S., Hennebelle P., Teyssier R., 2006, *Astron. Astrophys.*, 457, 371
- [249] Marinacci F., Vogelsberger M., Mocz P., Pakmor R., 2015, *Mon. Not. Roy. Astron. Soc.*, 453, 3999
- [250] Rasia E. et al., 2015, *Astrophys. J. Lett.*, 813, L17
- [251] Kolb E. W., Turner M. S., 1990, *Front. Phys.*, 69, 1547
- [252] Colonna G., Boltzmann and Vlasov equations in plasma physics, *Plasma Modeling : Methods and Applications*, <https://doi.org/10.1088/978-0-7503-1200-4ch1>
- [253] Saha M. N., 1921, *Proc. Roy. Soc. A: Mathematical, Physical and Engineering Sciences.*, 99, 135
- [254] Hinshaw G. et al., 2013, *Astrophys. J. Suppl.*, 208, 19
- [255] Fixsen D. J., 2009, *Astrophys. J.*, 707, 916
- [256] Funchal R. Z., Schmauch B., Geisen G., 2013, *The Physics of Neutrinos*, ArXiv:hep-ph/1308.1029.
- [257] Rich J., 2010, *Fundamentals of Cosmology*, Chapter 1(p34), Springer Science Press.
- [258] Abdelali M. L., Mebarki N., 2015, *J. Phys.: Conf. Ser.*, 593, 012013
- [259] Dodelson S., 2003, *Modern Cosmology*, Chapter:3,4, Academic Press.
- [260] Gopal R., Sethi S., 2005, *Mon. Not. Roy. Astron. Soc.*, 363, 521
- [261] Banerjee R., Jedamzik K., 2004, *Phys. Rev.*, D70, 123003
- [262] Berezhiani Z., Dolgov A.D., 2004, *Astropart. Phys.*, 21, 59
- [263] Tsagas C. G., 2005, *Class. Quant. Grav.*, 22, 393
- [264] Maknickas A. A., 2013, *J. Mod. Phys.*, 4, 105
- [265] Deng Y., Mannheim P. D., 1988, *Gen. Relat. Gravit.*, 20, 969
- [266] Hadamard J., 1923, *Lectures on Cauchy's Problem*, Yale Univ. Press, New Haven, CT.
- [267] Skrotskii G. V., 1957, *Sov.Phys.-Dokl.*, 2, 226
- [268] Plebanski J., 1960, *Phys. Rev.*, 118, 1396
- [269] Abdelali M. L., Mebarki N., 2014, *Science & Technology A*, 40, 105
- [270] Wojtak R., Hansen S. H., Hjorth J., 2011, *Nature*, 477, 567
- [271] Wojtak R., Davis T. M., Wiis J., 2015, *JCAP*, 07, 025
- [272] Fischer E., 2008, *Energy Loss by Gravitational Viscosity*, arXiv:0805.1638 [astro-ph]

## BIBLIOGRAPHY

- [273] Yatsunenko Y. A., Budagov J. A., 2011, Red Shift in a Laboratory Environment, arXiv:1103.0808 [physics.gen-ph]
- [274] Schuster D., 2007, An Alternative Explanation for Cosmological Redshift, arXiv:0706.2885 [physics.gen-ph]
- [275] Ivanov M. A., 2002, *Class. Quant. Grav.*, 19, 1351
- [276] Crawford D. F., 2011, *J. Cosmology*, 13, 3875
- [277] Moore M., Dunning-Davies J., 2007, Reflections and Thoughts on Tired Light, arXiv:0707.3351 [physics.gen-ph]
- [278] Crawford D. F., 2011, *J. Cosmology*, 13, 3947
- [279] Crawford D. F., 1999, *Austral.J.Phys.*, 52, 753
- [280] Ji-Xiong P., Chao C., 2004, *Chinese Phys. Lett.*, 21, 1268
- [281] Bisht N. S., Yadav B. K., Kanseri B., Kandpal H. C., Sharma E. K., 2010, *Optik*, 121, 581
- [282] Rojas H. P., Querts E. R., 2009, *Phys. Rev.*, D79, 093002
- [283] Rojas H. P., Querts E. R., Helayel-Neto J. A., 2011, *Int. J. Mod. Phys.*, E20, 176
- [284] Shabad A. E., Usov V. V., 1986, *Astrophysics and Space Science*, 128, 377
- [285] Shabad A. E., 2004, *J. Experimental and Theoretical Phys.*, 98, 186
- [286] Wolf E., 1987, *Nature*, 326, 363
- [287] Bocko M. F., Douglass D. H., Knox R. S., 1987, *Phys. Rev. Lett.*, 58, 2649
- [288] Faklis D., Morris G. M., 1988, *Optics Letters*, 13, 4
- [289] James D. F. V., 1998, *Pure Appl. Opt.*, 7, 959
- [290] Roy S., Kafatos M., Datta S., 1999, preprint(arXiv:astro-ph/9904061)
- [291] Gbur G., Visser T. D., Wolf E., 2001, *Phys. Rev. Lett.*, 88, 013901
- [292] Popescu G., Dogariu A., 2002, *Phys. Rev. Lett.*, 88, 183902
- [293] Hobson M. P., Efstathiou G. P., Lasenby A. N., 2006, *General Relativity : An Introduction for Physicists*, Cambridge University Press, Cambridge U.K.
- [294] Guenther R. D., 1990, *Modern optics*, John Wiley & Sons, U.S.A.
- [295] Abdelali M. L., Mebarki N., 2019, Redshift effects implications on revised models of Stephan's quintet, *Modern Physics Letters A*, 1950342, DOI: 10.1142/S0217732319503425, arXiv:1806.02899v1 [gr-qc]
- [296] de Sabbata V., Gasperini M., 1985, *Introduction to Gravitation*. World Scientific Publishing
- [297] Gertsenshtein M. E., 1962, *Sov. Phys. JETP Lett.*, 14, 84

## BIBLIOGRAPHY

- [298] Zeldovich Y. B., 1973, *Sov. Phys. JETP*, 65, 1311
- [299] Kolosnitsyn N. I., Rudenko V. N., 2015, *Phys. Scripta*, 90(7), 074059
- [300] Cillis A. N., Harari D. D., 1996, *Phys. Rev.*, D54, 4757
- [301] Pshirkov M. S., Baskaran D., 2009, *Phys. Rev.*, D80, 042002
- [302] Ejlli D., 2013, *Phys. Rev.*, D87, 124029
- [303] Grishchuk L. P., 2003, preprint(arXiv:gr-qc/0306013)
- [304] Abdelali M. A., Mebarki N., 2012, *AIP: Conference Proceedings*, 1444, 413
- [305] Hulse R. A., Taylor J. H., 1975, *Astrophys. J.*, 195, L51
- [306] Weisberg J. M., Nice D. J., Taylor J. H., 2010, *Astrophys. J.*, 722, 1030
- [307] Brown W. R., Kilic M., Hermes J. J., Prieto C. A., Kenyon S. J., Winget D. E., 2011, *Astrophys. J. Lett.*, 737, L23
- [308] Kronberg P., 1994, *Rep. Prog. Phys.*, 57, 325
- [309] Bahcall N., 1998, *Astrophys. J.*, 504, 1
- [310] Valle J. P., 1990, *Astron. J.*, 99, 459
- [311] Al Mamon A., Das S., 2017, *Eur. Phys. J. C.*, 77, 495
- [312] Pierre Auger Collaboration, 2007, *Science*, 318, 938
- [313] Wibig T., 2004, *C. Eur. J. Phys.*, 2, 2
- [314] Farrar G. R., Piran T., 2000, *Phys. Rev. Lett.*, 84, 3527
- [315] Massaglia S., 2009, *Nuclear Phys. B Proc. Suppl.*, 190, 79
- [316] Dedenko L. G., Podgrudkov D. A., Roganova T. M., Fedorova G. F., 2008, The most energetic cosmic rays and their possible sources, arXiv:0811.0722 [astro-ph]
- [317] Amelino-Camelia G., Piran T., 2001, *Phys. Rev.*, D64, 036005
- [318] Barcaroli L., Brunkhorst L. K., Gubitosi G., Loret N., Pfeifer C., 2017, *Phys. Rev.*, D95, 024036
- [319] Harari D., 2014, *Physics of the Dark Universe*, 4, 23
- [320] Berezhinsky V., Kachelriess M., Vilenkin A., 1997, *Phys. Rev. Lett.*, 79, 4302
- [321] Sigl G., 2002, *Annals of Physics*, 301, 53
- [322] Mebarki N., Abdelali M. L., 2017, On a possible solution to the UHECR GZK cut off, in *Actes de Conference : Lumiere et astronomie Alger 22-23 decembre 2015*, p. 54-58, ISBN 978-9947-0-4967-9
- [323] Kampert K.-H. et al., 2013, *Astropart. Phys.*, 42, 41
- [324] Mucke A., Enge R., Rachen J. P., Protheroe R. J., Stanev T., 1999, *Comput. Phys. Communications*, 124, 2

## BIBLIOGRAPHY

- [325] Franco J. M., 2004, *Applied Numerical Mathematics*, 50(3), 427
- [326] Davoudifar P., 2016, *J. Phys.: Conf. Ser.*, 738, 012035
- [327] Collins D. C., Xu H., Norman M. L., Li H., Li S., 2010, *Astrophys. J. Suppl.*, 186, 308
- [328] Bryan G. L. et al., 2014, *Astrophys. J. Suppl.*, 211, 19
- [329] Wang P., Abel T., 2009, *Astrophys. J.*, 696, 96
- [330] Vazza F., 2011, *Mem. Soc. Ast. It.*, 82, 609
- [331] Vazza F., Bruggen M., Gheller C., Wang P., 2014, *Mon. Not. Roy. Astron. Soc.*, 445, 3706
- [332] Shu C.-W., Osher S., 1988, *J. Comput. Phys.*, 77, 439
- [333] van Leer B., 1977, *J. Comput. Phys.*, 23, 276
- [334] Harten A., 1983, *J. Comput. Phys.*, 49, 357
- [335] Eisenstein D. J., Hu W., 1997, *Astrophys. J.*, 511, 5
- [336] Dedner A., Kemm F., Kroner D., Munz C.-D., Schnitzer T., Wesenberg M., 2002, *J. Comput. Phys.*, 175, 2, 645
- [337] Wang P., Abel T., Kaehler R., 2010, *New Astron.*, 15, 581
- [338] Kravtsov A. V., 2003, *Astrophys. J.*, 590, L1
- [339] Turk M. J., Smith B. D., Oishi J. S., Skory S., Skillman S. W., Abel T., Norman L. M., 2011, *Astrophys. J. Suppl.*, 192, 9
- [340] Eisenstein D. J., Hu W., 1998, *Astrophys. J.*, 498, 137
- [341] Abdelali M. L., Mebarki N., 2017, Impacts of a new non cosmological redshift effect on cosmological parameters estimation, in *Actes de Conference : Lumiere et astronomie Alger 22-23 decembre 2015*, p. 59-64, ISBN 978-9947-0-4967-9
- [342] Freedman W. L. et al., 2001, *Astrophys. J.*, 553, 47
- [343] Keel W. C., 2007, *The Road to Galaxy Formation*, Springer.
- [344] Gibson C. H., Schild R. E., 2007, preprint(arXiv:0710.5449 [astro-ph])
- [345] Cluver M. E. et al., 2010, *Astrophys. J.*, 710, 248
- [346] Iglesias-Paramo J., Lopez-Martin L., Vilchez J. M., Petropoulou V., Sulentic J. W., 2012, *Astron. Astrophys.*, 539, A127
- [347] Gutierrez C. M., Lopez-Corredoira M., Prada F., Eliche M.C., 2002, *Astrophys. J.*, 579, 592
- [348] Gibson C. H., Schild R. E., 2003, preprint(arXiv:astro-ph/0304107)
- [349] Duc P.-A., Cuillandre J.-C., Renaud F., 2018, *Mon. Not. Roy. Astron. Soc.: Lett.*, 475, L40-L44

## BIBLIOGRAPHY

- [350] Renaud F., Appleton P. N., Xu C. K., 2010, *Astrophys. J.*, 724, 80
- [351] Williams B. A., Yun M. S., Verdes-Montenegro L., 2002, *Astron. J.*, 123, 2417
- [352] Geng A., Beck A. M., Dolag K., Burzle F., Beck M. C., Kotarba H., Nielaba P., 2012, *Mon. Not. Roy. Astron. Soc.*, 426, 3160
- [353] Hwang J.-S., Struck C., Renaud F., Appleton P., 2012, *Mon. Not. Roy. Astron. Soc.*, 419, 1780
- [354] Nikiel-Wroczyński B., Soida M., Urbanik M., Beck R., Bomans D. J., 2013, *Mon. Not. Roy. Astron. Soc.*, 435, 149
- [355] Brammer G. B., van Dokkum P. G., Coppi P., 2008, *Astrophys. J.*, 686, 1503
- [356] Brescia M., Cavuoti S., Longo G., De Stefano V., 2014, *Astron. Astrophys.*, 568, A126
- [357] Butsky I., Zrake O., Kim J., Yang H., Abel T., 2017, *Astrophys. J.*, 843, 113
- [358] Nagamine K., Fukugita M., Cen R., Ostriker J. P., 2001, *Astrophys. J.*, 558, 497
- [359] Betoule M. et al., 2014, *Astron. Astrophys.*, 568, A22
- [360] Goobar A. et al., 2017, *Science*, 356, 291
- [361] Spiegel M. R., 1999, *Schaum's Mathematical Handbook of Formulas and Tables*, McGraw-Hill Publishing Company.

## انزياح أحمر جديد وتأثيراته

### عبد العالي محمد لمين

### ملخص

يحتوي علم الكونيات الحديث على العديد من الملاحظات الفيزيائية الفلكية غير المبررة والتي لا تزال متناقضة. من بين تلك الألغاز ، نجد تبايناً في تقديرات المعاملات الكونية ، والتوسع المتسارع في الكون ، وأصول الحقول المغناطيسية الكونية ، والعديد من الحالات الشاذة الصغيرة الحجم مثل العناقيد الصغيرة أو ارتباطات المجرات والكوازارات والأشعة الكونية عالية الطاقة. الجهود المبذولة في مجال علم الكونيات القائمة على تحديث أدوات الرصد لم تحل تلك الأسئلة. علاوة على ذلك ، تم اقتراح العديد من النظريات كتكملة أو استبدال كامل للنظريات القياسية مثل النظرية النسبية العامة لأينشتاين أو النموذج المعياري لفيزياء الجسيمات لشرح الملاحظات المتناقضة. لكنهم فشلوا في اجتياز جميع الاختبارات الكلاسيكية ولم يقدموا شرحاً تاماً لكل الملاحظات الفلكية.

في هذا البحث ، نتبنى منهجاً مختلفاً يتم فيه إعادة النظر في تفسيرنا لنتائج الرصد الفلكي في ضوء تأثيرات جديدة وغير مدروسة سابقاً تساهم في البيانات الكوسمولوجية ، خاصةً انزياح أحمر ملاحظ. من المتوقع أن يكون التأثير الجديد نتيجة التفاعل التجاذبي بين الفوتونات والمجالات المغناطيسية الثابتة التي تخلق موجات جاذبية. تتجلى الطاقة التي تحملها هذه الموجات على أنها انزياح أحمر للفوتون يساهم في تلك الانزياحات الحمراء الملاحظة. يتم تفسير المساهمات الناتجة عن هذا التأثير على أنها ناتجة عن تأثير دوبلر أو انزياح أحمر جاذبي. تستخدم الطرق التحليلية والأساليب الرقمية في هذه الأطروحة لتقدير بصمة التأثير الجديدة. مع الطرق التحليلية ، تم العثور على حلول جديدة لمعادلات ماكسويل التي تثبت الحفاظ على المجالات المغناطيسية البدائية. باستخدام الطرق الرقمية ، تم تطوير العديد من البرامج الحاسوبية مثل SCOPE و RPC والنسخة الموسعة من CRPROPA وتستخدم لتقديم التفسيرات المحتملة لعدد من الظواهر التي لم يتم فهمها.

يتم استخدام الإضافات لكلا من البرنامجين الحاسوبيين ENZO و YT لدراسة بصمة التأثيرات الحمراء باستخدام المحاكاة الكونية. لقد أظهر تحليل الملاحظات التركيبية مساهمة كبيرة من انزياحنا الأحمر الذي يؤثر على النماذج المعدلة لأعضاء خماسية ستيفان وتقديرات المعاملات الكونية وخاصة ثابت هابل. تم تحقيق عدد كبير من النتائج باستخدام البرامج الحاسوبية المطورة ، ومازلنا بحاجة إلى مزيد من التأكيد بعد المزيد من التطوير والتوسعات في الأبحاث المستقبلية.

**الكلمات المفتاحية:** المجالات المغناطيسية، موجات الجاذبية، الانزياح نحو الأحمر، محاكاة عددية، المعاملات الكونية، خماسية ستيفان، الأشعة الكونية عالية الطاقة.

# Nouveau redshift et ces implications

M. L. Abdelali

## Résumé

La cosmologie moderne a plusieurs observations astrophysiques inexplicées et paradoxales. Parmi ces mystères, on trouve des divergences dans les estimations des paramètres cosmologiques, l'expansion accélérée de l'Univers, l'origine des champs magnétiques cosmiques et plusieurs anomalies à petite échelle comme les amas compacts ou les associations galaxie-quasar et les rayons cosmiques à ultra haute énergie. Les efforts déployés dans le domaine de la cosmologie observationnelle n'ont pas résolu ces questions. De plus, plusieurs théories ont été proposées comme extensions ou remplacements complets de théories standards telles que la relativité générale d'Einstein ou le modèle standard de la physique des particules pour expliquer des observations paradoxales. Mais, ils n'ont pas réussi à passer tous les tests classiques et n'ont pas fourni d'explication cohérente de toutes les observations.

Dans cette recherche, nous adoptons une approche différente dans laquelle notre interprétation des observations est réexaminée à la lumière d'effets nouveaux et auparavant ignorés contribuant aux données cosmologiques, notamment le redshift observé. Un nouvel effet devrait être le résultat de l'interaction gravitationnelle entre les photons et des champs magnétiques constants créant des ondes gravitationnelles. L'énergie transportée par ces ondes se manifeste par un redshift de photons contribuant à ceux observés. Les contributions de cet effet sont mal interprétées comme étant causées par l'effet Doppler ou le décalage vers le bas gravitationnel. Des méthodes analytiques et en particulier des méthodes numériques sont utilisées dans cette thèse pour estimer l'impact ce nouvel effet. Avec les méthodes analytiques, de nouvelles solutions ont été trouvées pour les équations de Maxwell prouvant la préservation des champs magnétiques primordiaux lisses après la recombinaison. Avec les méthodes numériques, plusieurs codes tels que SCOPE, RPC et une version étendue de CRPROPA sont développés et utilisés pour présenter des explications possibles sur un certain nombre de phénomènes incompris.

Des extensions aux codes ENZO et YT sont utilisées pour étudier l'impact de notre effet à l'aide de simulations cosmologiques. L'analyse des observations synthétiques a montré une contribution significative de notre redshift aux modèles révisés des membres du Quintet de Stephan et les estimations des paramètres cosmologiques, en particulier la constante de Hubble. Nos codes nous a permis d'obtenir un grand nombre de résultats, qui nécessitent encore des confirmations après de nouveaux développements et extensions dans les recherches futures.

**Mots clés :** Champs magnétiques; ondes gravitationnelles; redshift; simulations numériques; paramètres cosmologiques; Le quintette de Stephan; rayons cosmiques ultra haute énergie.

## Abstract

Modern cosmology has several unexplained astrophysical observations which are still paradoxical. Among those mysteries, we find discrepancy in cosmological parameters estimations, accelerated expansion of the Universe, cosmic magnetic fields origins and several small scale anomalies like compact clusters or galaxy-quasar associations and ultra high energy cosmic rays. Efforts made in the field of observational cosmology didn't solve those questions. Moreover, several theories has been proposed as extensions or complete replacement of standard theories such as Einstein's general relativity or standard model of particle physics to explain paradoxical observations. But, they failed to account for all classical tests and didn't provide a consistent explanation of all observations.

In this research, we adopt a different approach in which our interpretation of observations is re-examined in light of new and previously unconsidered effects contributing to cosmological data especially observed redshift. A new effect is predicted to be the result of the gravitational interaction between photons and constant magnetic fields creating gravitational waves. The energy carried by these waves is manifested as a photon redshift contributing to those observed redshifts. Contributions from this effect are misinterpreted as caused from Doppler Effect or gravitational redshift. Analytical methods and especially numerical methods are used in this thesis to estimate this new effect impacts. With analytical methods, new solutions are found for Maxwell's equations proving a preservation of smooth primordial magnetic fields after recombination. With numerical methods, several codes such as SCOPE, RPC and extended version of CRPROPA are developed and is used to present possible explanations to a number misunderstood phenomena.

Extensions to both codes ENZO and YT are used to study our redshift effect impacts using cosmological simulations. The analysis of synthetic observations has shown a significant contribution of our redshift affecting revised models of Stephan's Quintet members and cosmological parameters estimations especially Hubble constant. A large number of results has been achieved using our code and still need further confirmations after more development and extensions in future research.

**Keywords :** Magnetic fields; gravitational waves; redshift; numerical simulations; cosmological parameters; Stephan's Quintet; ultra high energy cosmic rays.